Structural Investigations of Metal and Semiconductor Interfaces

Eilish McLoughlin (B.Sc.)

School of Physical Sciences

Dublin City University

A thesis submitted to

for the degree of

Doctor of Philosophy

Research Supervisor

Dr. A.A. Cafolla

September 2000

Declaration

I hereby certify that this material, which I now submit for assessment on the programme of study leading to the award of Doctor of Philosophy is entirely my own work and has not been taken from the work of others save and to the extent that such work has been cited and acknowledged within the text of my own work.

Signed: Eilish McLoughlin ID Number: 94971099

Date: 18/9/00

Contents

Abstract

Two contrasting studies of metal and semiconductor interfaces are presented.

The first study examines the coverage dependent structural transitions of Sn/Cu{100} examined by Low Energy Electron Diffraction (LEED), Auger Electron Spectroscopy (AES) and Temperature Programmed Desorption (TPD). A model consistent with both the Sn surface coverage and the complex split beam LEED pattern observed is suggested for the low coverage (θ_{Sn} = 0.21ML) ordered phase, based on a p(2×2) structure with light antiphase domain walls. For the higher coverage phases, rotated domain p(2×6) (θ_{Sn} = 0.37ML) and p(3√2x√2)R45^0 (θ_{Sn} = 0.50ML) structures are observed. Double scattering simulations based on c(2×2) local periodicity are presented for these phases. The possibility of surface alloy versus overlayer models is discussed. The monolayer phase (θ_{Sn} = 0.625ML) appears to involve de-alloying of the c(2×2) mixed layer to form an ordered Sn overlayer above Cu{100}.

In the second investigation the initial stages of formation of the Ge/GaAs(001) interface are studied by Normal Incidence X-Ray Standing Wave Spectroscopy (NIXSW) and Core Level Photoelectron Spectroscopy (PES). After submonolayer deposition of Ge onto the As-rich GaAs(001)-(2×4) surface and annealing to 875K, a sharp (1×2) LEED pattern is observed which is attributed to Ge-Ga dimerization along the [$\bar{1}$10] direction. This is explained by oudiffusion of the first layer arsenic atoms and the germanium dimerizing with the second layer gallium atoms. A model based on the formation of Ge-Ga dimers is presented based on the NIXSW and PES results. As the thickness of the Ge overlayer is increased beyond 4ML, additional weak fractional-order spots from a (2×1) reconstruction appear. From about 6ML coverage an equal intensity double domain (1×2)+(2×1) pattern is observed which is attributed to Ge-Ge dimerization as found on elemental Ge(100).

In memory of my parents

Chapter One

Introduction

"The surface was invented by the devil" said the famous physicist Wolfgang Pauli, after his frustrating attempts to understand its properties. Surfaces represent the interface between a condensed phase of matter (i.e. solid or liquid) and another phase (solid, liquid or gas). The properties exhibited by a surface are largely determined by the composition of the outermost layers of the material. While the bulk composition of a solid can to a large extent be controlled, the composition of the surface tends to critically depend on the processing steps involved in its preparation. The structural and chemical composition of a surface can be significantly different from the bulk material and consequently it may have substantially different properties. The aim of surface science is to understand the relationship between surface properties and the chemical composition of the surface.

The adsorption of metal submonolayers, monolayers and multilayers to form modified bimetallic surfaces and thin films with different lattice constants and/or crystal structures is an area receiving increased attention. These systems are potentially important in fields as diverse as heterogeneous catalysis, corrosion passivation and magnetic data storage. The Sn/Cu system is an excellent example of a complex bimetallic combination which is becoming increasingly popular in microelectronics.

Zincblende surfaces are technologically important semiconductor materials. As a consequence, numerous experiments have been performed on the deposition of many different kinds of adsorbates on zincblende substrates. The most common zincblende surface for deposition experiments is the (001) surface since it corresponds to the primarily grown plane of these materials. The adsorption of adatoms induces the formation of adsorbate-substrate bonds in addition to novel adsorbate-adsorbate structures. Bonding of an adatom to the substrate affects both the structure of the adatoms on the substrate and the kinetic processes of the overlayer formation. The zincblende compound GaAs, and elemental Ge semiconductors provide an attractive system for theoretical studies. They have the same tetrahedral crystal structure and have a negligible lattice mismatch (~0.2%).

In the late 1950s, the rise of the solid-state device-based electronics industry and the availability of economical ultrahigh vacuum provided surface science with new challenges and opportunities, resulting in an explosion of techniques. Clean surfaces of single crystals could be studied for the first time, and the preparation of surfaces and

interfaces with known atomic structure and controlled composition was driving the development of microelectronics and computer technologies. Since the 1960s, new surface instrumentation and techniques have been developed that permit the study of surface properties on the atomic scale.

Five surface science techniques were used in the course of this work to structurally investigate the initial interface formation of the Sn/Cu bimetallic system and the semiconductor Ge/GaAs heterostructure. These are (a) low energy electron diffraction (LEED), (b) Auger electron spectroscopy (AES), (c) temperature programmed desorption (TPD), (d) X-ray standing wave spectroscopy (XSW) and (e) photoelectron spectroscopy (PES).

(a) Low energy electron diffraction (LEED)

Monoenergetic electrons below ~500 eV are elastically back-scattered from a surface and detected as a function of energy and angle. LEED studies can provide information both on the symmetry of the surface structure and on the absolute positions of surface and near-surface atoms relative to one another. The symmetry of the LEED pattern reflects the symmetry of the atomic arrangement on the surface. By computational analysis of the intensity of the diffraction beams as a function of primary electron energy (I-V) it is possible to make a determination of all the atom positions.

(b) Auger electron spectroscopy (AES)

In Auger electron spectroscopy, core hole electron excitations are created, usually by 1-10keV incident electrons. Auger electrons with characteristic energies are then emitted through a two-electron process as the electrons decay to their ground state. The kinetic energy of the Auger electrons is independent of the energy of the incident electrons and are solely characteristic of the electrons within the atom. Hence, Auger electrons may be used for elemental investigation.

(c) Temperature programmed desorption (TPD)

An adsorbate-covered surface is heated, usually at a linear rate, and the desorption of atoms or molecules are detected with a mass spectrometer. This gives information on the nature of the adsorbate species and some information on adsorption energies and the surface structure.

(d) X-ray standing wave (XSW) spectroscopy

When X-rays are Bragg reflected from a set of scattering planes, the incident and reflected waves constructively interfere to set up a standing wave with a periodicity in intensity equal to that of the spacing of the associated scattering planes. It can be shown that within the field of the standing wave the phase shifts by half the bulk layer spacing of the scattering planes. Hence by measuring the absorption of X-rays by adsorbed atoms as the intensity of the wavefield shifts, it is possible to deduce the location (vertical height) of the absorber relative to the scattering planes.

(e) Photoelectron spectroscopy (PES)

In this technique electrons photoemitted from atomic core levels are detected as a function of energy. Since the binding energy of electrons is both element specific and sensitive to chemical environments, photoelectron spectroscopy can provide information about the chemical and electronic structure of a solid. With careful selection of the experimental parameters, the observed photoelectrons will only come from the first few atomic layers of the sample, that is the technique is surface sensitive under these conditions.

All of these techniques provide some structural information on the system being studied, complementing the main structural techniques of LEED I-V and XSW. Dynamical LEED I-V calculations are commonly used to investigate metal surfaces and interfaces, with many structural investigations reported in the last few decades. The calculations for semiconductor systems are however more difficult. XSW is a relatively new structural technique, which is suitable for studies of both semiconductor and metal interfaces.

In Chapter Two, the physical basis behind the techniques used in this work is discussed. The LEED, AES and TPD experiments were carried out in Dublin City University, while the XSW and PES investigations were performed at Daresbury Synchrotron Source, UK. The experimental considerations for these techniques are given in Chapter 3. In the study the of Sn/Cu{100} system, LEED I-V profiles were measured for four phases occurring at submonolayer coverages of Sn. New structural models were proposed for the observed LEED patterns based on double scattering simulation codes. TPD and AES were used as complementary techniques to differentiate between proposed models in this investigation. The results for the Sn/Cu{100} bimetallic system

are presented in Chapter Four. The initial stages of formation of the Ge/GaAs(001) interface are discussed in Chapter Five. This semiconductor system was investigated using the synchrotron-based techniques, X-ray standing wave spectroscopy and core level photoelectron spectroscopy.

Chapter Two

Physical Basis of Experimental Techniques

This chapter describes the physical basis of the experimental techniques used to investigate the initial stages of formation of Sn/Cu{100} and Ge/GaAs(001) interfaces. In order to understand the formation of interfaces, an introduction to the surface structure of bulk crystals and the growth behaviour of adsorbates on crystal surfaces is presented in Section 2.1. A discussion of the Low Energy Electron Diffraction (LEED) and Auger Electron Spectroscopy (AES) techniques that use electrons as surface sensitive probes is given in Sections 2.2 and 2.3. Temperature Programmed Desorption (TPD) studies are described in Section 2.4 for the investigation of the reactivity of the substrate and adsorbate/substrate structure. These three techniques were used for investigation of the Sn/Cu{100} interface. A description of the synchrotron radiation based techniques, such as X-ray Standing Wave spectroscopy (XSW) and Photoelectron Spectroscopy (PES), which provide information on structural and chemical properties of surfaces and interfaces, is presented in Sections 2.5 and 2.6. These two techniques are used to examine the initial stages of formation of the Ge/GaAs(001) interface.

2.1 Introduction

Copper forms a face centred cubic crystal, while GaAs has a zincblende structure. The ideal atomic arrangement for the low index planes of these two crystal structures is illustrated in Section 2.1.1. However, in real crystals, relaxation or reconstruction of the surface atoms occurs when a surface forms. These phenomena are discussed in Section 2.1.2. When metals and semiconductors are adsorbed on crystal surfaces, the surface adsorbate growth is characterised by the formation of overlayer or surface alloy structures. An overview of the different growth modes is presented in Section 2.1.3. The structure of the surface and the initial interface between heterostructures may be examined both experimentally and theoretically. Surface sensitive techniques are required to study properties of both the adsorbate and the crystal selvedge. Surface scientists refer to the "selvedge" region as the area near the surface where the crystal properties are different from those of the bulk. It generally relates to the top four or five layers of the crystal, although the actual thickness is dependent on the material being studied. In Section 2.1.4, electrons are shown to be highly surface sensitive probes that may be used for structural investigations.

2.1.1 Crystal Structure

Single crystal structures have atoms arranged in a regular repeating lattice structure. For example, metals adopt close-packed crystal structures such as face-centred-cubic, fcc (e.g. Cu, Ni, Pd); body-centred-cubic, bcc (e.g. Fe, Cr, Mo) and hexagonal-closed packed, hcp (e.g. Co, Ti, Ru). Examples of simple crystal structures based on fcc structures are diamond (e.g. Si, Ge) and zincblende (e.g. GaAs and InSb). For a more detailed description of crystal structures see Kittel [Kittel 1976]. Figure 2.1 shows the unit cell of a cubic lattice with different cross-sections yielding different surface atomic arrangement, which are identified by their Miller indices. Shown are the surface atomic arrangement for the {100}, {110} and {111} planes of a fcc crystal and a zincblende crystal, respectively.

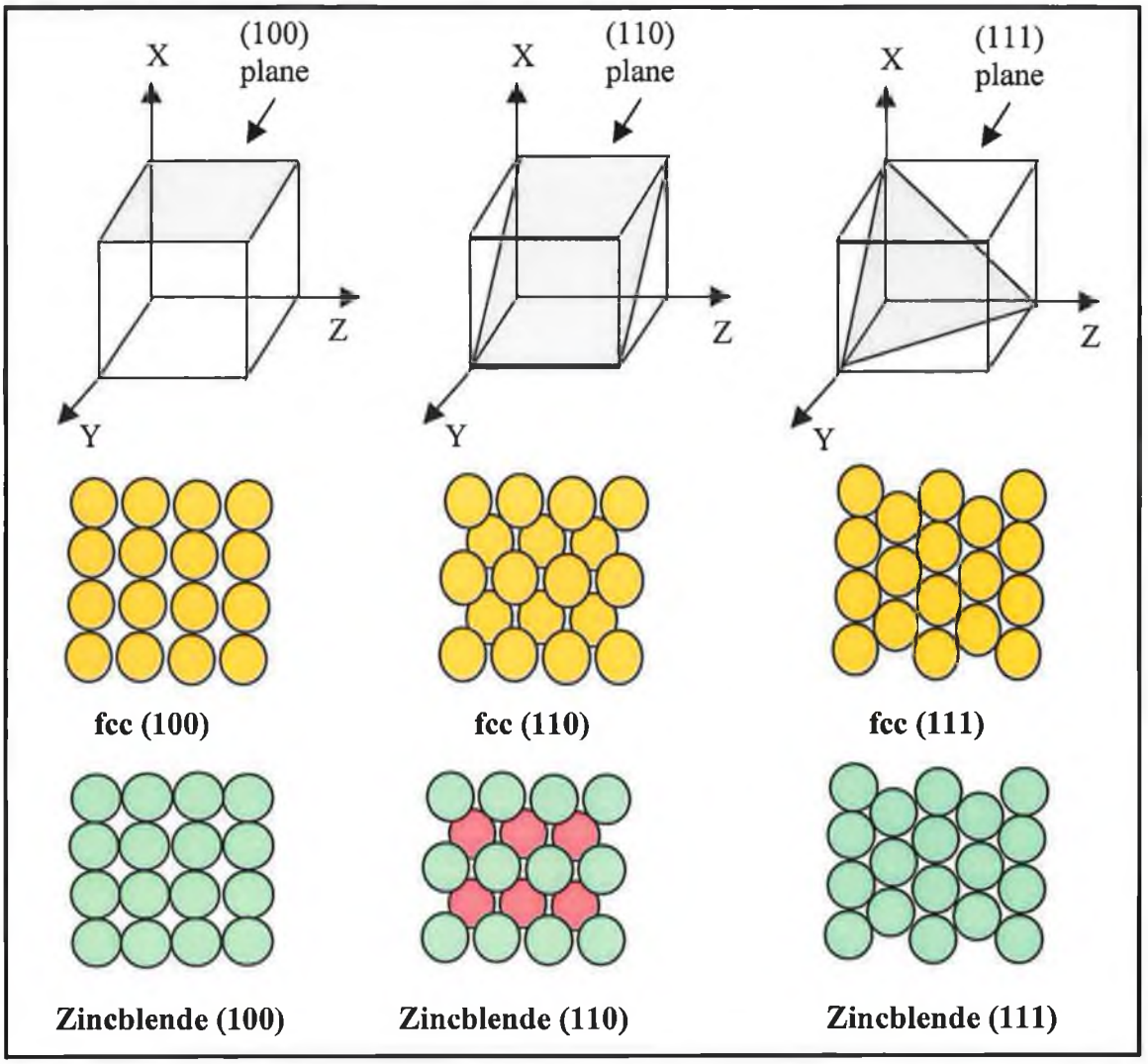

Figure 2.1 *Unit cell of a single cubic lattice showing the {100}, {110}, {111} surface planes and the atomic arrangement of these planes for a fcc and zincblende crystal.*

2.1.2 Surface Structure

The structure at the surface can differ from the bulk crystal because the surface atoms have lost some of their nearest neighbour atoms. For example, in the case of the low-index surfaces shown in Figure 2.1, atoms in the {100}, {110} and {111} fcc planes have lost 7, 8 or 9 nearest atoms compared to their normal coordination number of 12 in the bulk [Attard 1998]. In order for the surface to compensate for the 'loss' of bonding, it may undergo *surface relaxation* in the form of an oscillatory change in the interlayer spacing Δd. This occurs by the first layer atoms contracting towards the second layer to increase their coordination. The third layer atoms respond by expanding away from second layer atoms and hence compensating for the over-coordination of the second layer. This oscillation in Δd penetrates deeper into the surface until, eventually, it is completely damped. The region of the surface that may be distinguished from the bulk is typically 5-6 atomic layers thick and is termed the selvedge. Surface relaxation is, in general, largest for low atomic density (more open), high energy surfaces. Hence, for fcc metals, the surface energy decreases in the order: {110} > {100} > {111}.

If the surface energy is sufficiently large, not only will surface relaxation occur but also gross restructuring of the surface plane. This increases the coordination of surface atoms and hence produces a lower surface energy. When simple truncation of the bulk crystal does not lead to the 'expected' surface periodicity, the effect is termed *surface reconstruction*. Surface reconstruction is particularly common in semiconductors, which tend to exhibit more localised covalent bonding [Luth 1993].

2.1.3 Growth Modes

Due to scientific and technological interest, many studies are concerned with growth modes of adsorbates on metal and semiconductor substrates. Temperature, deposition rate and defects of both the substrate and of the growing film drastically influence the growth modes in homoepitaxial systems of metals and semiconductors. For heterogeneous systems, the lattice mismatch must also be accommodated during growth by the formation of either (a) epitaxial or overlayer structures or (b) surface alloy structures.

(a) Epitaxial Growth

The term epitaxial growth is used when an ordered overlayer structure is formed upon deposition on a single crystal surface. In many cases, such as the adsorption of metals and semiconductors on solid surfaces, the adsorption does not terminate upon the completion of a single monolayer and multilayer structures may be fabricated. Growth of overlayers with a lattice structure (e.g. fcc, bcc, hcp) different from that of the bulk structure is possible under the influence of the substrate. Hence, growth of such films offers an exciting range of possibilities for the creation of new materials with chemical and physical properties not encountered naturally. A more restricted definition of epitaxial growth, pseudomorphic growth, would include only those examples where the substrate imposes its own crystal structure, orientation and lattice parameter on the adsorbed layer [Pashley 1999] [Somorjai 1994] [Henzler 1993].

Epitaxial growth was broadly classified into three growth modes, based on their original investigators, namely, (i) Frank-van der Merve (FM), (ii) Volmer-Weber (VW) and (iii) Stranski-Krastanov (SK) modes, shown in Figure 2.2 [Bauer 1986]. According to the quasi-equilibrium description given by Bauer these three modes are governed by the surface free energies of the deposited adatoms (γ_A), the substrate (γ_S) and the interface energy ($\gamma_{A\text{-}S}$) according to the parameter:

$$\Delta\gamma = \gamma_A + \gamma_{A-S} - \gamma_S \qquad (2.1)$$

(i) *Frank-van der Merve (FM) : Monolayer by monolayer growth*

$$\Delta\gamma \leq 0$$

If there is a large difference between the two surface free energies then the parameters γ_A and γ_S will strongly influence the growth mechanism. In FM growth the adatoms are more strongly bound to the substrate than to each other. The initial adatoms condense to form a complete monolayer. Then a less tightly bound second layer covers this. If the decrease in bonding is monotonic towards the value of the bulk crystal then layer growth may occur. Whether FM growth persists to high coverages is strongly dependent on the strain energy, that is the lattice mismatch between the substrate and adsorbate atoms. If the mismatch is large then continued FM growth is unlikely, however it is possible in systems with large lattice mismatch provided that the strain energy within the layers can be relieved (i.e. by defect mechanisms). In reality, true FM growth can

only occur for homogeneous systems where the strain energy is zero, (e.g. Cu grown on Cu).

(ii) *Volmer-Weber (VW): Island growth*

$$\Delta\gamma > 0$$

In this mode adatoms grow as three-dimensional islands. The adatoms are more strongly bound to each other than to the substrate and small clusters nucleate directly on the surface as adsorbate growth progresses.

(iii) *Stranski-Krastanov (SK): Monolayer plus islanding growth*

$$\Delta\gamma < 0$$

SK growth refers to growth of islands following the deposition of one or more complete monolayers. Any factor that disrupts the monotonic decrease in binding energy with coverage, thereby resulting in a high free energy as the adlayer surface, may cause layer growth to become unfavourable. The bonding energetics of a system, large lattice mismatches and the method of adsorbate growth, are the major influences on the development of a SK growth mode.

Auger electron spectroscopy (see Section 2.3) is a valuable technique frequently employed to monitor epitaxial film growth. Auger electron emission from the substrate atoms decreases in intensity, whereas Auger emission from the adsorbate increases in intensity as a function of coverage. Figure 2.2 demonstrates the distinct behaviour of the Auger signal versus time (AS-t) plots for each growth mode. Two additional growth modes were suggested from AS-t plots, by Argile and Rhead in 1989, namely simultaneous multilayer growth (SM), and monolayer plus simultaneous multilayer growth (MSM) [Argile 1989]. The SM mode can be considered in an idealised case arising from negligible surface mobility. Each vapour atom impinging on the surface sticks where it hits with no lateral motion and growth progresses by layers building up randomly. In MSM mode there is sufficient surface mobility to produce uniform continuous growth of the first monolayer before the mobility drops to a negligible level and growth is subsequently SM.

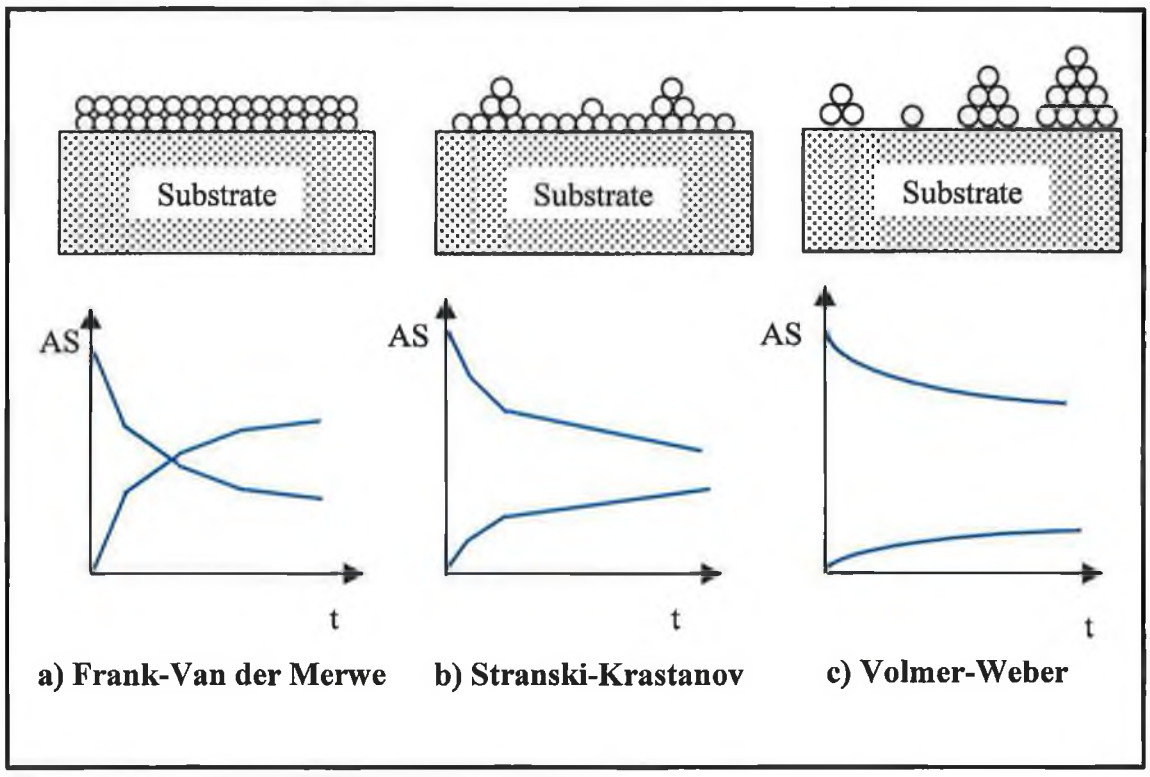

Figure 2.2 *Epitaxial Growth Modes: (a) Frank-Van der Merwe; (b) Stranski-Krastanov; and (c) Volmer-Weber.*

(b) Surface Alloying through metal-on metal deposition

The three idealised growth modes described above neglect the possibility that the substrate atoms are mobile and may segregate to the surface of the adlayer or inter-diffuse with the arriving adatoms during film growth. Increasing the substrate temperature activates inter-diffusion and surface segregation [Rodriguez 1996] [Bardi 1994].

Inter-diffusion or *surface alloying*, to form stable two-dimensional mixtures at the free surface, has been found for elements that are known to be immiscible in the bulk. Such surface-confined mixing is expected quite generally in systems that are dominated by the atomic size mismatch. Mismatch renders the elements immiscible in the bulk, and confines the minority species to the surface [Tersoff 1995].

Surface segregation can be considered a special form of substrate/adlayer inter-diffusion where a whole layer or layers, rather than single adatoms, are buried in the substrate. Segregation may occur when the surface free energy of the substrate atoms is

lower than the adlayer surface free energy. This situation favours island (VW) growth. The islands, once formed, can lower their surface energy by allowing themselves to be coated by a thin film of the substrate atoms, i.e. the adsorbate atoms are shown to have gone *subsurface*.

2.1.4 Surface Sensitivity

Electron-based probes have commonly been used in surface science experiments [Powell 1994]. This section gives an introduction to the surface sensitivity of electrons and their suitability as surface probes in techniques such as Low Energy Electron Diffraction in Section 2.2 and Auger Electron Spectroscopy in Section 2.3.

The surface sensitivity of electron-based probes of surfaces arises from the very strong inelastic scattering of low-energy electrons in the range 40-100eV, in solids. An electron travelling through a solid will have a certain inelastic mean free path (IMFP), that is, a characteristic length that it can travel without suffering an energy loss. Seah and Dench have provided the most comprehensive study of inelastic mean free path (IMFP) lengths in solids for energy in the range 0-10keV, see Figure 2.3.

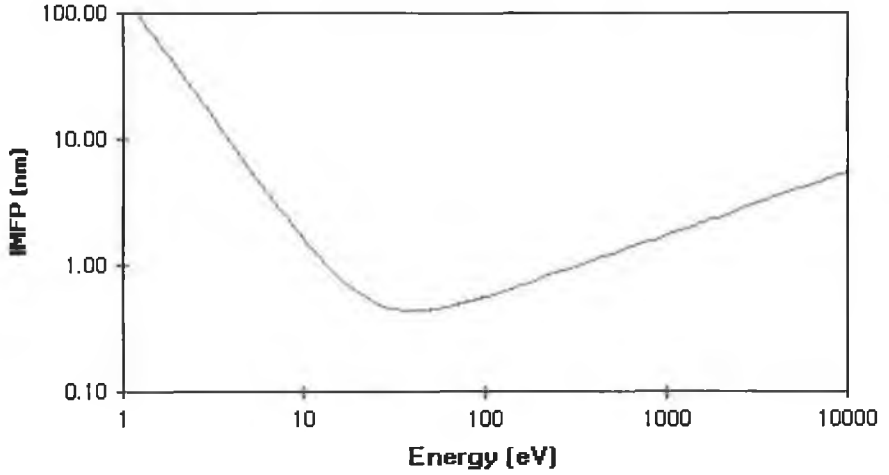

Figure 2.3 *Universal Inelastic Mean Free Paths versus electron kinetic energy for solids [Nix 1996].*

The empirical expression for the photoelectron escape depth in an element (e.g. Cu) is given by:

$$\lambda_m = 538E^{-2} + 0.41(aE)^{1/2} \qquad (2.2)$$

and in an inorganic solid (e.g. GaAs) by:

$$\lambda_m = 2170E^{-2} + 0.72(aE)^{1/2} \quad (2.3)$$

where E is the electron energy above the Fermi level (eV) and a is the thickness of a monolayer in nanometres [Seah 1979]. The IMFP is shown to vary quite significantly with the kinetic energy of the electron. Essentially at very low kinetic energies, electrons are unable to excite any of the loss mechanisms, e.g. plasmon excitation, and the IMFP is subsequently long. At very high energies the cross section for these losses is also low and again the mean free path is long. The most important point to note is that electrons with kinetic energies in the 40-150 eV range have the shortest mean free paths <1nm and thus are highly surface sensitive.

Knowing the value of the IMFP of a material allows the calculation of the thickness of an adsorbate layer. The electron intensity, I, will be attenuated, due to inelastic scattering of some of the electrons as they traverse through the adsorbate layer. In the presence of an adsorbate layer of unknown thickness, t, the electron intensity is defined as:

$$I = I_0 \exp(-t/\lambda) \quad (2.4)$$

where I_0 is the electron intensity in the absence of the adsorbate and λ is the IMFP of the substrate.

2.2 Low Energy Electron Diffraction (LEED)

2.2.1 Introduction

LEED crystallography for the study and determination of the atomic structure of surfaces was born in 1927, with the famous experiment of Davisson and Germer, proving that electrons are waves and can be diffracted by crystal surfaces [Davisson 1927]. Rather little experimental LEED work was carried out during the period between its original discovery and the early 1960's. This was presumably due both to the technological complexity of the measurement and the lack of an adequate theory. It wasn't until the 1970's that experimental and theoretical advances made LEED a functional tool for surface-structure determination.

Electrons with energies varying from about 10 to 500eV penetrate 1-10 atomic layers. These electrons have wavelengths of 1.0-0.1Å which are of the same order of magnitude as the inter-atomic spacing at the surface of a single crystal [Jona 1982].

$$\lambda = \left(\frac{h}{mv}\right) = \left(\frac{150}{V}\right)^{1/2} \text{ Å} \tag{2.5}$$

where mv is the electron momentum and V is the voltage through which the electrons have been accelerated. These electrons are ideal probes for surface studies as they are very easily scattered, both elastically and inelastically by atoms and are back-scattered out of the crystal revealing atomic arrangement of atoms in the first few layers.

The elastically reflected electrons can produce a diffraction pattern, from which the two-dimensional periodicity of the surface unit may be deduced from the positions of the diffracted beams. Variations in the unit cell size induced by adsorption can also be observed. From the variations of spot intensities with beam energy, the complete surface geometry, including bond lengths and angles, can be determined [Clarke 1985].

2.2.2 Theory of Low Energy Electron Diffraction

Diffraction theory can be explained in terms of the electron wavevectors and the reciprocal lattice vectors. The magnitude of the incident wavevector $\mathbf{k_0}$ is defined as:

$$|\mathbf{k_0}| = \frac{2\pi}{\lambda} \tag{2.6}$$

Substituting the de Broglie electron relationship:

$$\lambda = \left(\frac{h}{mv}\right) \tag{2.7}$$

leads to

$$|\mathbf{k_0}| = \frac{2\pi}{h} mv \tag{2.8}$$

Substituting into the diffraction equation

$$\sin\theta_a = \frac{n\lambda}{a} \tag{2.9}$$

and eliminating λ, gives

$$|\mathbf{k_0}| \sin\theta_a = \left(\frac{2\pi}{a}\right) n \tag{2.10}$$

where $|\mathbf{k}_0|\sin\theta_a$ is the momentum component parallel to the surface ($\mathbf{k}_{0||}$ in Figure 2.4). a is the lattice spacing and θ_a is the angle at which the constructive interference condition is satisfied at integer values of n. $\left(\frac{2\pi}{a}\right)$ is the magnitude of the one-dimensional reciprocal lattice vector [Attard 1998].

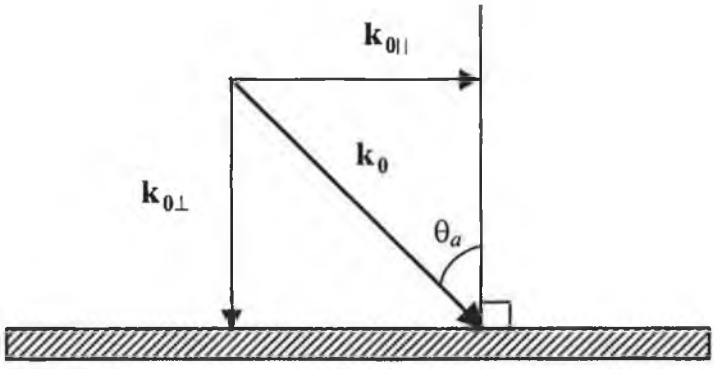

Figure 2.4 *Resolution into parallel and perpendicular components of an electron with incident wave vector* $\boldsymbol{k}_0$.

For a one-dimensional array of atoms, the diffraction pattern consists of a single set of parallel lines. For periodicity in a second orthogonal direction with lattice constant b, another set of diffracted beams with an inversely proportional relationship to the lattice spacing, $\left(\frac{2\pi}{b}\right)$, is produced. The exchange of parallel momentum can then be represented by a two-dimensional reciprocal lattice vector ($\mathbf{G}^*$),

$$\mathbf{G}^* = \Delta\mathbf{k}_{||} = n\frac{2\pi}{a} + m\frac{2\pi}{b} \tag{2.11}$$

or represented as

$$\mathbf{G}^* = n\mathbf{a}^* + m\mathbf{b}^* \tag{2.12}$$

where

$$|\mathbf{a}^*| = \frac{2\pi}{|\mathbf{a}|},\ |\mathbf{b}^*| = \frac{2\pi}{|\mathbf{b}|},\ \mathbf{a}\times\mathbf{b}^* = \mathbf{a}^*\times\mathbf{b} = 0$$

and n,m are integers and $\boldsymbol{a}$ and $\boldsymbol{b}$ are the lattice vectors of the surface two-dimensional unit cell and $\mathbf{a}^*$ and $\mathbf{b}^*$ are the reciprocal lattice vectors.

The condition of diffraction is then represented by:

$$\mathbf{k}_{0||} = \mathbf{k}_{S||} \pm \mathbf{G}^* \tag{2.13}$$

where $\mathbf{k}_{s_{\|}}$ is the parallel component of the scattered electron wavevector. The conservation of momentum $\mathbf{k}_{0_{\|}} = \mathbf{k}_{s_{\|}} \pm \mathbf{G}^*$ means that if a **G*** vector is exchanged with the surface, the incident electron must undergo a change in direction in order to conserve momentum. As the incident electron beam energy increases, $|\mathbf{k}_0|$ increases, more and more spots will appear on the LEED screen. The spacing between the spots will progressively decrease and the pattern converges towards the centre of the screen. The LEED pattern is a direct image of the reciprocal space, so the distance between adjacent points in a LEED pattern is inversely proportional to the distance between points in the corresponding direction of the real surface unit mesh.

2.2.3 Interpretation of LEED patterns

The simple production of a LEED photograph, without an analysis of the intensities of the individual spots, is by far the most widespread use of LEED. It is routinely used to check for cleanliness and the order of surfaces being prepared for other experiments. The pattern of LEED spots can be used to obtain information about surface symmetry or surface reconstruction, or about imperfections in the surface, such as steps or islands. It may also be used to determine if molecules on the surface are adsorbed in an ordered or random way. If the overlayer is ordered, its surface unit mesh can be determined.

An ideal surface may be identified easily by reference to the bulk plane of termination e.g. Cu{100}. However, it is common for the atoms in the top most layer to reconstruct into a new net which is different from the bulk termination. A form of nomenclature is required, which describes the orientation of the new net of the reconstructed surface on the bulk and which can also be used to describe the orientation of adsorbed overlayers on any surface. Two notations are commonly used to describe LEED patterns for single crystals and adsorbate structures, namely Matrix notation or Wood's notation.

In matrix notation, the reciprocal unit cell vectors of the overlayer $\mathbf{a}_0^*$ and $\mathbf{b}_0^*$ are defined in terms of a linear combination of the reciprocal substrate mesh vectors $\mathbf{a}_S^*$ and $\mathbf{b}_S^*$.

$$\mathbf{a}_0^* = G_{11}^* \mathbf{a}_S^* + G_{12}^* \mathbf{b}_S^*$$

$$\mathbf{b}_0^* = G_{21}^* \mathbf{a}_S^* + G_{22}^* \mathbf{b}_S^* \tag{2.14}$$

To convert from reciprocal space to real space an 'inverse transpose' of the matrix G* is calculated.

$$G = \left(\left[G^* \right]^{-1} \right)^t = \frac{1}{\det G^*} \begin{bmatrix} G_{22}^* & -G_{21}^* \\ -G_{12}^* & G_{11}^* \end{bmatrix} \tag{2.15}$$

where det G* is the determinant of the matrix G* and is obtained by cross multiplication.

$$\det G^* = (G_{22}^* \cdot G_{11}^*) - (G_{21}^* \cdot G_{12}^*) \tag{2.16}$$

The matrix $G = \begin{pmatrix} G_{11} & G_{12} \\ G_{21} & G_{22} \end{pmatrix}$ relates the real space overlayer vectors ($\mathbf{a}_0$ and $\mathbf{b}_0$) in terms of the real space substrate unit vectors ($\mathbf{a}_S$ and $\mathbf{b}_S$).

$$\begin{pmatrix} \mathbf{a}_0 \\ \mathbf{b}_0 \end{pmatrix} = \begin{pmatrix} G_{11} & G_{12} \\ G_{21} & G_{22} \end{pmatrix} \begin{pmatrix} \mathbf{a}_S \\ \mathbf{b}_S \end{pmatrix} \tag{2.17}$$

where G_{11}, G_{12}, G_{21} and G_{22} are constants and the subscripts refer to the position of the constants in the matrix.

Wood's notation takes the form

$$M(h,k,l) - i\left(\frac{|\mathbf{a}_0|}{|\mathbf{a}_S|} \times \frac{|\mathbf{b}_0|}{|\mathbf{b}_S|}\right) - R\alpha^\circ - A \tag{2.18}$$

where *M* is chemical symbol of the substrate; *(h,k,l)* the Miller index of the surface plane; *i* is either "p" (for primitive) or "c" (for centred) according to the way the unit cell of the overlayer is formed; $|\mathbf{a}_S|$ and $|\mathbf{b}_S|$ are the magnitudes of the substrate net vectors; $|\mathbf{a}_0|$ and $|\mathbf{b}_0|$ are the magnitudes of the overlayer net vectors; α is the angle between the substrate and overlayer meshes and *A* is the chemical symbol of the adsorbed species.

To illustrate matrix and Wood's notation, two examples are shown in Figure 2.5. The (100) surface of the FCC clean copper crystal has a square lattice structure with $|\mathbf{a}_0| = |\mathbf{b}_0|$ and can be represented in Wood's notation as a p(1×1) structure as shown in Figure 2.5 by blue vectors. This is represented in matrix notation as $\begin{pmatrix} 1 & 0 \\ 0 & 1 \end{pmatrix}$.

If an adsorbate A forms an overlayer on Cu{100} defined by $\mathbf{a}_0 = \frac{1}{2}\mathbf{a}_S + 0\mathbf{b}_S$ and $\mathbf{b}_0 = 0\mathbf{a}_S + \mathbf{b}_S$ then, as shown by the red vectors in Figure 2.5, the superlattice is represented in Woods notations as

$$\text{Cu (100)-p(2×1)-A}$$

and in matrix notation as $\begin{pmatrix} 2 & 0 \\ 0 & 1 \end{pmatrix}$.

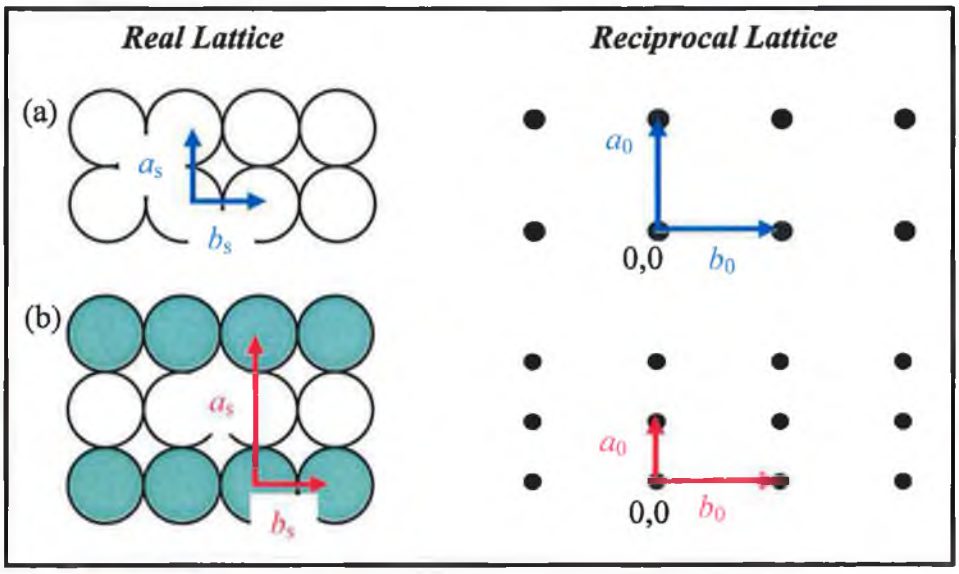

Figure 2.5 *Example of (a) (1×1) and (b) (2×1) overlayer structures.*

LEED studies can provide information both on the symmetry of the surface structure and on the absolute positions of the surface and near-surface atoms relative to one another. However, because of the energy spread and angular divergence of the incident beam the electrons have a limited *coherence length* at the surface, typically 50-100Å [Vickerman 1997]. Features that occur on a larger scale than this will not be detected.

Real surfaces are far from ideal and contain atomic steps and other defects. Hence, instead of one large two-dimensional domain, a surface adsorbate generally consists of an array of domains of diameters between 20 and several hundred angstroms, separated by areas of clean surface. As the surface coverage is increased, the domain density rises, until the whole surface is covered with an array of densely packed islands with boundaries between them. The arrangement of the adsorbed atoms and molecules on a surface relative to the underlying substrate (the superlattice) may be termed as either (i) commensurate or (ii) incommensurate.

A *commensurate overlayer* forms when the substrate-adsorbate interaction tends to dominate over any lateral adsorbate-adsorbate interaction. Each adsorbate adopts an inter-adsorbate separation that is either equal to that of the substrate atoms or a simple multiple of the substrate spacing. In the case of an *incommensurate overlayer*, the adsorbate-adsorbate interactions are of similar magnitude to those between adsorbate and substrate. The spacing adopted is a compromise between minimising both adsorbate-substrate and adsorbate-adsorbate interaction energy. This leads to an adsorbate-adsorbate spacing that is irrationally related to the substrate lattice spacing and a wide range of different local adsorption sites. Matrix notation can be used to describe overlayer structures that are both commensurate and incommensurate, while Wood's notation is limited to commensurate structures.

An important consideration in the pattern symmetries is the occurrence of domains (also called mosaics). Domains are a form of long-range imperfection in which distinct patches of the surface coexist. These different patches have mutually identical structures, but they do not mesh together without breaks in the periodicity [Van Hove 1986]. This results in domain boundaries across which the periodicity is broken. There are several kinds of domain symmetries: transitional, rotational, mirrored and combinations thereof, e.g. glide-plane symmetry combines translation and mirrored. In translation domains the position of each domain is related to another domain by a translation through a multiple substrate lattice vector. *Antiphase domains* occur in some translational domains when the fractional-order spots receive contributions from both sides of a domain boundary that are exactly out-of-phase. The structure in Figure 2.6 (a) is described as a (2×1) superlattice with rotational domains. Figure 2.6 (b) shows the corresponding diffraction pattern where the (1×2) superlattice represents a (2×1) domain rotated by 90°, or simply a double domain (2×1) superlattice.

If the domains present on a surface are large compared to the coherence length of the incident electron beam, then each domain can be considered to contribute independently to the diffraction pattern. The pattern then becomes the sum of the individual diffraction patterns of each domain. Smaller domains of irregular sizes produce disorder effects in the diffraction pattern, such as weakened and broadened fractional-order spots and diffuse intensity distributions.

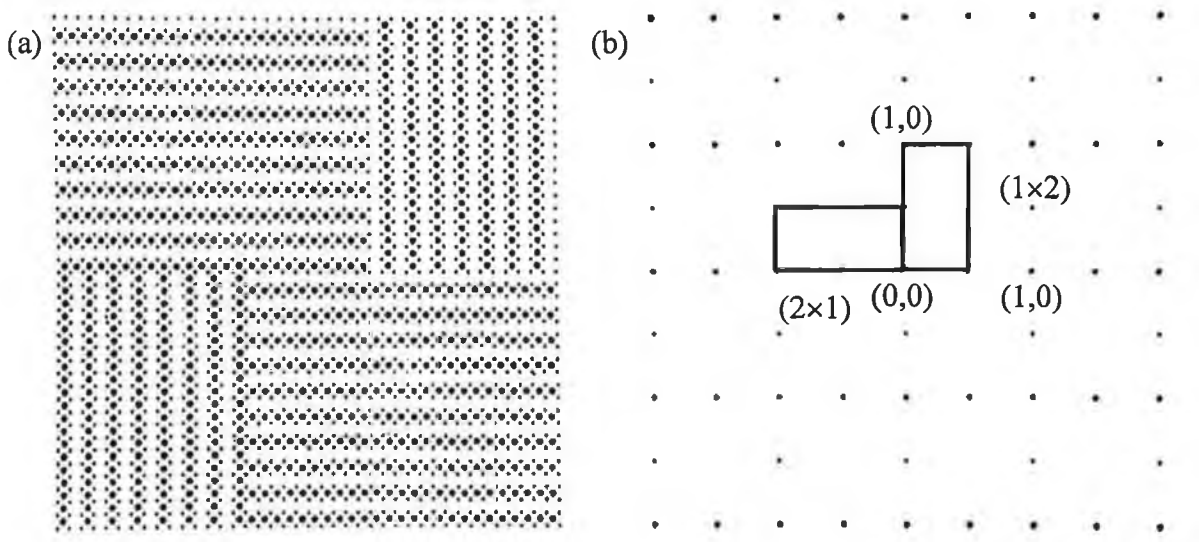

Figure 2.6 *(a) 2×1 superlattice (large dots) on a square lattice (small dots) with rotational domains. (b) The corresponding diffraction pattern with the (2×1) and (1×2) superlattices indicated [Van Hove 1986].*

Another feature observed in diffraction patterns is *spot splitting*, where a cluster of spots appears that are obviously derived from a single spot. Splitting of the integral order beam is observed as a result of stepped surfaces. Splitting occurs for all integral-order spots simultaneously and varies with the electron energy. Patterns that display spot splitting of just the fractional order beams may occur for overlayers, when the adatom coverage is varied or during annealing of overlayer structures. The general cause of splitting of fractional-order beams is the coexistence of antiphase domains. The observed LEED pattern strongly reflects the superlattice structure existing within each domain but because of the regular antiphase arrangement, a larger surface lattice exists. This causes spot splitting of the fractional-order beams with the ratio of the spot splitting to the integral-order spot separation corresponding to the size of the domain. That is, for a domain size of N unit cells, the spot-to-spot-distance in the split diffraction beam is equal to 1/N. The orientation of the spot splitting indicates directly the relative orientation of the domains. If the domains have a random orientation, then the result is diffuse spot splitting. There is also the possibility that domains form in small patches, as shown in Figure 2.6. In this example, an ordered array of domains can exist in both surface directions and spot splittings can occur in both directions as well [Van Hove 1986].

2.2.4 Quantitative analysis of Low Energy Electron Diffraction

The previous section illustrated how much structural information may be extracted from a LEED pattern, without attempting to analyse the intensities of the diffracted beams. To obtain additional structural data about the surface, for example atomic coordinates, bond lengths, bond angles, adsorption sites, it is necessary to study the beam intensities [Van Hove 1986] [Jona 1982] [Marcus 1982]. A plot of Intensity versus Electron Voltage (I-V) of the LEED beams possesses characteristic peak positions and intensities for a given surface structure. These structures can be interpreted by carrying out calculations using either (a) the kinematic theory or (b) the dynamically theory of diffraction.

(a) Theoretically the most convenient situation arises when only single scattering occurs, in this case an electron that has been scattered once by a surface atom will not be scattered again by a surface atom. This describes the kinematic limit of diffraction and leads to a relatively simple theory for the interpretation of diffraction data.

(b) The dynamical theory of LEED, includes the effects of multiple scattering of the diffracting electron occurring within an individual atom and multiple scattering of the diffracting electron occurring between the atoms of the crystal structure.

(a) Kinematic LEED Theory

Kinematic theory is used to describe the diffraction of electrons incident on the surface suffering only a single scattering event when interacting with the ion cores. Much of the kinematic theory is based on the theory of optical scattering. In order to explain the LEED process, diffraction from a one-dimensional periodic grating is considered [Gasser 1985].

<u>One-dimensional grating</u>

The incident and scattered waves are defined by the unit vectors $\mathbf{S_0}$ and $\mathbf{S}$, which identify the direction of the waves. The wave with vector $\mathbf{S_0}$ is incident at an angle θ_i on a grating consisting of a row of point scatterers with separation defined by a vector $\boldsymbol{d}$. The outgoing wavevector $\mathbf{S}$ is at an angle θ_r, as shown in Figure 2.7. The path difference Δ between waves scattered by adjacent atoms satisfies the condition

$$\Delta = \mathbf{d}(\sin\theta_r - \sin\theta_i) \tag{2.19}$$

The overall path difference can be expressed as:

$$\Delta = \mathbf{d}\cdot\mathbf{S} - \mathbf{d}\cdot\mathbf{S}_0 = d\cdot(\mathbf{S}-\mathbf{S}_0) \tag{2.20}$$

For constructive interference between the outgoing wavevectors, the path difference Δ must be an integral number of wavelengths, that is

$$n\lambda = \mathbf{d}\cdot(\mathbf{S}-\mathbf{S}_0) \tag{2.21}$$

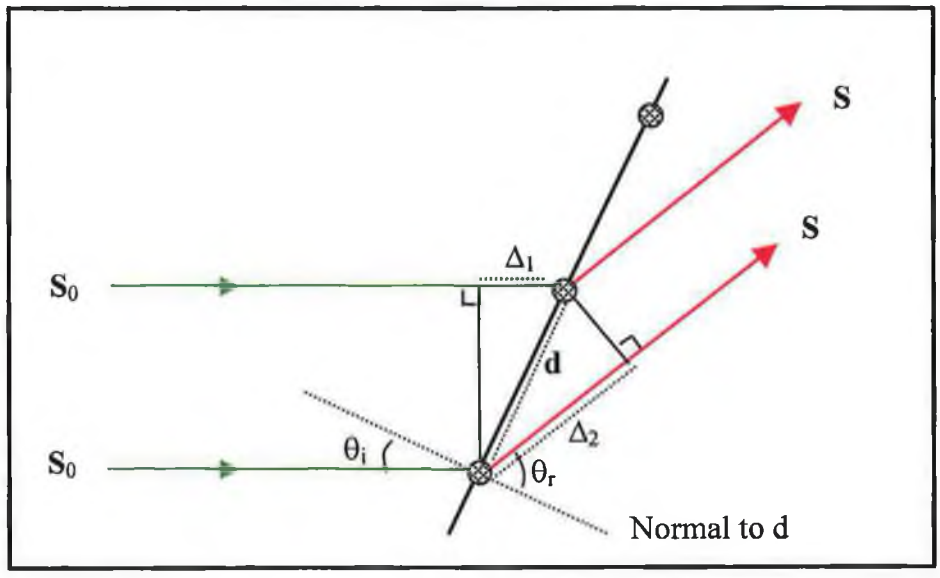

Figure 2.7 *Scattering by a one-dimensional grating of spacing* ***d****, where* $\boldsymbol{S_0}$ *is the incident-wave unit vector and* ***S*** *is the scattered wave unit vector.*

A scattering vector ***K*** is now defined as

$$\mathbf{K} = \frac{2\pi}{\lambda}(\mathbf{S}-\mathbf{S}_0) \tag{2.22}$$

Thus

$$2\pi n = \mathbf{d}\cdot\mathbf{K} \tag{2.23}$$

This is called the Laue condition for constructive interference for a one-dimensional lattice. If there are M scattering centres giving rise to interference, the intensity I(***K***) of the scattered wave is

$$I(\mathbf{K}) = \frac{A^2\sin^2\{(M/2)\mathbf{K}\cdot\mathbf{d}\}}{\sin^2(\frac{1}{2}\mathbf{K}\cdot\mathbf{d})} \tag{2.24}$$

where A is the amplitude of the incident beam [Gasser 1985].

Two-dimensional grating

The approach adopted in the previous section can be extended to analyse a two-dimensional array of scattering points, i.e. a surface. If the vectors defining the unit mesh are ***a*** and ***b***, the Laue interference conditions become two simultaneous equations

$$\mathbf{K}\cdot\mathbf{a} = 2\pi h \qquad (h=0,1,2,\ldots)$$
$$\mathbf{K}\cdot\mathbf{b} = 2\pi k \qquad (k=0,1,2,\ldots) \qquad (2.25)$$

The scattering intensity is then a function of both $\mathbf{K}\cdot\mathbf{a}$ and $\mathbf{K}\cdot\mathbf{b}$. The equation analogous to (2.24) for a linear grating is [Gasser 1985]:

$$I(\mathbf{K}) \propto A^2 \frac{\sin^2(\frac{1}{2}M_1\mathbf{K}\cdot\mathbf{a})}{\sin^2(\frac{1}{2}\mathbf{K}\cdot\mathbf{a})}\frac{\sin^2(\frac{1}{2}M_2\mathbf{K}\cdot\mathbf{b})}{\sin^2(\frac{1}{2}\mathbf{K}\cdot\mathbf{b})} = I.F. \qquad (2.26)$$

This expression is known as the interference function (I.F.) where M_1 and M_2 are the number of scatterers in the **a** and **b** directions, respectively. At this stage the theory predicts that scattering from a two-dimensional array will lead to a pattern of spots of equal intensity. The spacing of these spots depends on the surface unit mesh vectors ***a*** and ***b***. The scattering strength of the atoms is accounted for by the scattering factor. The amplitude of the scattered wave when just a single unit mesh is contributing is called the structure factor and is defined by

$$F = \sum_{n=0}^{N-1} f_n(-i\mathbf{K}\cdot\mathbf{r}_n) \qquad (2.27)$$

where f_n is the atomic scattering factor for an atom n, N is the number of atoms in the unit mesh and $\boldsymbol{r}_n$ is the position of an atom within the unit mesh. The diffraction function is defined as F^2. It is this function which is the proportionality constant between the intensity and the interference function, that is,

$$I(K) = F^2(I.F.) \qquad (2.28)$$

The diffraction function has the effect of altering the relative intensities of the scattered beams thus comparing intensities at different energy will yield structural information. As electrons penetrate a few layers into the surface the intensities cannot be accounted for without taking into consideration the inner layers of atoms. The interference function is then rewritten as

$$I.F. = (I.F.)_{surface} \times (I.F.)_{innerlayers} \qquad (2.29)$$

where

$$(I.F.)_{innerlayers} = \frac{\sin^2(\frac{1}{2}M_3\mathbf{K}\cdot\mathbf{c})}{\sin^2(\frac{1}{2}\mathbf{K}\cdot\mathbf{c})} \qquad (2.30)$$

where $\boldsymbol{c}$ is the unit mesh vector perpendicular to the surface and into the bulk of the crystal and M_3 is the number of scatterers in the **c** direction. The contribution of the inner layer does not significantly affect the position of the spots because the number of scatterers, M_3, is small, since the electrons penetrate only about four to five layers, but the intensities of the spots are strongly effected by this additional term. This can be explained by considering the top two layers of a crystal as shown in Figure 2.8. The angle θ_h at which a diffracted beam is detected is determined by

$$\delta = a\sin\theta_h \quad \text{or} \quad \mathbf{K}\cdot\mathbf{a} = 2\pi h \tag{2.31}$$

However, the wavelength λ' of an electron within the crystal is different depending on whether the electrons which penetrate the first layer and are scattered by the second layer emerge in phase or out of phase with the surface scattered electrons.

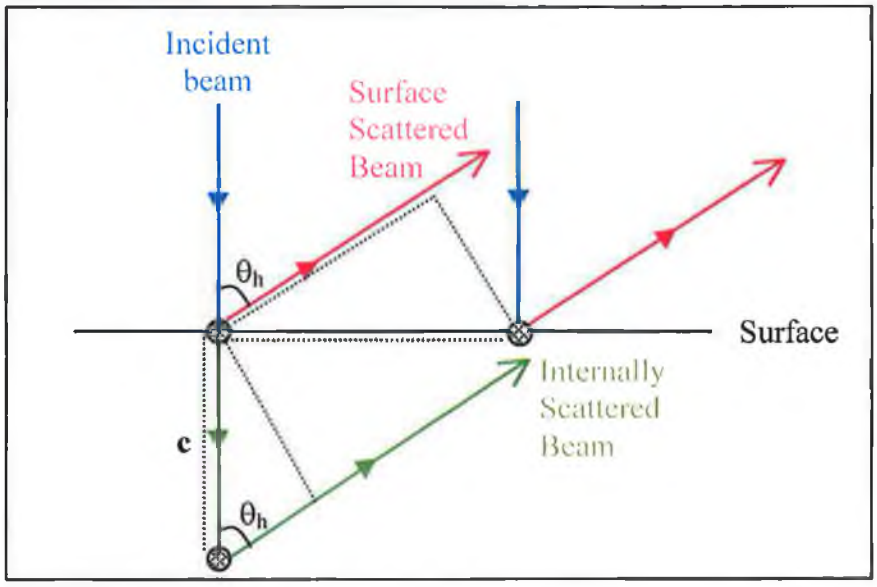

Figure 2.8 *Surface and internally scattered electron beams.*

Maximum intensity will be recorded when the path difference Δ is an integral number of wavelengths

$$\Delta = c(1+\cos\theta_h) = \text{integer}(l) \times \text{wavelength of electron} \tag{2.32}$$

However, the wavelength λ' of the electron within the crystal differs from that in free space because the electron is now experiencing the inner potential V_0 of the crystal. The new wavelength is given by

$$\lambda' = \left(\frac{150}{V+V_0}\right)^{1/2} \tag{2.33}$$

In the case of the (0,0) beam $\theta_h = 0$ and constructive interference will occur when

$$2c = l \times \lambda' \tag{2.34}$$

Combining (2.33) and (2.34) yields, for planes of spacing c,

$$V = \frac{l^2 \times 150}{4c^2} - V_0 \tag{2.35}$$

Therefore, a plot of the Bragg peak energies versus (integer)^2 should yield a straight line of slope ($150/4c^2$) and intercept $-V_0$. This yields a method of determining the interlayer spacing c and the inner potential V_0 of the crystal from measuring the positions of the Bragg peaks in I-V experimental data. If the strong peaks in the I-V spectra are close to the Bragg peak positions the material is relatively kinematic. However, if no obvious connection exists between Bragg energies and strong peaks, then dynamical scattering effects must be considered.

(b) Dynamical LEED Theory

While kinematic theory simulates well the position of Bragg peaks in I-V spectra, it does not account for non-Bragg like reflections arising from multiple scattering of electrons. Dynamical or multiple scattering theory accounts for multiple scattering sites as well as multiple interactions within the top few layers as opposed to the topmost layer. Since the majority of the electrons are scattered from the topmost layer, LEED spots always have positions that can be determined kinematically. However because multiple scattering is prominent for low energy electrons, kinematic theory alone is inadequate for solving surface structures. Two other factors also need to be addressed.

Firstly, in kinematic theory, the structure factor is simplified to include only s-wave phase shifts. In dynamical theory, the structure factor includes a large number of phase shifts to simulate the interaction between the incident electron and the many different electrons of different momentum within the core atoms.

Secondly, as the surface temperature increases in a LEED experiment, the diffraction spots broaden, the spots intensities decrease and the background intensity visible between the spots increases. These effects are due to the positional disorder of the vibrating surface atoms. The spot broadening can be described as due to momentum exchange of the electrons with phonons. The decrease in spot intensities is attributed to destructive interference between waves scattered by slightly disordered atoms and can

be described by the Debye-Waller factor of the crystal. The background intensity can be explained as thermal diffuse scattering and corresponds to the energy that is lost though the Debye-Waller factor. Debye-Waller factors are usually calculated at 0K in the kinematic approximation, as no reliance is placed on absolute beam intensities in kinematic calculations. A dynamical LEED analysis includes all the effects of thermal vibrations of surface atoms.

An iterative procedure, based on dynamical theory, has been developed by Pendry to determine the geometric arrangement of surface atoms within the surface mesh from an experimental set of I-V curves [Pendry 1974]. The starting point for the calculation is an initial guess at the arrangement of atoms on the surface, which is chosen to be consistent with the symmetry of the LEED pattern. The intensity of a number of the diffracted beams expected for this arrangement is then calculated as a function of electron beam energy. The resulting I-V curves are compared to the experimental result and the guessed atomic arrangement is adjusted and a new set of curves is calculated. The process is repeated until satisfactory agreement is obtained. In practice, this procedure is very difficult and requires enormous computational effort.

In general, in the analysis of LEED data, the agreement between experiment and theory is not always good, and there may sometimes be more than one computed structure which fits equally well with the data. This can lead to arbitrary and subjective assignments. An attempt to overcome this is the use of reliability factors (r-factors), which attempt to provide objective criteria for the quantitative evaluation of the closeness of curve fitting. There are various ways of calculating r-factors, e.g. Pendry r-factor, Zanazzi-Jona r-factor, but in general they are designed to emphasis features of the LEED data which are sensitive to structural details, such as peak positions and shape. Usually, a fit to LEED data will have an r-factor associated with it; the lower the value, the better the fit [Vickerman 1997]. Using this iterative procedure with dynamical theory allows determination of bond lengths with an accuracy of ~0.02Å.

2.3 Auger Electron Spectroscopy (AES)

Auger electrons are named after their discoverer Pierre Auger, from his investigations in 1923. The basic Auger process starts with an incident electron (or photon) causing ionisation of a core level electron. The electron vacancy or hole created in the core level may be neutralised by an electron transition from an electron level of lower binding energy. A quantum of energy, (ΔE), the difference between the core hole and the electron falling into it is transferred to a third electron which escapes as an Auger electron.

The kinetic energy of an Auger electron is calculated from:

$$E_{kin} \approx E_K - E_{L_1} - E_{L_{2,3}} \tag{2.36}$$

for the Auger process shown in the example in Figure 2.9, where $E_K - E_{L_1}$ is the quantum of energy released by an electron falling from the L_1 shell to the core hole in the K shell and $E_{L_{2,3}}$ is the binding energy of the electron in the $L_{2,3}$ shell. This Auger transition is assigned the term $KL_1L_{2,3}$.

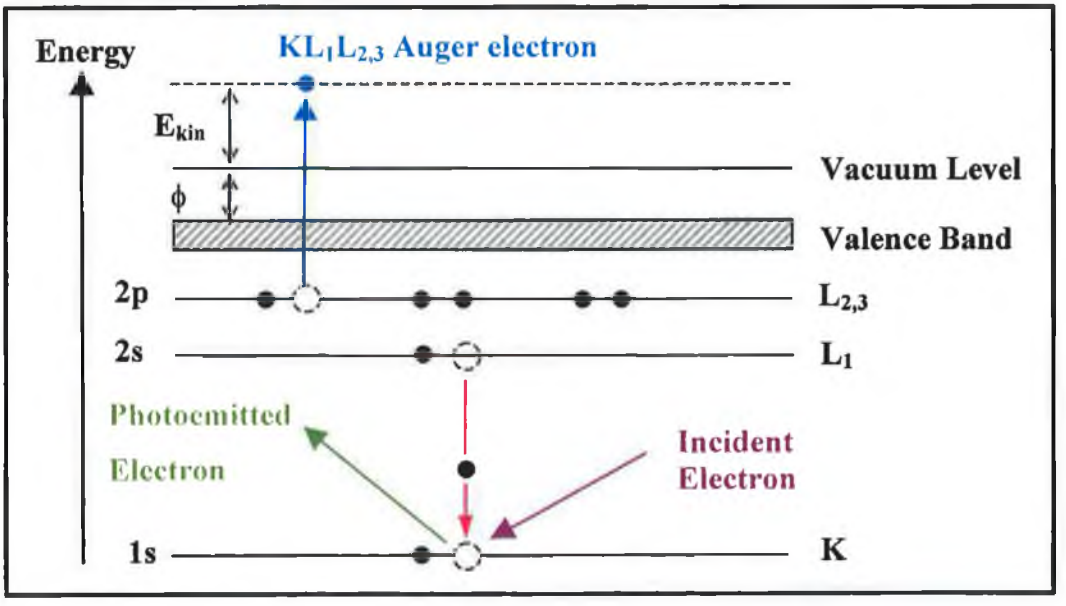

***Figure 2.9** Energetics of the Auger process.*

The probability of relaxation by Auger emission is the dominant process for core holes with binding energies below about 2keV for K shell ionisation. The kinetic energy of the Auger electron is independent of the energy of the ionising particle or the incident radiation giving rise to the initial core hole. The kinetic energy of the Auger electron is

characteristic solely of the binding energies of the electrons within the atom. Hence, Auger electrons may be used for chemical identification [Attard 1998].

For many systems monitoring of the Auger signals (AS) from the substrate and the adsorbate as a function of the deposition time (t), at a constant flux, is means of calibration of an evaporation source. The AS-t plot may also be used to distinguish between different growth modes, as shown for the three epitaxial growth modes discussed in Section 2.1.3 [Argile 1989].

Auger excitation is usually carried out using electron sources due to the relative ease of producing sufficiently energetic beams of high intensity. For the light elements (atomic number Z<20) Auger emission is more probable than X-ray emission for a K-shell initial-state hole and for Z<15 it is almost the exclusive process. For higher Z, Auger processes dominate for initial state holes in outer shells. The use of electron beams to produce the initial ionisation process is advantageous in that the incident beam can be focused thus giving good spatial resolution.

2.4 Temperature Programmed Desorption (TPD)

The desorption of adsorbed atoms and molecules is one of the most fundamental elementary surface kinetic processes and can provide information concerning the strength of the interactions between the surface and the adsorbed species. Apker introduced TPD as a surface analysis technique in 1948 [Apker 1948].

In TPD, one or more molecular species is adsorbed onto the sample at a temperature that is low compared to its desorption temperature. A temperature ramp, preferably linear, is applied to the sample and the rate of desorption is followed by monitoring the amount of adsorbate desorbed into the gas phase as a function of temperature. More rigorous considerations must be given to sample mounting to produce a heating rate (β) linear with time (t) which obeys a relationship of the form:

$$T(t) = T_0 + \beta t \tag{2.37}$$

where the initial sample temperature is T_0. The heating should be restricted ideally only to the sample, thus avoiding desorption from other surfaces such as a sample holder. In practice the most common method of achieving this is by suspending the sample by thin

support wires attached to the edges of the sample. Resistive heating is achieved by passing an electric current through the support wires and the wires heat the sample by conduction. A thermocouple is attached to the sample for accurate temperature measurements. This arrangement yields typical heating rates range between 1 and 100 Ks^{-1} [Attard1998].

A mass spectrometer is used to register the desorption by measuring the partial pressures of different ions. The mass spectrometer is usually orientated in line of site and close to the sample, typically around 2-5cm. This arrangement ensures that the surface coverage is proportional to the area under the measured spectrum, provided the pumping speed of the vacuum chamber remains constant during the desorption process.

By heating the sample and observing the temperature, at which specific molecules desorb, it is possible to draw conclusions about the binding energies of different adsorbates. A graph of the rate of desorption versus temperature, for first order kinetics, is shown in Figure 2.10.

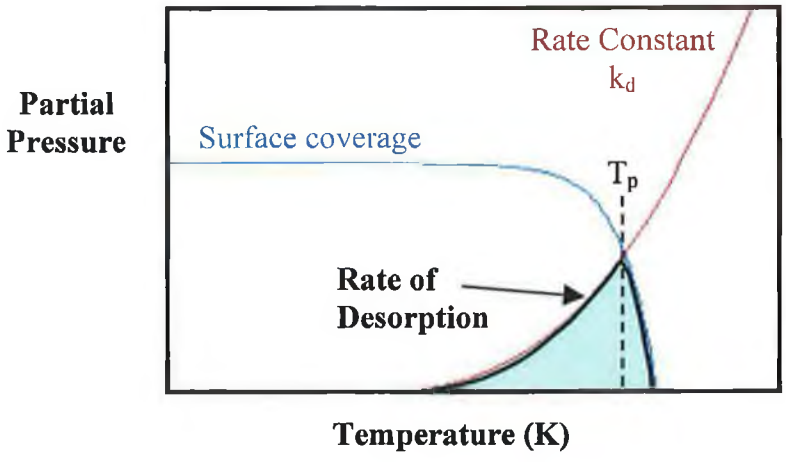

Figure 2.10 *The rate of desorption (black curve) as a convolution of changes in surface coverage and rate constant as a function of temperature is shown for first-order desorption.*

The rate of desorption curve shows that the partial pressure increases at the temperature at which the molecules start to desorb, reaches a maximum at the so-called desorption peak temperature T_p, and then falls off as the surface runs out of the adsorbed molecules.

The rate of desorption per unit surface area may be formulated as: [Attard 1998]

$$-\frac{dN}{dt} = k_d N^m \tag{2.38}$$

where m is the order of the reaction and N is the number of adsorbed molecules. The desorption rate constant k_d, obeys an Arrhenius dependency and shows an exponential increase with temperature:

$$k_d = A\exp(-E_d / RT) \tag{2.39}$$

where E_d is defined as the activation energy for desorption and A is the pre-exponential factor. For first order desorption, A is assumed to be of the same order of magnitude as the molecular vibration frequency and is usually accepted to be be about $10^{13}s^{-1}$ [Attard 1998]. Actual values, measured by other techniques such as Molecular Beam Relaxation Spectroscopy (MBRS), however, may differ from this value by as much as 10^5 [Hudson 1998].

Substituting for k_d and the heating rate $\beta = \frac{dT}{dt}$ into (2.38) yields:

$$-\frac{dN}{dT} = N^m \frac{A}{\beta}\exp(-E_d/RT) \tag{2.40}$$

When T = T_p the rate of desorption reaches a maximum, (i.e. $\frac{d^2N}{dT^2} = 0$) as shown in Figure 2.10.

Hence, by differentiating equation (2.40) with respect to T and equating to zero, a general equation relating T_p , E_d and N, can be expressed as:

$$\frac{E_d}{RT_p^2} = \frac{A}{\beta} mN^{m-1} \exp\left(-\frac{E_d}{RT_p}\right) \tag{2.41}$$

where R is the gas constant 8.314 $mol^{-1}K^{-1}$. Thus, as β and T_p are experimentally measured parameters, the activation energy E_d may be evaluated.

For first order desorption, this can be simplified to:

$$\frac{E_d}{RT_p^2} = \frac{A}{\beta}\exp\left(-\frac{E_d}{RT_p}\right) \tag{2.42}$$

where T_p is constant for first order desorption and dependent on the initial coverage N for higher desorption orders [King 1975] [Chan 1978]. This leads to an asymmetric curve for first-order desorption, as shown in Figure 2.10 and a symmetric curve in the case of second order desorption.

Using a method devised by Redhead, equation (2.42) for first order desorption, can be simplified to calculate the activation energy from: [Redhead 1962]

$$E_d = RT_p\left[\log_e\left(\frac{AT_p}{\beta}\right) - 3.46\right] \tag{2.43}$$

where T_p is measured in Kelvin.

As can be seen in equations (2.42) and (2.43), the desorption peak maximum is independent of adsorbate coverage N for first order kinetics. Therefore, by increasing adsorbate coverage the desorption peak maximum remains at a constant temperature and simply increases in intensity.

Since mass spectrometric detection is used in TPD the sensitivity of the technique is high, with attainable detection limits below 0.1% of a monolayer of adsorbate [Nix 1996]. Three important characteristics of the surface reactivity can be obtained from studying the rate of desorption curve.

(i) The area under the peak is proportional to the surface coverage, providing that the pumping speed of the vacuum remains constant during desorption experiments. This is also providing that all other variables that effect the mass spectrometer, e.g. detector gain, distance between sample and mass spectrometer, heating rate, etc., are kept constant. Thus, simple integration of the area under two TPD curves yields the relative coverage directly.

(ii) The position of the peak temperature, Tp, is related to the enthalpy of adsorption, i.e. to the binding energy of the adsorbate to the surface. In some adsorption systems, exhibiting first order kinetics, increasing exposure leads to the desorption peak maximum shifting to lower temperature. Furthermore, low temperature peaks can often appear at the highest exposure. The existence of multiple desorption peaks and coverage-dependent shifts in peak maxima may arise from:
(a) the presence of more than one distinct binding site with differing activation energies for desorption (e.g. atop, hollow, bridge); and
(b) coverage-dependent lateral interactions between adsorbates.

(iii) The kinetics of desorption (obtained from the peak profile and the coverage dependence of the desorption characteristics) give information on the state of

aggregation of the adsorbed species, e.g. molecular versus dissociative. As adsorbate molecules may decompose into a range of products of differing mass, this experiment requires the simultaneous monitoring of several masses. This can be achieved by allowing the mass spectrometer to switch between several detected masses as the temperature of the system is increased. Thus while truly simultaneous monitoring is not possible, a quasi-continuous output is obtained.

For example, the decomposition of formic acid (HCOOH) on copper{100} can be investigated by TPD by monitoring the masses of the parent ion (HCOOH = 46 amu), hydrogen (H_2 = 2 amu) and carbon dioxide (CO_2 = 44 amu) as the sample temperature is ramped. Hydrogen desorption is observed below room temperature, followed by simultaneous evolution of CO_2 and H_2 at higher temperatures. As separate experiments studying CO_2 and H_2 alone indicate the desorption of both CO_2 and H_2 is complete below room temperature, the only explanation for the high temperature desorption peak is the decomposition of an intermediate containing carbon, hydrogen, and oxygen into the products CO_2 and H_2, which desorb immediately. This process is termed *reaction limited desorption*.

A formate intermediate has been proposed [Attard 1998]. The following reaction mechanism has therefore been suggested to account for HCOOH decomposition on Cu{100}:

$$HCOOH_{(ad)} \rightarrow HCOOH_{(ad)} + H_{(ad)}$$

$$2H_{(ad)} \rightarrow H_{2(g)} \text{ (with a peak at 275K)}$$

$$2HCOO_{(ad)} \rightarrow 2CO_{2(g)} + H_{2(g)} \text{ (with a peak 475K)}$$

This reaction mechanism forms the basis of the TPD experiments for formic acid on the Sn/Cu{100} interface in Section 3.4.

2.5 X-Ray Standing Wave Spectroscopy (XSW)

2.5.1 Introduction to X-ray standing wave spectroscopy

The X-ray standing waves technique, pioneered by Batterman [Batterman 1964, 1969] is a method for structure determination at crystal surfaces. When X-rays are incident onto a crystal at the Bragg condition,

$$n\lambda = 2d\mathrm{Sin}\theta \qquad (2.44)$$

reflection occurs. Constructive interference between the incident and the back-scattered waves leads to an X-ray standing wave, both inside the crystal and extending into the space outside the crystal. The phase of the backscattered wave in the region of total reflectivity is a strong function of the angle of incidence, θ, and the photon energy hc/λ. This makes it possible to shift the nodes and antinodes of the standing wave relative to the atomic scattering planes by scanning through the Bragg condition either in angle or in energy. Any atom placed in the field of the standing wave will absorb the radiation in proportion to the intensity of the standing wave field. Since the position of the nodes of the X-ray standing wave field is known, it is possible to locate the absorber atom relative to the crystal scattering planes by monitoring its photoexcitation as a function of angle or energy. The basic setup for the XSW technique is shown in Figure 2.11. The only limitation in locating the position of an adsorbate is the periodicity of the standing wave field, which means that the absorber position can only be determined as a fraction of the distance between the Bragg planes.

The basic theory of this process has been known since 1960's, but initially it was difficult to find sufficiently intense and monochromatic X-ray sources. XSW experiments were performed by scanning the angle of incidence of the X-rays and for this, perfect crystals, as well as highly monochromatic light were required. In this case the Bragg condition has to be satisfied to within a fraction of a degree. The increased popularity of XSW as a surface structure technique is due to the greater availability of synchrotron radiation, which offers two main advantages: a high flux and a tuneable wavelength. Woodruff *et al.* [Woodruff 1988] introduced a modification to the XSW technique that removed the restrictions on alignment and crystal perfection. This is the normal incidence XSW (NIXSW), where the incident beam is normal to the scattering planes and scanning through the Bragg condition is carried out by varying the photon energy rather than rocking the crystal. With an angle of incidence of 90°, the $d\mathrm{Sin}\theta/d\theta$

term becomes zero, and this implies that the Bragg condition will be much less sensitive to small deviations (of the order of 1°) in angle.

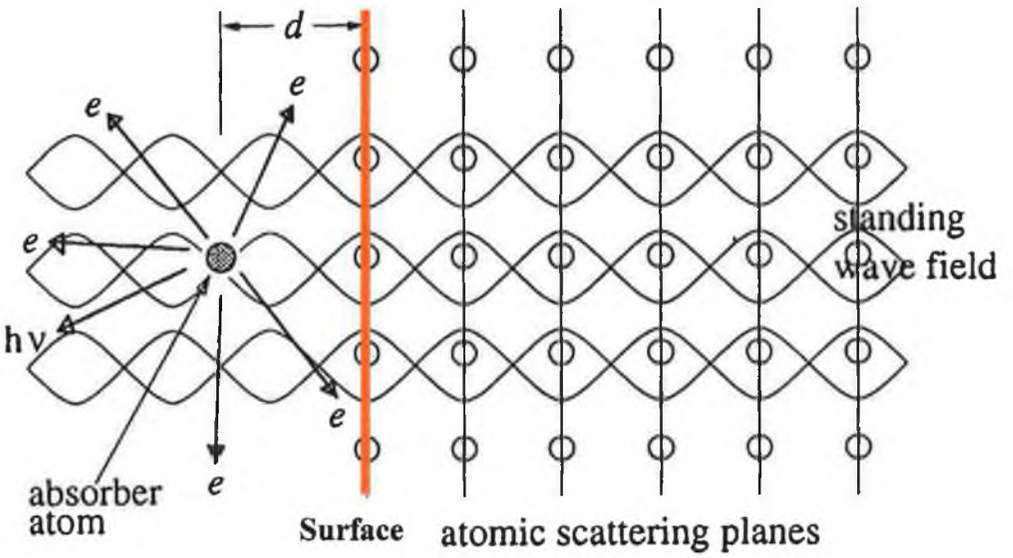

Figure 2.11 *A standing wave field set up in a crystal with an absorber atom on the surface. Adsorption is measured by monitoring the emission from the absorber atom.*

2.5.2 X-ray Standing Wave basic theory

The underlying theory of XSW has been presented in recent reviews [Zegenhagen 1993] [Woodruff 1998], while some of the key aspects of the underlying dynamical theory of X-ray diffraction are contained in standard texts [Kittel 1976]. Figure 2.12 shows the wavevector and scattering plane geometry for an incident wavevector $\mathbf{K_0}$ and a reflected wavevector $\mathbf{K_H}$.

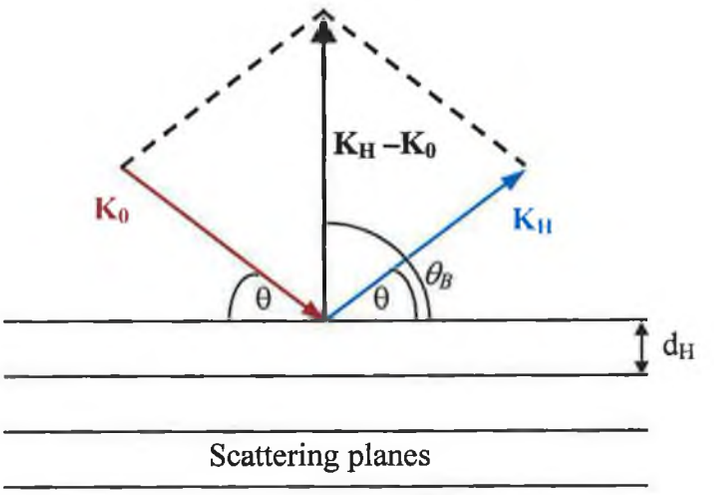

Figure 2.12 *Wavevector and scattering plane geometry.*

The intensity of the X-ray standing wavefield in the crystal is simply the modulus squared of the sum of the incident and reflected X-ray amplitudes. Taking the incident amplitude to be unity, and assuming σ-polarisation (electric vectors of incident and scattered X-rays are parallel), the intensity may then be written as

$$I = \left|1 + \left(\frac{E_H}{E_0}\right)\exp(-2\pi i \mathbf{H}\cdot\mathbf{r})\right|^2 \tag{2.45}$$

where E_H and E_0 are the amplitude of the reflected and incident X-rays respectively. **H** is the reciprocal lattice vector associated with the Bragg reflection being studied and **r** is a real-space vector defining the position at which the intensity is measured (the atomic absorber position). The scalar product **H.r** can be expressed in terms of the interlayer spacing d_H, yielding an expression for intensity of

$$I = \left|1 + \left(\frac{E_H}{E_0}\right)\exp\left(\frac{-2\pi i z}{d_H}\right)\right|^2 \tag{2.46}$$

where z is the adsorbate distance in angstroms above the reflection plane.The scattered X-ray amplitude is determined by the geometrical structure factors F_H and $F_{\overline{H}}$ for the reflections defined by **H** and **-H.**

$$\frac{E_H}{E_0} = -\left(\frac{F_H}{F_{\overline{H}}}\right)^{1/2}\left[\eta \pm \left(\eta^2 - 1\right)^{1/2}\right] \tag{2.47}$$

where F_H and $F_{\overline{H}}$ are the complex structure factors for the **H** and $\overline{\mathbf{H}}$ reflections. The structure factor is a complex number, its real part corresponds to the scattering strength of the plane and its imaginary part corresponds to any absorption, and corresponding phase shift that takes place during the scattering. For a scattering plane with the reciprocal lattice vector **H** the strcuture factor can be expressed as

$$F_H = \sum_{i=1}^{n} f_i e^{2\pi i \mathbf{H}\mathbf{r}_i} \tag{2.48}$$

where f_i is the atomic scattering factor of an atom labelled i at the point $\mathbf{r}_i$ in the unit cell and n is the number of atoms in the unit cell. Thermal vibration of atom i reduces the atomic scattering factor f_i by the Debye-Waller factor e^{-M_i}, where $M = 2\pi^2\left\langle u_H^2\right\rangle / d_H^2$ and $\left\langle u_H^2 \right\rangle$ is the mean square vibrational amplitude of the atoms in the direction **H.** The parameter η is a measure of how far the scattering conditions are from the midpoint of the reflectivity curve. Traditionally this parameter was written in terms of an angular displacement, with the experiment being performed by 'rocking' the

sample through the Bragg angle θ_B (defined in the usual way for X-ray diffraction as the grazing incidence angle to the scatterer planes such that normal incidence corresponds to a value of 90°). In the case of the NIXSW technique the scattering angle is held fixed and one scans through the X-ray energy (E) or wavelength (λ), so it is more convenient to express η in terms of the deviation in X-ray energy, ΔE, from the value at the Bragg condition.

$$\eta = \frac{-2(\Delta E/E)\mathrm{Sin}^2\theta_B + \Gamma F_0}{|P|\Gamma(F_H F_{\bar{H}})^{1/2}} \tag{2.49}$$

where P is a polarisation factor which is always unity for NIXSW (σ polarisation), although at a more general incidence angle and in π-polarisation this factor is $\mathrm{Cos}(2\theta_B)$. F_0 is the structure factor for the (000) reflection while Γ is given by

$$\Gamma = \frac{e^2}{4\pi\varepsilon_0 mc^2} \cdot \frac{\lambda^2}{\pi V} \tag{2.50}$$

where V is the volume of the unit cell, e and m the charge and mass of an electron, ε_0 the permittivity of free space and *c* the speed of light. These equations highlight two important results of the dynamical theory of X-ray diffraction which differ from the simple kinematical theory in which one predicts a peak in the reflectivity (and thus $|E_H|^2$) of the infinitesimal width at the exact Bragg condition. For a non-absorbing crystal (for which F_0 and $F_H F_{\bar{H}}$ are real) one has a finite range of total reflectivity corresponding to the range of η between -1 and +1. This energy range, obtained by inverting equation (2.49) is

$$\Delta E = \pm \frac{E|P|\Gamma(F_H F_{\bar{H}})^{1/2}}{2\pi\mathrm{Sin}^2\theta_B} \tag{2.51}$$

The second point of note is that this total reflectivity range is not centred around the kinematical Bragg condition, but is offset, as may be seen from the ΓF_0 term in equation (2.49) which is independent of ΔE.

From the perspective of the utility of the XSW method, the important aspect of these equations is that the phase of the term E_H/E_0 varies as one scans through the reflectivity range and varies η. For a non-absorbing crystal the modulus squared of the term in η in equation (2.47) is always unity, but this term is actually complex indicating

a variable phase. One general way of writing this is to recognise that $|E_H E_0|^2$ is simply the (intensity) reflectivity, R (which is a real quantity). One can therefore write

$$E_H / E_0 = \sqrt{R}\exp(i\phi) \tag{2.52}$$

with ϕ varying by π across the reflectivity range in a fashion wholly predictable by the equations given above. Using this form, equation (2.45) can be written as

$$I = \left|1 + \sqrt{R}\exp(\phi - 2\pi i z / d_H)\right|^2 \tag{2.53}$$

leading to

$$I = 1 + R + 2\sqrt{R}\,\mathrm{Cos}(\phi - 2\pi z / d_H) \tag{2.54}$$

It is necessary to include in equation (2.54) some distribution of possible positions, due to vibrational or static disorder, or to several different discrete sites. The intensity I can be represented by a distribution of z values, with a probability of a given value being given by, say f(z).dz within a range dz about the value z. Equation (2.54) is then rewritten as

$$I = 1 + R + 2\sqrt{R}\int_0^{d_H} f(z)\,\mathrm{Cos}(\phi - (2\pi z / d_H))\,dz \tag{2.55}$$

which can also be expressed as

$$I = 1 + R + 2f_{co}\sqrt{R}\,\mathrm{Cos}(\phi - (2\pi D / d_H)) \tag{2.56}$$

in terms of two parameters: (i) the coherent fraction f_{co} and (ii) the coherent position D.

(i) Coherent fraction (f_{co}): The coherent fraction is a number between 0 and 1 that defines the homogeneity of the position. A coherent fraction of 1 means that all the atoms are in the same position relative to the scatterer planes. A fraction of zero generally implies incoherence (random height distribution) in a particular direction. In the case of more than one position the fraction is affected by the relative heights of the two positions.

(ii) Coherent position (D): The coherent position is a number between 0 and 1 that defines the average height of the absorber atoms as a fraction of the spacing (d_H) of scattering planes. For example, a position of 0.5 means that the absorber atoms are half-way between the scattering planes and for surface atoms this would imply a distance of half the lattice spacing above the surface. It should be noted that a height of one and a half times the layer spacing would also give the

same result. If the coherent fraction is one then the position is exact, otherwise it is an average position.

These two parameters totally define the structural dependence of the measured absorption profile, and are thus the parameters which emerge from the analysis of the experimental data. Evidently for the idealised case of a singly occupied layer spacing with no disorder (i.e. f(z) is a delta function at a particular value of z) the coherent fraction is unity and the coherent position is simply the actual layer spacing. This is effectively what we have assumed in describing the examples mentioned so far. These parameter names can be most readily understood by rewriting this equation in the form

$$I = f_{co}(1 + R + 2\sqrt{R}\ \mathrm{Cos}(\phi - (2\pi D / d_H))) + (1 - f_{co})(1 + R) \qquad (2.57)$$

The first bracketed term is now the right-hand side of equation (2.54) (the ideal single-site absorption in a perfectly coherent standing wave-field) multiplied by f_{co}. The second term is $(1 - f_{co})$ (i.e. the 'incoherent fraction') multiplied by (1+R), that is the wavefield intensity sum of the incident and reflected waves in the absence of coherent interference. More generally, the simplest way of relating these parameters to the actual position distribution is

$$f_{co} \exp(2\pi i D / d_H) = \int_0^{d_H} f(z) \exp(2\pi i z / d_H)\, dz \qquad (2.58)$$

Equations (2.57) and (2.58) show that the coherent fraction and the coherent position give the amplitude and phase of one Fourier component of f(z). Other components of this same distribution function can be obtained by studying higher order reflections from the scatterer planes (with smaller values of d_H). More generally, the spatial distribution of the adsorbate positions is a function in three-dimensional space, and one can probe this in different directions using different X-ray reflections from non-parallel scatterer planes. The formal connection to the Fourier components of the real space structure and to the complementary information provided by X-ray diffraction has been discussed further by Zegenhagen [Zegenhagen 1993].

An alternative representation is to construct a simple graphical representation of the way in which the measured quantities f_{co} and D relate to the integral over a real spatial distribution function [Woodruff 1998]. This is achieved using an Argand diagram - each layer spacing in the spatial distribution is represented by a vector, the direction being defined by the phase angle $2\pi z / d_H$ relative to the positive x-axis, while the length is

f(z) which is the probability of this value; the resultant (the vector sum of these components) is a vector of length f_{co} and phase angle $2\pi D/d_H$. To illustrate the utility of this approach, some simple applications are discussed. The simplest case to consider, is that of adsorbate co-occupation of two distinct surface sites. Such a situation is not at all implausible in practise. There are, for example, many surface structures with a good long-range order having two or more adsorbed atoms or molecules per unit surface mesh. Also, a molecular adsorbate may contain two or more atoms of the same species in equivalent geometries relative to the substrate. In this case, for some arbitrary Bragg reflection, two distinct layer spacings z_1 and z_2 are expected. If the fractional occupation of these two sites are f_1 and f_2 (with $f_1 + f_2 = 1$), then the integral on the right hand site of equation (2.58) reduces to a sum over two terms:

$$f_{co}\exp(2\pi iD/d_H) = f_1\exp(2\pi iz_1/d_H) + f_2\exp(2\pi iz_2/d_H) \qquad (2.59)$$

A particularly simple case is when the two sites are equally occupied, so $f_1 = f_2 = 0.5$ and it may be shown [Woodruff 1998] that

$$D = (z_1 + z_2)/2 \qquad \text{and} \qquad f_{co} = \left|\mathrm{Cos}(\pi(z_1 - z_2)/d_H)\right| \qquad (2.60)$$

Figure 2.13(a) shows the vector representation of this situation on an Argand diagram, where the coherent position is simply the mean of the two layer spacings. However, as shown in Figure 2.13(b), a special case of this general problem occurs when the two layer spacings differ by one half of the scatterer plane layer spacing d_H.

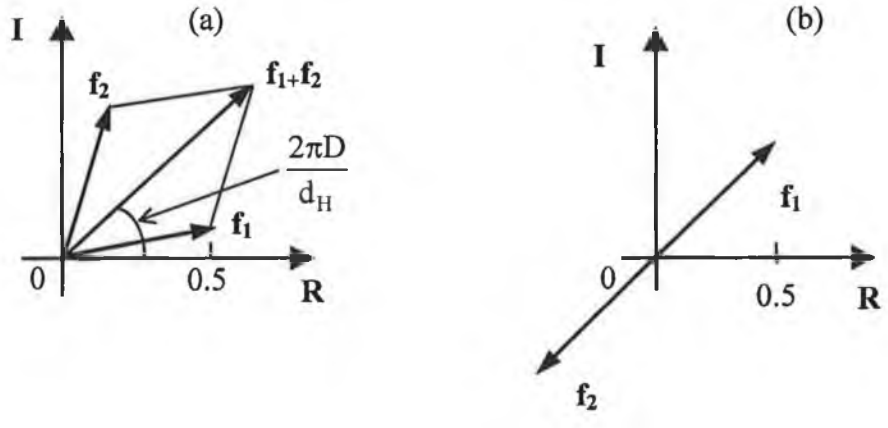

Figure 2.13 *Argand diagram representation of the summation of XSW contributions from two equally weighted layer spacings. (a) shows the components and resultant for the general case. (b) shows the special case of two components with layer spacings differing by half the bulk layer spacing. R and I denote the real and imaginary axes.*

In this case, the two component vectors cancel to give a coherent fraction of zero. This situation might more generally be associated with 'total disorder', despite the fact that it actually results from a structure compromising two distinct well-ordered sites. Thus, while it is common to think of the coherent fraction as a measure of the degree of order, this is clearly not necessarily the case when one has two or more distinct sites occupied.

If an absorber atom is placed in a X-ray standing wave field, there are a number of processes that can occur after the absorption of a photon. The X-ray absorption can be monitored by detecting the X-ray fluorescence following core-hole decay. However, in surface structural studies it is often more convenient, as well as more surface specific, to monitor this absorption via the Auger electron emission associated with core hole decay, or more directly through the intensity of the associated photoemission. These latter methods are especially relevant for experiments involving Bragg reflections close to normal incidence to the scattered planes, which occur at relatively soft X-ray energies (typically 2-5keV). Monitoring of the photoemission offers the special advantage of chemical state sensitivity due to the photoelectron binding energy differences found in core level photoemission from atoms of the same elemental species in different bonding situations. It also generally offers a superior signal to background ratio relative to Auger peak monitoring for low atomic number species having only shallow core levels.

In principle it is possible to determine the structure of a relaxed or reconstructed surface with XSW. However this is difficult because the signal will be strongly dominated by bulk emission since the standing wave field penetrates deeply into the crystal. Unlike an adsorbate, a surface consists of the same atoms as the bulk, so that there is no simple way of separating the two signals. Using low energy Auger transitions the surface electrons may be separated from the substrate signal. This is done by recording the XSW absorption profile both on the Auger line and on the inelastic background as demonstrated by Woicik *et al.* [Woicik 1992]. The off-peak background signal will come almost entirely from the bulk and can be used as a reference signal. The surface signal is then extracted in the following way: the total on-peak signal is a sum of bulk and surface

$$T = S + \alpha B \tag{2.63}$$

where B is the off-peak (bulk) signal scaled to compensate for the decrease in the inelastic background. If the on-peak signal is divided by the off-peak signal, the result will be:

$$\frac{T}{B}=\frac{S+\alpha B}{B}=\frac{S}{B}+\alpha \qquad (2.64)$$

The ratio $S/B+\alpha$ can be fitted with the ratio of two profiles $Y(\upsilon)/Y(0)+\text{constant}$ where Y(0) is a profile for a coherent distance of 0 (this is the bulk) and $Y(\upsilon)$ is a profile at the (unknown) coherent distance υ, by which the surface atoms have moved out of the bulk lattice spacing. This method has the advantage that it is not necessary to estimate the relative magnitudes of surface Auger emission, bulk Auger emission, Auger emission stimulated by bulk photoelectrons and the inelastic background.

Being an elemental specific technique NIXSW has proven to be an extremely powerful tool for providing information about atomic positions both on a surface and at an interface. The experimental details for NIXSW studies are discussed in Section 3.4. This technique is suitable for both metal and semiconductor structures. In this work NIXSW has been used to accurately determine the position of Ge atoms adsorbed on the GaAs(001) surface. The results of this structural investigation are presented in Chapter Five.

2.6 Photoelectron Spectroscopy

2.6.1. Introduction to Spectroscopy

The application of photoelectron spectroscopy as a technique to study the chemical and electronic structure of solids has its origins in the work of Siegbahn and co-workers [Siegbahn 1982] at the University of Uppsala, Sweden in the fifties. Their research was based on improving the energy resolution and sensitivity of electron spectrometers, enabling a determination of the binding energies of electrons in a wide range of materials. From the analysis of the electronic binding energies it was possible to build up a chemical "fingerprint" of the solid. With the correct choice of experimental parameters, photoelectron spectroscopy can be used to probe the first few monolayers at the surface of a solid. In most materials an electron has its minimum escape at an energy of approximately 40eV, as was discussed in Section 2.1.4. The surface sensitivity of the experiment can therefore be optimised by selecting a suitable photon energy so that the photoelectrons have a suitable kinetic energy.

Although synchrotron sources, which provide a continuous range of photon energies are commonly used in modern day high resolution photoemission work, photoemission measurements are still commonly divided into two regimes. (i) Core-level photoemission (also termed X-ray photoelectron spectroscopy (XPS)), and (ii) valence band photoemission (also termed ultraviolet photoelectron spectroscopy (UPS)). Only core level photoemission studies are employed in the course of this work.

The basic process of photoemission in both XPS and UPS, is the absorption of a photon with energy hν and the ejection of an electron bound in a solid with the binding energy E_B. The kinetic energy E_{kin} of the emitted photoelectron, can be expressed by the Einstein equation:

$$E_{kin} = h\nu - E_B - \phi \qquad (2.65)$$

where ϕ is the work function of the material. If the difference $(h\nu - E_B)$ is larger than the work function, the electron can leave the solid, as shown in the example in Figure 2.14.

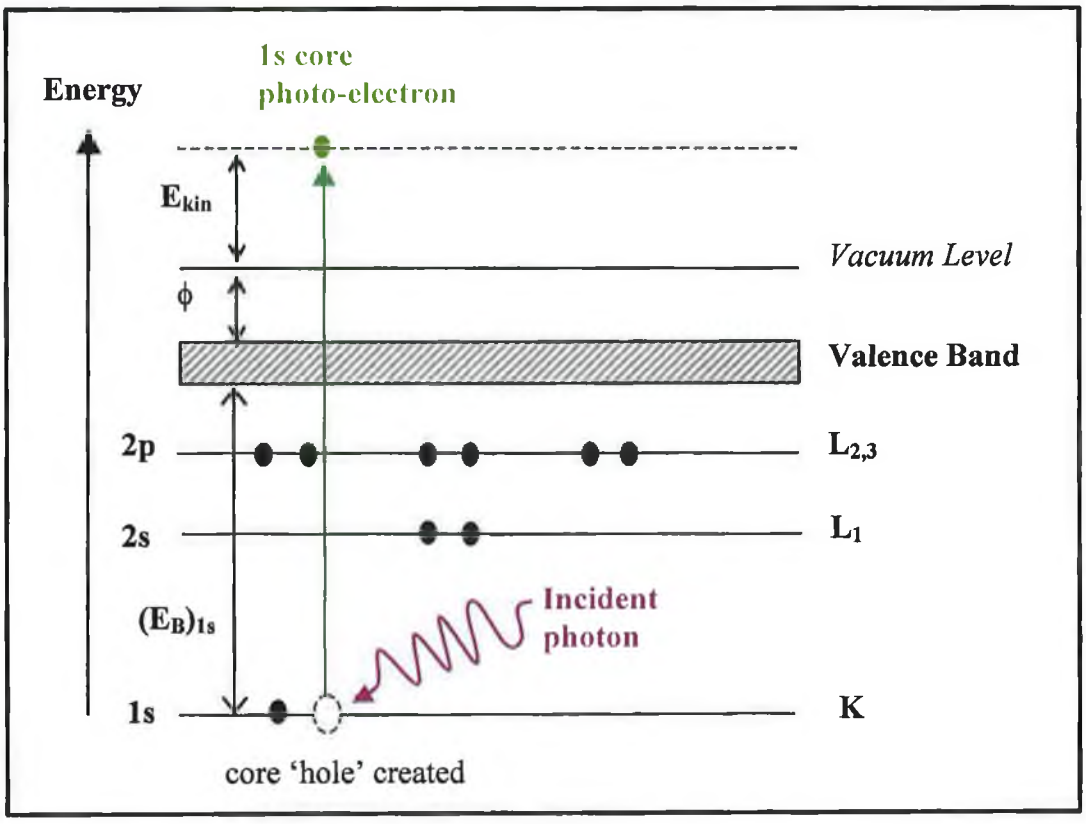

Figure 2.14 *An example of the photoemission process, where an incident X-ray photon transfers it's energy to a 1s core level electron.*

In angle integrated photoemission the energy distribution of photoelectrons at a given photon energy hv should simply be the electronic density of states at or near the surface, shifted up by hv. This simple picture becomes more complicated in reality because the photoemission cross section depends on photon energy, polarisation and angle of incidence, and the availability of final states. One way to avoid some of these difficulties is to repeat experiments at different photon energies to minimise the danger of observing spurious effects at one photon energy. The use of a wide range of photon energies has become possible in the last twenty years with synchrotron radiation as a photon source.

2.6.2 Core level photoelectron spectroscopy

In the study of Ge/GaAs(001) presented in Chapter 5, the As 3d, Ge 3d and Ga 3d core levels are studied for different coverages of Ge. In principle the more tightly bound s or p orbitals could be studied, but this would require photon energies outside of the range of the monochromator (Section 3.6.1). The interaction cross sections for the s and p levels are ~100 times lower than those for d levels. For example, at photon energy of 80eV, the photoionisation cross section for Ge 3d is 7 Mb, for Ge 4s is 0.14 Mb and the Ge 4p is 0.04 Mb, where 1Mb is equal to 10^{-22} m^2 per atom. A typical core level photoemission spectrum for the As 3d, Ge 3d and Ga 3d core levels is shown in Figure 2.15, where count rates are plotted against electron kinetic energy.

These core level peaks sit on top of a background due to inelastically scattered electrons. This intensity background increases towards low kinetic energy. The valence band is situated at high kinetic energies close to the Fermi level, but it is not visible in the spectrum below. Also, the cross sections for the orbitals that form the valence bands are low at this photon energy. Since each element has a characteristic core level spectrum, it is possible to carry out chemical identification with XPS. Moreover in different chemical environments the core levels are slightly shifted in energy, so photoelectron spectroscopy can be used to distinguish between metal gallium and gallium arsenide or from surface and bulk atoms.

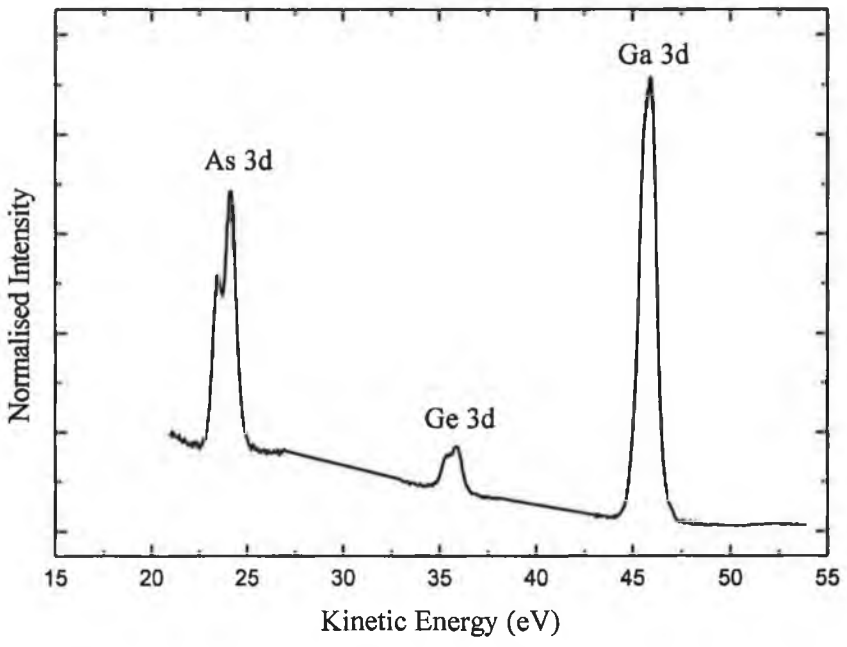

Figure 2.15 *A photoemission spectrum recorded with an incident photon energy of 70eV showing the As 3d, Ge 3d and Ga 3d core levels sitting on an inelastically scattered background.*

A core level line is produced by exciting photoelectrons from a deep lying atomic level. There is a natural linewidth associated with the finite lifetime of the corehole which will give the line a Lorentzian (resonance curve) broadening. The overall lineshape is a convolution of the Lorentzian profile with the Gaussian (statistical) broadening due to the limited resolution of monochromator and detector and also the surface inhomogeneity. This type of line profile is called a Voigt profile. It must be calculated by numerical integration for every point of the curve since the results can not be given in an analytic form. This means that core-level fitting requires some computing power to perform the iterations.

Figure 2.16 shows a Voigt profile with some further parameters that characterise a core level spectrum. The Voigt profile full width at half maximum (FWHM) is a combination of the Gaussian and Lorentzian linewidths which are fitted separately. If the atomic orbital from which the electron is excited, is not an s-orbital, it's orbital angular momentum *l* will interact with the electron spin s. This spin-orbit interaction will cause the energy of the orbital to split into two components with relative intensities

$$\frac{I_1}{I_2} = \frac{2(l-s)+1}{2(l+s)+1} \tag{2.67}$$

Due to diffraction and alignment effects, the intensity ratio of the two components will never be exactly at the theoretical value, but the theoretical ratios (1/2 for p-orbitals and 2/3 for d-orbitals) are good starting points for fits. The energy shift between the two spin-orbit-split components is usually fitted once and then kept constant at that value, since it is not influenced by external factors. As shown in Figure 2.16 the core level lines sit on a background of inelastically scattered electrons, which is usually approximated with a polynomial. This is only a simple approximation and it may become necessary to use more accurate ones for a fit, for example a Shirley background which approximates a step function for the inelastic scattering [Shirley 1972].

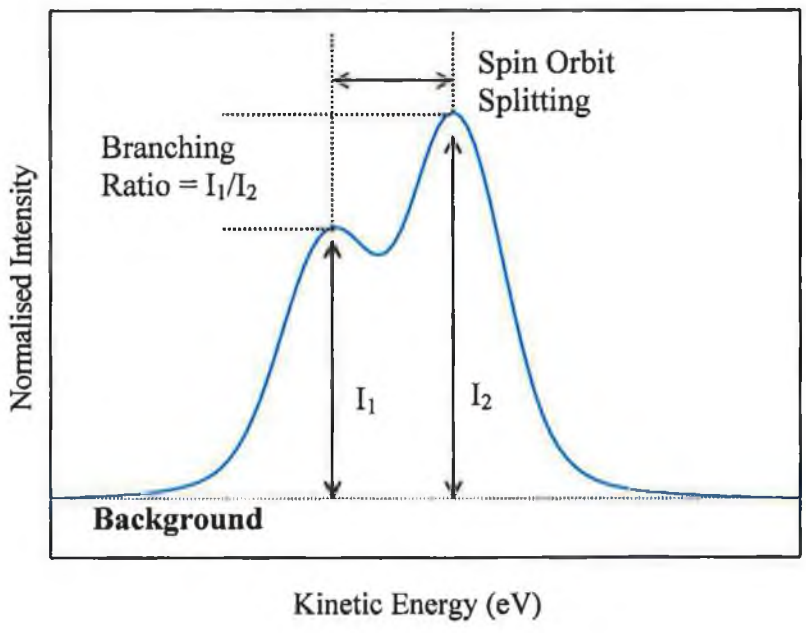

Figure 2.16 *A Voigt profile illustrating some parameters of a core level photoemission spectrum.*

Before setting out to fit a core level spectrum one should have a clear idea of how many components at which relative positions the spectrum is composed. On a clean surface core level spectra usually have two components, one due to bulk atoms and the other to the surface atoms which are in a somewhat different chemical environment. The conditions at the surface (possible charge transfers or changes in the Madelung potential cause a surface core level shift (SCLS)). Since this shift is not very large (usually less than 0.5eV), bulk and surface components are difficult to separate and the surface core level shift must be determined by comparing spectra taken at high and low emission angles or at different photon energies. At high emission angles relative to the surface normal more emission will come from the surface layer and therefore the surface

component will have a higher intensity. Different photon energies correspond to different escape depths which will change the relative intensity of the bulk component in a spectrum. In practice the value of the SCLS is taken from literature.

Surface atoms generally have a lower coordination than equivalent atoms in the bulk. This results in a surface core level shift where the surface atoms contribute a component to the spectrum that is shifted in binding energy relative to the bulk component. Figure 2.17 shows an As 3d core level spectrum from GaAs(001) with surface shifted components. Each component is due to a different chemical environment for the As atoms, one for the As in bulk GaAs and the other two are surface core level shifts. This core level has been fitted by a method described in Chapter 3. It is convenient to visualise the surface shift as being due to a charge transfer to or from the surface atom. Such a charge transfer will shift the core level to lower or higher binding energy, respectively, relative to the bulk position. This is the basis for identifying chemical bonds specific to the surface of the material. There is a problem with calculating the charge transfer involved in a surface chemical bond. Although the surface chemical shift is easily found from the core level spectra, the calculation of the amount of charge transfer relies on accurate knowledge of the length of the relevant surface chemical bond. Surface bond lengths may be found from methods such as I-V LEED or the X-ray standing wave technique. Without accurate knowledge of these bond lengths, the charge transfer involved cannot be calculated.

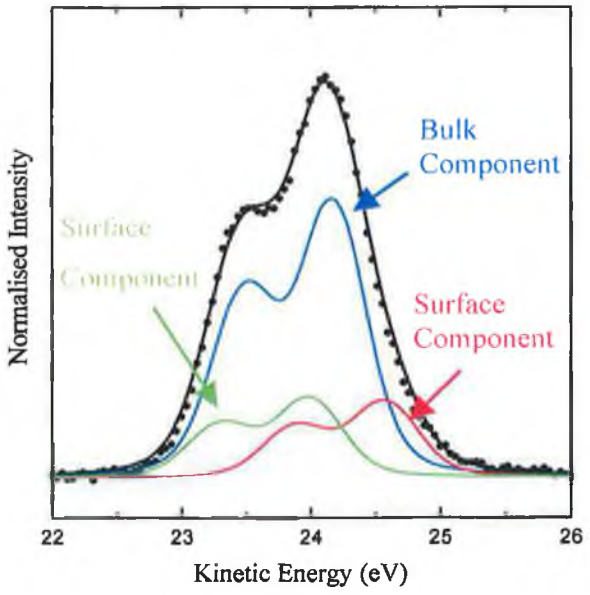

Figure 2.17 *As 3d core level spectrum fitted with three components showing the surface shifted components.*

In this work, core level photoelectron spectroscopy studies to investigate the Ge/GaAs(001) interface were carried out at Daresbury Synchrotron Source, UK. The As 3d, Ge 3d and Ga 3d core level spectra were measured for different coverages of Ge. The experimental details for photoelectron spectroscopy are discussed in Section 3.6. The results obtained for photoelectron spectroscopy studies of Ge/GaAs(001) are presented in Chapter Five.

Chapter Two References

Argile C. and Rhead G.E., Surf. Sci. Rep. 10 (1989) 277, Adsorbed layer and thin film growth modes monitored by Auger electron spectroscopy.

Apker L.R., Industrial and Engineering Chemistry 40 (1948) 846, Surface phenomena useful in vacuum technique.

Attard G. and Barnes C., Surfaces, Oxford University Press (1998).

Bardi U., Rep. Prog. Phys. 57 (1994) 939, The atomic structure of alloy surfaces and surface alloys.

Batterman B.W. and Cole H., Rev. Mod. Phys. 36 (1964) 681, Dynamical diffraction of X-rays by perfect crystals.

Batterman B.W., Phys. Rev. Lett. 22 (1969) 703, Detection of foreign atom sites by their X-ray fluorescence scattering.

Bauer E. and van der Merwe J.H., Phys. Rev. B 33 (1986) 3657, Structure and crystalline superlattices: From monolayers to superlattice.

Chan C.M., Aris R. and Weinberg W.H., Appl. Surf. Sci. 1 (1978) 360, An analysis of thermal desorption mass spectra I.

Clarke L.J., Surface Crystallography, John Wiley & Sons, Ltd. (1985).

Davisson C.J. and Germer L.H., Phys. Rev. B 30 (1927) 558.

Gasser R.P.H., An introduction to chemisorption and catalysis by metals, Clarendon Press, (1985).

Henzler M., Prog. Surf. Sci. 42 (1993) 297, Growth Modes in Homo- and Heteroepitaxial Growth.

Hudson J.B., Surface Science, John Wiley & Sons, Inc. (1998).

Jona F., Strozier J.A. and Wang W.S., Rep. Prog. Phys. 45 (1982) 527, Low energy electron diffraction for surface structure analysis.

King D.A., Surf. Sci. 47 (1975) 384, Thermal desorption from metal surfaces: A review.

Kittel C., An Introduction to Solid State Physics, John Wiley & Sons, Inc. (1976).

Lüth H., Surfaces and interfaces of solids, Springer-Verlag Berlin Heidelberg (1993).

Marcus P.M., Appl. Surf. Sci. 11/12 (1982) 20, LEED and surface structure.

Nix R., http://www.chem.qmw.ac.uk/surfaces/scc/ (1996).

Pashley D.W., Mater. Sci. Tech. 15 (1999) 2, Epitaxy growth mechanisms.

Pendry J.B., Low Energy Electron Diffraction, Academic Press Inc. (1974).

Powell C.J., Surf. Sci. 299/300 (1994) 34, Inelastic interactions of electrons with surfaces: application to Auger-electron spectroscopy and X-ray photoelectron spectroscopy.

Redhead P.A., Vacuum 12 (1962) 203, Thermal desorption of gases.

Rodriguez J.A., Surf. Sci. Rep. 24 (1996) 223, Physical and chemical properties of bimetallic surfaces.

Seah M.P. and Dench W.A., Surf. Interface Anal. 1 (1979) 2, Quantitative electron spectroscopy of surfaces: A standard database for electron inelastic mean free paths.

Shirley D.A., Phys. Rev. B 5 (1972) 4709, High-resolution X-ray photoemission spectrum of the valence bands of gold.

Siegbahn K., Science, 217 (1982) 111, Electron spectroscopy for atoms, molecules and condensed matter.

Somorjai G.A., Introduction to surface chemistry and catalysis, John Wiley & Sons Inc. (1994).

Tersoff J., Phys. Rev. Lett. 74 (1995) 434, Surface-confined alloy formation in immiscible systems.

Van Hove M.A., Weinberg W.H and Chan C.-M., Low-Energy Electron Diffraction, Springer Verlag Berlin Heidelberg (1986).

Vickerman J.C., Surface Analysis - The principle techniques, John Wiley & Sons Ltd. (1997).

Woicik J.C., Kendelewicz T., Miyano K.E., Cowan P.L., Boulin C.E., Karlin B.A., Pianetta P. and Spicer W.E., Phys. Rev. Lett. 68 (1992) 341, X-ray standing-wave determination of the clean InP(110) surface reconstruction.

Woodruff D.P., Seymour D.L., McConville C.F., Riley C.E., Crapper M.D., Prince N.P. and Jones R.G., Surf. Sci. 195 (1988) 237, A simple X-ray standing wave technique for surface structure determination - Theory and an application.

Woodruff D.P., Prog. Surf. Sci. 57 (1998) 1, Normal incidence X-ray standing wave determination of adsorbate structures.

Zegenhagen J., Surf. Sci. Rep. 18 (1993) 199, Surface structure determination with X-ray standing waves.

Chapter Three

Experimental Techniques

This chapter describes the five experimental techniques used in the study of the Sn/Cu{100} and the Ge/GaAs(001) systems. In Section 3.1 the operation of a Knudsen cell evaporator is described for the deposition of tin on Cu{100} and germanium on GaAs(001). The experimental details for LEED I-V studies and a description of the double scattering simulation code is given in Section 3.2. The experimental details for the acquisition of Auger Electron Spectroscopy (AES) and Temperature Programmed Desorption (TPD) of tin on Cu{100} are presented in Sections 3.3 and 3.4. Normal Incidence X-ray Standing Wave (NIXSW) and Photoemission Spectroscopy (PES) experiments were used for investigation of germanium on GaAs(001). A description is given of these two synchrotron based techniques in Section 3.5 and 3.6.

3.1 Knudsen Cell

A Knudsen cell (W.A. Technology) as shown in Figure 3.1 was used to deposit both the germanium and tin adsorbates used in these studies.

Figure 3.1 *Knudsen cell from W.A. Technology.*

The Knudsen cell uses the principle of molecular effusion demonstrated by Knudsen in 1909. The material to be deposited is heated to provide a suitable vapour pressure in an isothermal enclosure. Molecular effusion is the flow of gas through an aperture whose diameter is small compared by the distance between molecules of the gas with an effusion rate, r which is inversely proportional to the square root of its molar mass:

$$r \propto \sqrt{\frac{1}{M}} \tag{3.1}$$

The deposition rate is extremely stable being determined by the temperature of the graphite furnace that is accurately controlled with a Proportional Integral Derivative (PID) controller. The graphite furnace of the cell is designed as a removable cartridge

that contains the crucible, heater element and heat shields. The heater filament is a tantalum foil, which is isolated with pyrolytic boron nitride (PBN) shields and is water-cooled. The temperature of the furnace is monitored by a R-type thermocouple which is carefully placed in the graphite in order to accurately reflect the internal temperature of the furnace. The deposition material is placed in a PBN crucible and nestled inside the furnace.

The temperature required for evaporation of germanium and tin can be established from the following table or from Figure 3.2.

	Temperature (K)									
Vapour Pressure (Torr)	10^{-9}	10^{-8}	10^{-7}	10^{-6}	10^{-5}	10^{-4}	10^{-3}	10^{-2}	10^{-1}	1
Ge	1015	1085	1150	1220	1310	1410	1530	1670	1830	2050
Sn	898	955	1020	1080	1170	1270	1380	1520	1685	1885

Table 3.1 *Temperature (K) versus vapour pressure (Torr) for tin and germanium.*

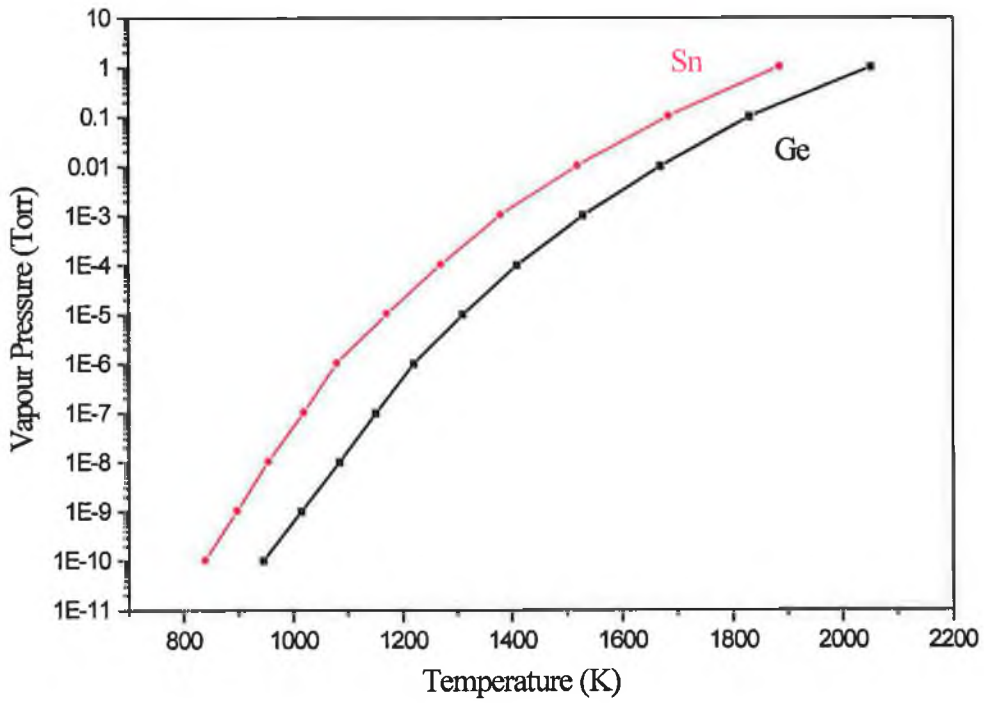

Figure 3.2 *Graph of vapour pressure (Torr) versus Temperature (K) for tin and germanium.*

The ratio of effusion of germanium and tin is calculated from the mass number of germanium (M_{Ge}=72.59) and tin (M_{Sn}=118.69) to be:

$$\text{Ratio} = \frac{\sqrt{M_{Ge}}}{\sqrt{M_{Sn}}} \approx 1.2 \qquad (3.2)$$

This ratio compares the evaporation temperatures determined experimentally for each element.

$$\text{Ratio} = \frac{1350\text{K}}{1175\text{K}} \approx 1.2 \qquad (3.3)$$

Hence, an evaporation temperature of 1350K for germanium and 1175K for tin provide a good constant flux rate that was accurately controlled by the PID controller to ± 2K.

3.2 Low Energy Electron Diffraction (LEED)

This section describes the experimental details for the LEED setup used to analyse the Sn/Cu{100} system. A description of the LEED analysis software used to generate LEED patterns for overlayer and surface alloy structures is presented.

3.2.1 Experimental Setup

The experiments were performed in an ion and titanium sublimation pumped ultra-high-vacuum chamber operating at a base pressure of $1\text{x}10^{-10}$ torr, shown in Figure 3.3. The system is equipped with 4-grid Vacuum Generators (VG) reverse view LEED optics, which could also be utilised as a retarding field analyser (RFA) for Auger Electron Spectroscopy (AES). A Vacuum Generators Quasar quadrupole mass spectrometer (QMS) was used for residual gas analysis and as a detector for Temperature Programmed Desorption (TPD) studies.

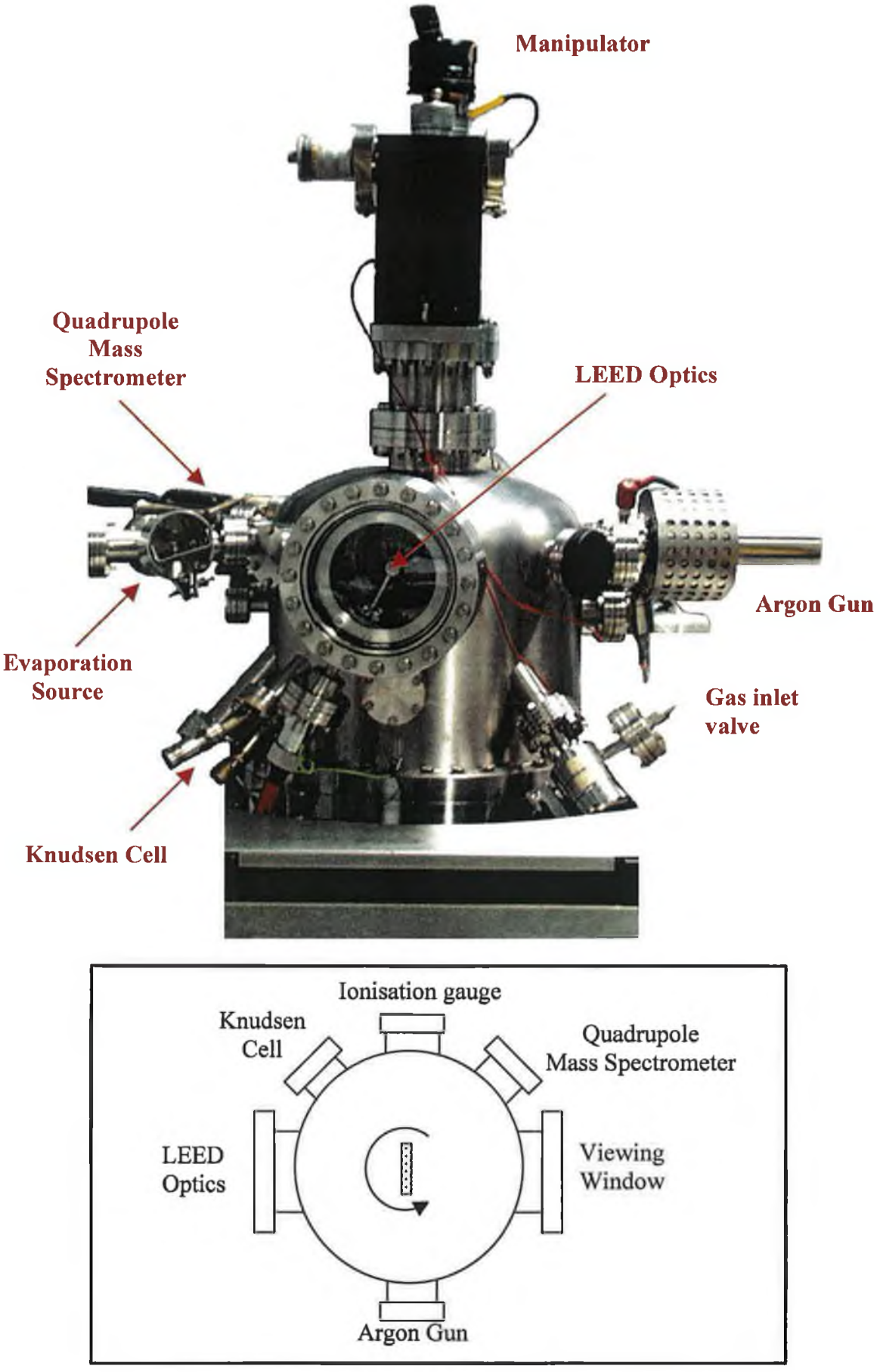

Figure 3.3 *Picture and schematic layout of UHV chamber.*

A schematic of the VG LEED optics and associated electronics is shown in Figure 3.4. A tungsten thoriated filament is enclosed within a Wehnelt cylinder and emits electrons when a current of approximately 2.2A are passed though it. These electrons are collimated by an Einzel lens arrangement and finally leave the drift tube with the desired beam energy (Ep), which can be varied from 0kV to 1kV for LEED and 0kV to 3kV for Auger analysis. The electrons traverse a field free region in the drift tube and are only deflected by stray magnetic fields on their path to the sample. With the sample held at ground, normal incident electrons strike the surface generating back-scattered electrons. The backscattered electrons pass though a series of grids (four in this case), before impinging on a fluorescent screen.

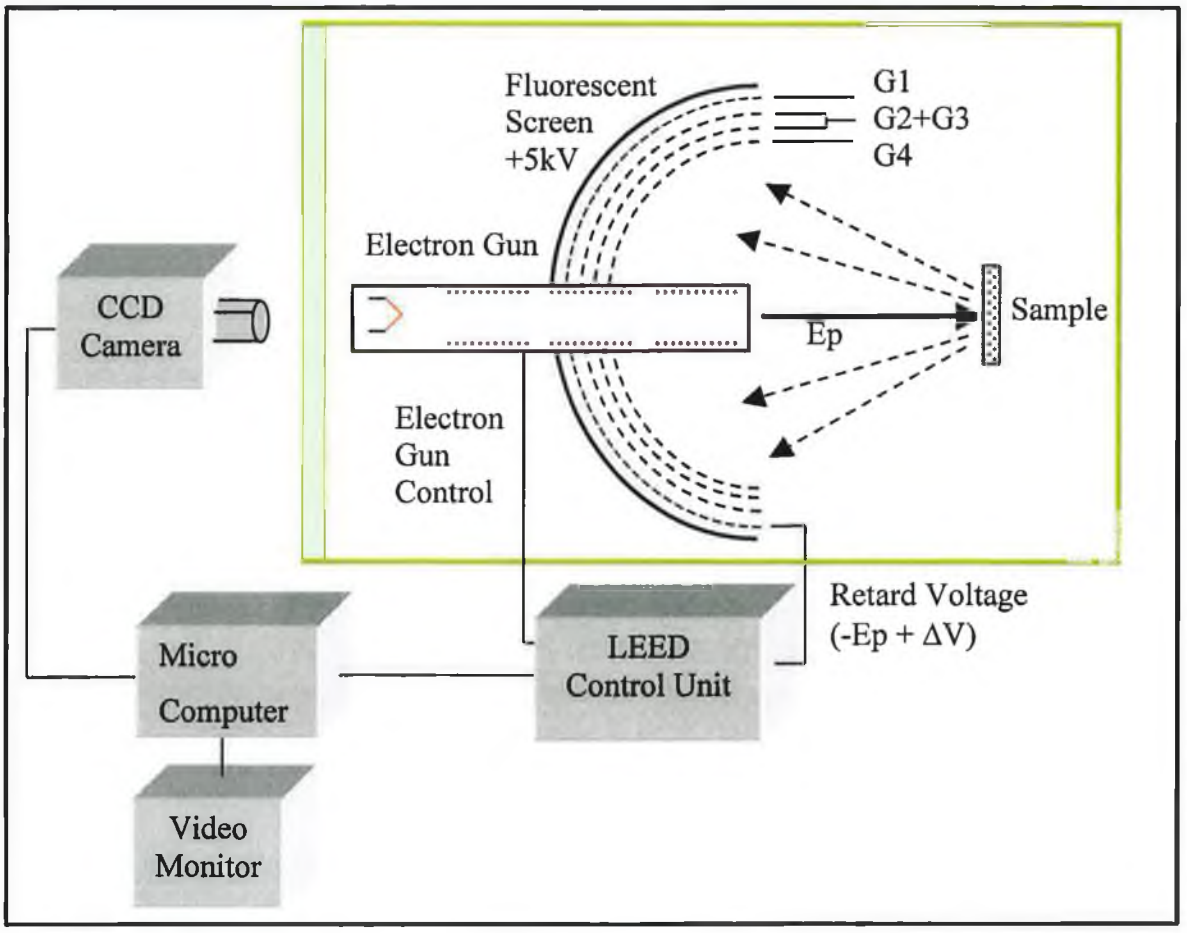

Figure 3.4 *Schematic of experimental setup for LEED studies.*

In the 4-grid LEED optics the fourth grid (G4) is only present to increase the energy resolution for AES. The first grid (G1) is always grounded to provide a field free region which prevents the electrons from being deflected. For the LEED operation mode the second and third grids (G2 & G3) are connected together and also grounded. The fourth grid (G4), closest to the fluorescent screen acts as a retard mesh. It is held at a negative

potential (-Ep+ΔV) whose magnitude is slightly smaller than the electron gun energy (Ep) by an amount ΔV ~10-20V and therefore repels the inelastically scattered electrons. After passing the fourth grid (G4) scattered electrons are accelerated onto a fluorescent screen by a positive potential of 5kV. The screen thus exhibits diffraction spots with positions determined by the reciprocal lattice geometry as described in Section 2.2.

Diffraction data was acquired with a high sensitivity Hitachi Denshi KP-M1E/K CCD camera interfaced to a micro-computer. Quantitative measurements of spot intensities and beam profiles were acquired with software provided by Data-Quire Corporation (Stony Brook, New York). The Data-Quire LEED software allowed simultaneous selection and tracking of symmetrically equivalent beams. Rectangular windows, typically in the range of 10-20×10-20 pixels are centred on each diffraction spot. The intensity for each beam was the accumulated intensity inside each window and a background for each beam was measured from the perimeter of each window. The beams may then be autotracked in the range from 10eV to 500eV. This experimental background subtraction was adequate for the integral beams from clean copper but not for the fractional order beams for the Sn/Cu{100} phases. A Q-Basic program was written to subtract the background intensity from this data. The I-V plots for all symmetrical beams were then averaged and smoothed. Equivalent beam averaging is necessary to reduce random errors associated with the data-collection process and to eliminate systematic errors resulting from any incident beam misalignment [Clarke 1985].

A calibration of the true beam energy with the value recorded by the Data-Quire LEED software was carried out. It was found that a linear energy calibration was required as shown in Figure 3.5. This calibration was checked at the start and at the end of the experiment to verify that the linear relationship remained constant throughout. All I-V data presented was energy corrected by the equation:

$$E_{beam} = 0.925E_{measured} + 3.656 \qquad (3.4)$$

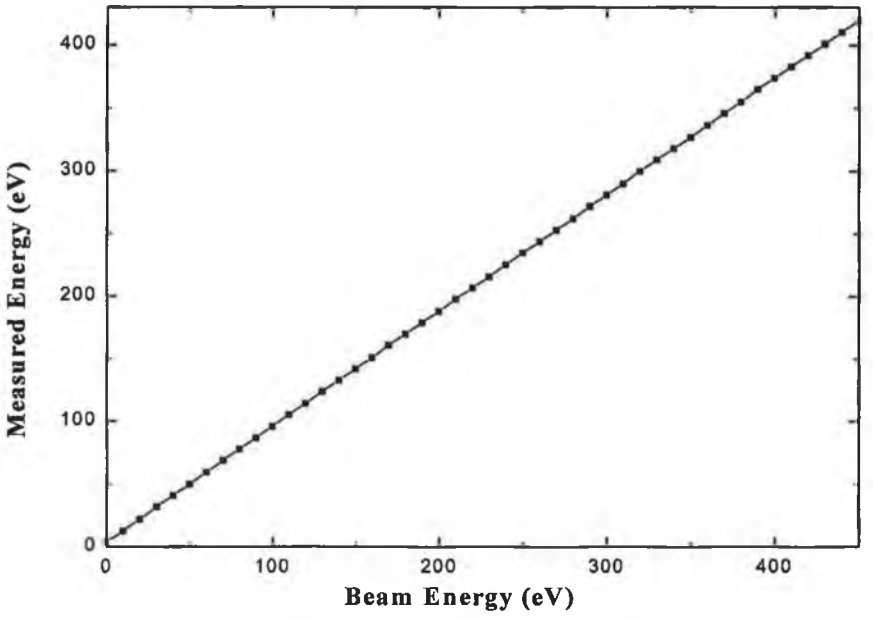

***Figure 3.5** Energy Calibration graph for LEED controller.*

3.2.2 LEED Analysis Software

The LEED simulation program used in this work was a modified code based on a fortran program from Panagiotides *et al.* [Panagiotides 1991]. This program was initially implemented in Dublin City University by Blair in 1997 [Blair 1997]. The modified code is listed in Appendix A.

This program was designed to simulate the LEED pattern from a model structure for comparison with experimental LEED patterns. The programme can model commensurate and incommensurate structures, as well as domain walls and disordered systems. The model structure is set up as a layered array, each array consisting of about 30×30 scatterers. Two or more layers are included, with no constraints on the selvedge structure. If one or more of the layers are not periodic, then the x,y and z components of the position vectors of all the atoms in these layers must be provided as input. The program includes both single and double scattering of the electron beam, so that it is not restricted to the kinematic model as in the case of laser simulation of diffraction patterns [Fedak 1968]. The program performs all calculations of individual scatterer and individual scatterer pair contributions to the scattered wavefield. The scatterers must lie in a user defined rectangular area typically 100Å on each side. A grid in k-space is defined with a resolution of 64×64. The centre and sides of this grid are user determined in units of the substrate reciprocal lattice vectors. The program calculates the single and double scattering contributions to each point (k_x,k_y) of the grid by summing the Fourier

components of the atomic scattering wavefield corresponding to (k_x,k_y) over all scatterers (for single scattering) and over all pairs of scatterers (for double scattering). Several approximations were made to reduce computational time:

(i) The wavefunction of the scattered electron wave is taken in the asymptotic limit.

(ii) Only the zeroth-order terms in the partial wave expansion of the scattered electrons are included (i.e. s-wave).

(iii) No temperature effects are included in the calculations.

The main program requires two parameter sets as inputs:

(a) Non-structural parameters

(b) Structural parameters corresponding to each individual structure model.

(a) Non-structural parameters

These inputs specify the experimental conditions and allow user defined values for energy range, observed k-space dimensions, double scattering to single scattering ratio and s-wave phase shifts for substrate and overlayer. These parameters are listed in Table 3.2 and a more detailed description is presented.

Parameter	Units	Description	Range
E	eV	Primary beam energy incident on crystal	30-650eV
DAN	degrees	Angular dispersion of beam in real LEED gun	0.5
D1	rad	Phase shift of s-wave scattering from adsorbate	0-π
D2	rad	Phase shift of s-wave scattering from substrate	0-π
TEMP		Temperature Effect: 0=None; 1=Calculate Effect	0,1
AMP		Intensity Scale	$100\text{-}1\times10^{8}$
COEF		Double scattering to single scattering ratio 0=no double scattering; 1= equal contributions >1 Double scattering dominates.	$0.01\text{-}1\times10^{6}$
CEN 1	0-n	k-space x centre co-ordinate	0-3 $Å^{-1}$
WID 1	0-n	k-space x width	0-5 $Å^{-1}$
CEN 2	0-n	k-space y centre co-ordinate	0-3 $Å^{-1}$
WID 2	0-n	k-space y width	0-5 $Å^{-1}$

Table 3.2 *Non-structural parameters for LEED simulation program.*

E: Initially this was set at 125 eV as this was a good experimental beam energy to observe all four phases of tin on copper {100} as shown later for photographs of LEED patterns in Figures 4.11 and 4.12. But it is recommended that the structure be simulated at different energies to avoid overlooking some spots that may be weak or extinguished at certain energies.

D1 and **D2**: The phase shifts for the substrate and the adsorbate. These parameters were found to have a significant effect on the simulated diffraction pattern. Choosing random values for the phase shifts caused artefacts, which appeared as random spots, in the LEED pattern. It is therefore essential to calculate the correct phase shift values for the adsorbate and substrate. The Barbieri/Van Hove Phase Shift package [Barbieri 1995] was used to calculate the phase shifts for s-wave scattering. This package is used to produce phase shifts (up to 13) for full dynamic LEED analysis packages. The phase shift calculation is performed in several steps:

(i) calculation of the radial charge density for a free atom.

(ii) calculation of the radial muffin-tin potential for atoms embedded in a surface defined by the user (the surface is represented by a slab that is periodically repeated in 3 dimensions, within vacuum between the repeated slabs); various approximations to the exchange potential are available [Schwarz 1972] and relativistic effects are taken into account.

(iii) calculation of phase shifts from the muffin-tin potential.

(iv) elimination of π-jumps in the energy dependence of the phase shifts.

The s-wave phase shifts calculated as a function of energy for tin and copper are shown in Figure 3.6. In order to check that the procedure for calculating the phase shifts was correct, the copper phase shift results were compared to published values from Barbieri and Van Hove [Barbieri 1995]. The Cu phase shift values from Barbieri and Van Hove were reproduced exactly. This indicates that this code may be used to produce a reliable calculation of Sn phase shifts. The tabulated values are shown in Appendix B. For simulation of a diffraction pattern at one energy only, the corresponding values of **D1** and **D2** are entered, e.g. for **E**=125eV, **D1**=1.37194 for Sn and **D2**=1.36472 for Cu.

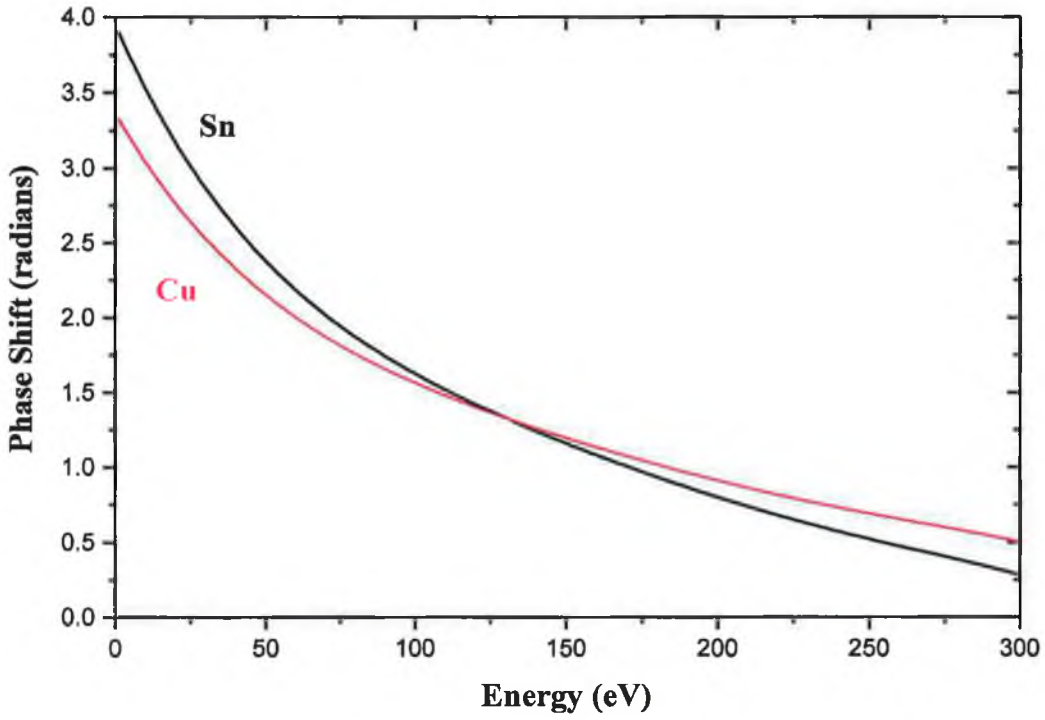

***Figure 3.6** S-wave phase shifts for copper and tin versus energy.*

TEMP: The finite temperature subroutine was not invoked and a value of 0K was used for all results presented. All data was recorded at 300K and no temperature dependence of the LEED patterns was measured.

AMP, COEF: AMP is a scaling factor applied to the total intensity in the calculations. COEF is the ratio of double to single scattering. The sum of the intensities from single scattering is added to COEF times the sum of the intensities from double scattering contributions. AMP then scales the total sum. Since the real ratio of the double to single scattering is unknown in this two/three layer approximation, a constant value of 5.0×10^3 was used in all of the results presented.

CEN1, CEN2: The user-defined centre of k-space was set to 0,0 in all cases for direct comparison of simulated LEED patterns.

WID1, WID2: The dimensions of the LEED pattern in k-space used were 2.9, 2.9 which represents -2.9Å^{-1}1 to 2.9Å^{-1}×-2.9Å^{-1} to 2.9Å^{-1}. This is the k-space for 125eV calculated using $\lambda = \sqrt{\frac{150.4}{E(eV)}}$ Å where $k = \frac{2\pi}{\lambda}$ Å^{-1}. The energy is proportional to the k-vector. As the beam energy is varied, the k-vectors are scaled accordingly so that the positions of the diffracted beams remain unchanged in the output file.

Simulated diffraction patterns at defined energies were generated for comparison of different structural models. However, it is more rigorous to compare results over an energy range (100-200eV) than at a fixed energy to avoid overlooking some spots that may be weak or extinguished at certain energies. Therefore the program was modified to allow adding of LEED patterns calculated at different energies. In order to do this another input file was supplied to the program which contained beam energy in 1 or 5eV steps with corresponding s-wave (L=0) phase shifts for the adsorbate and the substrate at that energy.

An example of a non-structural parameter file for the Sn/Cu{100} system is shown in Table 3.3.

Non-structural parameter file: Sample Input		
125.00	0.5	E ; DAN
1.37194	1.36472	D1 ; D2
0		TEMP
1.0e8	5.0e3	AMP ; COEF
0.00	2.9	CEN1 ; WID1
0.00	2.9	CEN2 ; WID2

Table 3.3 *Example of non-structural parameters input file used.*

(b) Structural parameters corresponding to each individual structure model.

The structural input parameters depend on the type of structure being studied. The structural parameters required by the program are sample size, interlayer distance, unit cell vectors for overlayer and substrate and the coordinates of the atom positions for each cell/layer. The structure can be defined as (i) commensurate or (ii) incommensurate where four options are available in defining the adsorbate and substrate system in terms of uniform or non-uniform structures. A short description of structural parameters is given in Table 3.4.

Parameter	Units	Description	Range
XSIZE,YSIZE	Å	Size of sample with centre (0,0) from $-\frac{XSIZE}{2}$ to $\frac{XSIZE}{2}$ and $-\frac{YSIZE}{2}$ to $\frac{YSIZE}{2}$.	0-100
MINAB	Å	Minimum lattice parameter of substrate.	0-10
DZ	Å	Interplanar spacing	0-10
COMENS		1= Commensurate structure 0= Incommensurate structure	0 or 1
UNIF1		1= Uniform overlayer structure 0= Non-uniform overlayer structure	0 or 1
UNIF2		1= Uniform substrate structure 0= Non-uniform substrate structure	0 or 1
A1X,A1Y **B1X,B1Y**	Å	Overlayer lattice vectors for UNIF1=1	0±15 0±15
NTOP		Number of atoms in overlayer lattice for UNIF1=1	0-300
FX1,FY1,FZ1	Å	Coordinates of atoms from 1 to NTOP in overlayer lattice for UNIF1=1	0-50
IMAX		Total number of overlayer atoms in sample for UNIF1=0	0-300
X1,Y1,Z1		Coordinates of all overlayer atoms (1-IMAX) in sample for UNIF1=0	0-50
A2X,A2Y **B2X,B2Y**	Å Å	Substrate lattice vectors for UNIF2=1	0±15 0±15
NSUB		Number of atoms in substrate lattice for UNIF2=1	0-3000
FX2,FY2,FZ2	Å	Coordinates of atoms from 1 to NSUB in substrate lattice for UNIF2=1	0-50
KMAX		Total number of substrate atoms for UNIF2=0	0-3000
X2,Y2,Z2		Coordinates of all substrate atoms (1-KMAX) in sample for UNIF2=0	0-50

Table 3.4 *Structural Parameters for LEED simulation program.*

When the structural parameter file is called, the program reads in the values for the sample dimensions, the lattice parameter and the interlayer spacing. There are five different formats for structural parameter files that depend on the type of structure being simulated (see Appendix C). They are:

(a) *A commensurate structure*

(b) An incommensurate structure; Uniform Overlayer, Uniform Substrate (1,1)

(c) An incommensurate structure; Uniform Overlayer, Non-uniform Substrate (1,0)

(d) *An incommensurate structure; Non-uniform Overlayer, Uniform Substrate (0,1)*

(e) *An incommensurate structure; Non-uniform Overlayer, Non-uniform Substrate (0,0)*

The (1,1), (1,0), (0,1) and (0,0) values are the unif1, unif2 options as described in Table 3.4.

As a specific example, the structural parameters of one of the Sn/Cu{100} surface reconstructions to be discussed in Chapter Four is described in detail here. Two examples of real structural parameter files are presented here in order to explain the differences in defining an overlayer and a surface alloy model. Option (d), an incommensurate structure with a non-uniform overlayer on a uniform substrate, is chosen for both models. This means that all of the coordinates of the adsorbate atoms must be included in the structural parameter file. This option gives flexibility in defining the adsorbate atom positions and allows the inclusion of lateral and vertical displacements. The unit cell for the substrate atoms is different for an overlayer and a surface alloy model. An overlayer structure model is defined as a two-layer system: the overlayer adsorbate atoms and the substrate atoms. For surface alloy models three layers are defined: the second layer substrate atoms and a mixed top layer with adsorbate atoms and substrate atoms.

An example of a uniform tin overlayer on a Cu{100} surface is shown in Figure 3.7 (a). The overlayer model contains two layers of atoms, the grey circles represent the top layer tin atoms and the orange circles represent the second layer copper atoms. The copper substrate unit cell $\begin{pmatrix} A2X & A2Y \\ B2X & B2Y \end{pmatrix}$ can be defined as a p(1×1) lattice with one copper atom per unit cell as indicated in Figure 3.7 (a). A surface alloy model for the same tin coverage is illustrated in Figure 3.7 (b). The positions of the top layer tin atoms (grey circles) and the second layer copper atoms (orange circles) remain unchanged. A third layer of atoms is also defined, where the green circles in Figure 3.7 (b) represent

the copper atoms in the top layer which form a mixed surface alloy with the tin atoms. The copper substrate unit cell is now defined as a p(2×6) lattice with 12 copper atoms (orange circles) in the second layer and 7 copper atoms (green circles) in the mixed top layer.

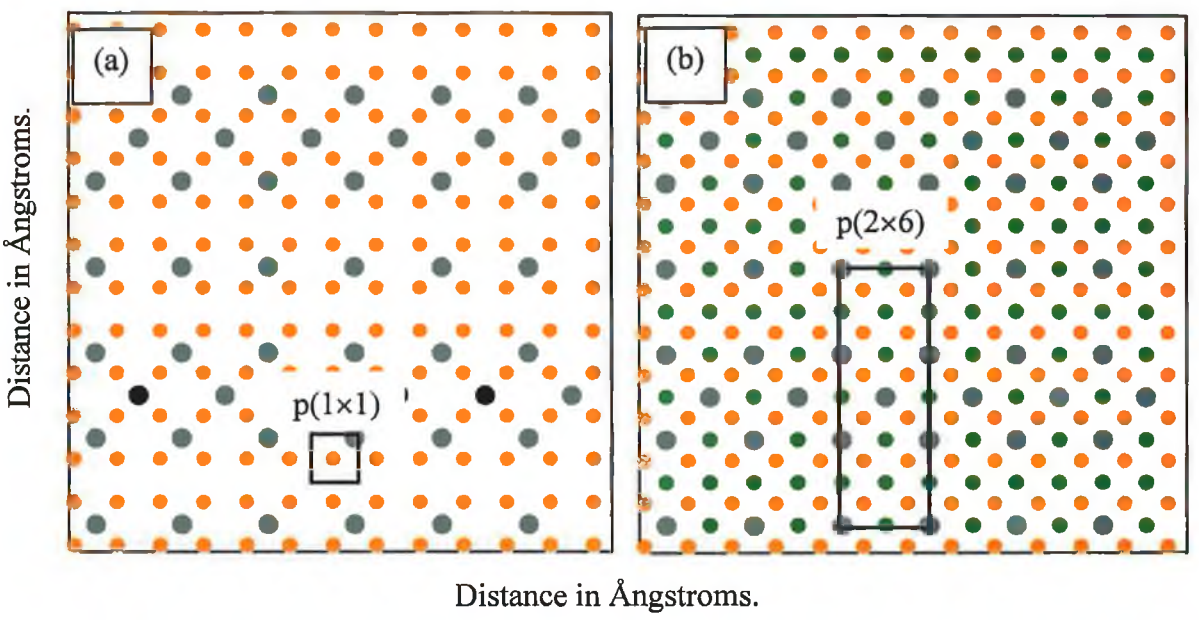

Figure 3.7 *The atom positions for (a) an overlayer and (b) a surface alloy model are shown. The grey circles represent the top layer tin atoms, the orange circles represent the second layer copper atoms and the green circles represent the top layer copper atoms. The substrate unit cell* $\begin{pmatrix} A2X & A2Y \\ B2X & B2Y \end{pmatrix}$ *is illustrated in black for each model.*

The structural parameter files for the overlayer and alloy models shown in Figure 3.7 are described in Table 3.5. Both the overlayer and surface alloy structures are defined as incommensurate with a non-uniform overlayer and a uniform substrate layer. Therefore the coordinates of all the tin atoms in the sample area must be calculated in the range from $-\frac{XSIZE}{2}$ to $\frac{XSIZE}{2}$ and from $-\frac{YSIZE}{2}$ to $\frac{YSIZE}{2}$, an area of 1664.64Å^2 in this example. In this case, there are 104 tin atoms in the top layer for both the overlayer and surface alloy model and the coordinates are listed in Appendix C. The MINAB value used is 2.55Å as this is the lateral spacing between the atoms in the Cu{100} plane. The copper {100} interlayer spacing is 1.8Å for the bulk crystal. DZ is calculated to be 2.27Å for the tin copper interlayer spacing with tin atoms occupying four-fold hollow sites, based on 12-fold co-ordinate metallic radii [Alcock 1990]. The top layer tin atoms are

positioned at z = 0 Å and the second layer substrate copper atoms are positioned at -DZ Å.

Structural Parameters for overlayer			
40.8,40.8			XSIZE,YSIZE
2.55,2.27			MINAB,DZ
0			COMENS
0,1			UNIF1,UNIF2
104			IMAX
{X1,Y1,Z1}			Coordinates for 104 tin atoms
2.55	0		A2X A2Y
0	2.55		B2X B2Y
1			NSUB
-1.275	-1.275	0.0	FX2, FY2, FZ2

Structural Parameters for surface alloy			
40.8,40.8			XSIZE,YSIZE
2.55,2.27			MINAB,DZ
0			COMENS
0,1			UNIF1,UNIF2
104			IMAX
{X1,Y1,Z1}			Co-ordinates for 104 tin atoms
5.1	0		AX AY
0	15.3		BX BY
19			NSUB
-1.275	-1.275	0.0	FX2, FY2, FZ2
1.275	-1.275	0.0	
-1.275	1.275	0.0	
1.275	1.275	0.0	
-1.275	3.825	0.0	
1.275	3.825	0.0	
-1.275	6.375	0.0	
1.275	6.375	0.0	
-1.275	8.925	0.0	
1.275	8.925	0.0	
-1.275	11.475	0.0	
1.275	11.475	0.0	
2.55	0.0	1.8	
0.0	2.55	1.8	
2.55	5.1	1.8	
0.0	7.65	1.8	
2.55	7.65	1.8	
2.55	10.2	1.8	
0.0	12.75	1.8	

Table 3.5 *Comparison of structural parameters used to define an overlayer and a surface alloy structure for the Sn/Cu{100} system.*

In the case of the overlayer structure, the copper substrate is defined as a p(1×1) unit cell of $\begin{pmatrix} 2.55 & 0 \\ 0 & 2.55 \end{pmatrix}$ where 2.55Å is the real dimension of the copper lattice vectors. One atom per unit cell (NSUB=1) is positioned by the FX2, FY2, FZ2 coordinates so that the tin occupy hollow sites. The p(1×1) unit cell is repeated over all the sample area of 1664.64Å^2, generating 256 second layer copper atoms. The x and y coordinates of the 104 tin atoms and the 256 second layer copper atoms were output to a file and plotted to visually ensure correct surface geometry as shown in Figure 3.7 (a). For the surface alloy structure a p(2×6) unit cell was defined as $\begin{pmatrix} 5.1 & 0 \\ 0 & 15.3 \end{pmatrix}$ by the real dimensions (in

angstroms) of the lattice vectors. This cell consists of 19 copper atoms; 12 second layer copper atoms at 0Å and 7 copper atoms incorporated in the top layer, occupying lattice co-ordinate sites at an interlayer spacing of 1.8Å. The coordinates for these copper atoms are listed in Table 3.5. The top layer tin atoms protrude above the top layer copper atoms by 0.47Å (2.27Å -1.8Å). The p(2×6) unit cell is repeated over all the sample area of 1664.64Å^2, generating 256 second layer copper and 152 copper atoms alloyed with tin atoms in the top layer. The atom positions for the surface alloy model is shown in Figure 3.7 (b). The 104 top layer tin atoms (grey circles) are uniform across the surface at a DZ=0Å. The 152 copper atoms in the top layer (green circles) are at a DZ = -0.47Å with respect to the tin atoms in the top layer. The 256 copper atoms (orange circles) are at a DZ = -2.27Å with respect to the top layer tin atoms.

The simulated LEED patterns for these two structural models will be presented in Chapter Four. The structural parameter files in Table 3.5 are shown for only one domain of the overlayer and surface alloy models i.e. the $\begin{pmatrix} 2 & 0 \\ 0 & 6 \end{pmatrix}$ structure. The reconstruction is a double domain structure with an equal density $\begin{pmatrix} 6 & 0 \\ 0 & 2 \end{pmatrix}$ structure coexisting, which is rotated by 90°. The structural parameters for the overlayer and surface alloy model for this domain may be similarly calculated. The simulated LEED pattern for each domain must then be added for comparison with experimental observations.

Other models for the four sub-monolayer phases (I-IV) of the Sn/Cu{100} system with double domain structures were similarly analysed. The atom positions for each domain were simulated separately and the diffraction patterns were then co-added. An example of the structural parameter files for each model used in this work, are listed in Appendix C. Table 3.6 gives a summary of the structural parameter files listed in Appendix C, illustrating the number of tin and copper atom coordinates that must be defined for each model. The simulated diffraction patterns for these models are presented and discussed in Chapter Four.

Phase	Model	Sample Size Å×Å	No. of Sn atoms in top layer	No. of Cu atoms in top layer	No. of Cu atoms in 2nd layer
I	Overlayer	71.4×71.4	140	0	784
I	Surface Alloy	71.4×71.4	140	644	784
II	Argile and Rhead	40.8×40.8	112	0	256
II	Overlayer	40.8×40.8	104	0	256
II	Surface Alloy	40.8×40.8	104	152	256
III	Argile and Rhead	30.6×30.6	76	0	144
III	Overlayer	30.6×30.6	76	0	169
III	Surface Alloy	30.6×30.6	76	76	140
IV	Argile and Rhead	35.7×35.7	97	0	169
IV	Overlayer	35.7×35.7	109	0	196
IV	Surface Alloy	35.7×35.7	109	54	144

Table 3.6 *Summary of sample structural parameter files listed in Appendix C.*

3.3 Auger Electron Spectroscopy (AES)

The UHV system shown in Figure 3.3 was equipped with 4-grid Vacuum Generators (VG) reverse view LEED optics which could also be utilised as a retarding field analyser (RFA) for Auger Electron Spectroscopy (AES). In order to perform Auger analysis with this system, it is necessary to apply a modulation (5V peak to peak) to the retarding mesh voltage and to detect the resultant modulation of the electron beams reaching the screen. In addition, the electron gun energy is increased up to 3keV in order to excite the Auger transitions. The schematic diagram of the Auger equipment setup is shown in Figure 3.8.

In Auger analysis mode the four grids are configured with G1 and G4 earthed while G2 and G3 are at the retard voltage (Ep+ΔV). The LEED control unit which is a 8011 RVLO is designed to be operated in conjunction with a model 340 Lock-In Amplifier (LIA) and a model 318 spectrometer control unit. A pre-amplifier is also used which is factory tuned to the second harmonic of the output control of the internal oscillator of the LIA at around 4.75kHz.

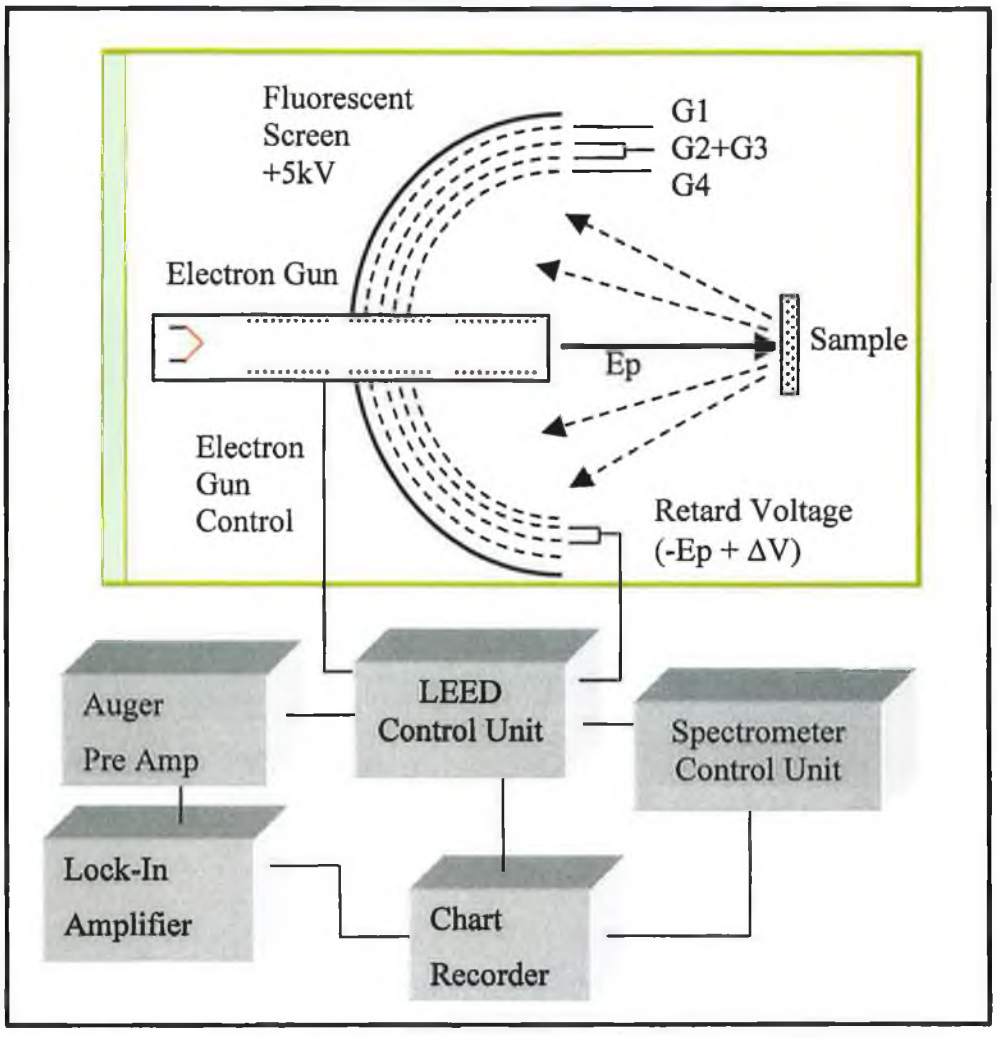

Figure 3.8 *Schematic of experimental setup for Auger analysis.*

The difficulty encountered in Auger spectroscopy is that the spectrum recorded (N(E) versus kinetic energy) generally consists of Auger electron peaks seen as small inflections on a high background. The background is due to secondary electrons, i.e. electrons that have undergone multiple energy losses by excitation of plasmons and/or interband transitions. To extract Auger transition signals from this background the electron energy distribution is electronically differentiated to yield a dN(E)/dE curve where the energetic position of this peak is taken at the minimum of this curve, see Figure 3.9. In terms of quantification of surface species it may be shown that the peak to peak height of the differentiated signal is directly proportional to the area under the N(E) curve, providing peak changes do not occur as a function of coverage. The peak to peak height may then be used as an approximation of surface concentration.

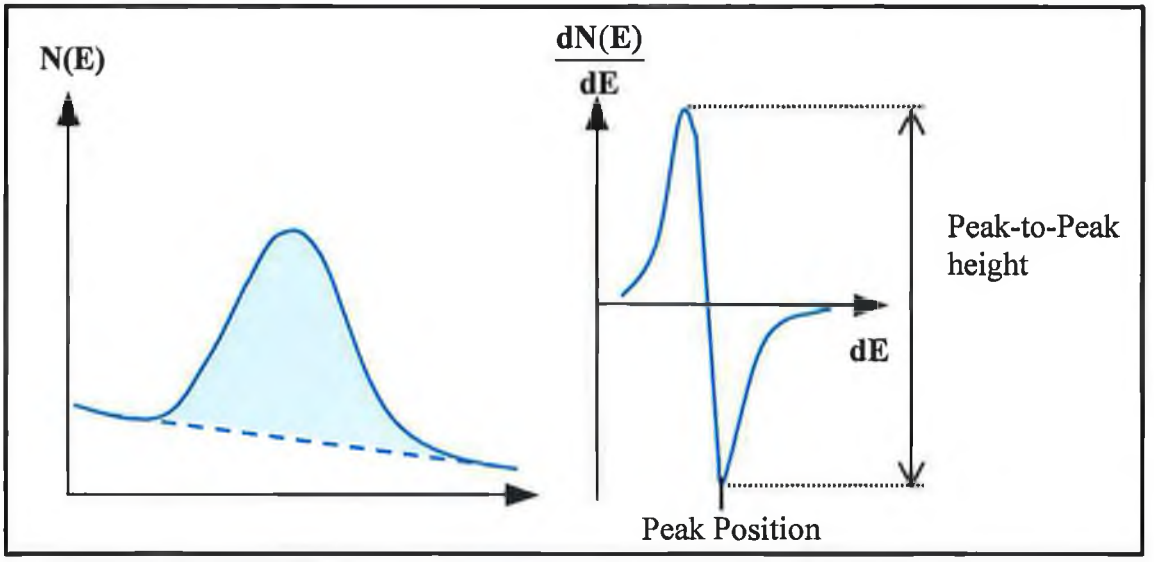

Figure 3.9 *Illustration of Auger (N(E) peak and differentiated Auger peak (dN(E)/dE).*

For many systems the monitoring of the Auger signals from the substrate and the adsorbate as a function of duration of exposure to a constant flux of impinging adsorbate is a means of identifying the growth mechanism. The plot obtained is an Auger signal versus time (AS-t) plot [Argile 1989]. The three main epitaxial growth modes, Stranski-Krastanov, Volmer-Weber and Frank van der Merwe, are discussed in Section 2.1.3 and the effect on AS-t plots for all three growth modes is shown in Figure 2.2.

3.4 Temperature Programmed Desorption (TPD)

Temperature programmed desorption is used as a measure of surface reactivity and was carried out in the same UHV chamber as the LEED and AES experiments as shown in Figure 3.3. A Vacuum Generators Quasar quadrupole mass spectrometer (QMS) was used for residual gas analysis and as a detector for TPD. For desorption studies formic acid (HCOOH) with 98% purity (Aldrich Chemicals) was used. The formic acid was stored in stainless steel gas handling lines and was further purified by several freeze-pump-thaw cycles prior to dosing. Gas purity was checked using the quadrupole mass spectrometer. The experimental TPD setup is shown in Figure 3.10. Dosing of the formic acid was performed by backfilling the UHV chamber with exposures measured using a Bayard Albert ionisation gauge. In this study, the sample was exposed to saturation coverages of formic acid of about 10L, (where 1L $=10^{-6}$ torr/sec).

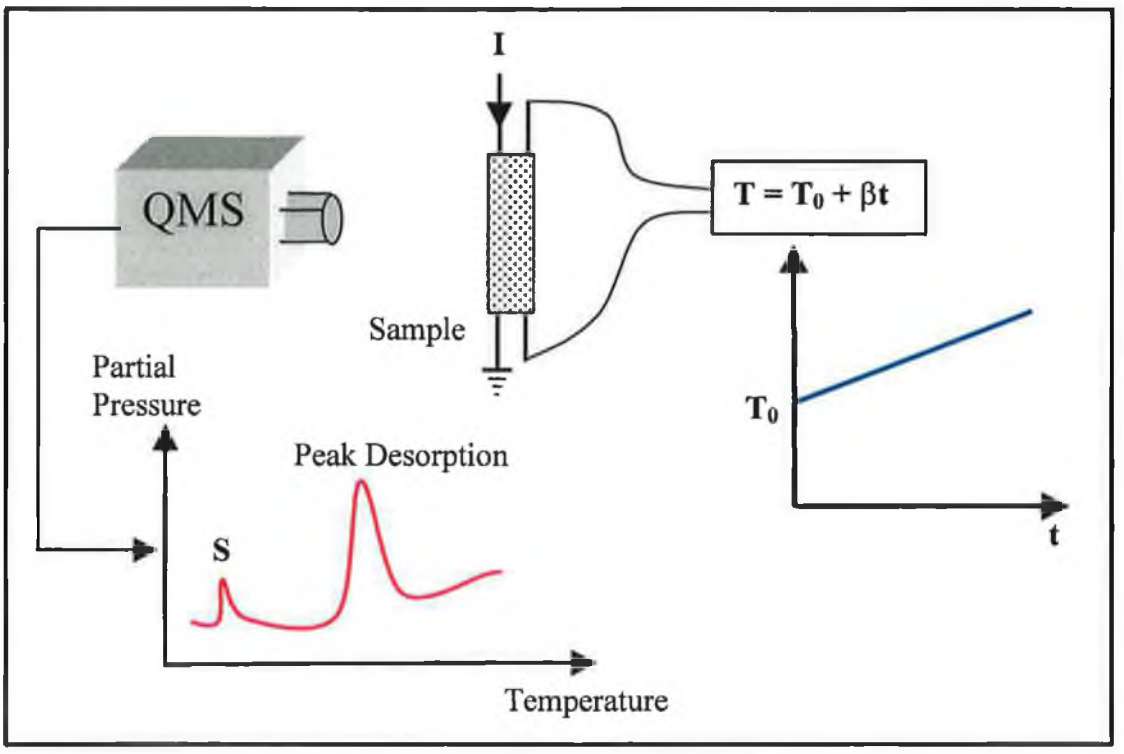

Figure 3.10 *Schematic of experimental setup for temperature programmed desorption studies.*

A linear temperature ramp β was applied to the sample situated close to the mass spectrometer. The heating rate β is the most important experimental value in TPD studies. Higher β values shifts the desorption peak to a higher temperature. Analysis of TPD spectra requires that β is linear over the temperature range studies. Typical β values are in the range 1-10K/s. The sample was heated resistively by passing a direct current through the support wires of the sample. The desorption of the formic acid from these support wires yields the weaker intensity signal, labelled **S**, in Figure 3.10. Continuing heating at a constant heat rate yields a desorption peak for specific gas adsorbates on the sample. The QMS is used to measure different e/m fragments simultaneously. The distance between the sample and the detector is small, typically 2-5cm, to ensure maximum detecting efficiency and is kept fixed to ensure that the integrated areas of different TPD spectra can be compared quantitatively. The distance used in the present setup was about 3cm.

The results for the temperature programmed desorption of formic acid on the Sn/Cu{100} system are presented in Section 4.6.

3.5 X-ray Standing Wave Spectroscopy (XSW)

3.5.1 Synchrotron Radiation

As discussed in Section 2.5.1, the principle of the XSW technique was discovered over three decades ago. However, the technique progressed very little until the advent of synchrotron radiation sources. These sources produce X-ray radiation which is of the order of 10^6 times more intense than conventional sources, and are in addition, continuously tuneable. There are now over 20 sites world-wide where synchrotron radiation research is carried out, including the Synchrotron Radiation Source (SRS) at Daresbury near Manchester, UK. The synchrotron radiation is produced from a high-energy electron storage ring. At Daresbury SRS, an electron beam is produced by a 12 MeV linear accelerator. Pulses of these electrons are injected tangentially into a small booster synchrotron, where they are accelerated by 500 MHz radio frequency radiation. This causes the electrons to travel in bunches, with the separation between bunches dictated by the radio frequency (i.e. the electrons travel in synchronous orbit). The electrons are steered around the ring by dipole magnets. When the electron energy is 600 MeV, the electrons are injected tangentially into the main storage ring (around 32m in diameter), where RF power (from klystron cavities) is again used to raise the electron energy to 2GeV. In this energy region, the electrons are travelling at velocities close to the speed of light, and emit electromagnetic radiation with a continuous distribution from the infrared to the hard X-ray part of the spectrum. The radiation is predominantly plane polarised, and emerges tangentially in pulses of length 0.17 ns and spacing 2.0 ns (in normal operation). The energy lost to synchrotron radiation emission is replaced by RF power. Although the storage ring itself is under high vacuum, electrons are removed by collisions with gas molecules, so that the beam current decays appreciably over a 24-hour period. At Daresbury SRS, a new beam is injected once in every 24 hours during normal operation. The radiation frequency required is selected using a monochromator. For photon energies up to around 1500 eV, a ruled Bragg diffraction grating can be used. At higher energies, the wavelengths are so small that cut crystals (e.g. InSb(111), Ge(111)) may be used to diffract out the required component. The broad range of frequencies available means that synchrotron radiation is suitable for a wide variety of different techniques, including XSW and photoemission [Vickerman 1997].

3.5.2 X-ray Standing Wave experimental details

The XSW results obtained in the study of the Ge/Ga(001) interface and presented in Section 5.5 were performed on beamline 6.3 of the Daresbury SRS. Light was taken from bending magnet 6 on the 2 GeV synchrotron radiation source and focused through the monochromator with a toroidal premirror at 0.5° grazing angle, to a spot of area $5mm^2$. The experimental station is equipped with a permanent UHV chamber as shown in Figure 3.11. The analysis chamber contained a Vacuum Generators HPLT sample manipulator, a cylindrical mirror analyser (Perkin Elmer), a hemispherical analyser (VSW HA100), a fast entry load lock and a Knudsen cell. The chamber was pumped by means of a single turbo molecular pump and a titanium sublimation pump (TSP). After a 24 hour bake at ~180°, a vacuum of 2×10^{-10} mbar could readily be achieved.

The semiconductor sample was mounted on a high precision manipulator (VG HPLT) incorporating sample translation in the x,y,z directions 360° rotation in the horizontal plane and ±90° in the azimuthal plane. The sample was maintained in good electrical contact with the manipulator plate by using tantalum clips. This ensured the absence of any charging effects and good thermal contact to the heating backplate. The manipulator also incorporated an integral electron beam (e-beam) heating facility and a calibrated thermocouple. Two levels were available in the chamber; the upper level being used for LEED observations and sample heating/material deposition, whilst at the lower level NIXSW measurements were performed.

For XSW measurements the HA100 hemispherical analyser was used. The HA100 had better resolution than the cylindrical mirror analyser (CMA) for higher electron energies. In addition, the HA100 incorporated an electron lens system allowing greater flexibility of the analyser-sample positioning. For all spectra the analyser was found to give best results whilst operating in Fixed Analyser Transmission (FAT) 90 mode, that is a constant absolute resolution with a pass energy of 90eV. This gave an analyser energy resolution of ~2eV, similar to that of the beamline absolute resolution. The analyser has the capability of operating with much higher resolution but this produced a seriously diminishing count rate making XSW detection time very long.

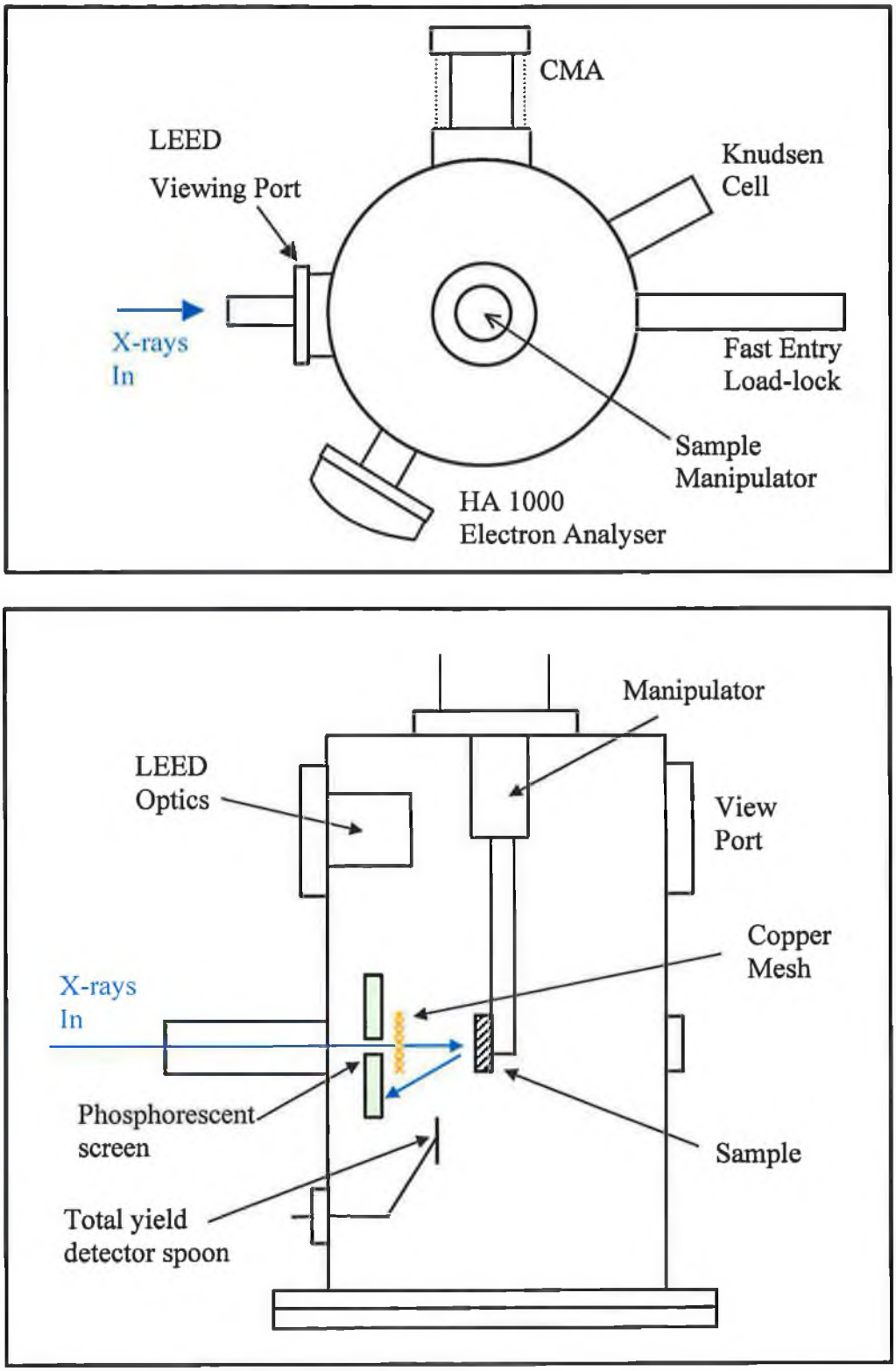

Figure 3.11 *Schematic of the experimental UHV chamber for X-ray standing wave studies.*

The tuneable monochromatic photon source required for XSW experiments were provided by a double crystal monochromator housing InSb(111) and Ge(111) crystal pairs. With these two crystal pairs an energy range of 1780-6000eV was available [MacDowell 1986]. The flux output of both crystal pairs was measured by recording the drain current from the copper mesh placed in the beam after the monochromator stage and are shown in Figure 3.12. Notice that the curves are not smooth but show a sharp decrease in flux throughput at certain energies. The presence of small glitches (G) can be attributed to Bragg reflection within one of the crystals and/or contamination absorption edges [MacDowell 1986].

The reflections used to monitor NIXSW for Ge/GaAs(001) as discussed in Section 5.5, were the [111] reflections at a Bragg energy of 1900eV and the [220] reflections at a Bragg energy of 3093eV. It was found that the InSb(111) crystal pair had the highest flux for photon energies of 1900eV and the Ge(111) crystals were better for measurements at 3093eV. For XSW experiments the sample crystal planes were aligned for normal incidence Bragg reflection by setting the monochromator energy to ~5-10eV above the Bragg condition. The reflected beam could then be observed on the phosphorescent screen mounted around the entrance port to the chamber. By alternately varying the sample position and reducing the monochromator energy the diffracted beam was aligned so it was reflected back into the beamline. This was observed through an increase of flux (measured as a drain current from a gold grid in the beamline) by about 10%. Usually the diffracted beam was moved by about 2° off-normal incidence so that the reflected intensity did not show in the normalisation spectra measured on the gold grid.

For the results reported in Section 5.5, the NIXSW profiles were measured by recording both photoelectron and Auger electron spectra. In all cases the substrate and adsorbate signals were measured both on the selected photoelectron or Auger peak and on the background at an energy of about 10eV greater than the kinetic energy of the peak position. The off-peak spectra were used to provide a signal for background subtraction. This is necessary as the actual signal (which is a measure of absorption) sits on a background of inelastically scattered electrons which must be subtracted. An example of the on-peak and off-peak positions for the As $2p_{3/2}$ photoemission peak is shown in Figure 3.13.

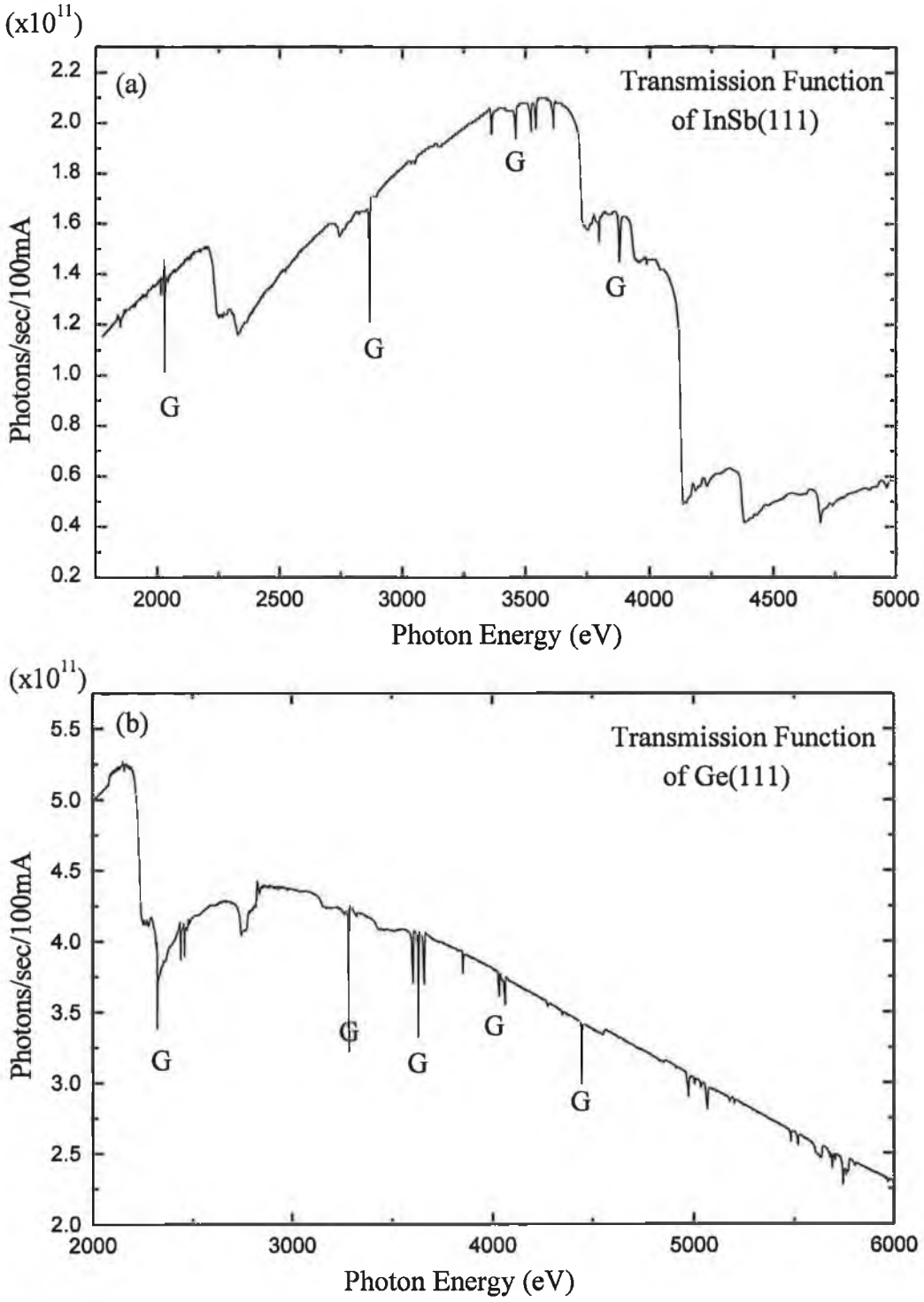

Figure 3.12 *(a) InSb(111) and (b) Ge(111) flux output from station 6.3 at Daresbury SRS [MacDowell 1986].*

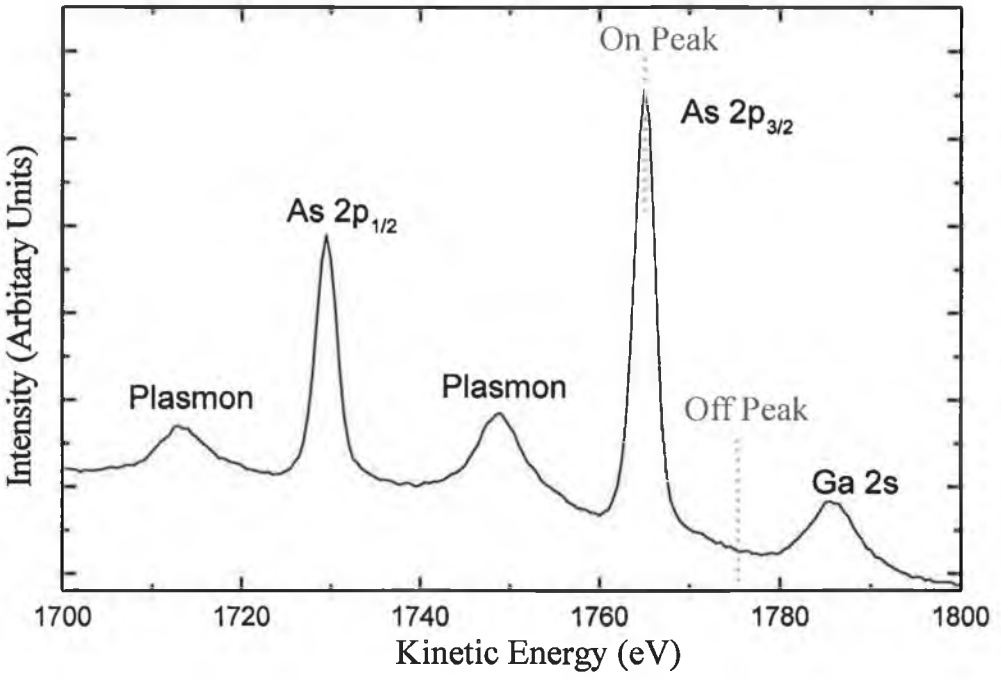

Figure 3.13 *EDC of the As 2p core level at a photon energy of 3093eV. The kinetic energies of the On peak and Off peak positions used for XSW detection are indicated.*

3.5.3 X-ray Standing Wave data analysis

The recorded on-peak and off-peak spectra were normalised to the photon energy and were background subtracted. The resulting spectra were then analysed using a fortran program provided by the group of Prof. Woodruff in Warwick. This program is used to fit a profile to the absorption curve. The crystal lattice spacing, structure factors, Debye-Waller factor and unit cell volume are read in from a parameter file and the Bragg peak position and the instrumental resolution from the (bulk like) off-peak spectrum are determined. The coherent distance and the coherence fraction are then extracted by fitting to the normalised profile. The structure factors for the [111] and [220] Bragg reflection for GaAs were calculated with the program package 'shadow' on the xserv1 workstation in Daresbury. The crystal geometry, the Bragg planes and the real part of the atomic scattering factors for the different atoms in the crystal are supplied by the user as an input file. The program then calculates the real and imaginary part of the structure factor.

The coherent fraction and coherent position of the absorber atoms dramatically influence the shape of the Bragg profile. The calculated profiles in Figure 3.14 show the

effect of different coherent distances D relative to the Bragg planes for the $[1\,\bar{1}\,1]$ reflection of Ge/GaAs(001). When the absorber is positioned exactly in a Bragg plane, D = 0 or 1, the XSW profile has a characteristic shape with a dip before and a peak after the Bragg energy.

To understand these features, it is important to recall that the scan through the Bragg energy results in a variation in the phase of the standing wave. When the nodes of the standing wave coincide with the Bragg planes, the intensity impinging on the absorber atoms is at a minimum and this produces a dip in the XSW profile. When the antinodes of the standing wave coincide with the Bragg planes maximum intensity is reached, this produces the peak in the XSW profile. When the absorber atom is at a position between the Bragg planes it will encounter the nodes and antinodes of the standing wave at different energies relative to the Bragg energy. This results in the variation of profiles for different coherent positions, as shown in Figure 3.14. When, for example, the coherent position is 0.5, the absorber atom will encounter the antinodes before and the nodes after the Bragg energy, and the XSW profile appears as the inverse of the profile for D = 0. The influence of the coherent fraction on the shape of the XSW profile is shown in Figure 3.15. It can be observed that a reduction in the coherent fraction reduces the height of the XSW profile. A reduced instrumental resolution (not shown here) broadens the XSW profile.

Using this fitting procedure and four sets of Bragg reflection planes, the position of Ge on the GaAs(001) surface could be accurately determined as described later in Section 5.5.

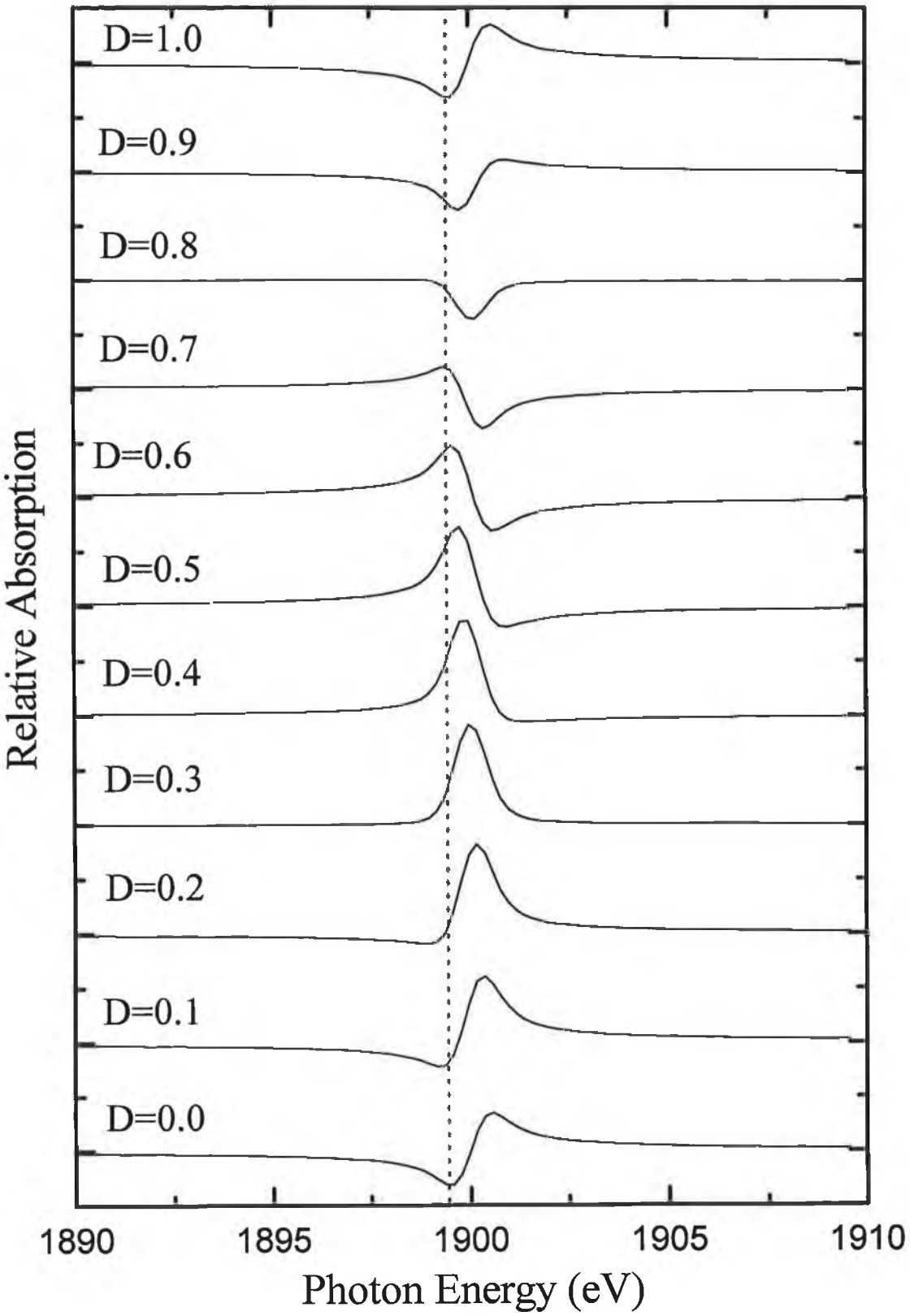

Figure 3.14 *NIXSW profile for the* $[1\bar{1}1]$ *Bragg reflection in GaAs calculated for coherent distances from 0 to 1.* F_{co} *is 0.8,* E_{Bragg} *is 1899.5eV and an instrumental resolution of 0.5eV.*

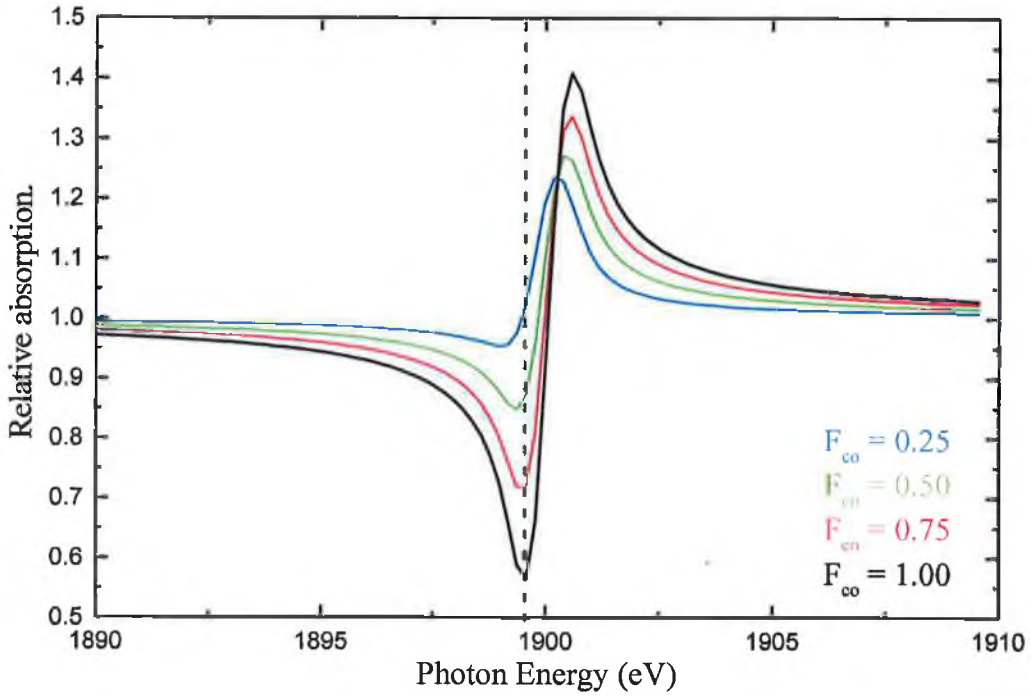

Figure 3.15 *NIXSW profiles calculated for a range of coherent fractions, where the* E_{Bragg} *is 1899.5 eV, D is 1.0 and an instrumental resolution of 0.5eV. A reduction in coherent fraction reduces the height of the XSW profile but does not broaden it.*

3.6 Photoelectron Spectroscopy

3.6.1 Experimental setup

The photoelectron spectroscopy results presented for the Ge/Ga(001) interface in Section 5.6, were performed on beamline 6.2 of the Daresbury SRS. This experimental station is designed for surface sensitive experiments. A layout of the experimental chamber is shown in Figure 3.16. A base pressure of 10^{-10} mbar was readily achieved on this system after a 24-hour bakeout. The standard equipment on this chamber included a sample manipulator with electron beam heating facilities, LEED optics and a fast entry load lock for sample transfer. A Knudsen cell operating at 1350K was mounted for Ge evaporation.

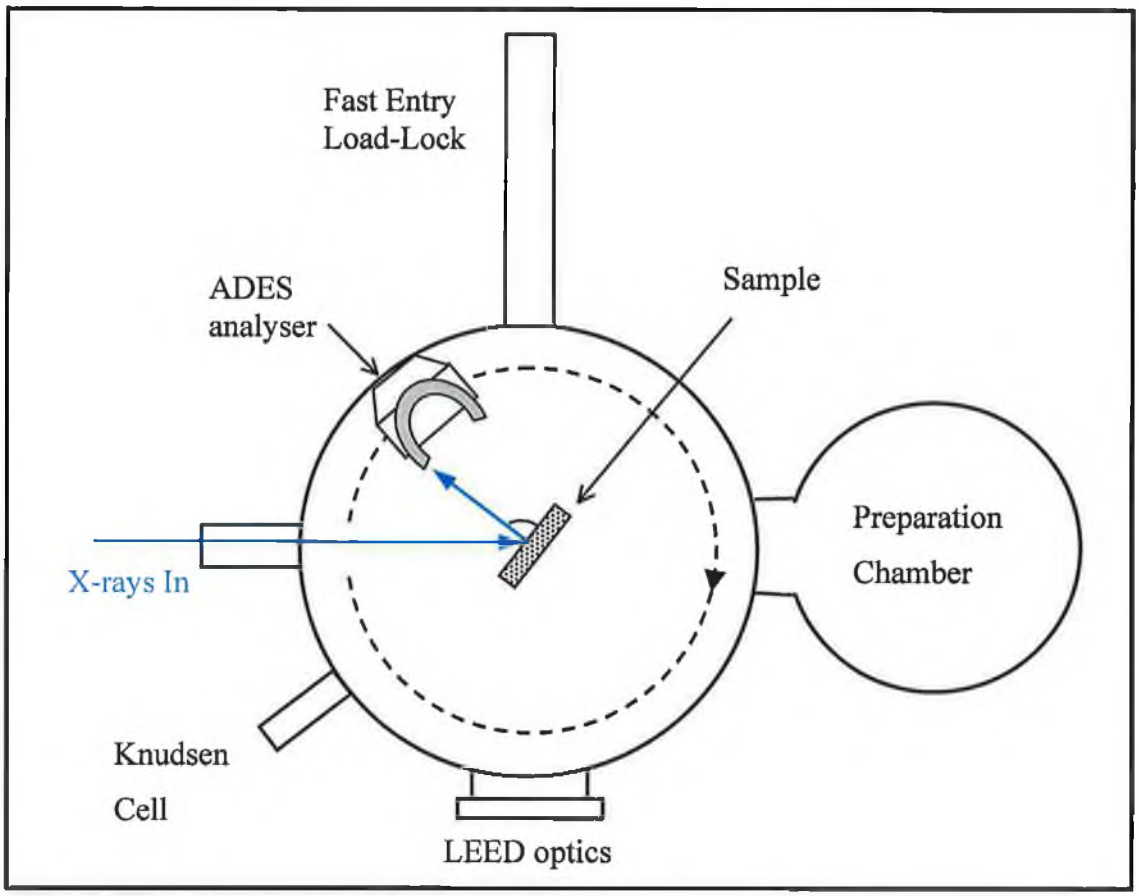

Figure 3.16 *The experimental chamber setup at station 6.2, Daresbury SRS, which used for photoelectron spectroscopy studies.*

A toroidal grating monochromator with two gratings were available on beamline 6.2. The first is a low energy grating with 710 l/mm (G1) and the second, the high energy grating has 1800 l/mm (G2). The transmission characteristics of the gratings were such that the low energy grating G1 (15-45eV) is most useful for work on the low lying electronic levels in the valence band while the high energy grating G2 (40-110eV) provides photons with an energy suitable for recording core level spectra. The flux output from each of these gratings is shown in Figure 3.17. Only the 1800 line/mm grating was used in this investigation.

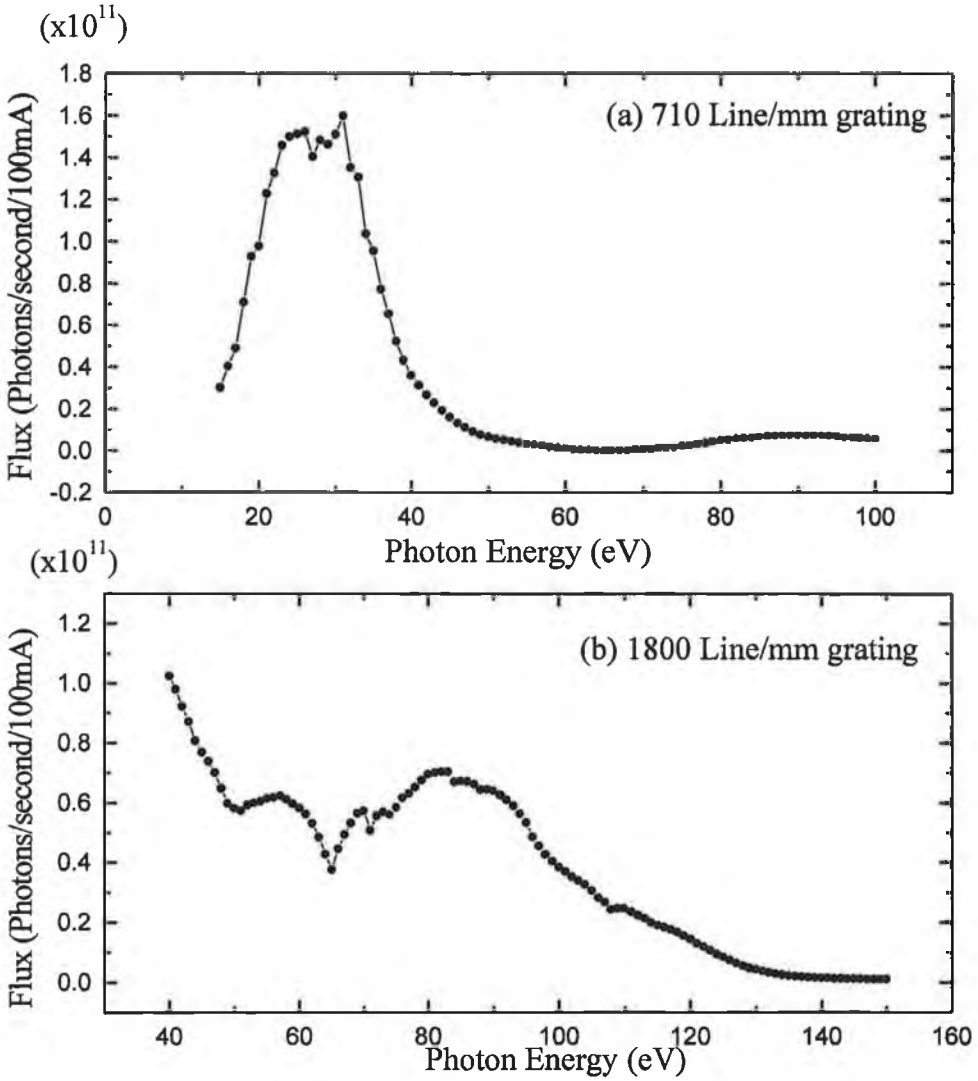

Figure 3.17 *Flux output from (a) the 710 line/mm and (b) the 1800 line/mm gratings, which were used in the toroidal grating monochromator at beamline 6.2 [Turner 1992].*

The minimum photon energy required to probe the As 3d, Ge 3d and Ga 3d core levels relevant to this work are shown in Table 3.7 [Ley 1979]. In this study a photon energy of 70eV is preferable for the atomic levels listed below.

Core Level	**Binding Energy (eV)**	**Electron Kinetic Energy (eV) (hv = 70eV)**
Ga $3d_{5/2}$	18.7	51.3
Ge $3d_{5/2}$	29.9	41.3
As $3d_{5/2}$	41.7	28.3

Table 3.7 *The binding energies of the As 3d, Ge 3d and Ga 3d core levels studied in this work. The electron kinetic energies for a photon energy of 70eV are shown [Ley 1979].*

A concentric hemispherical analyser (ADES 400) was used to record the photoelectron spectra. This analyser could be rotated by 300° in the plane of the synchrotron radiation and by 90° in the plane perpendicular to this. Given that the photoelectrons are emitted from a sample in all directions, this spectrometer can be used to record electron spectra at different polar and azimuthal angles relative to the surface. Positioning the analyser at grazing incidence to the surface may increase the surface sensitivity. The highest count rate is achieved for 'normal emission' geometry, that is when θ in Figure 3.16 is 90°.

3.6.2 Evaluating Core Level Spectra

A core level spectrum usually contains one component for each chemically inequivalent state. Each component is a convolution of the experimental broadening with the intrinsic lineshape of the core level known as a Voigt function. As the binding energy difference of the different components is about the same size as the width of the various Voigt functions, the components usually appear as a single broad peak. To determine the contribution of each component to the spectrum a peak fitting procedure is required to resolve the desired peak shapes [Joyce 1989]. Parameters used in such procedures include the background, the peak shape (Gaussian, Voigt, Lorentzian, asymmetric, or mixtures thereof), the peak position, the peak height and peak width. The program used for peak fitting was 'TCFIT' [Cafolla 1998], which can fit core level spectra with up to four Voigt profiles using an Evolutionary Strategy algorithm. This program has two routines for fitting the background: (a) a polynomial function or (b) a Shirley background. A cubic polynomial background was found to be most suitable for the low kinetic energy electrons studies in this work. After the background has been determined, initial guesses were made for each of the parameters listed above. For spectra containing severely overlapping peaks, the results obtained from peak fitting may depend on the initial starting parameters chosen (i.e., the algorithm converges to a local minimum instead of a global minimum). It is therefore necessary to run the program several times with different starting parameters to ensure that a best fit is obtained. The clean surface results are used to ascertain the starting values for the natural linewidth, the spin-orbit splitting and the branching ratio. The intensities of each component and the binding energies of the surface and bulk components, as well as the Gaussian widths, are also determined. Simultaneous fitting of spectra obtained at different photon energies substantially improves the reliability of this analysis. Additional information can be

used to constrain peak parameters such as peak position and width during the initial iterations of the fitting procedure. Once the algorithm is close to convergence these constraints can be removed.

Using this algorithm good fits were obtained for the core level photoemission data for the Ge/GaAs(001) interface. The values obtained for the different fit parameters, along with their significance, are discussed in Section 5.6.

Chapter Three References

Alcock N. W., Bonding and structure: structural principles in inorganic and organic chemistry, New York, Ellis Horwood, (1990).

Argile C. and Rhead G.E., Surf. Sci. Rep. 10 (1989) 277, Adsorbed layer and thin film growth modes monitored by Auger electron spectroscopy.

Barbieri A. and Van Hove M.A., (1995) (http://electron.lbl.gov/leedpack/), private communication.

Blair D., M Sc. (1997), LEED simulation studies of surfaces using computer and optical simulation methods.

Cafolla A.A., Surf. Sci. 402 (1998) 561, A new stochastic optimisation strategy for quantitative analysis of core level photoemission data.

Clarke L.J., Surface Crystallography, John Wiley & Sons, Ltd. (1985).

Fedak D.G., Fischer T.E. and Robertson W.D., J. Appl. Phys. 39 (1968) 5658, Surface-structure analysis by optical simulation of LEED patterns.

Joyce J.J., Del Giudice M. and Weaver J.H., J. Electron Spectrosc. 49 (1989) 31, Quantitative analysis of synchrotron radiation photoemission core level data.

Ley L. and Cardona M., Photoemission in Solids II, Springer-Verlag Berlin Heidelberg (1979).

MacDowell A.A., Norman D. and West J.B., Daresbury Laboratory (1986), Soft X-ray beamline for surface EXAFS studies in the energy range 60< hv<11000eV at the Daresbury SRS.

Panagiotides N., Batchelor D.R. and King D.A., Chem. Phys. Lett. 177 (1991) 419, Simulation of LEED patterns from complex surface structures.

Schwarz K., Phys. Rev. B 5 (1972), Optimization of the Statistical Exchange parameter α for the free atoms H through Nb.

Turner T.S. and Teehan D., Daresbury Laboratory (1992), Characteristics of TGM6.

Vickerman J.C., Surface Analysis - The principle techniques, John Wiley & Sons Ltd. (1997).

Chapter Four

Tin on Cu {100}

In this chapter a review of some relevant bimetallic systems involving copper and tin is presented. The Sn/Cu{100} system is re-examined by LEED, AES and TPD, providing further insight into the surface phases formed and their coverage dependent transitions. Data showing that Sn adsorption leads to significant perturbation of the copper selvedge, consistent with adsorbate induced reconstruction/surface alloy formation is presented. New models are suggested for the four sub-monolayer structures, based on double scattering simulation. These models are shown to be in good agreement with observed LEED patterns.

4.1 Introduction

Intermixing, alloying, dealloying and strain-induced reconstructing at surfaces are important phenomena in the growth of thin films on metal surfaces. Many studies show that these processes may influence strongly the electronic structure and change many chemical and physical properties of film surfaces [Rodriguez 1996]. In recent years, the interaction of alkali and transition metals with the Cu{100} surface has been extensively studied both experimentally and theoretically. Interest in these systems has been motivated by the fact that Cu-based bimetallic catalysts show very useful properties, particularly in respect to their industrial applications, such as material selectivity, structural stability and catalytic activity in comparison to their single-metal counterparts [Campbell 1990] [Somorjai 1996]. These properties can be controlled by tailoring the local composition of the bimetallic surface.

The investigation of copper for use as an interconnection metal in the ultra large–scale integration (ULSI) era of silicon integrated circuits has accelerated in the past few years [Murarka 1995]. As chip die sizes have reduced due to advances in fabrication technology, the size of the aluminium interconnnects has also decreased, increasing their capacitance to a level where signal delays across the chip have become significant. The advantages of using copper to replace the currently used aluminium are related its lower resistivity (1.7 μΩcm for Cu versus 2.7 μΩcm for Al), and its higher resistance to electromigration, which is several orders of magnitude higher than aluminium [Lloyd 1999] [Clevenger 1998]. Cu(Sn) alloys exhibit even better electromigration activation energies than pure copper (1.14eV for Cu(2 wt % Sn) compared to 0.73eV for pure Cu) [Lee 1995] [Huang 1997]. Using copper interconnects allows smaller die sizes, faster

chips and paves the way for the next generation of gigaHertz-class CPUs. IBM's latest 400MHz PowerPC 740/750 CPU is the first commercial implementation of this technology achieving 0.2 micron linewidths.

Practically all microelectronic assemblies in use today utilize Pb-Sn solders for interconnection. With the advent of chip scale packaging technologies, the use of solder connections has increased. The most widely used Pb-Sn solder has the eutectic composition. Emerging environmental regulations worldwide, most notably in Europe and Japan, have targeted the elimination of Pb usage in electronic assemblies, due to the inherent toxicity of Pb. This has made the search for suitable "Pb-free" solders an important issue for microelectronics assembly. A recent review by Abtew, identifies 69 Pb-free solder alloys that have been proposed thus far [Abtew 2000]. Indications are that Sn-rich alloys will be the Pb-free solder alloys of choice with studies concentrating on binary Sn alloys (e.g. Sn-Bi, Sn-Ag, Sn-Au and Sn-Zn) and also some ternary Sn alloys. Research on this topic continues at the present time at a vigorous pace, in view of the importance of the issue.

The Cu-Sn bimetallic system, whether in the thin-film reaction or in the soldering reaction, is thus technologically important [Tu 1996].

4.2 Review of Bimetallic Systems

Bimetallic surfaces can be prepared by two methods, (a) by cutting and polishing a bulk single-crystal alloy or intermetallic compound of the two elements followed by cleaning and annealing in UHV or (b) by vapour deposition of one metal onto a clean well-defined single-crystal surface of the second pure metal in UHV [Campbell 1990]. The topological classification in which the vapour deposited thin films can grow is divided into three distinct modes, as discussed in Section 2.1.3. These growth modes were named after their original investigators: (i) Frank and van der Merwe, monolayer-by-monolayer or FM growth; (ii) Stranski and Krastanov, layer growth up to one or a few monolayers followed by 3D crystallites growth, SK growth; and (iii) Volmer and Weber, formation of 3D crystallites without a preceding adsorbed layer, VW growth [Bauer 1986] [Rhead 1981a]. Two additional modes were suggested by Argile and Rhead in 1989, namely simultaneous multilayer growth (SM), and monolayer plus

simultaneous multilayer growth (MSM) [Argile 1989]. Argile and Rhead then used their new classification in a general review of some 440 investigations of 220 adsorbate/substrate systems. Somorjai published a more recent review of adsorbate/substrate systems in 1994 [Somorjai 1994]. Biberian showed that an interpretation of LEED patterns based on symmetry and limited adsorption sites can be used to model structures for monolayers adsorbed on (100) faces of cubic metals [Biberian 1976].

Thin film alloys have also been prepared by annealing the surface during or after the vapour deposition of the adsorbate to enable the interdiffusion of the two metals. Alloy films have been reported in two main structures: (a) a surface alloy with a mixed adsorbate/substrate top layer or (b) a top layer consisting of substrate atoms with the adsorbate atoms subsurface occupying the second layer. Bardi reported a review of 34 different surface alloy systems in 1994 [Bardi 1994]. A theoretical study based on surface energy, interface energy and strain energy showed that surface alloy formation is expected quite generally in systems which are dominated by the atomic size mismatch, even if the two metals are immiscible in the bulk [Tersoff 1995] [Venables 1994].

As can be seen from the reviews mentioned above, bimetallic systems have very complex behaviours. Some relevant bimetallic systems involving tin and copper are introduced in the following sections. In Section 4.2.1, a summary of different metal adsorbates on the Cu{100} surface is presented. Bimetallic systems using tin as an adsorbate on metal substrates are discussed in Section 4.2.2. The Sn/Cu bimetallic system has a highly complex bulk phase diagram, as shown in Section 4.2.3, with alloys forming throughout the composition range including a range of intermetallic compounds. Despite the technological importance of the tin-copper system, it has received little experimental or theoretical interest. In Section 4.2.4, a review of earlier studies of Sn/Cu{100} by LEED, Rutherford Back Scattering (RBS) and segregation studies is reported.

4.2.1 Metal Adsorbates on Copper {100}

A brief discussion of the growth of some relevant metal adsorbates on Cu{100} is presented to demonstrate the complex behaviour of bimetallic systems. From the inference of Tersoff [Tersoff 1995], that the ratio of the metallic radii of the adsorbate and substrate atoms can be used to predict surface alloy formation, this ratio is listed for each element listed. The ratios quoted are based on the 12-fold coordinate metallic radii [Alcock 1990]. A summary of 14 different metal adsorbates on Cu{100} is presented in Table 4.1.

Ag (Z = 47, F.C.C, a=4.09Å, $r_{Ag}/r_{Cu} = 1.13$)

A c(10×2) pattern was reported by LEED and AES studies for the deposition of 1 ML Ag on a Cu{100} substrate for substrate temperatures ranging from 80-474K with no tendency for Ag to form a surface alloy [Palmberg 1968b]. Angle Resolved Photoelectron Spectroscopy (ARPES) studies confirm this structure as single close-packed hexagonal overlayer at monolayer coverages [Tobin 1986]. An XPD study of this system shows surface alloy formation for coverages from 0.04 to 0.2ML with c(9×9) clusters forming in the overlying hollow sites up to 0.3ML coverage and a two-domain c(10×2) overlayer structure from 0.3 - 1ML [Hayoz 1997].

Au (Z = 79, F.C.C, a=4.08Å, $r_{Au}/r_{Cu} = 1.13$)

In 1968 the formation of a well-defined surface alloy was reported after the deposition of Au on Cu{100} [Palmberg 1968a]. After depositing approximately 0.5 ML of Au, with the Cu{100} substrate cooled to 220K to inhibit alloying, a weak c(2×2) structure was first detected upon warming to 250K with a well ordered alloy observed at room temperature. The same pattern was also found upon room temperature deposition of 0.5ML and was similar to the bulk Cu_3Au {100} surface. Qualitative LEED studies by Fujinaga confirmed these findings and showed evidence for surface alloy formation of Au on Cu{110} and Cu{111} [Fujinaga 1979]. LEED I-V calculations proved that Au/Cu{100} is indeed a top layer mixed surface alloy [Wang 1987]. Further investigations by ARPES, LEED, AES, ISS, ARUPS, XPS, PhD, STM, LEIS and MEIS have since been reported [Hansen 1987] [Graham 1987] [Wang 1988] [Tobin 1990] [Naumovic 1992] [Chambliss 1992] [Brown 1999]. Further deposition of Au between

0.6ML and 1.2ML, leads to dealloying, causing a segregation of the Au from the mixed c(2×2) layer to the overlayer [Shen 1996].

Bi (Z = 83, Rhombohedral, a=4.75Å, $r_{Bi}/r_{Cu} = 1.33$)

The first study of binary metal monolayers involved the coadsorption of bismuth and lead on Cu{100} [Argile 1978a]. For the adsorption of Bi on room temperature Cu{100} a surface alloy forms at θ = 0.35ML. At a coverage between 0.43-0.49ML the Bi dealloys to form a c(2×2) structure at θ = 0.5ML, with the Bi atoms located in four-fold hollow overlayer sites. The higher Bi coverages of 0.56ML and 0.6ML, with LEED patterns of c(9√2×√2) and (√41×√41) (better described as a p(10×10) structure), respectively, can be regarded as "heavy" antiphase domain structures. The principal difference between the two structures is that the c(9√2×√2) is a one-dimensional domain-wall structure, whereas the p(10×10) is a two-dimensional dislocation array. These dislocations meet in a "pinwheel" arrangement with an offset of one unit cell spacing between the incoming dislocations on either side [Delamare 1973] [Blum 1991] [Li 1992] [Meyerheim 1997,1998].

Pd (Z = 46, F.C.C, a=3.89Å, $r_{Pd}/r_{Cu} = 1.08$)

A well developed c(2×2) surface alloy structure (like Cu_3Pd{100}) is formed at submonolayer Pd coverages upon deposition at 300K which appears to be best developed at a Pd coverage between 0.5 and 0.8 ML. The structure was shown to have a top layer of an ordered 50%-50% mixture of Pd and Cu atoms, and no ordered content in deeper layers, analogous to the structure found for Au/Cu{100}. Alloys of palladium and copper are interesting in the field of catalysis and have been investigated intensively both experimentally and theoretically [Fujinaga 1979] [Lu 1988] [Graham 1990] [Yao 1995] [Pope 1995] [Shen 1996] [Murray 1996] [O'Connor 1997]. Recent diffuse LEED studies on the low Pd coverage range from 0.1-0.5 ML indicate that the Pd substitutes into the outermost copper layer occupying substitutional lattice sites with reconstructions based on c(4×4) and p(2×4) at 0.125ML and p(2×2) at 0.25ML [Barnes 2000].

Pb (Z = 82, F.C.C, a=4.95Å, $r_{Pb}/r_{Cu} = 1.37$)

The deposition of Pb on Cu{100} was found to exhibit only two types of ordered structure: c(2×2) domain wall overlayer phases in the low-temperature, high-coverage region and a c(4×4) surface alloy in the medium-temperature low-coverage region. Further deposition above 0.6ML leads to the formation of 3D islands, in a Stranski-Krastanov growth mode. The c(4×4) surface alloy is shown to consist of parallel Pb and Cu corrugated chains [Gauthier 1996]. Similar alloying processes take place for Pb/Cu{110} and Pb/Cu{111}. These processes were unexpected as Pb and Cu are immiscible in the bulk [DeBeauvais 1995] [Nagl 1994]. The monolayer phase of $(5\sqrt{2}\times\sqrt{2})R45°$ was described as an ordered array of linear boundaries separating antiphase domains of c(2×2) overlayer structure. In the structures observed at low temperatures, the atoms are all localised near hollow sites forming "heavy" domain wall c(2×2) structures forming a two dimensional array. LEED patterns demonstrate the appearance of spot splitting at the half-order spot positions due to the presence of the domain boundaries. The models show the domain wall structures vertices meet in a "pinwheel" arrangement as shown for Bi/Cu{100} [Bocquet 1997, 1998]. Both the large lattice mismatch a_{Pb}/a_{Cu} = 1.37 and the small cohesive energy ratio E_{Pb}/E_{Cu} = 0.58 between the bulk lead and copper are responsible for such surface superstructures. Numerous experimentally and theoretically studies have been completed on this bimetallic structure [Henrion 1972] [Sepulveda 1977] [Argile 1978a] [Hosler 1982, 1986] [Nagl 1995] [Robert 1996] [Tan 1997].

In (Z = 49, Tetragonal=4.59Å, $r_{In}/r_{Cu} = 1.30$)

In/Cu{100} bears some similarity to the c(4×4) structure found on Pb/Cu{100}. It was found to form a surface alloy with In chains aligned along <100> directions resulting from competing repulsions between In atoms aligned along the <110> direction and attractive interactions between In atoms aligned along the <100> direction [Breeman 1992,1994].

It is to be expected that row formation and one-dimensional ordering are not restricted to the In/Cu and Pb/Cu systems. It was found that size difference between the adsorbate and the substrate atoms plays a crucial role in the tendency of atoms to form rows in the top surface layer. Therefore it is likely that for metal-metal systems for which the ratio

of the atomic radii is in the narrow range from 1.25-1.35, surface alloying will result. If the ratio is <1.25 the repulsive interactions in the close-packed directions will be too small for row formation, whereas for a ratio >1.35 the adsorbate will stay on the surface as an adatom [Breeman 1994].

A summary of the growth modes of 14 various metal adsorbates on Cu{100} is presented in Table 4.1. The table is listed in order of increasing atomic radii ratio. The table can be divided into three regions, dependent on the ratio of atomic radii.

(i) It is observed that for elements with an atomic radii ratio <1.25, there are two types of behaviour: (a) for Ni and Ir that are immiscible in the bulk phase with copper, alloy formation occurs at low coverages, <1ML, with the Ni and Ir located subsurface; and (b) for Mn, Pd, Pt and Au, that are miscible in the bulk phase with copper, surface alloys form over a wide coverage range, 0-0.6ML. These alloy structures are based on a 50%-50% ratio of adsorbate to substrate in the topmost layer.

(ii) For elements with the ratio of atomic radii between 1.25 and 1.37 surface alloy structures form at coverages <0.4 ML, e.g. Ag, Li, In, Bi, Pb. With increased coverage the adsorbate atoms dealloy to form overlayer structures. This alloy formation is unexpected, when the adsorbates are immiscible with copper in the bulk phase.

(iii) For adsorbates with larger atomic radii ratios, >1.37, e.g. Na and K, overlayer structures are reported for all coverages.

These observations of the different behaviours of adsorbates grown on Cu{100} are in good agreement with the conclusions of Tersoff [Tersoff 1995].

Adsorbate	Growth Mode	Temp (K)	θ (ML)	LEED Pattern	Matrix	Radii Ratio	Reference
Ni	Ni Subsurface	300-450	1	p(1×1)		0.98	Heinz 1999 Kim 1997
Mn	Surface Alloy Surface Alloy	300	<0.5 0.5	diffuse c(2×2)		0.99	Brown 1999 Wuttig 1993
Ir	Surface Alloy Ir subsurface	200 620	<1 0.6	p(1×1) p(2×1)		1.06	Gilarowski 1999
Pd	Surface Alloy Surface Alloy	300	<0.5 0.5-0.8	diffuse c(2×2)		1.08	Lu 1988 Pope 1995
Pt	Surface alloy	530	0.5-0.6	c(2×2)		1.09	Reilly 1999
Au	FM Surface Alloy Dealloys	<220 300 300	1 0.5 0.6-1.2	c(14×2) c(2×2)	$\begin{pmatrix} 2 & 0 \\ -1 & 7 \end{pmatrix}$ $\begin{pmatrix} 1 & 1 \\ 1 & -1 \end{pmatrix}$	1.13	Palmberg 1968a Wang 1987 Shen 1996
Ag	Surface alloy FM	 80- 475	<0.3 0.3-1	c(9×9) c(10×2)	$\begin{pmatrix} 2 & 0 \\ -1 & 5 \end{pmatrix}$	1.13	Hayoz 1997
Li	4-fold hollow overlayer Surface alloy Surface alloy Overlayer/Alloy	180 300	0.25-0.55 0.2-0.4 0.45 0.55	c(2×2) p(2×1) p(3×3) p(4×4)	$\begin{pmatrix} 1 & 1 \\ 1 & -1 \end{pmatrix}$	1.22	Mizuno 1993 Diehl 1996 Sasaki 1999
Sn						1.27	Present Work
In	Surface alloy		0.05-0.25			1.30	Breeman 1992 Breeman 1994
Bi	Surface Alloy 4-fold hollow 1D domain wall 2D domain wall	300	0.35 0.5 0.56 0.60	p(1×1) c(2×2) c(9√2×√2) p(10×10)		1.33	Argile 1978a Blum 1991 Meyerheim 1997,1998
Te	4-fold hollow overlayer		0.25	p(2×2)		1.33	Johnson 1983
Pb	2D Domain walls based on c(2×2) 4-fold hollow site overlayer surface alloy 4-fold hollow site 2D domain walls c(2×2) overlayer	160-220 300	0.24 0.57 0.375 0.5 0.6	(√61×√61)-Rtan^{-1}(5/6) (5×5)-Rtan^{-1}(3/4) c(4×4) c(2×2) c(5√2×√2)-R45°	$\begin{pmatrix} 6 & 5 \\ -5 & 6 \end{pmatrix}$ $\begin{pmatrix} 4 & 3 \\ -3 & 4 \end{pmatrix}$	1.37	Bocquet 1997 Bocquet 1998 Robert 1996 Gauthier 1996 Nagl 1995 Hosler 1982 Hosler 1986 Henrion 1972 Tan 1997
Na	4-fold hollow overlayer	100-300	0.5	c(2×2)	$\begin{pmatrix} 1 & 1 \\ 1 & -1 \end{pmatrix}$	1.50	Mikkelsen 1999 Diehl 1996
K	Liquid Quasi-hexagonal overlayer Hexagonal overlayer	330	0.18-0.26 0.28 0.33		$\begin{pmatrix} 2 & 3 \\ 0 & 5 \end{pmatrix}$ $\begin{pmatrix} 2 & 2 \\ 0 & 3 \end{pmatrix}$	1.86	Aruga 1984 Diehl 1996 Diehl 1997

Table 4.1 *: Metal adsorbates on Cu{100}, listed in order of increasing ratios of 12-fold coordinate metallic radii, where the radius of Cu =1.278Å.*

4.2.2 Comparative Bimetallic Systems

The adsorption of tin on other {100} and {111} surfaces of metal with similar lattice mismatches may also be considered.

(a) Sn/Al{100}, $r_{Sn}/r_{Al} = 1.13$.

Early work of Sn/Al{100} at room temperature reported a p(1×1) at low coverages and a c(2×2) overlayer optimised at 0.5ML. For tin coverages from 0.5-0.67ML the c(2×2) structure and a $\begin{bmatrix} 2 & 0 \\ 1 & 3 \end{bmatrix}$ structure were shown to coexist. A complete $\begin{bmatrix} 2 & 0 \\ 1 & 3 \end{bmatrix}$ or c(2×6) structure formed at a monolayer coverage of 0.67 ML. Kinematic intensity calculations indicate that this structure is an overlayer of dense tin rows [Argile 1978b].

(b) Sn/Pt{100}, $r_{Sn}/r_{Pt} = 1.26$.

Tin was evaporated on a Pt{100} substrate monitored by AES peak-to-peak amplitude versus Sn deposition time and investigated by LEISS, TDMS, XPS and LEED experiments [Paffett 1991]. A c(2×2) LEED pattern is observed for Sn coverages of 0.2-0.55 ML and annealing temperature from 320-800K with a p(3√2×√2)R45° pattern observed at higher anneal temperatures of 950-1050K for coverages of 0.65-0.7 ML. These two structures are observed to coexist for coverages of 0.55-0.65ML. The proposed structures are surface alloys with a mixed 50%-50% Sn-Pt first layer surface alloy at 0.5ML coverage for the c(2×2) phase and a p(3√2×√2)R45° pattern at 0.67ML coverage due to a periodic surface reconstruction with tin atoms occupying domain boundaries [Paffett 1991].

(c) Sn/Ni{100}, $r_{Sn}/r_{Ni} = 1.30$.

A surface alloy with a c(2×2) structure has been observed using LEED and AES after adsorbing 0.5ML of Sn on Ni{100} at 250K [Oda 1980]. This structure is due to substitution of 0.5ML of tin with the first layer nickel atoms, with Sn protruding slightly (0.44Å) above the first Ni layer. The "best" c(2×2) pattern was observed upon warming to 500-800K but annealing to 900K caused a complex LEED pattern with a splitting of the (½, ½) beams into a quartet attributed to domain formation [Li 1994].

(d) Sn on FCC {111} surfaces

Deposition of 0.33 ML of Sn on {111} surfaces of Cu, Ni and Pt shows the formation of a p($\sqrt{3}\times\sqrt{3}$)R30° surface alloy structure upon annealing to 40% of the substrate melting temperature (1356K for Cu, 1726K for Ni and 2045K for Pt). Although in each system the Sn is incorporated into the surface, a strain induced rippling is shown to be linearly correlated to the lattice constant of the substrate (3.61Å for Cu, 3.52 Å for Ni and 3.92 Å for Pt). For Sn adsorption on Pt{111} a p(2×2) surface alloy structure, for coverages of 0.25ML with subsequent annealing was observed. This structure was not observed on the Cu and Ni substrates [Ku 1992] [Overbury 1992].

Tin and copper have a metallic radii ratio of 1.27, similar to the values calculated for the Sn/Pt (1.26) and Sn/Ni (1.30) systems. These systems are shown to exhibit surface alloy formation for <1ML coverages. Sn on the Cu{111} system also shows the formation of a surface alloy.

4.2.3 Tin/Copper bulk phase

The Sn/Cu system is an excellent example of a complex bimetallic combination. Copper forms a face centred cubic structure of lattice constant 3.61Å. Tin exists in two structures in the solid state. White or β-tin has a body-centred tetragonal crystal structure, with interatomic distances along the a axis of 5.832Å and c axis of 3.182Å, and is stable at room temperature. Gray or α-tin which has a diamond cubic crystal structure and a nearest neighbour distance of 2.81Å is thermodynamically stable below 286K. For room temperature growth a large lattice mismatch of 26% exists in the 12-fold metallic radii. Interestingly at 300K, under high pressure (39kbar), a second tetragonal phase can form with a=3.18Å and c=3.48Å. Hence, a compression along the a-axis and expansion along the c-direction would result in a good lattice match of this phase with Cu{100}.

The Cu/Sn bimetallic system has a highly complex bulk phase diagram, Figure 4.1, with alloys forming throughout the composition range including a range of intermetallic compounds [Hansen 1958]. While Sn diffusion into copper is kinetically limited at 300K in bulk alloys, diffusion of Cu into Sn occurs via an interstitial mechanism with a

small activation barrier of approximately 0.2-0.3eV, hence interdiffusion may be significant even at 300K [Dyson 1967] [Abel 1990].

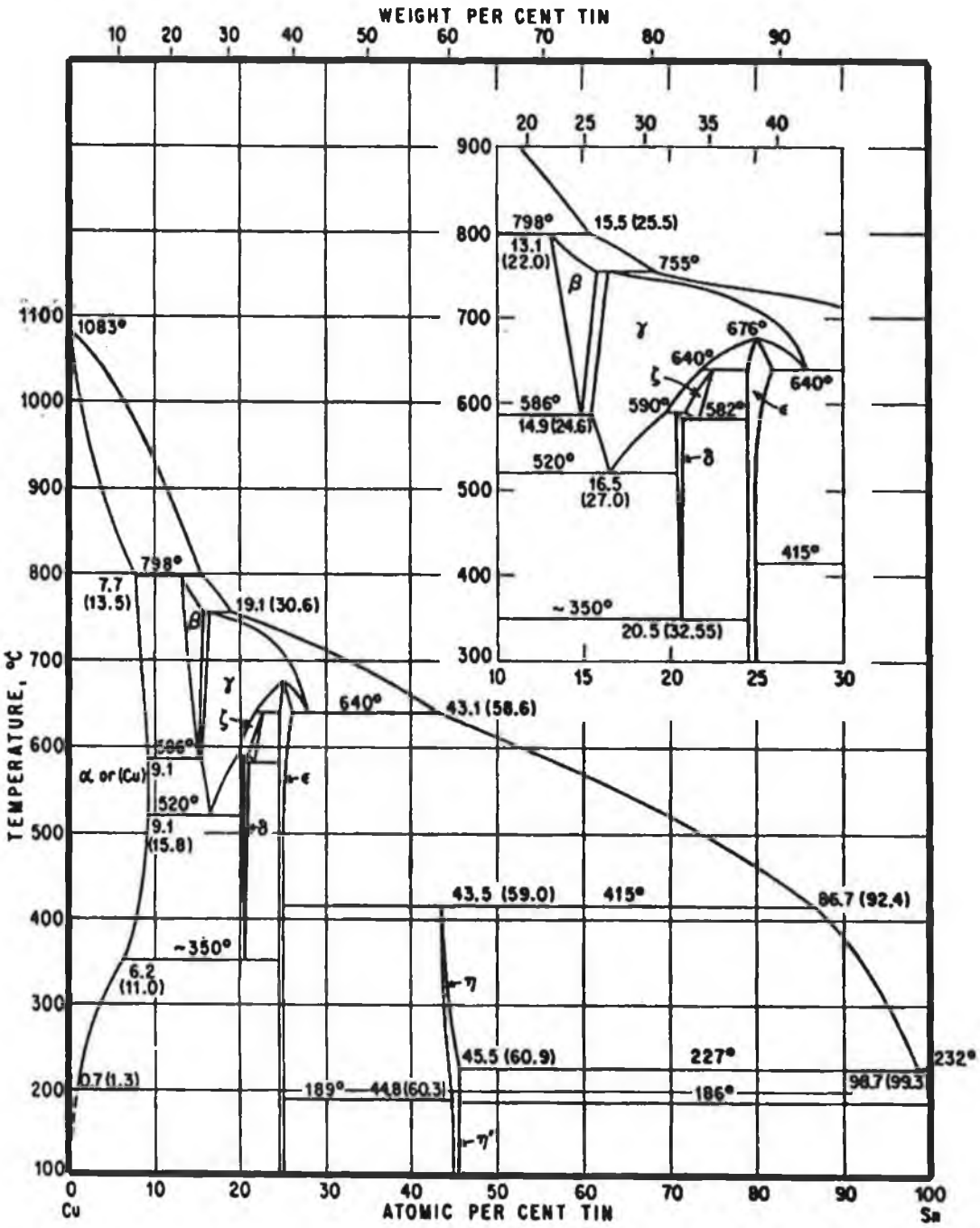

Figure 4.1 *Bulk Phase Diagram of Sn-Cu Alloy [Hansen 1958].*

4.2.4 Review of Sn/Cu{100}

The adsorption of Sn/Cu{100} was first studied by Argile and Rhead [Argile 1982, 1983] using Auger Electron Spectroscopy (AES) in combination with LEED. Four ordered phases were discovered in the submonolayer regime, namely, Phase I: a "complex" pattern with unidentified unit cell; Phase II: a rotated domain p(2×6); Phase III: a rotated domain p(3√2×√2)R45° and Phase IV: a p(2√2×2√2)R45° monolayer at a tin coverage of 0.625ML with respect to the Cu{100}-(1×1) density of 1.538×10^{15} atoms cm^{-2}. The observed LEED patterns along with the proposed overlayer structures for each phase are shown in Figure 4.2. Further tin deposition results in the Auger signal versus time (AS-t) plot of the Cu substrate saturating indicating alloy formation for higher coverages and a Stranski Krastanov growth mode. Phases II-IV have been explained in terms of overlayer structures consistent with the determined surface coverages and the symmetry/periodicity of the LEED patterns. For phases II and III it has been observed that the LEED beams in the c(2×2) positions (i.e. the (½,½) spots) are significantly brighter over a wide energy range than the other superlattice reflexes. This is suggestive of either multiple phase formation or alternatively that phases II and III originate from a c(2×2) superstructure with additional weaker reflexes arising from a longer range modulation in the c(2×2) due for example, to strain in the adlayer-substrate combination. This is not consistent with the structural models presented by Argile and Rhead.

One obvious suggestion for the origin of a c(2×2) structure would be a surface alloy formed by substitution of 0.5ML of Sn into the outermost copper layer. This structure has been identified for a number of transition metal adsorbates on Cu{100} including Pd, Au, Mn, Pt as shown in Section 4.2.1. Systems involving the adsorption of metals on copper, with the ratio of metallic radii in the range 1.25 to 1.37, show the formation of a surface alloy for initial adsorbate coverages up to about 0.37ML. The adsorbate atoms then dealloy to form overlayer structures at increased coverages. The atomic radii ratio for Sn/Cu of 1.27 is within the range of this group of elements. For tin deposition on the {100} surface of Pt and Ni, reported in Section 4.2.2, a c(2×2) surface alloy formation is reported for up to 1ML coverage. The Sn/Pt and Sn/Ni phase diagrams shows these systems to be miscible in the bulk phase.

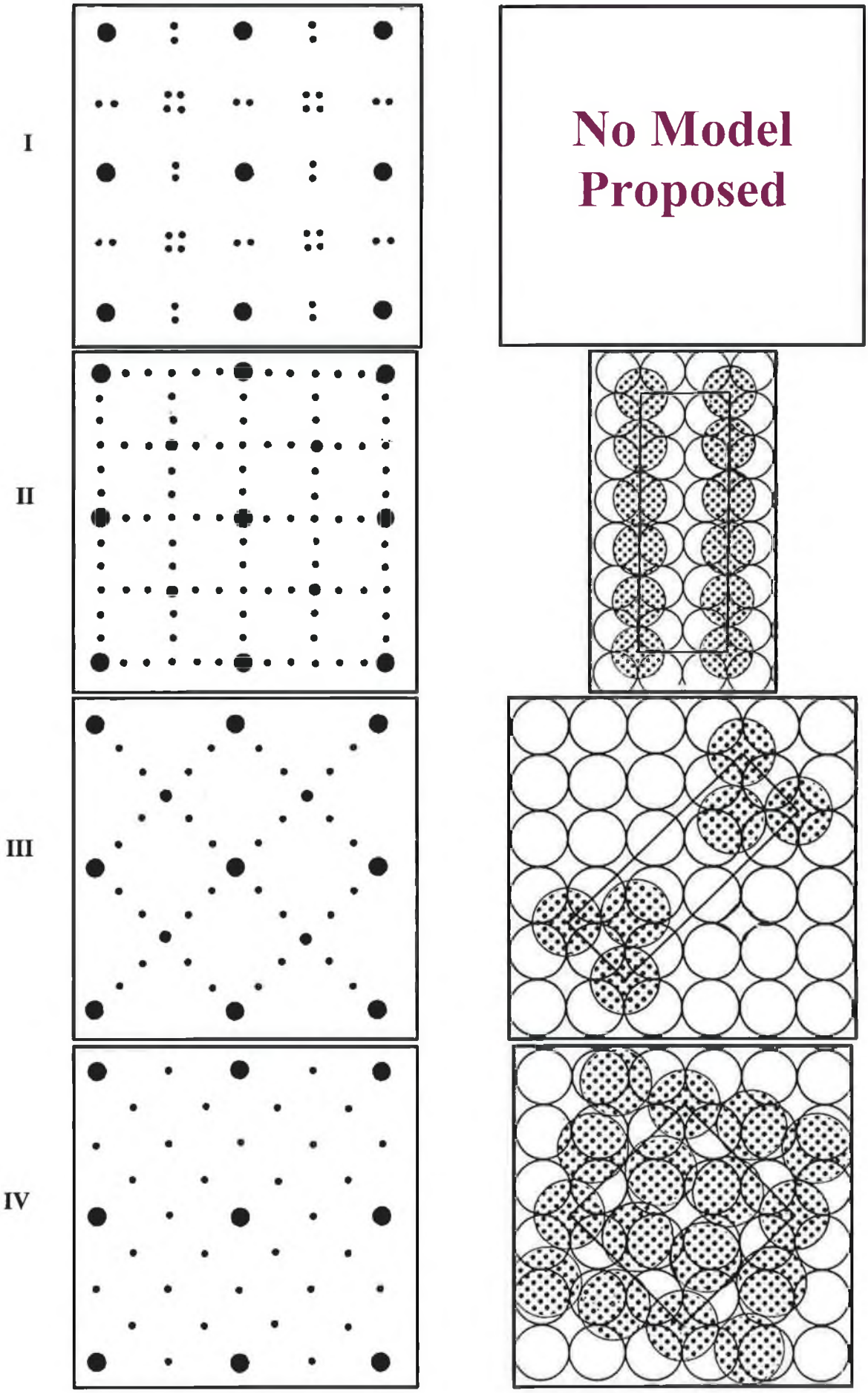

Figure 4.2 *LEED patterns and models for phases I-IV [Argile 1982].*

Evidence for surface alloy formation in the Sn/Cu{100} system has been provided by Abel *et al.* [Abel 1990] using Rutherford Backscattering Spectroscopy (RBS) but no specific models were proposed. These authors report a p(1×1) LEED pattern for Sn adsorption at 170K upon deposition of 5×10^{14} Sn atoms cm^{-2} (0.32ML), while a p(2×2) LEED pattern appears upon warming to 250K. In the case of deposition of 9×10^{14} atoms cm^{-2} (approximately 0.6ML), annealing to above 330K produces a p(2√2×√2)R45° two-domain structure while further annealing to around 400K leads to the formation of the p(3√2×√2)R45° rotated domain structure (phase III). Most interestingly, submonolayer Sn deposition was found to lead to an increase in the Cu RBS surface peak. If overlayer tin atoms covered the copper atoms, the backscattered peak would be attenuated. Abels results [Abel 1990] are explained as each Sn atom displacing one Cu atom from their four-fold hollow lattice site. An AES growth study from 0-7ML at 200K indicates a linear increase of the Sn signal (and a linear decrease of the Cu signal) up to 1ML, above which, the signal plateaus. This is attributed to the formation of a flat monolayer of pure Sn on top of the Cu substrate, without islanding, implying the existence of surface tin mobility even at 200K. A deposition plus annealing experiment between 170-525K demonstrated an increase of Cu surface concentration with anneal temperature showing evidence of two-dimensional commensurable phase formation whose structure depends strongly on anneal temperatures and Sn coverage [Abel 1990].

Segregation studies of tin on {111} and {100} surfaces of copper monitored by AES were also carried out. These studies revealed that at maximum segregation levels of tin, the surface is highly ordered. These ordered structures could be observed by LEED. Copper crystals doped with 0-0.5% tin revealed maximum segregation at 0.33ML with a (√3×√3)R30° structure on Cu{111} and at 0.25ML coverage with a p(2×2) on Cu{100} for temperatures of 800 to 1230K [Erlewein 1977] [Du Pleiss 1996]. Recent Modified Embedded Atom Potential (MEAM) calculations show that Sn deposition on the {111} and {100} surfaces of Cu results in the incorporation of Sn into the top copper layer [Aguilar 2000]. These ordered Cu-Sn alloy structures observed on the {111} and {100} surfaces are obtained either via deposition of Sn on Cu or migration of Sn to the surface from a bulk alloy [Overbury 1992] [Abel 1990].

There is sufficient evidence to suggest that the Sn/Cu{100} is not an overlayer structure at <1ML coverages as suggested by Argile and Rhead [Argile 1982]. Therefore this

system was re-investigated by testing the four sub-monolayer phases with models based on both overlayer and surface alloy structures.

4.3 Clean Cu{100} Preparation

The following section discusses the preparation of a clean Cu{100} surface and the evaluation of this surface by comparison with published results. An overview of possible sites for tin adsorption on Cu{100} is also presented.

A copper sample of dimensions 14 × 10 × 1.5mm was oriented in the {100} direction to an accuracy of better than 0.5°. The crystal was supplied from Metals Crystals and Oxides Limited, Cambridge, UK. Four 0.25mm diameter holes were spark eroded into the corners of the sample to aid sample mounting and to allow sample heating. A fifth 0.25mm hole was drilled for positioning of a chromel-alumel thermocouple for temperature measurement. The crystal was mounted on a high precision manipulator with polar and azimuthal rotations by suspending it between two stainless steel blocks with 0.25mm diameter tantalum wire secured through the four corner mounting holes. Sample heating was achieved by passing a direct current through the tantalum support wires allowing temperatures of up to 1000K to be attained. The sample was cleaned by repeated cycles of argon ion bombardment at 3kV and annealing to 800K. It was deemed clean when no contaminants (e.g. oxygen at 509eV and carbon at 262eV) could be observed above the AES noise level and a sharp p(1×1) LEED pattern with low background intensity was observed.

The quality of the sample was checked by comparing the measured LEED I-V spectra with accepted spectra in literature, for example from Noonan [Noonan 1980] or Jona et al. [Jona 1987a,b]. The study by Jona *et al.* incorporated five separate LEED experiments on Cu{100} to test methodologies and reproducibility. They concluded that although equivalent I-V curves may look very similar to one another, a quantitative analysis revealed that the energy scale might be shifted by as much as 10eV from experiment to experiment. The peak positions may fluctuate by ± 2.5eV and the peak intensities may vary by as much as 70%.

Figure 4.3 shows the structure of the copper bulk crystal. The p(1×1) unit cell is shown with copper to copper interatomic spacings along the [011] and [01$\bar{1}$] directions of

2.55Å. The interplanar distance for copper {100} planes is 1.81Å, half of the lattice constant 3.61Å of the FCC crystal.

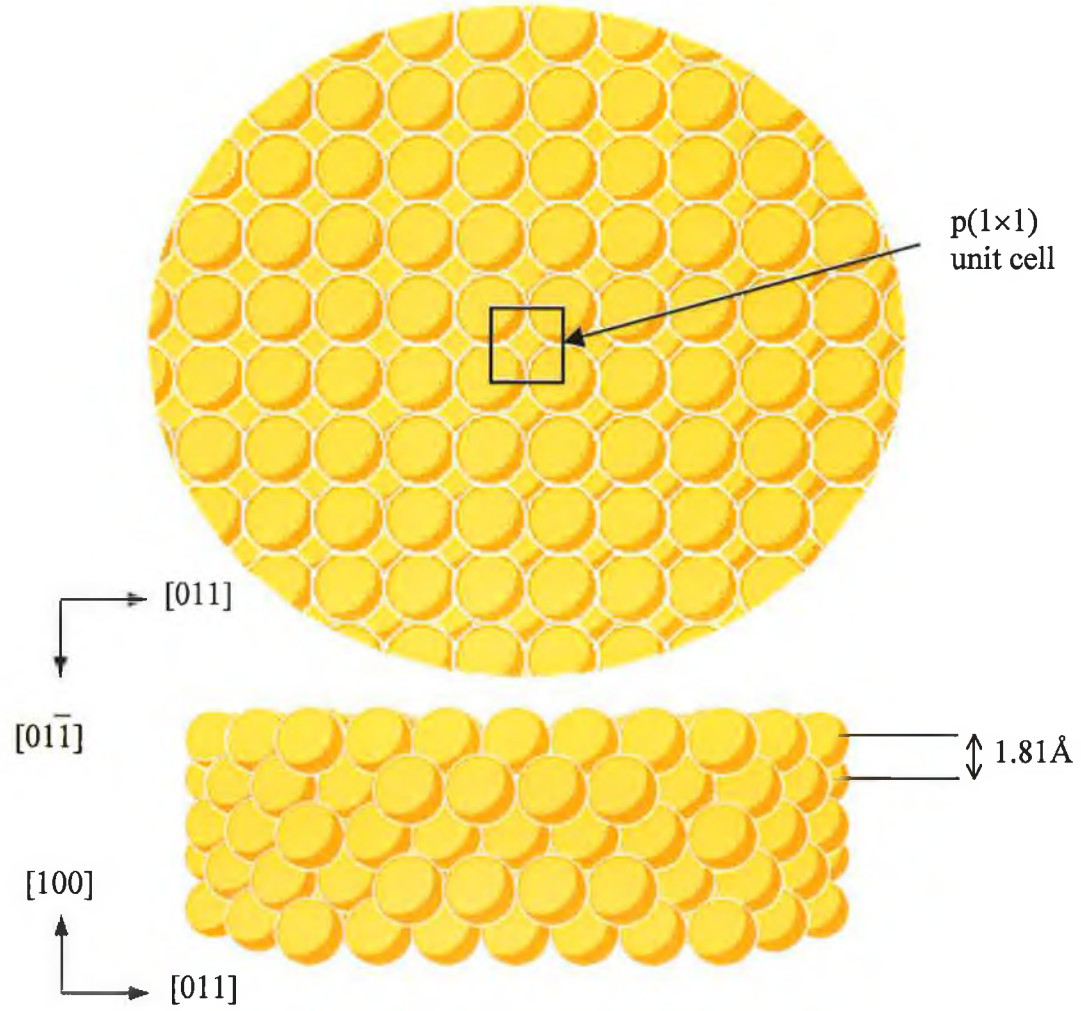

Figure 4.3 *Clean copper bulk crystal structure.*

The specular and integral order I-V spectra for the clean copper {100} crystal are shown in Figure 4.4. Note that the specular beam is measured at 10° off-normal incidence while the integral beams are measured at normal incidence. The energy scale of the I-V spectra is uncorrected for the effect of the inner potential. The (1,0) integral beam represents the average of the symmetrically equivalent (1,0), (0,1), ($\bar{1}$,0) and the (0,$\bar{1}$) beams and normalised intensities. Similarly the (1,1), (2,0) and (2,1) spectra shown in Figure 4.4, represent the average of the symmetrically equivalent integral beams. Davis and Noonan [Davis 1982] have shown that such averaging will not only reduce random errors associated with the data-collection process, but in addition may substantially reduce systematic errors which result from any incident beam misalignment.

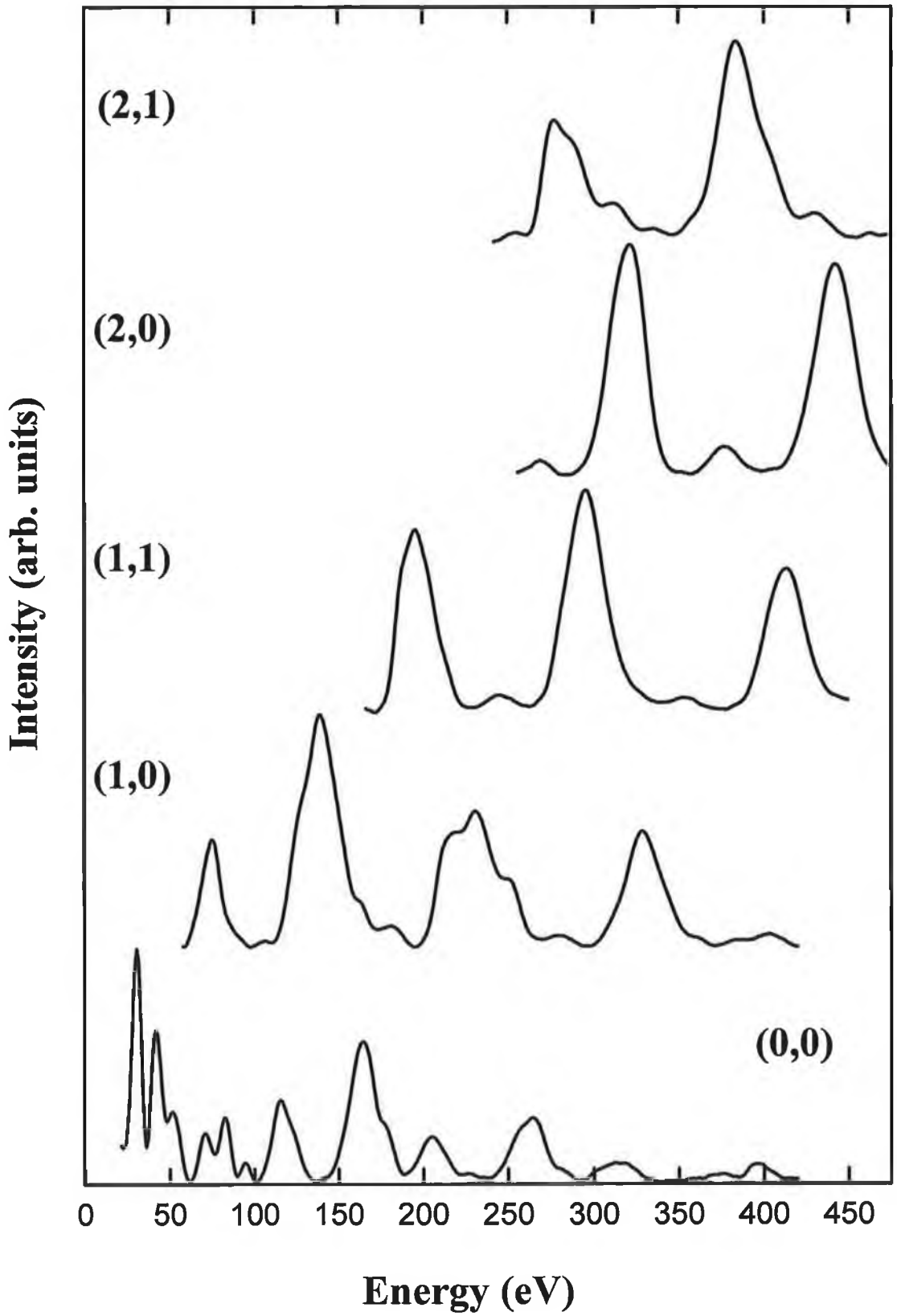

Figure 4.4 *Measured specular and integral order beam I-V profiles for clean Cu{100}.*

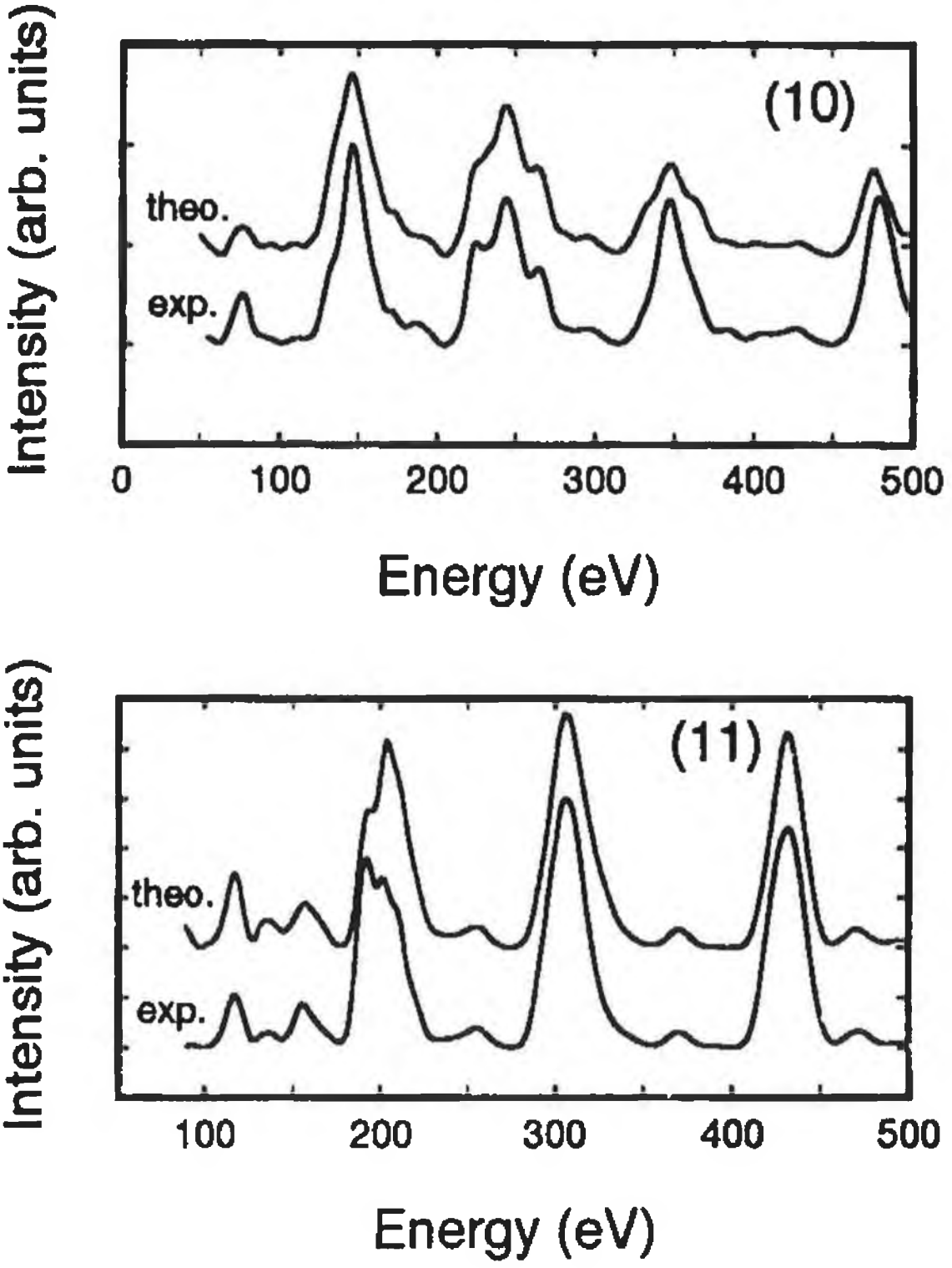

Figure 4.5 *Comparison of experimental and calculated best-fit spectra for clean Cu{100} integral beams [Muller 1995].*

The (1,0) and the (1,1) beams can be compared qualitatively, with the corresponding experimental and theoretical data in Figure 4.5 from Muller *et al.* [Muller 1995]. The theoretical data presented in Figure 4.5 represent full dynamical LEED calculations that determined the in-plane lattice contraction of clean copper to be 1% of the layer spacing. The relative peak positions and intensities for the (1,0) beams may be compared between 50-400eV and the (1,1) beams may be compared between 150-450eV.

No quantitative reliability can be placed on the comparison between the different spectra without carrying out full dynamical LEED calculations. The five measured integral beams shown in Figure 4.4 for the clean copper {100} crystals, have a total energy range of around 1500 eV. The I-V spectra for the (1,0) (1,1), (2,0) and (2,1) beams were also measured 10° off-normal but are not presented here. This total of nine beams measured at normal and off-normal incidence in 1eV steps, across a wide energy range, is sufficient for dynamical LEED structural analysis, as demonstrated by Jona [Jona 1982].

In Figure 4.6, the intensity experimentally measured as a function of energy of the specularly reflected (0,0) beam, is shown for the clean copper {100} surface measured at 10° off-normal incidence. The spectrum shows a great deal of structure in the curve, hence potentially much structural information may be obtained. In discussing the curve, it is convenient to divide energies into two ranges. Below 70eV the peaks are intense and have narrow peak widths of about 5-10 eV. The structure in the curves at these energies is very surface sensitive. Structure at higher energies above 70eV, appear as widely spaced peaks of irregular shape with broader peak widths, 20-30eV, and weaker intensities.

If the Bragg reflection theory is applied to LEED, the peaks in the (0,0) beams are caused by reflection from planes of atoms parallel to the surface. The condition for a Bragg peak is satisfied when reflections from successive planes are in phase.

$$\frac{2\pi}{\lambda} = n \times d \qquad (4.1)$$

where d is the spacing between these planes and n is an integer. λ is the wavelength of the electrons given by $\lambda = \left(\frac{150}{V}\right)^{1/2}$ in angstroms. Due to the inner potential well U_0, the wavelength inside the crystal is given by:

$$\lambda = 2\pi(2E - U_0)^{-1/2} \tag{4.2}$$

where E is the electron energy in eV. Substituting (4.1) into (4.2) yields:

$$E = \tfrac{1}{2}d^2(n)^2 + U_0 \tag{4.3}$$

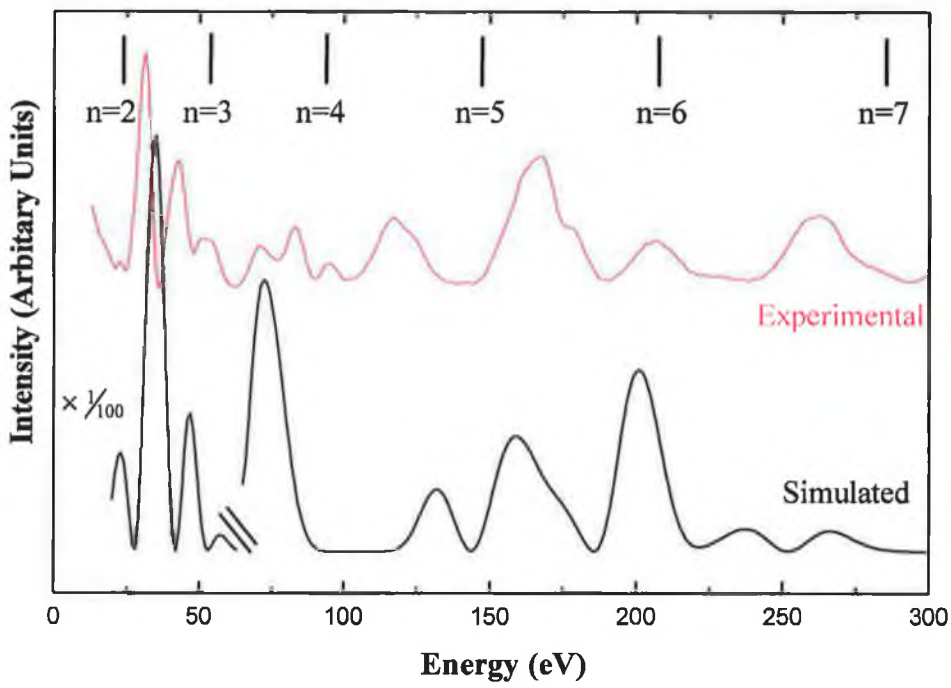

Figure 4.6 *Intensity of the (0,0) beam from Cu{100}, measured as a function of energy, recorded at θ=10° off normal incidence and theoretically generated at normal incidence using double scattering simulations with all copper atoms in ideal lattice sites.*

The bars on Figure 4.6 mark energies at which equation (4.3) is satisfied for U_0 = 0eV and calculated using d = 1.81Å. In the high energy range there is reasonable correlation with Bragg theory, as the electrons penetrate further into the crystal, but in the lower energy range there are more experimental peaks than Bragg theory predicts. Providing that peaks can be assigned to particular Bragg reflections, then plotting a graph of peak energies versus $(n)^2$ yields a straight line graph from which values for d and U_0 can be calculated. For Cu{100} the interplanar distance d is determined to be 1.81±0.01 Å and

the inner potential, U_0 is calculated to be –13.5eV [Pendry 1974] [Van Hove 1986]. Using this simple theory allows structural information to be extracted from the LEED intensities that is not available from the diffraction pattern.

The simulated curve presented in Figure 4.6, was generated using a double scattering LEED simulation of the clean copper crystal with all the copper atoms in their ideal lattice sites. This spectrum was simulated at normal incidence. The peak intensities in the energy range less that 70 eV, are scaled down by a factor of 100, for illustration purposes. There is no relaxation/contraction of the interlayer spacings included. Simulations were carried out to demonstrate the effect of relaxation in the top interlayer spacing. Figure 4.7 illustrates the generated I-V spectra for a first interlayer spacing, Δ_{12}, of 1.9 Å, 1.8 Å and 1.7 Å. A shift is observed in the peak positions of ±7eV, depending on the relaxation of the top layer Cu atoms. The peaks calculated at 1.7 Å are also broader than those calculated at 1.9 Å.

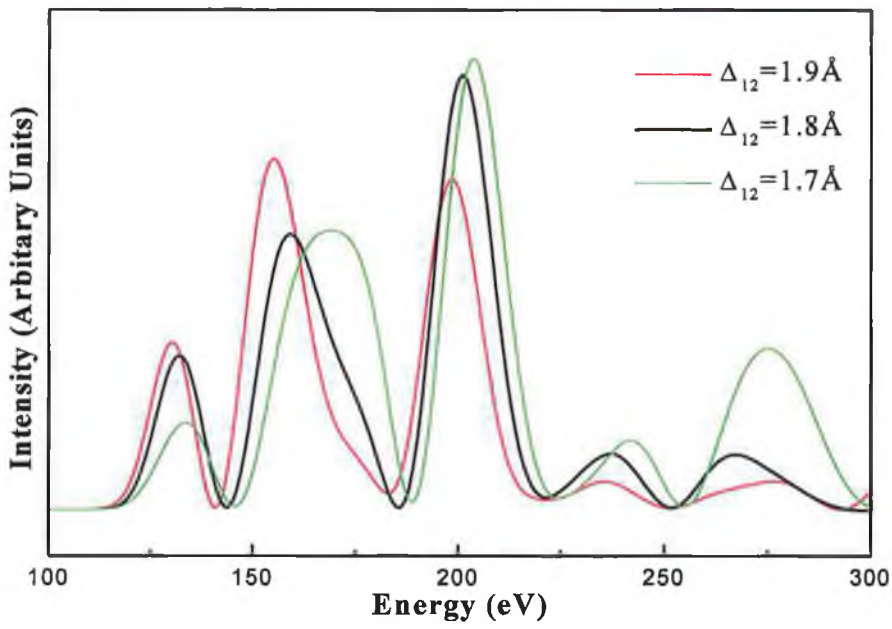

Figure 4.7 *The effect on Bragg peak positions by changing the top copper layer position by ±1Å from the bulk lattice spacing of 1.81 Å.*

This change in peak position and broadening of the peaks, explain why the double scattering simulation curve in Figure 4.6 does not exhibit exact agreement with the experimental curve. These results demonstrate the need for full dynamical LEED analysis to obtain reliable structural information.

Dynamical LEED results published for clean copper have shown that relaxation and contraction of the first two interlayer spacings Δ_{12} and Δ_{23} occurs. There is some discrepancies between the actual values quoted but they generally show an inward relaxation of the top layer copper atoms combined with an outward expansion of the second layer atoms. Experimental determinations for the relaxation on Cu{100} are shown in Table 4.2 for the first and second interlayer spacings Δ_{12} and Δ_{23}, expressed as % deviations from the bulk value of 1.81Å for copper{100} calculated at 300K.

Δd_{12} (%)	Δd_{23} (%)	Technique	Reference
-1.1	1.7	LEED	Davis 1982
-1.2	0.9	LEED	Lind 1987
-1.5	0.82	LEED *	Jona 1987a,b
-2.4	1.0	MEIS	Jiang 1991
-2.0	1.0	MEIS	Fowler 1995
-2.4	-0.1	LEED	Muller 1995
-1.0	0.0	LEED	Mikkelsen 1999

Table 4. 2 *Relaxation of the first two interlayer spacings Δd_{12} and Δd_{23} expressed as % deviations from the bulk value of 1.81Å calculated at 300K.*
**Average of five different LEED experiments of clean Cu{100}.*

As mentioned earlier, Jona (* above) [Jona 1987a,b] reported an international LEED intensity project in 1987 on Cu{100}, discussing the reproducibility of experimental spectra and the evaluation of structural parameters for five different LEED experiments. He concluded that the discrepancies in Δ_{12} and Δ_{23} values arise from the methodology of sample preparation and data collection, experimental errors and genuine differences between the copper surfaces. The choice of reliability factor affects the Δ_{12} and Δ_{23} values by a value on the order of about 1%. Substantial inter-laboratory variations were attributed to the effect that contaminants have on the ratios of adjacent peaks in a LEED spectrum. However, contaminants had little effect on the peak positions. The variation in peak positions was accounted for as mis-orientations of the different surfaces used in the different laboratories.

Figure 4.8 demonstrates possible sites for tin adsorption on clean Cu{100}using the 12-fold metallic radii values 1.623Å for Sn and 1.278Å for Cu [Alcock 1990]. The surface alloy site (a) occurs where the tin substitutes with the copper atoms in the top layer lattice site positions. Site (b) is tin in the four-fold hollow overlayer site at a height dz of 2.27Å, above the first layer copper atoms. Site (c) shows tin occupying a copper bridge site at a height dz of 2.6Å above the first layer copper atoms. Site (d) is a tin atom atop a copper atom at a spacing of 2.9 Å above the first layer copper atoms.

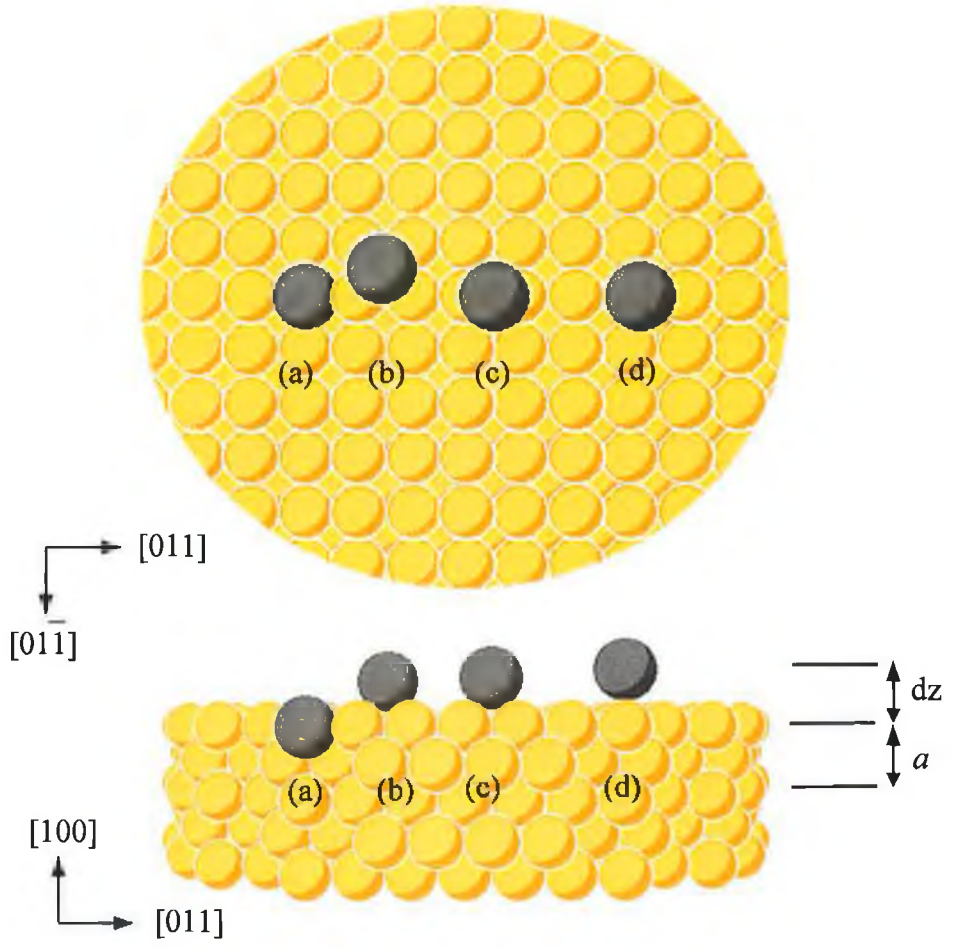

Figure 4.8 *Growth Sites for adsorbates on Cu{100}: (a) surface alloy; (b) four-fold hollow site; (c) bridge site and (d) atop site, where dz =0Å, 2.27Å, 2.6Å and 2.9Å, respectively, with the copper interplanar spacing* $\frac{1}{2}a_0$ *=1.81Å.*

4.4 Tin Evaporation Calibration

The evaporation of tin onto the Cu{100} surface was monitored by Auger signal versus time (AS-t) plots and compared to the AS-t plot obtained by Argile and Rhead [Argile 1982]. Both sets were measured by monitoring the Cu ($M_{2,3}VV$) auger peak at 63 eV and the Sn ($M_5N_{4,5}N_{4,5}$) auger peak at 430eV. For growth up to 1ML straight line plots are obtained for both the tin and copper signals, indicating constant sticking probability of tin on copper. This behaviour indicates a layer by layer (FM) growth mode as shown in Figure 4.9. The two sets of experimental data exhibit good agreement up to 1ML coverage.

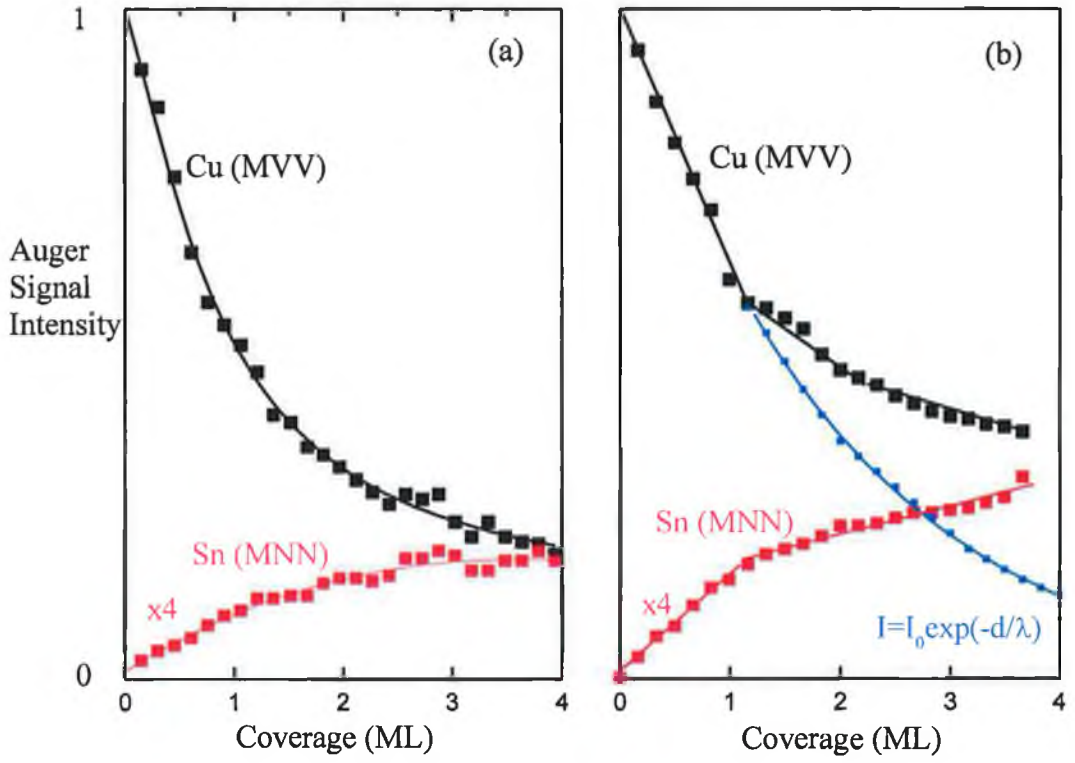

Figure 4.9 *Auger Signal (AS) versus coverage in monolayers for tin deposition on Cu{100} at 300K where (a) is taken from Argile 1982 and (b) this experiment. Both sets were measured by monitoring the Cu ($M_{2,3}VV$) auger peak at 63 eV and the Sn ($M_5N_{4,5}N_{4,5}$) auger peak at 430eV. The blue curve in (b) is the theoretical variation obtained by assuming a layer-by-layer growth mode.*

A break or "knee" appears at the completion on one monolayer before the start of the second layer. The blue curve in Figure 4.9 (b) indicates the theoretical behaviour of the copper Auger signal for true layer-by-layer growth, represented as:

$$I=I_0 \exp(-d/\lambda) \qquad (4.4)$$

from Seah and Dench [Seah 1979]. The copper Auger signal, shown by the black curve in Figure 4.9 (b) shows a significant deviation from layer-by-layer growth after a tin coverage of 1ML. The saturation of the substrate signal for long depositions is indicative of the formation of a CuSn alloy after the initial first unalloyed overlayer. CuSn alloy structures for 1-10ML coverages have been reported by Argile and Rhead [Argile 1983] [Rhead 1981a,b] [Argile 1989].

Argile & Rhead based their coverage assignments from the AS-t plot on the formation of phase II, the p(2×6) structure at 0.42ML. They deduced coverages for phases I-IV of 0.21ML, 0.42ML, 0.5ML and 0.625ML, respectively.

In order to accurately determine the tin coverage and the evolution of phases I-IV, the LEED spot profiles were monitored as a function of tin evaporation time. Figure 4.10 is a image taken with a CCD camera of the clean Cu{100} sample at 120eV. This picture is a negative image of the real LEED pattern. The (0,0) specular order beam and the symmetrically equivalent (1,0) and (1,1) integral order beams are illustrated.

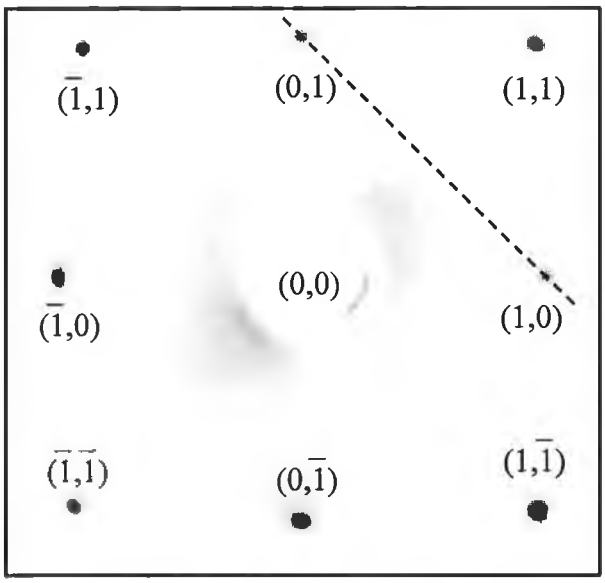

Figure 4.10 *A negative image of a LEED picture recorded at 120eV by a CCD camera for clean Cu{100} indicating the specular and integral order beams.*

Figures 4.11 and 4.12 are representative negative image LEED pictures recorded at 127±2eV for maximum perfection and intermediary stages of phases I-IV. The dashed line from the (0,1) beam to the (1,0) beam in Figure 4.10, 4.11 and 4.12 indicates the direction along which the LEED spot profiles were recorded.

Figures 4.13 and 4.14 show the LEED line profiles recorded for clean copper {100} and in one minute intervals during the evaporation of tin up to completion coverages for phase IV. The spectrum at 0 minutes represents the line profiles for the clean Cu{100}. No background subtraction or intensity normalising was carried out on these spectra. They were recorded in 1 minute intervals at an energy of 90eV ± 2eV and a constant line width of one pixel.

After 12 minutes evaporation, shown in Figure 4.13, two spots are best resolved from the split quartet of spots centred around the (½,½) position, indicating completion of phase I. Phase II reaches maximum perfection after 20 minutes. Between 13 to 16 minutes evaporation time phases I and II are observed to coexist. Representative LEED images for these three patterns are shown in Figure 4.11.

Phase II and III are shown in Figure 4.14 to coexist for evaporation times between 22 and 26 minutes. Phase III is best observed after 28 minutes evaporation of tin. Phase III and IV coexist between 29 and 39 minutes evaporation time, as illustrated by the dotted lines indicating the positions of the fractional order spots for phases III and IV. Completion of a full monolayer for phase IV was achieved after 40 minutes. Representative LEED images for these three patterns are shown in Figure 4.12.

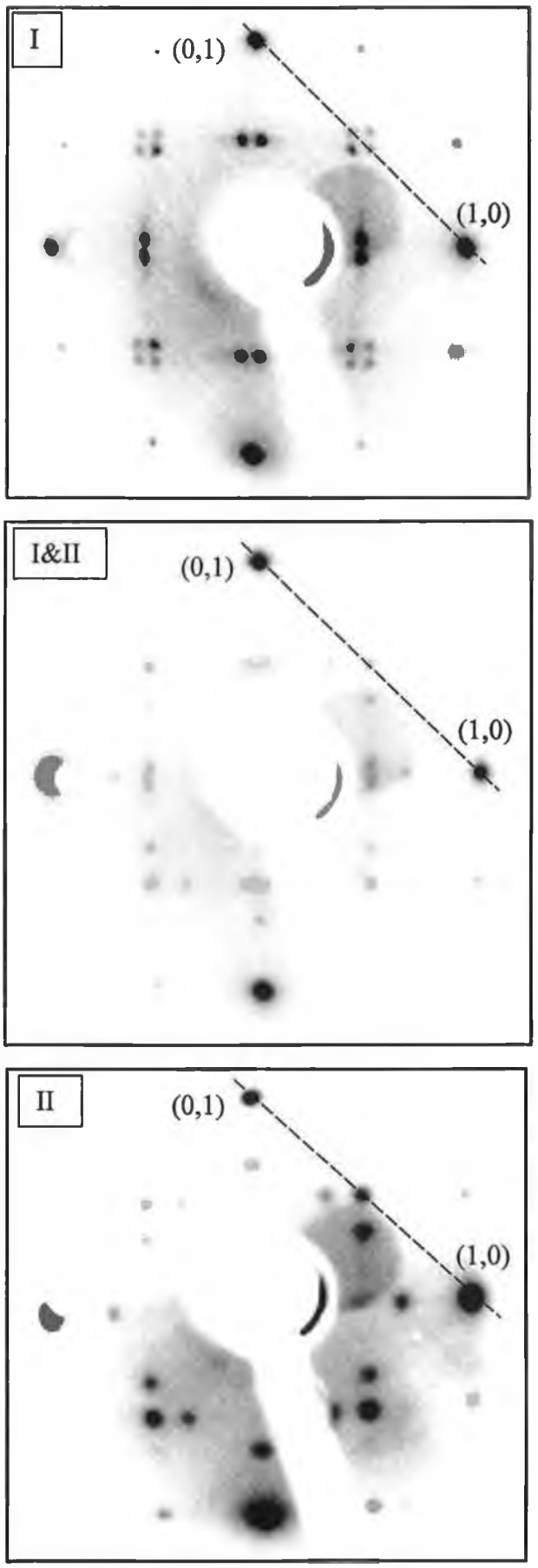

Figure 4.11 *CCD images of the LEED patterns at 127±2 eV for Phase I, mixed Phase I & Phase II and Phase II, respectively.*

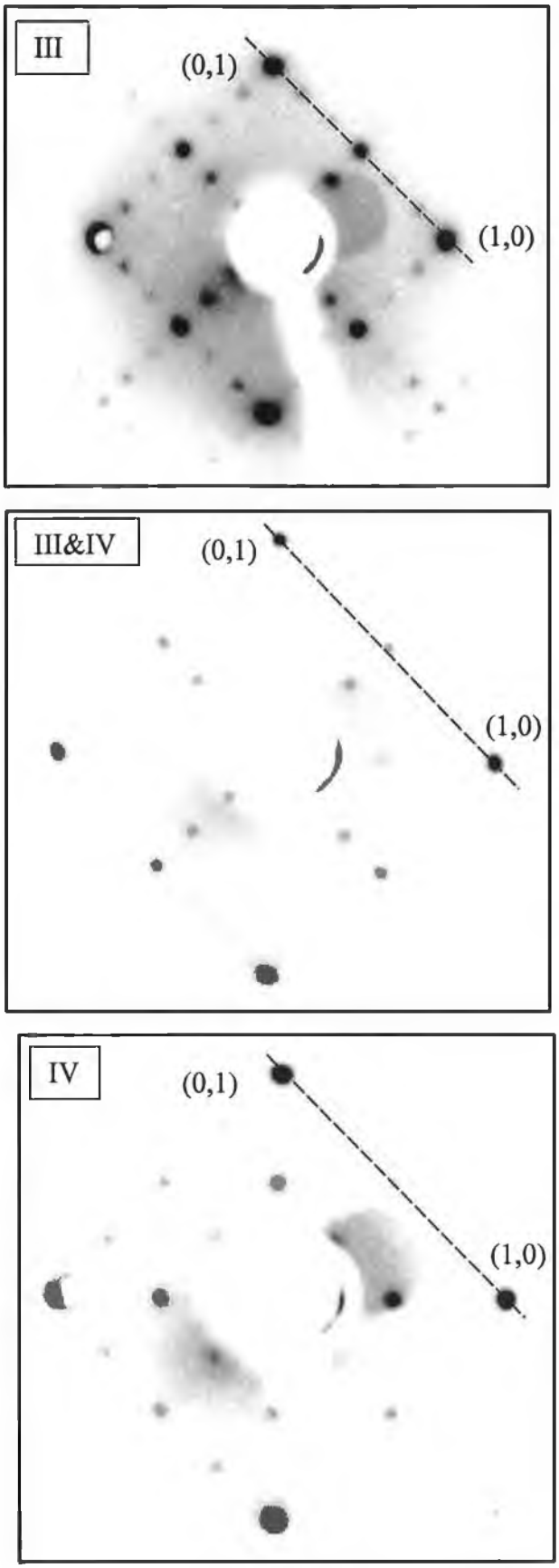

Figure 4.12 *CCD images of the LEED patterns at 127±2 eV for Phase III, mixed Phase III & Phase IV and Phase IV, respectively.*

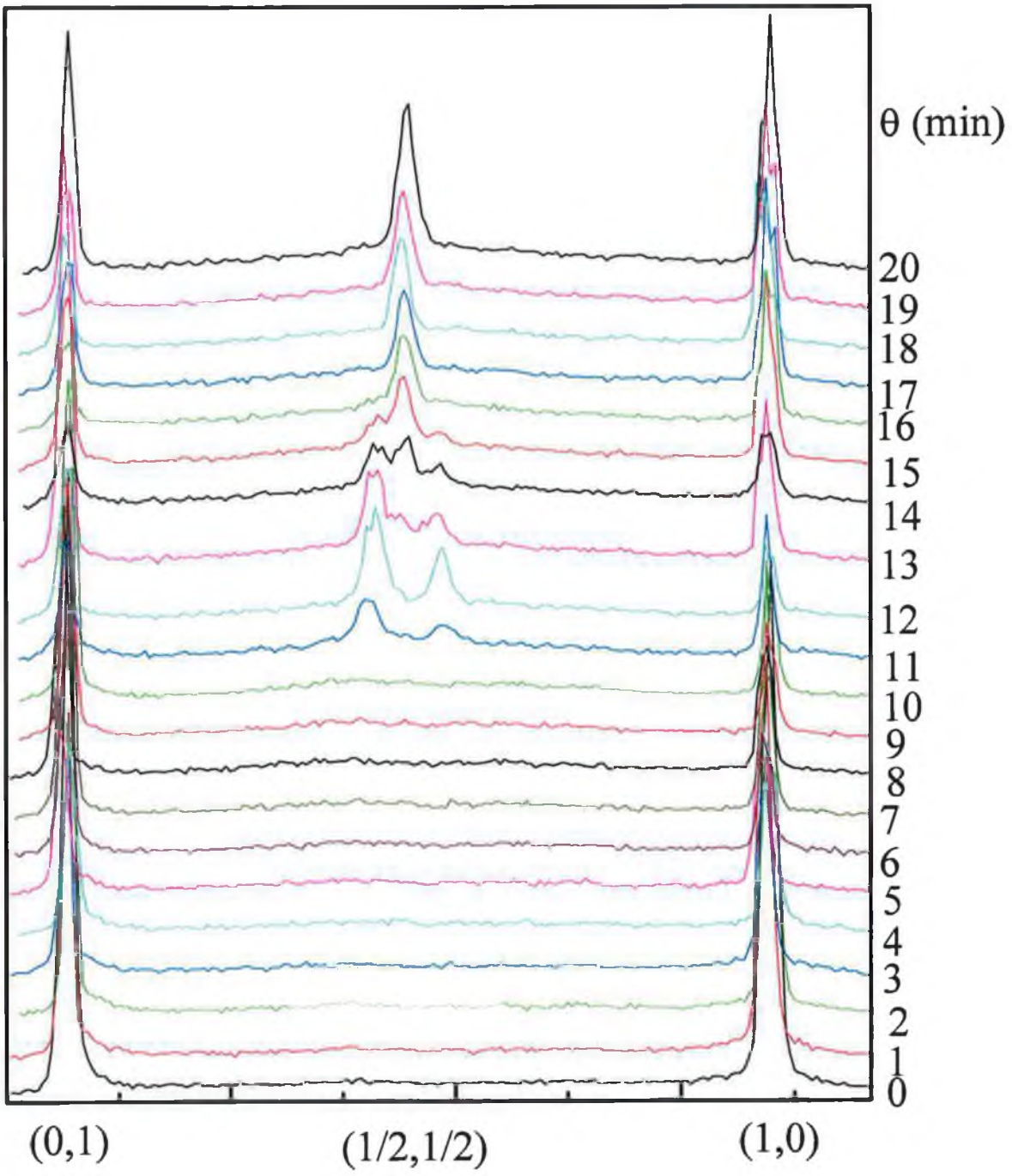

Figure 4.13 *The evolution of LEED line profiles along a line through the (0,1) to (1,0) integral beams taken at 90eV in 1 minute intervals during the evaporation of Sn on Cu{100} at 300K. The spectrum at 0 minutes represents the line profile for clean Cu{100}. After 12 minutes two spots are best resolved from the split quartets of spots centred around the (½,½) position, indicating completion of Phase I. Between 13 to 16 minutes the phases are seen to coexist. Phase II is reaches maximum perfection after 20 minutes deposition.*

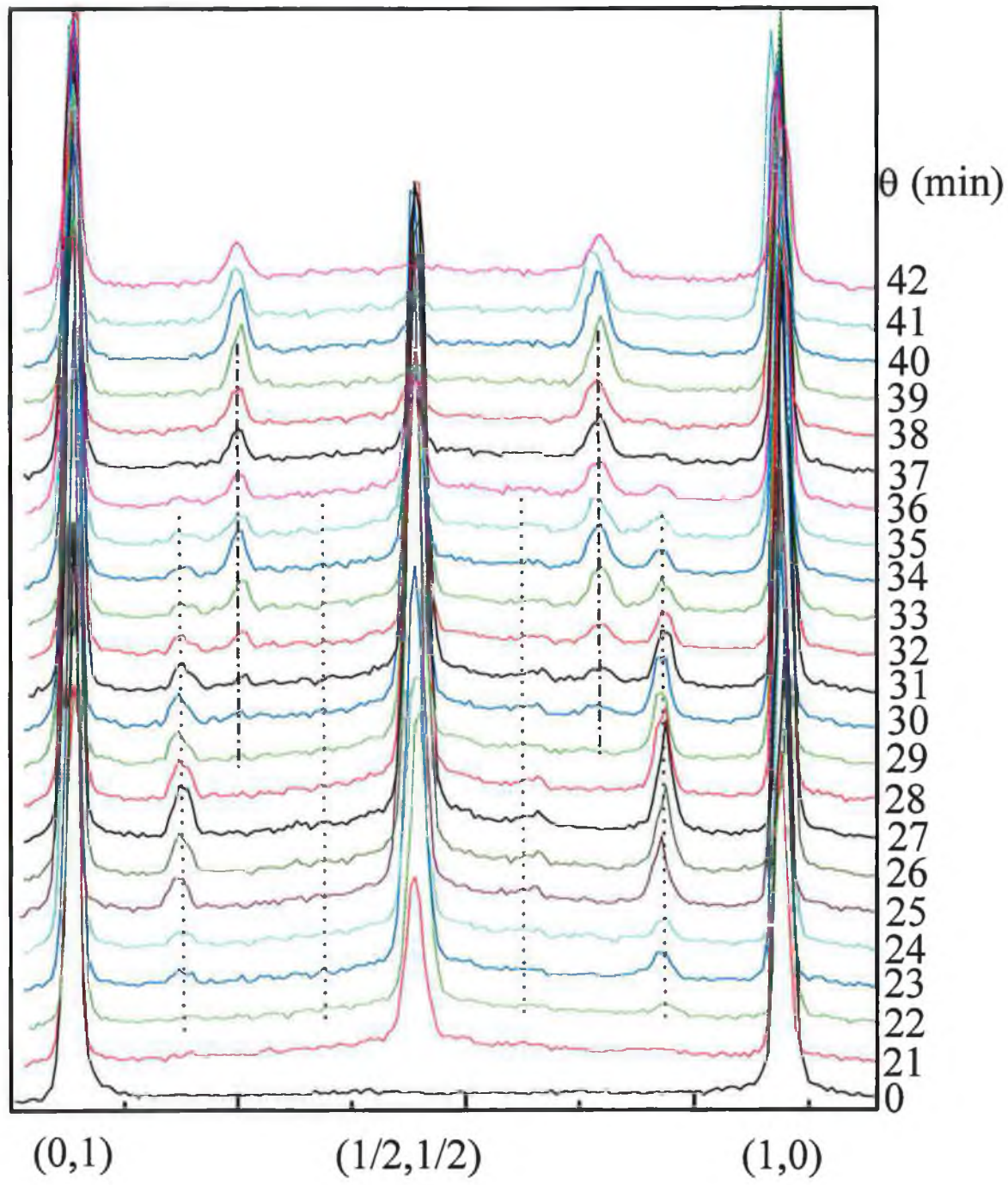

Figure 4.14 *The evolution of LEED spot profiles along the line from the (0,1) to (1,0) integral beams taken at 90eV in 1minute intervals for the evaporation of tin on Cu{100} at 300K. The spectrum at 0 minutes represents the line profile for clean Cu{100}. Phase II and III are shown to coexist up to 26 minutes, with maximum perfection of phase III after 28 minutes. Completion of a full monolayer for phase IV was achieved after 40 minutes. The dotted lines indicate the positions of fractional order spots for phases III and IV.*

A overview of the line profiles for the growth of Sn on Cu{100} is shown in Figure 4.15, with the profiles normalised to the intensity of the (0,1) spot. The (½,½) beam was observed to have maximum intensity in phase III. Coverage assignments were made on the assumption that (½,½) spots reach maximum intensity based on a c(2×2) structure at a coverage of 0.5ML. These coverage assignments are shown in Figure 4.15.

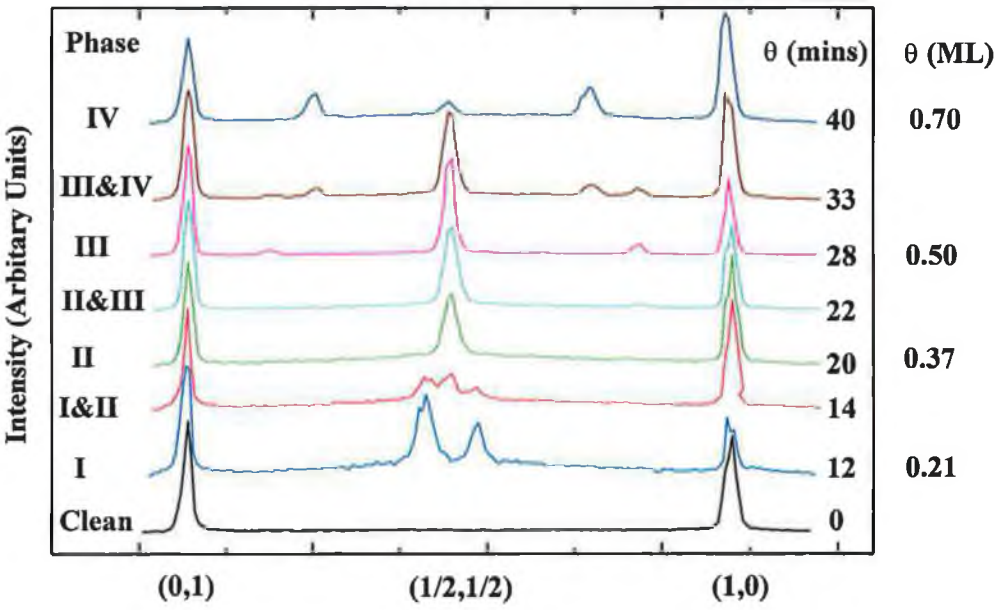

Figure 4.15 *A overview of line profiles for the growth of Sn on Cu{100} is shown with the profiles normalised to the intensity of the (0,1) spot. The (½,½) beam was observed to have maximum intensity in Phase III.*

On the basis of the AS-t plot, monitoring of the LEED patterns and measuring the LEED spot profiles the evaporation of tin from the Knudsen cell has a constant flux of 0.018 ML/min. This analysis indicated that phases I to IV reached maximum perfection at coverages of 0.21ML, 0.37ML, 0.50ML and 0.70ML respectively. These coverages compare with values of 0.42, 0.50 and 0.625 for phases II, III and IV determined by Argile and Rhead [Argile 1982] based on their own postulated structure for phase II as shown in Figure 4.2.

The spot profiles indicate that the transition between phases occurs by phase co-existence rather than sharp coverage dependent phase switching and consists of nucleation of domains of the higher coverage structure within the lower coverage phase.

4.5 Low Energy Electron Diffraction Results

In this section models of overlayer and surface alloy structures based on the coverage dependence of tin for completion of phases I-IV for Sn/Cu{100} are presented. The proposed overlayer models of Argile and Rhead are simulated for comparison. The models of surface alloy structures are based on a mixed tin and copper top layer. TPD results presented in Section 4.6, indicate that the Sn atoms do not form a subsurface alloy under a pure copper top layer as was reported for Ni and Ir in Section 4.2.1. Therefore this model was not simulated.

The models presented for Phases I-IV have been prepared using SARCH / LATUSE / PLOT3D (Surface ARCHitect/LATticeUSE / PLOT in 3D) Version 4.01, a freeware PC-based software package to create, visualise and analyse surface structures. This software was obtained through private communication with Michael Van Hove [Van Hove 1995].

To simulate the expected LEED pattern from all phases, the double scattering LEED simulation program of Panagiotides *et al.* discussed in Section 3.2.2 was utilised [Panagiotides 1991]. The program is limited to double scattering and uses only s-waves, producing the correct symmetry and periodicity but not quantitatively reliable absolute intensities. The patterns were simulated in the energy range 100-200eV in 5eV steps, with the resulting patterns being co-added and averaged to provide an overview of the LEED pattern over a reasonable energy range.

The geometric structure for all models is based on the clean surface structure of Cu{100} with tin atom positions determined by distances calculated geometrically based on the 12-fold coordinate radius of tin as shown in Figure 4.8.

4.5.1 Phase I

To date, no structure has yet been suggested for this phase, which produced the complex LEED pattern shown in Figure 4.16.

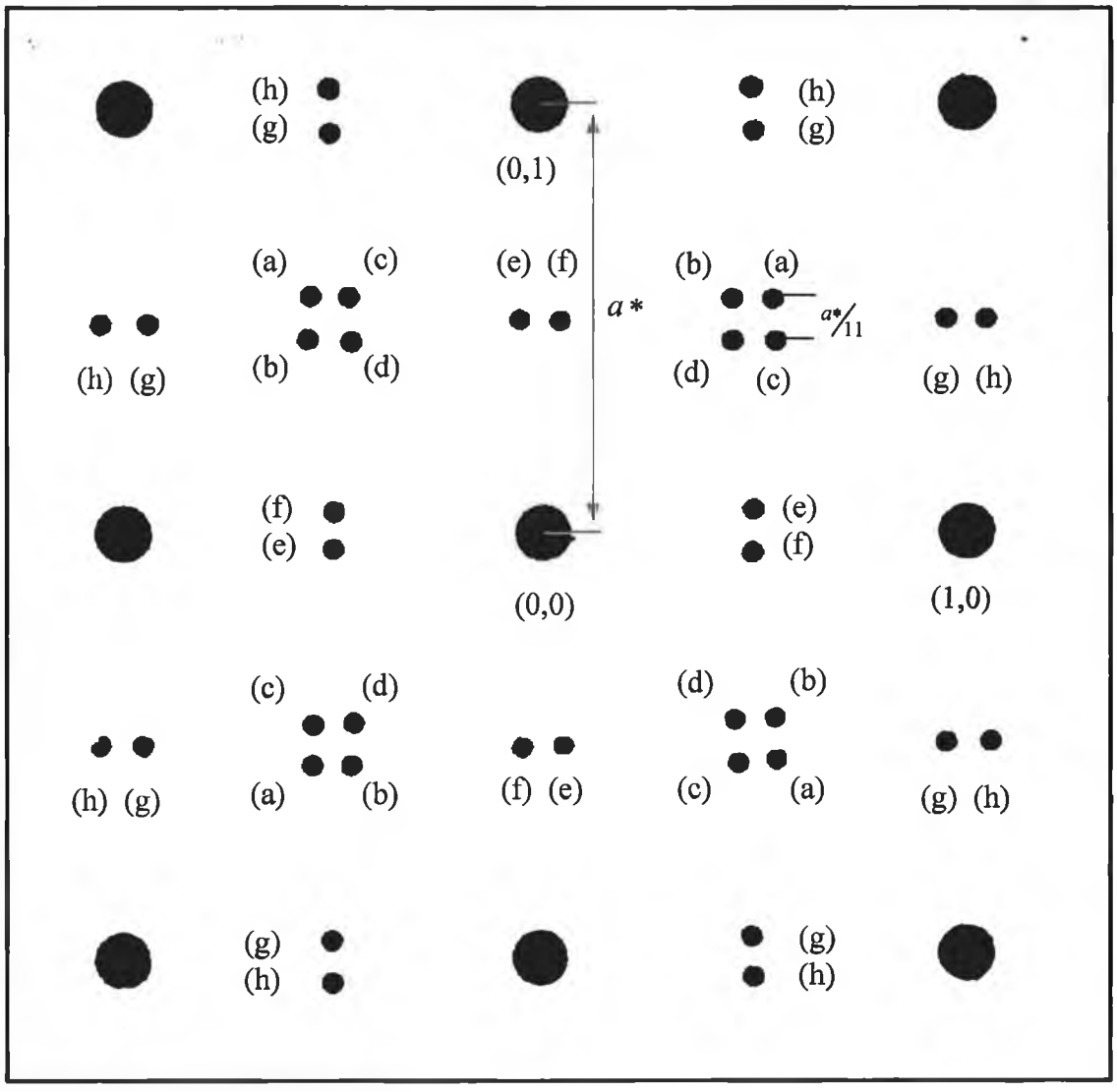

Figure 4.16 *Phase I LEED pattern, with labels (a) to (h) indicating the symmetrically equivalent fractional order beams. (a) –(d) represent the (½,½) spot splitting, (e) & (f) represent the (½,0) spot splitting and (g) & (h) represent the (½,1) spot splitting.*

However, Argile suggested that the spot splitting may be as a result of antiphase domain walls [Argile 1982]. This type of disorder is due to the existence of several subdomains of the same structure within an area smaller than the coherence zone of the electron beam. When the antiphase boundaries are parallel and regularly spaced, a splitting of beams will take place in a direction determined by the orientation of the boundaries; when the subdomains have irregular shape the LEED spots will be streaky or enlarged

[Estrup1971] [Van Hove 1986]. Spot splitting based on c(2×2) antiphase domain structures have been proposed to explain structures in Bi/Cu{100} and Pb/Cu{100} LEED patterns [Meyerheim 1998] [Bocquet 1998].

Measurements of the splittings of the (½,½) beams relative to the reciprocal lattice vector (a*) of the substrate in the [011] and [01 $\bar{1}$] directions were made from the LEED pictures and LEED line profiles for phase I, shown in Figures 4.11 and 4.13. These measurements indicate that the domain wall structure adopts a periodicity of $\frac{1}{11}th$ (0.09±0.01) of the reciprocal space lattice. The value of this splitting is constant for all beam energy ranges and does not vary with coverage up to completion of Phase I.

As the tin coverage is 0.21ML when phase I reaches maximum intensity and that the centre of gravity of the split beams is centred on positions of a p(2×2) superstructure, which would reach maximum perfection at a coverage of 0.25ML, phase I may be explained in terms of a p(2×2) periodicity with antiphase domain walls.

An initial attempt to model the spot splitting occurring in two directions in the (½, ½) beams the model for phase I was simulated by a double-domain structure which are described in Section 2.2.3. The structure consisted of long-range strips of domains of p(2×2) cells which were separated by antiphase domain walls in the [011] direction coexisting with long-range strips of domains of p(2×2) cells separated by antiphase domain walls in the [01 $\bar{1}$] direction. This double-domain structure failed to simulate the correct LEED pattern. The observed splitting in the LEED pattern for the (½,½) spots could only be achieved by simulating rectangular domains of p(2×2) cells separated by antiphase domain walls in both the [011] and [01 $\bar{1}$] directions simultaneously. This type of structure has been observed for the Bi/Cu{100} system [Meyerheim 1998]. The domain walls meet in an offset manner to create "pinwheel" structures, spiralling alternately clockwise and counter-clockwise. This is illustrated in Figure 4.17.

This is first representation of a "pinwheel" structure expressed in terms of four different superlattices with different matrices based on combinations of a single matrix, in this case a $\begin{bmatrix} n & 1 \\ 1 & n \end{bmatrix}$ matrix, where n is an integer multiple of the substrate lattice spacing. The proposed structure consists of a unit of nine p(2×2) cells separated by antiphase

domain walls in both the [011] and [01$\bar{1}$] directions. The units of nine p(2×2) cells can be considered as one superstructure with a unit cell based on a $\begin{bmatrix} n & 1 \\ 1 & n \end{bmatrix}$ superlattice. There are four possible types of $\begin{bmatrix} n & 1 \\ 1 & n \end{bmatrix}$ superlattices: the $\begin{pmatrix} n & 1 \\ 1 & n \end{pmatrix}$ and the $\begin{pmatrix} n & -1 \\ -1 & n \end{pmatrix}$ matrices which represent oblique lattices and the $\begin{pmatrix} n & 1 \\ -1 & n \end{pmatrix}$ and $\begin{pmatrix} n & -1 \\ 1 & n \end{pmatrix}$ matrices which represent square (n×n) lattices rotated off-normal by $\tan^{-1}(1/n)$. The correct LEED pattern for Phase I is best represented when this unique superstructure of all four different superlattices is present.

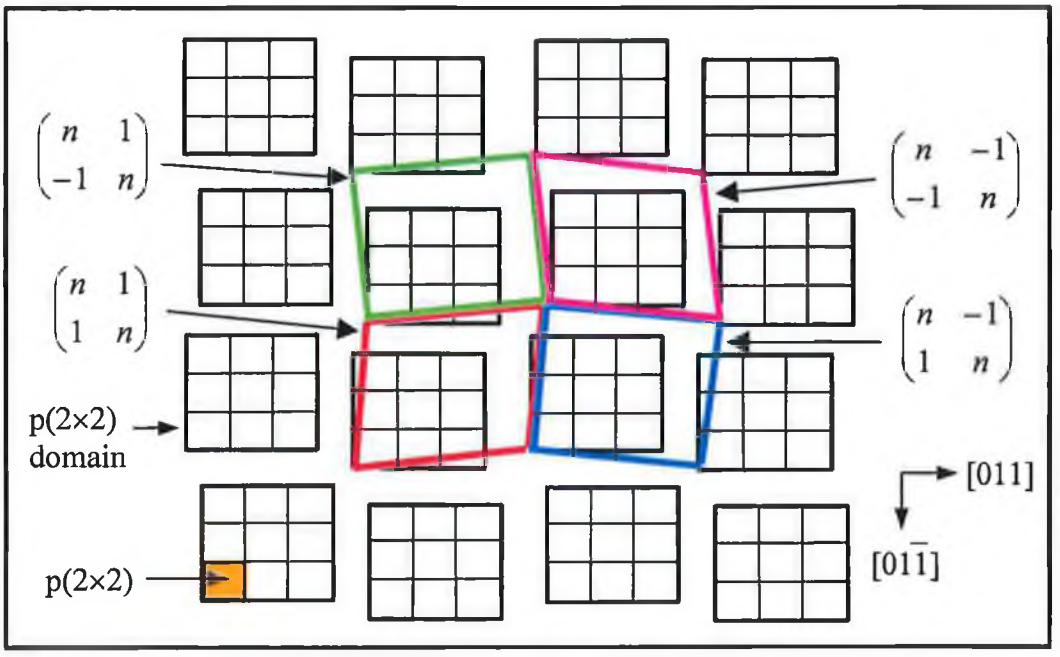

Figure 4.17 *Domains of a superstructure of nine p(2×2) unit cells separated by antiphase domain walls in a pinwheel arrangement.*

Several models based on a $\begin{bmatrix} n & 1 \\ 1 & n \end{bmatrix}$ superlattice were tested. If n is an odd number then no half order splitting is observed in the simulated LEED patterns. So models were tested for n equal to an even number. Models based on n = 2, 4, 6 failed to generate any spot-splitting. In order for the superlattice to represent antiphase domain wall structures, models were simulated for the $\begin{bmatrix} n & 1 \\ 1 & n \end{bmatrix}$ superlattice for n equal to an even numbers greater than six, i.e. n=8 and n=10.

The results of simulations based on n = 8 are shown in Figure 4.18. This model generates a LEED pattern with (½,½) beams split by $\frac{1}{9}th$ (0.11±0.01) of the reciprocal lattice spacing and has a coverage of 0.25ML. This model was rejected as both the spot splitting and the coverage were not consistent with observed values.

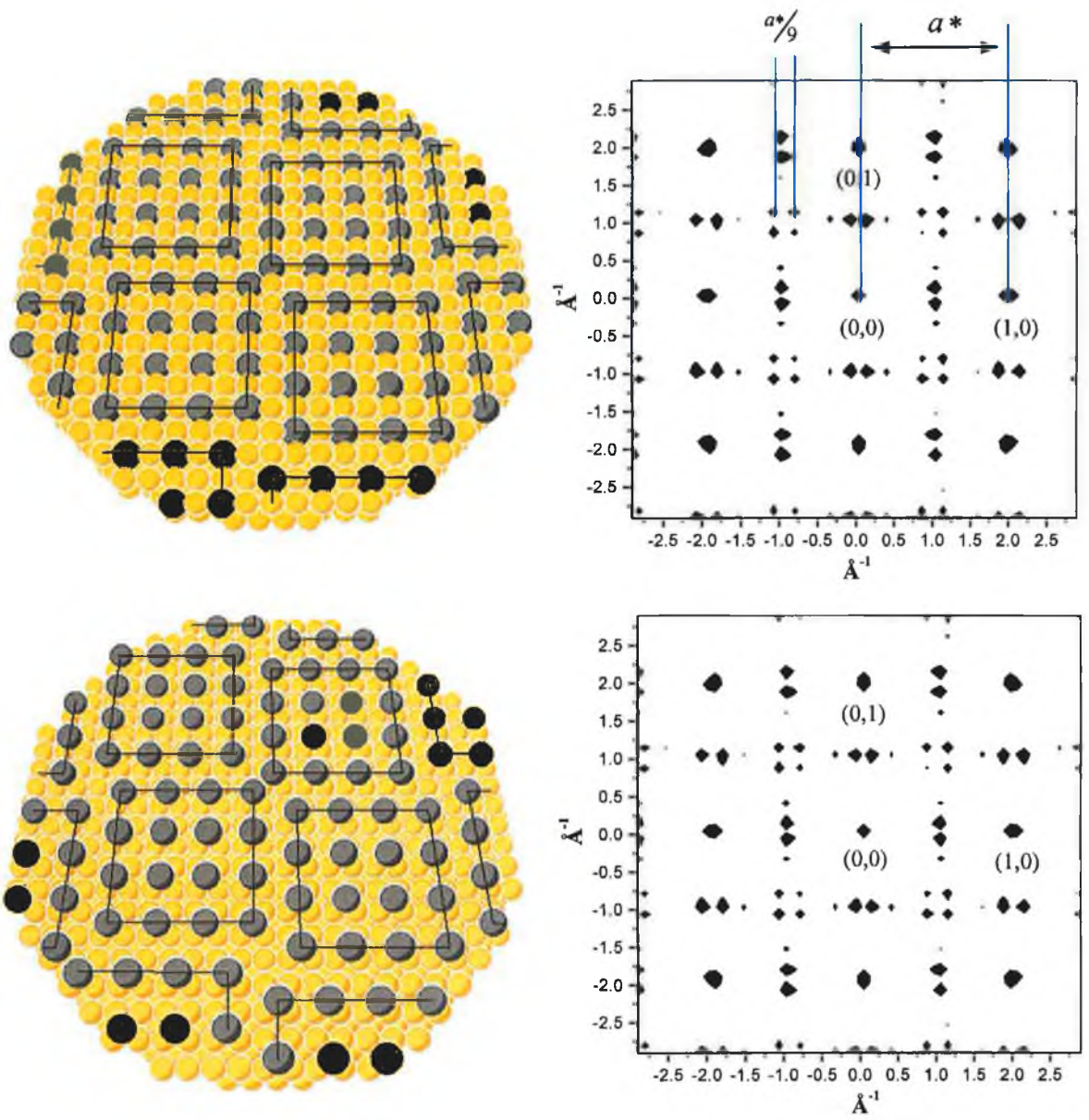

Figure 4.18 *Surface Alloy and overlayer models and simulated LEED patterns for Phase I based on an antiphase domain wall superstucture of* $\begin{bmatrix} 8 & 1 \\ 1 & 8 \end{bmatrix}$. *The (½,½) spot splitting of 1/9th of the integral order separation, in the simulated LEED pattern is not in agreement with the measured value from experimental LEED pictures of 1/11th.*

The best agreements with experimental observations are illustrated in Figures 4.19 and 4.20, for surface alloy and overlayer models. These models consist of unit cells of p(2×2) structure, with rows of copper atoms separating them in both the [011] and $[01\bar{1}]$ directions. These models correspond to a n=10 superlattice structure and a tin coverage of 0.18ML. These structures are classified as "light" antiphase domains as the overall coverage of 0.18ML is less than the 0.25ML coverage at which a p(2×2) structure would reach maximum perfection.

The LEED patterns generated are in excellent agreement with observations, producing (½,0) and (½,1) beams split into intense doublets and (½,½) centred beams split into quartets. The splitting of the (½,½) beams is measured to be $\frac{1}{11}th$ (0.09±0.01) of the reciprocal space lattice in excellent agreement with the observed LEED pattern in Figure 4.11.

As can be seen from Figure 4.18, 4.19 and 4.20 models based on both overlayer and surface alloys in which Sn atoms penetrate into the outermost copper layer yield similar LEED patterns which may not be easily differentiated without a full dynamic I-V analysis. While the double scattering simulation provides LEED patterns of the correct symmetry and periodicity it does not yield quantitatively reliable absolute intensities. However the simulated LEED patterns shown in Figures 4.19 and 4.20 demonstrate the capability of showing different relative intensities.

The normalised experimental I-V spectra recorded at normal incidence, for phase I are shown in Figures 4.21 and 4.22. The I-V data has been collected for full dynamical LEED analysis. A total of eight fractional order beams and four integral order beams with a total energy range of 2900eV are shown. The I-V data was measured in 1eV steps at both normal incidence and 10° off-normal incidence (not shown). Jona [Jona 1982] suggests that 9 to 10 beams across a wide energy range is required for a full structural analysis by dynamical LEED theory.

Some comparisons may be made from the I-V spectra. The specular and integral order beams in Figure 4.21 may be compared to their equivalent beams from clean Cu{100} and Phases II-IV for the Sn/Cu{100} system.

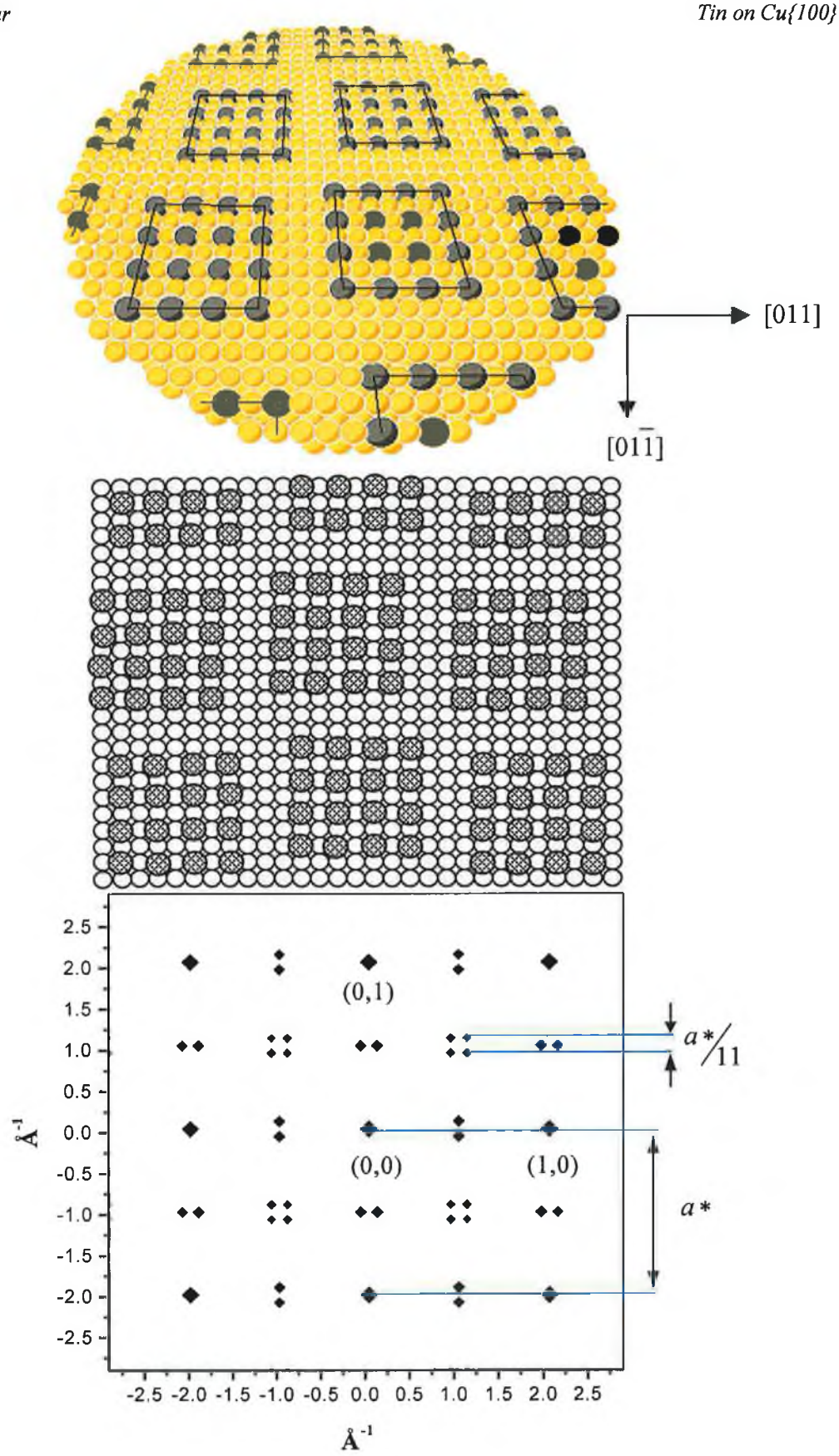

Figure 4.19 *Proposed surface alloy structure and simulated LEED pattern averaged over the range 100-200eV, for phase I, based on antiphase domain wall superstructures with n=10.*

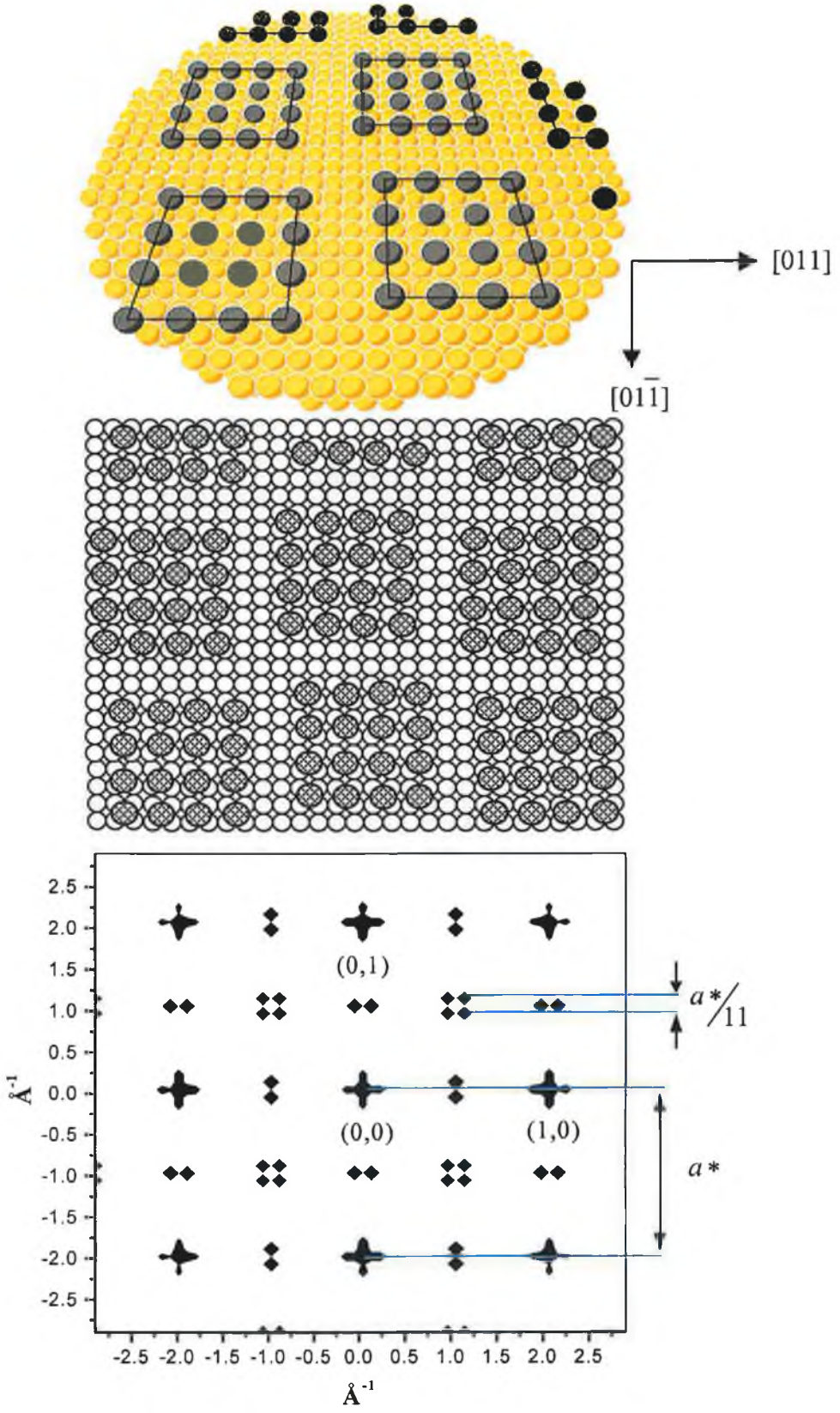

Figure 4.20 *Proposed overlayer structure and simulated LEED pattern averaged over the range 100-200eV, for phase I, based on antiphase domain wall superstructures with n=10.*

The fractional order beams are shown in Figure 4.22. In Figure 4.22 (i) the I-V spectra from the splitting of the (½,½) peaks into four individual quartets (a)-(d), as identified in Figure 4.16, is plotted. The top beam labelled (avg) was measured by recording the integrated intensity for all four beams. The four beams and their average show very similar characteristics from 80-200eV. In figure (ii) the (½,0) and the (½,1) doublet beams are shown. Figure 4.16 identifies the labelling (e)-(h) of these beams. The (½,0) beams, (e) and (f) show similar intensities from 50-200eV. However, the (½,1) beams, (g) and (h) display very little similarities in their I-V spectra.

Integrating the peak intensities of the (½,½) and the (½,0) spots, over an energy range from 100-200 eV for the experimental and simulated models gives a quantitative value for the relative intensities. The (½,½) values used were the integrated intensity of all four beams in the c(2×2) position, as shown in Figure 4.22(i)(avg), while the (½,0) are the integrated intensity of the split doublets, i.e. (e) and (f) in Figure 4.22(ii). A comparison of results for the experimental data and the simulated surface alloy and overlayer models is shown in Table 4.3.

Ratio	Experimental	Surface Alloy Model	Overlayer Model
$\frac{I(\frac{1}{2},\frac{1}{2})}{I(\frac{1}{2},0)}$	0.579	0.523	0.612

Table 4.3 *Comparison of experimental versus simulated relative intensities for Phase I over an energy range of 100-200eV, where the experimental data were measured at the same beam current.*

The experimental ratio of 0.579 is in between the value obtained for the surface alloy of 0.523 and the overlayer model of 0.612. This result demonstrates that it is not possible to conclude whether phase I is a surface alloy or an overlayer structure by double scattering simulations alone.

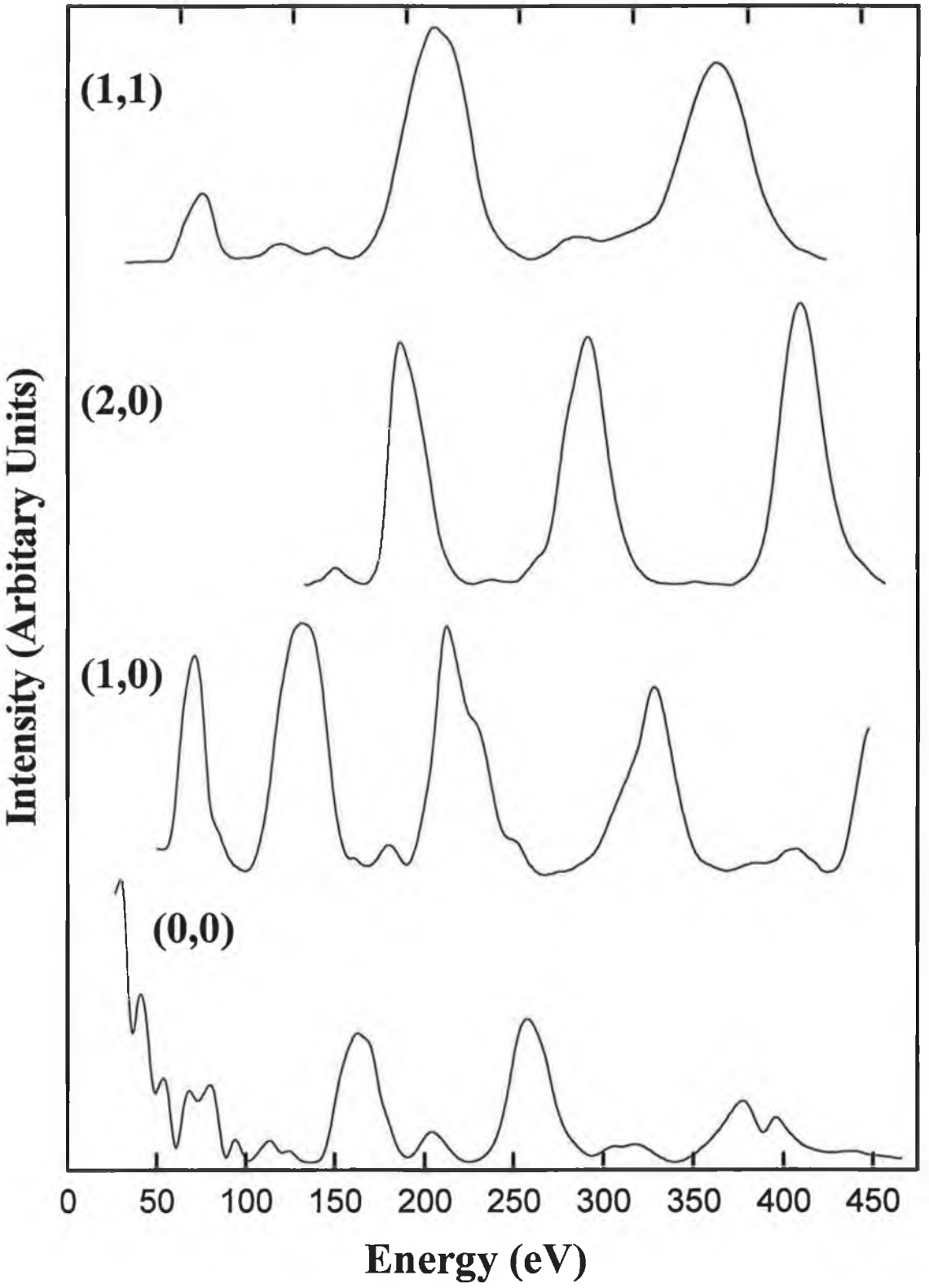

Figure 4.21 *The specular beam measured at 10° off-normal incidence and the integral order beams measured at normal incidence for phase I, 0.21ML of Sn/Cu{100}, uncorrected for Inner Potential.*

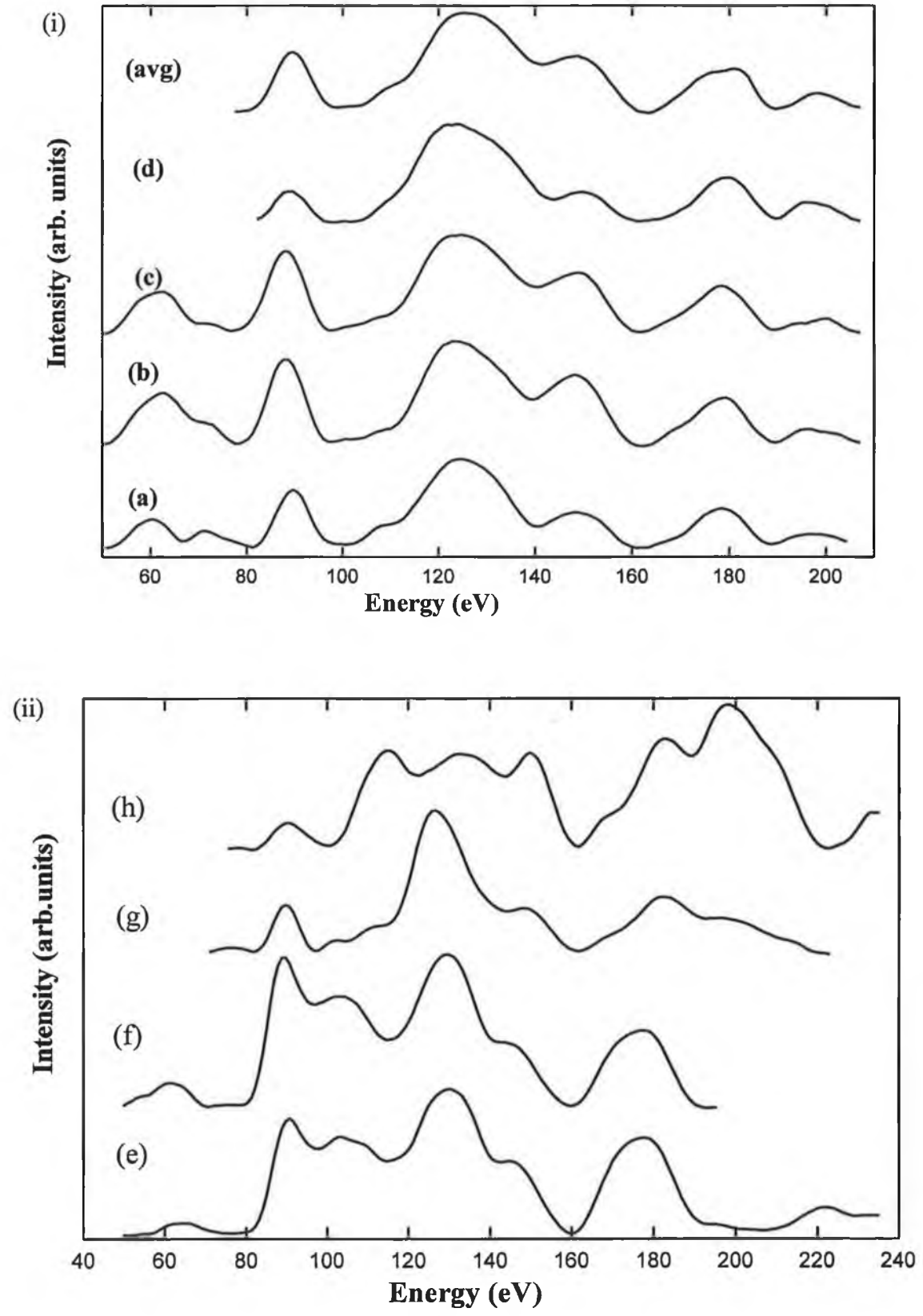

Figure 4.22 *LEED I-V plots for the symmetrically averaged fractional order beams for phase I of Sn/Cu{100}, uncorrected for Inner Potential. (i) The (½,½) beam where (a)-(d) are the four individual quartets and (avg) is the measurement of all four and (ii) (e) & (f) are the (½,0) doublet beams and (g) & (h) are the (½,1) doublet beams.*

4.5.2 Phase II

Figure 4.23 (a) illustrates the p(2×6) rotated domain model suggested by Argile and Rhead consisting of a coincidence mesh with five Sn atoms occupying six copper interatomic spacings in the [01 $\bar{1}$] direction. While this model is entirely consistent with the p(2×6) periodicity observed for a Sn coverage of 0.42ML, it would not be expected to produce (½,½) beams with considerably higher intensity than other superlattice beams as is observed experimentally. As illustrated in Figure 4.24 (a), the simulations based on this model confirm this expectation. It can be observed in the simulated LEED pattern for this model that the $(\frac{1}{2},\frac{5}{6})$ beams have more intensity than the (½,½) beam.

An alternative model for phase II, which maximises in intensity at 0.42ML and has its origin in a mixed c(2×2)/p(2×2) surface alloy structure is shown in Figure 4.23 (b). This structure consists of domains of c(2×2) CuSn surface alloy of two unit cells width, separated by a p(2×2) unit cell, leading to sixth order periodicity in the [011] and [01 $\bar{1}$] directions for the two rotated domains. Figure 4.24 (b) illustrates the LEED pattern generated by this model which exhibits strong (½,½) beams produced by the local c(2×2) structure within these narrow domains. A second possibility, shown in Figure 4.23 (c), is a p(2×6) unit cell consisting of a single c(2×2) unit cell with two p(2×2) unit cells on either side, yielding a coverage of 0.33ML. The simulated LEED pattern for a surface alloy structure, Figure 4.24 (c), is not dissimilar to that shown in Figure 4.24 (b) for the 0.42 ML coverage, the only difference is an increase in the intensity of the (½,0) beams relative to (½,½) beams.

Figure 4.25 illustrates models for an overlayer structure with coverages of 0.42 ML and 0.33 ML based on mixed c(2×2)/p(2×2) structures. In Figure 4.26 (b) and (d) the simulated LEED patterns are shown for each model. The simulated LEED patterns are similar for each coverage again, with the (½,0) beams having more intensity relative to (½,½) beams for the lower coverage model.

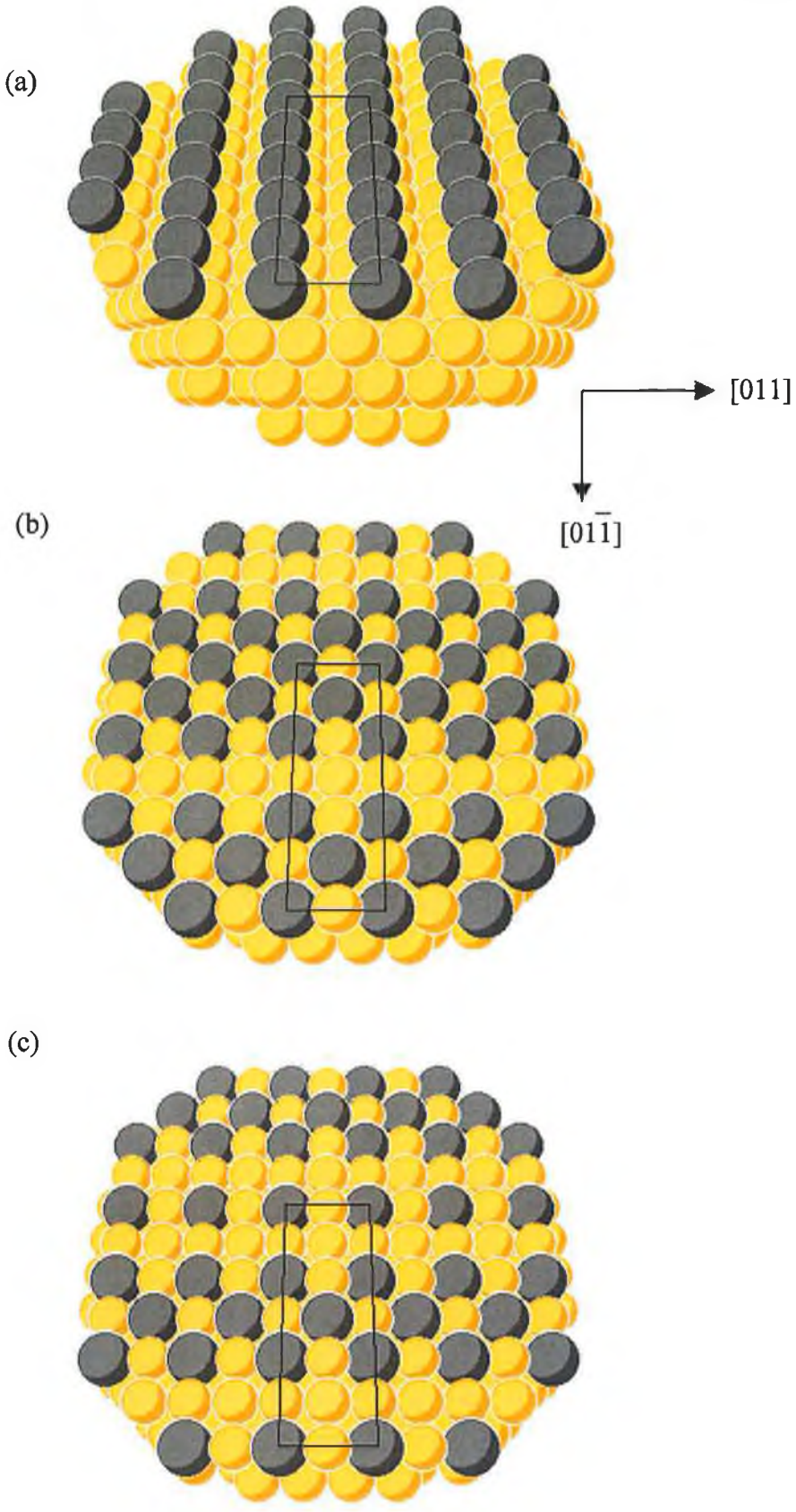

Figure 4.23 *p(2×6) structural models suggested for Phase II; (a) Argile and Rhead overlayer model, (b) the surface alloy model, θ=0.42ML, based on domains of c(2×2) separated by p(2×2) unit cells and (c)) the surface alloy model, θ=0.33ML, based on domains of p(2×2) separated by c(2×2) unit cells.*

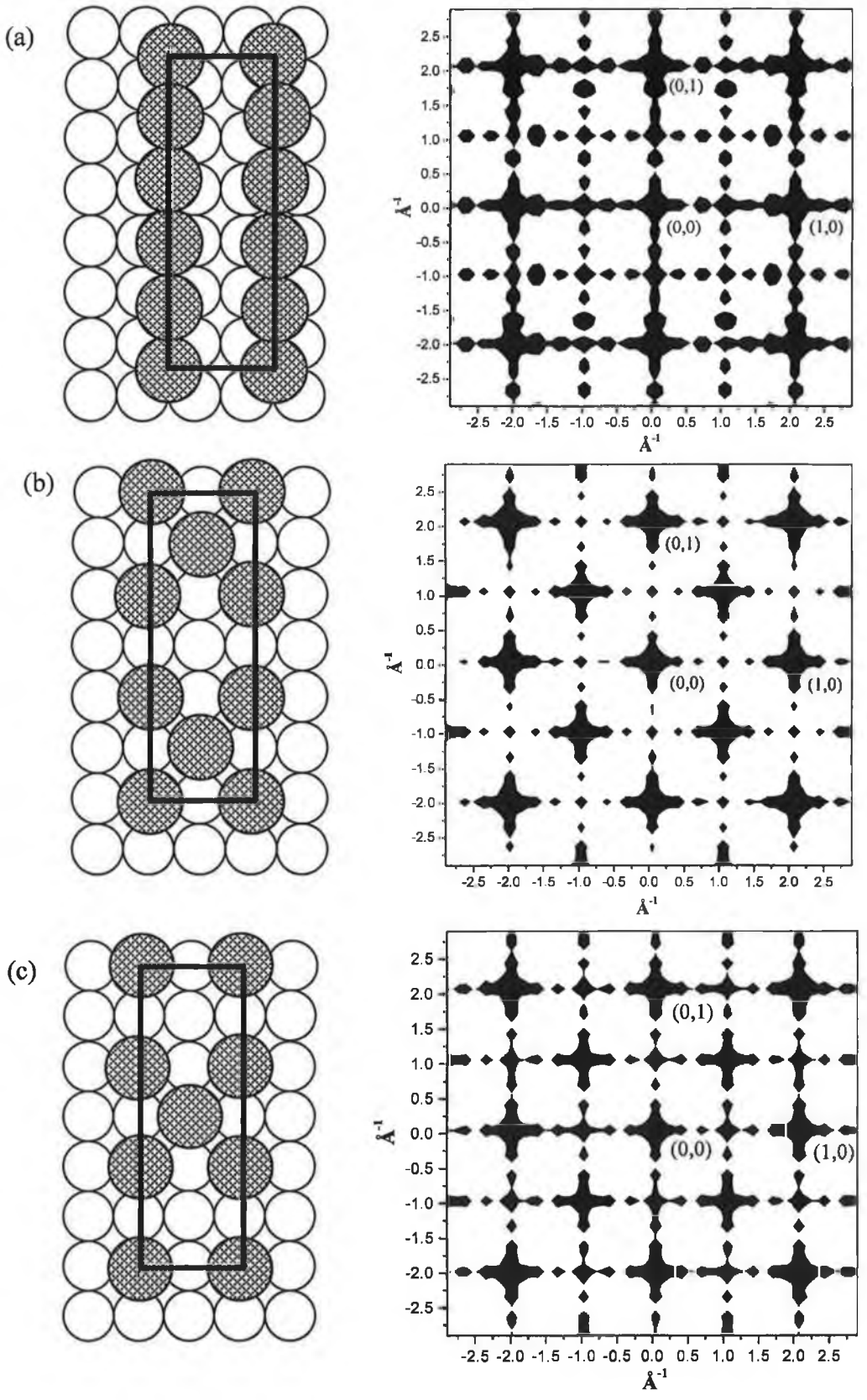

Figure 4.24 *p(2×6) models and generated LEED patterns (100-200eV) for Phase II; (a) Argile and Rhead overlayer model, (b) the surface alloy model, θ=0.42ML, based on domains of c(2×2) separated by p(2×2) unit cells and (c) the surface alloy model, θ=0.33ML, based on domains of p(2×2) separated by c(2×2) unit cells.*

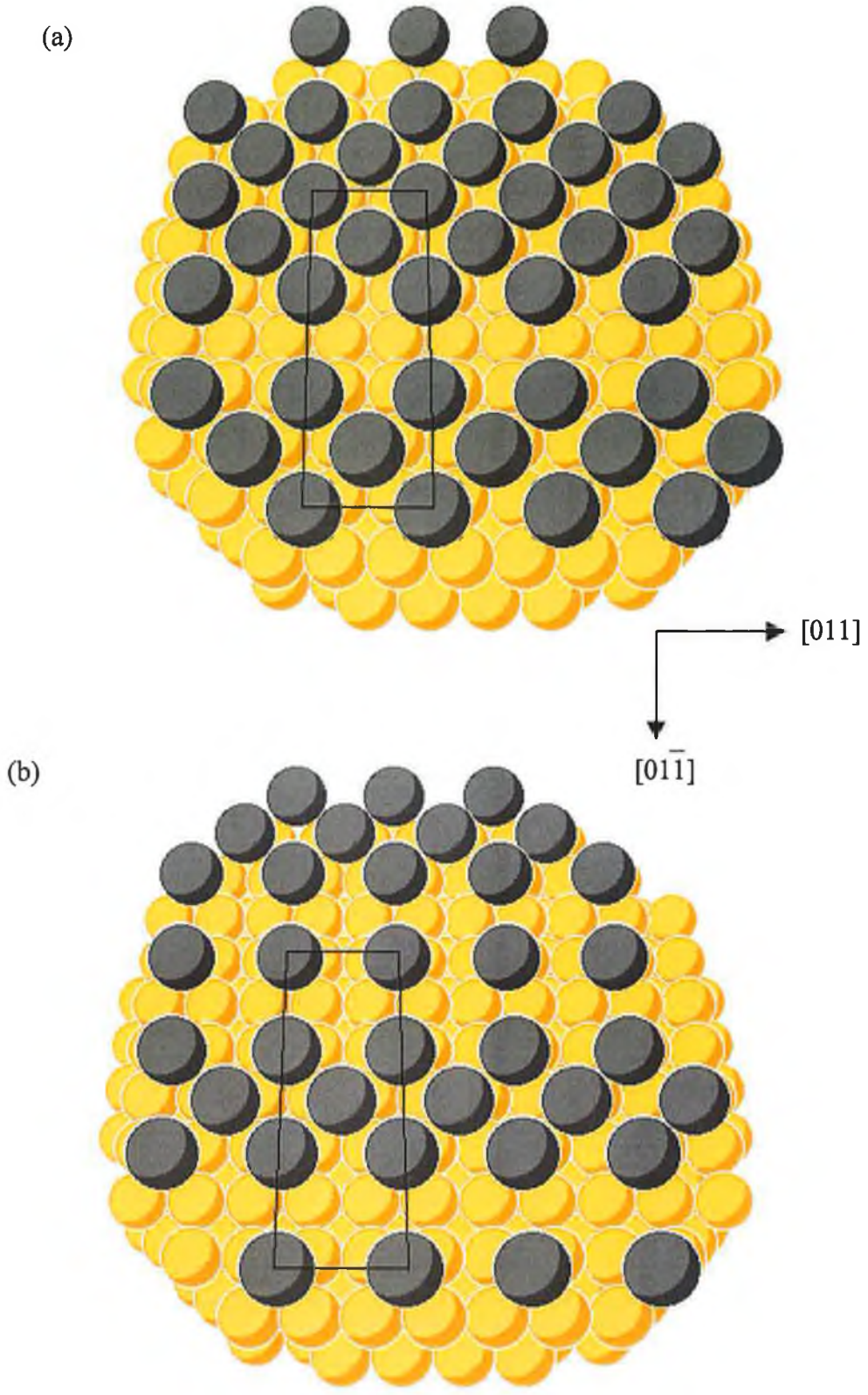

Figure 4.25 *p(2×6) overlayer models suggested for phase II (a) the overlayer model, θ=0.42ML, based on domains of c(2×2) separated by p(2×2) unit cells and (b) the overlayer model, θ=0.33ML, based on domains of p(2×2) separated by c(2×2) cells.*

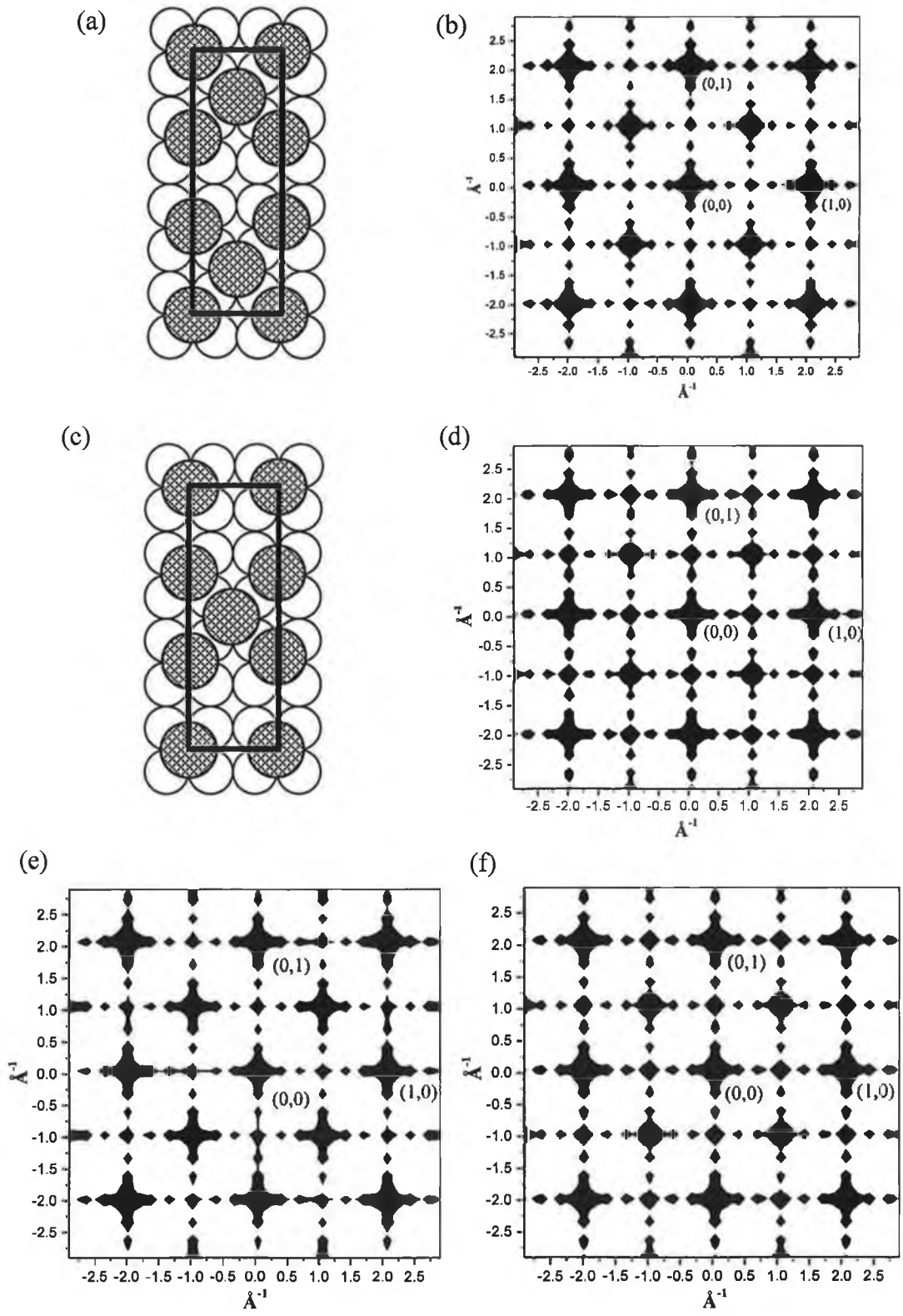

Figure 4.26 *p(2×6) models and simulated LEED patterns (100-200eV) for Phase II; (a), (b) the overlayer model, θ=0.42ML, based on domains of c(2×2) separated by p(2×2) unit cells and (c),(d) the overlayer model, θ=0.33ML, based on domains of p(2×2) separated by c(2×2) cells. (e) LEED simulation of surface alloy model with θ=0.37ML and (f) LEED simulation of overlayer model with θ=0.37ML*

The models proposed for phase I in Section 4.5.1 are based on a p(2×2) structure. It is difficult to explain the transition from the proposed p(2×2) structure to linear chains in the $[01\bar{1}]$ direction as per Argile and Rhead's model which is illustrated in Figure 4.23 (a). The proposed mixed c(2×2)/p(2×2) structures for phase II, offer a more reasonable explanation for the transition from phase I, with a tin coverage of 0.18ML, to phase II with a tin coverage of 0.33ML.

The structures shown here are only single domain models orientated in the $[01\bar{1}]$ direction. A second p(2×6) domain structure co-exists, rotated by 90° and orientated in the [011] direction The simulated LEED patterns shown are generated from co-adding the double domain p(2×6) structures averaged from 100-200eV.

It was observed experimentally that phase II maximises in intensity at 0.37ML, thus it is proposed that phase II consists of a mixture of domains of the structures illustrated in Figures 4.23 (b) and (c) in the Sn coverage range from 0.33ML predominantly p(2×2) cells to full phase completion at 0.42ML mostly c(2×2) cells. The simulated LEED patterns for a surface alloy model and an overlayer model with a 0.37ML tin coverage are shown in Figure 4.26 (e) and (f). These were calculated from averaging the results from θ=0.42ML and θ=0.33ML for each structure. The simulated LEED patterns show different relative intensities of the (½,½) to the (½,0) and (½,1) beams. The ratio of these intensities may be compared to the experimental I-V spectra for the LEED pattern shown in Figure 4.11.

The normalised experimental I-V spectra recorded at normal incidence, for phase II are shown in Figures 4.27. The I-V data has been collected for full dynamical LEED analysis. A total of eight fractional order beams and four integral order beams with a total energy range of 2700eV are shown. The I-V data was measured in 1eV steps at both normal incidence and 10° off-normal incidence (not shown).

The relative intensities of the (½,½) to the (½,0) and (½,½) to the (½,1) beams has been calculated for the experimental I-V spectra in Figure 4.27 and for each different model. The symmetrically equivalent beams were co-added and the integrated relative intensity ratios for the energy range from 100-200eV are given in Table 4.4.

To quantitatively compare the relative intensities of each simulated model to the experimental ratios, a standard deviation term Δ is defined.

$$\Delta = \sqrt{(R_1 - R_{1E})^2 + (R_2 - R_{2E})^2} \qquad (4.5)$$

where $R_1 = \frac{I(\frac{1}{2},0)}{I(\frac{1}{2},\frac{1}{2})}$ and $R_2 = \frac{I(\frac{1}{2},1)}{I(\frac{1}{2},\frac{1}{2})}$ are the calculated intensity ratios for each simulated model and R_{1E} and R_{2E} are the experimentally calculated ratios of 0.35 and 0.53, respectively.

	Figure Number	$R_1 = \frac{I(\frac{1}{2},0)}{I(\frac{1}{2},\frac{1}{2})}$	$R_2 = \frac{I(\frac{1}{2},1)}{I(\frac{1}{2},\frac{1}{2})}$	Δ
Experimental	4.27 (b)	0.35	0.53	
Argile and Rhead θ = 0.42	4.24 (a)	2.857	1.222	2.60
Overlayer θ = 0.42	4.26 (b)	0.056	0.056	0.56
= 0.37	4.26 (f)	0.135	0.135	0.45
= 0.33	4.26 (c)	0.269	0.268	0.27
Surface Alloy θ = 0.42	4.24 (a)	0.042	0.049	0.57
= 0.37	4.26 (e)	0.211	0.226	0.33
= 0.33	4.24 (b)	0.107	0.118	0.48

Table 4.4 *Comparison of relative intensities of selected fractional ordered beams to experimental values for phase II, with* $\Delta = \sqrt{(R_1 - R_{1E})^2 + (R_2 - R_{2E})^2}$ *where* R_{1E} *and* R_{2E} *the experimentally calculated ratios.*

As can be seen from Table 4.4 the Δ value for Argile and Rhead's model is much higher than the Δ values obtained for the mixed c(2×2)/p(2×2) models. The models giving the lowest Δ values from the simulated LEED patterns are the overlayer model with a tin coverage of 0.33ML and the surface alloy model with a 0.37ML tin coverage. Since the R_1 and R_2 ratios are similar for both the surface alloy and the overlayer model, no further conclusions as to which structure occurs can be made, without full dynamical LEED calculations.

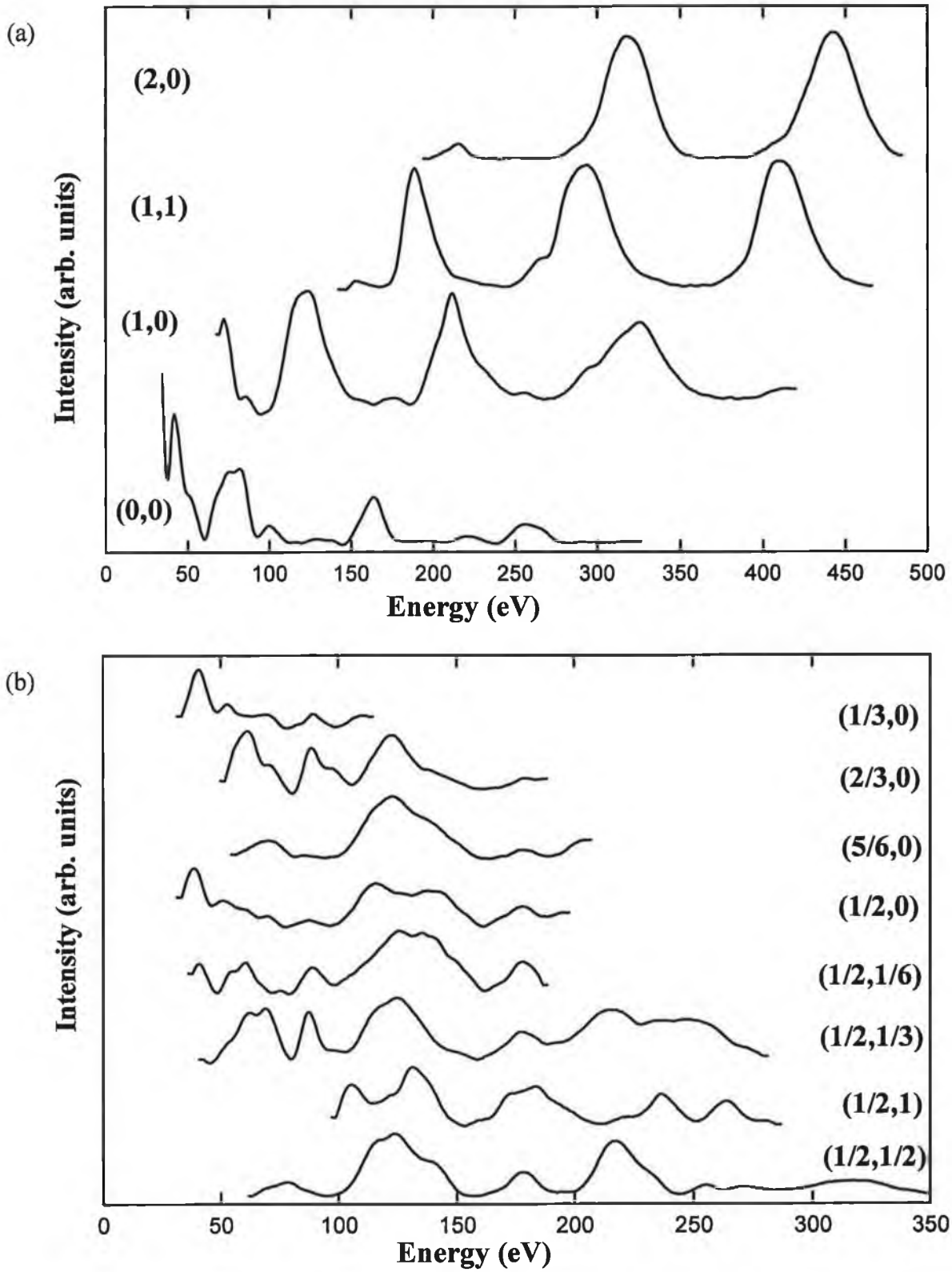

Figure 4.27 *I-V spectra for (a) the specular and integral order beams, and (b) fractional beams for Phase II, 0.37ML of Sn/Cu{100}, uncorrected for Inner Potential.*

4.5.3 Phase III

The transition between phase II and III is a most dramatic one in terms of the observed periodicity of the LEED pattern given that this transition is completed by addition of only an extra 0.08ML of Sn. The structural model suggested by Argile and Rhead is shown in Figure 4.28 (a). The simulated LEED pattern based on the model of Argile and Rhead is shown in Figure 4.29 (a). Their model generates the correct symmetry and periodicity but dominant (½ ,½) beams are not observed.

Based on the structural models proposed for phase II, clearly the obvious location of the additional Sn atoms is to fill the vacancy in the centre of the p(2×2) unit cells separating the c(2×2) domains and yielding the observed Sn coverage of 0.50ML. Simple substitution of Sn atoms into the c(2×2) sites in the vacant copper rows would lead to a perfect c(2×2) structure rather than the p(3√2×√2)R45° structure observed as shown in Figure 4.28 (b). Due to the larger metallic radius of Sn, a simple c(2×2) structure with Sn and Cu coplanar within a surface alloy model would lead to significant strain along the [001] directions. Models based on relief of this strain by buckling and/or small lateral displacements of Sn and Cu atoms are proposed. Figure 4.28 (c) shows an overlayer structural models for phase III, with Sn atoms occupying the four-fold hollow sites.

To model this strain relief, Figure 4.29 (b) and (c) show a c(2×2) surface alloy and overlayer structure with pairs of Sn atoms "pinched" together. The red lines indicate the lattice coordinate sites separated by 3.6Å and the arrows indicate the direction of tin atom displacement from these sites. This model is only one of many possibilities for which combined lateral and perpendicular motion of Cu and Sn atoms yield a p(3√2×√2)R45° unit cell. It serves to illustrate the principle that a model based on a c(2×2) structure, with minor modifications leads to the observed p(3√2×√2)R45° periodicity. In such models the magnitude of the lateral displacement of copper atoms controls the relative intensities of the (½ ,½) beams to the other superlattice beams. Simulations of models with larger displacements lead to stronger intensities of other superlattice reflexes compared to the (2×2) superlattice beams.

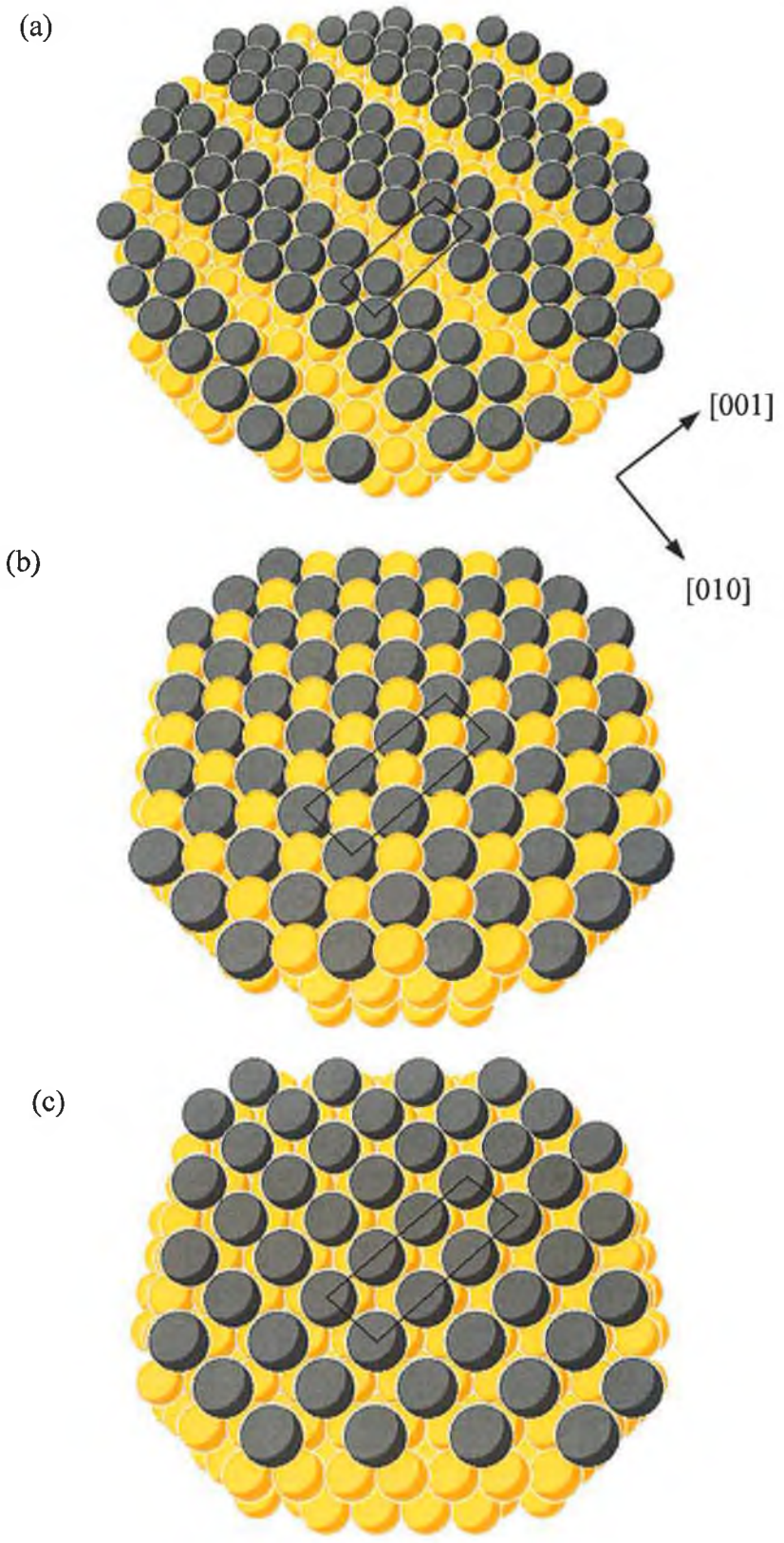

Figure 4.28 *Structural models for phase III, 0.5ML Sn/Cu{100}; (a) Argile and Rhead (b) surface alloy model and (c) overlayer model with Sn occupying the ideal four-fold hollow sites.*

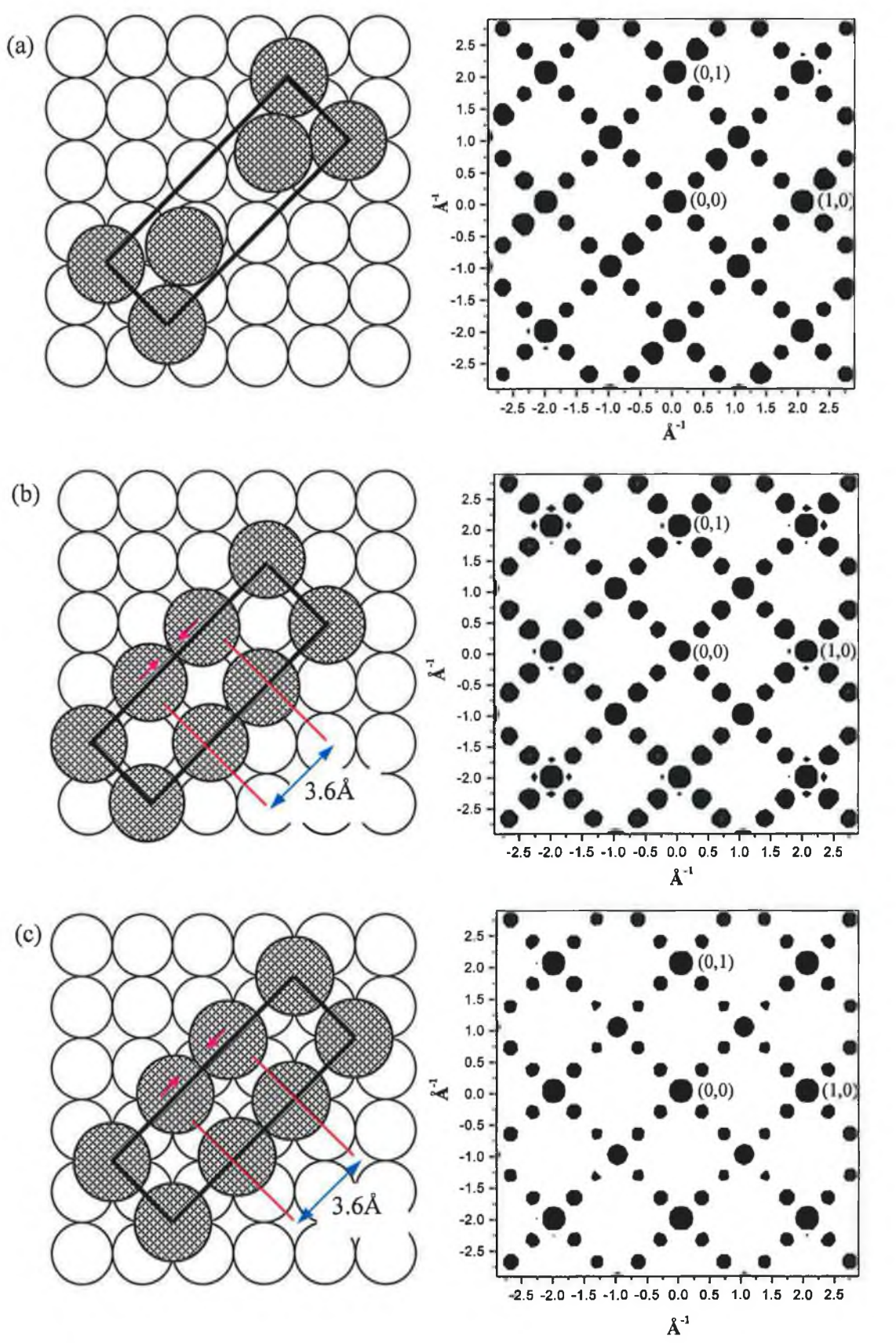

Figure 4.29 *Structural models and simulated LEED patterns for phase III, 0.5ML Sn/Cu{100}; (a) Argile and Rhead (b) surface alloy model and (c) overlayer model with Sn laterally shifted by 0.4Å. In (b) and (c) the red lines indicate the positions of lattice coordinate sites and the arrows indicate the direction of tin atom displacement.*

Figure 4.30 illustrates the simulated LEED patterns for varying degree of lateral displacement of Cu and Sn atoms along the [010] direction, indicating that a lateral shift of approximately 10% or 0.4Å yields the best qualitative agreement with the observed LEED intensities.

The structural models shown here are single domain models orientated in the [001] direction. A second domain p(3√2×√2)R45° structure co-exists, rotated by 90° and orientated in the [010] direction The simulated LEED patterns shown are generated from co-adding the double domain p(3√2×√2)R45° structures averaged from 100-200eV.

Figure 4.31 shows the I-V spectra for (a) the specular and integral order beams and (b) the fractional order beams. A total of four integral order and six fractional order beam intensities were recorded at normal incidence and at 10° off-normal incidence. To quantitatively measure the effect of the lateral distortion from ideal lattice sites, the symmetrically equivalent $(\frac{2}{3},\frac{2}{3})$, $(\frac{1}{2},\frac{1}{2})$ and $(\frac{1}{3},\frac{1}{3})$ beams were averaged and peak intensities integrated over the energy range from 100-200eV. The results are presented in Table 4.5 along with the relative intensities for each model.

To quantitatively compare the agreement of each model to the experimental ratios, a Δ term is used, as in Section 4.5.2. In this case:

$$\Delta = \sqrt{(R_1 - R_{1E})^2 + (R_2 - R_{2E})^2} \qquad (4.6)$$

where $R_1 = \frac{I(\frac{2}{3},\frac{2}{3})}{I(\frac{1}{2},\frac{1}{2})}$ and $R_2 = \frac{I(\frac{1}{3},\frac{1}{3})}{I(\frac{1}{2},\frac{1}{2})}$ are the calculated ratios for each simulated model and R_{1E} and R_{2E} are the experimentally calculated ratios, 0.255 and 0.54, respectively. The value for Δ is calculated for each model in Table 4.5.

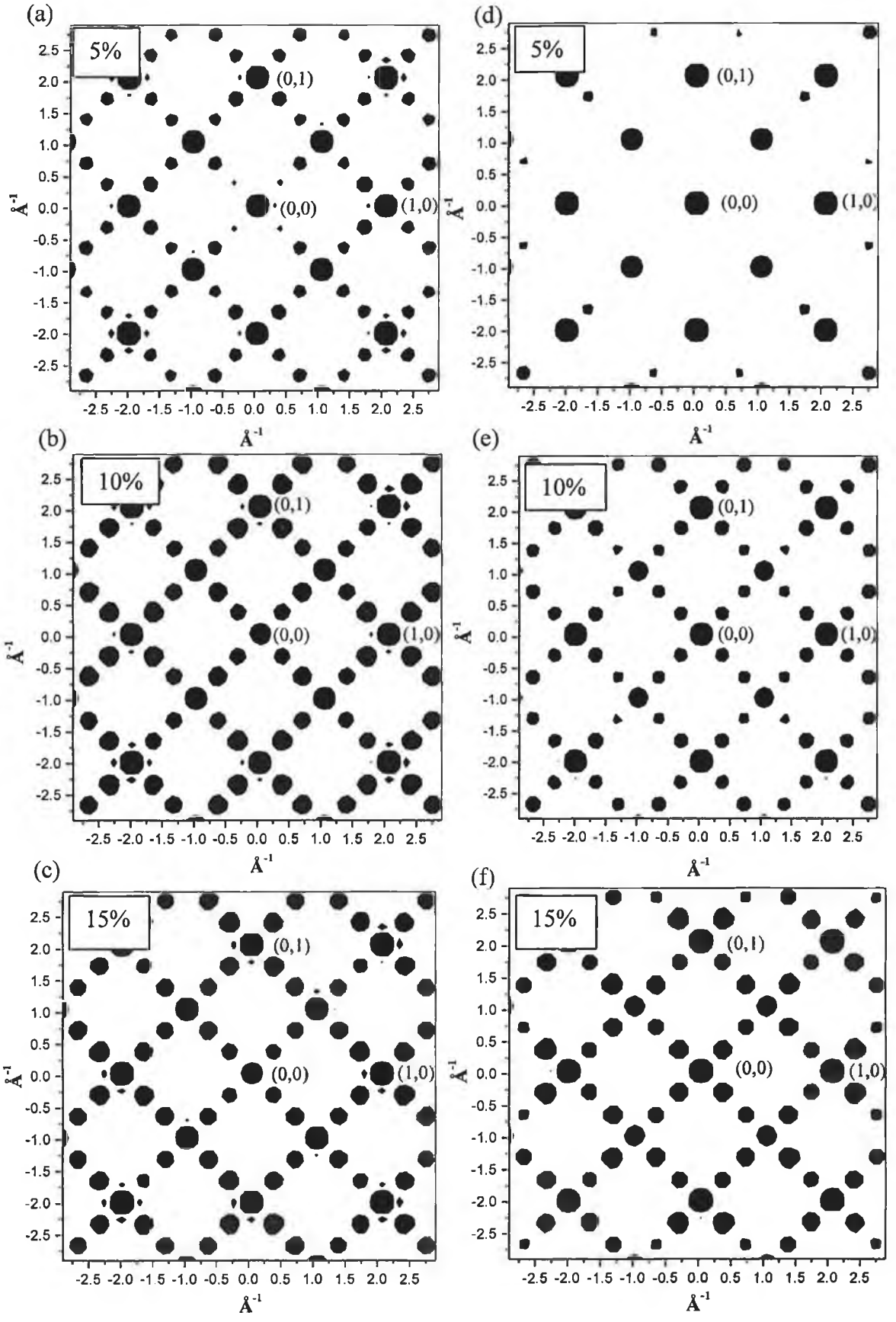

Figure 4.30 *Simulated LEED patterns for surface alloy (left) and overlayer (right) structures for Phase III, with increasing lateral movement (a)&(d) 5%, (b)&(e) 10%, (c)&(f) 15%, of Sn atoms along the [010] direction from lattice coordinate sites.*

	Figure Number	$R_1 = \frac{I(\frac{2}{3},\frac{2}{3})}{I(\frac{1}{2},\frac{1}{2})}$	$R_2 = \frac{I(\frac{1}{3},\frac{1}{3})}{I(\frac{1}{2},\frac{1}{2})}$	Δ
Experimental	4.31 (b)	0.255	0.54	
Argile and Rhead	4.29 (a)	0.284	1.12	0.58
Overlayer shift = 5%	4.26 (d)	0.015	0.039	0.56
10%	4.26 (e)	0.18	0.255	0.29
15%	4.26 (f)	1.214	0.46	0.93
Surface Alloy shift = 5%	4.26 (a)	0.1197	0.126	0.19
10%	4.26 (b)	0.2543	0.387	0.15
15%	4.26 (c)	0.232	0.242	0.30

Table 4.5 *Relative intensity ratios for fractional order beams for phase III where Δ is a comparative term defined as* $\Delta = \sqrt{(R_1 - R_{1E})^2 + (R_2 - R_{2E})^2}$ *with* R_{1E}*=0.255 and* R_{2E}*=0.54.*

As can be seen from Table 4.5 the experimental (½, ½) beam is more intense than the $(\frac{2}{3},\frac{2}{3})$ and the $(\frac{1}{3},\frac{1}{3})$ beams. The ratios calculated for the models of Argile and Rhead show a similar value for R_1 and an incorrect R_2 ratio. All of the simulated surface alloy models for the p(3√2×√2)R45° structure show better agreement than the overlayer models. The simulation of the surface alloy model with a 10% distortion produces the best agreement. These results would indicate that phase III with a coverage of 0.5ML, is based on a c(2×2) surface alloy structure. Strain relief occurs as lateral and/or perpendicular displacements of the tin atoms along the [001] and [010] directions forming a double domain p(3√2×√2)R45° structure.

The I-V spectra have been measured for this system as shown in Figure 4.31 and full dynamical LEED I-V analysis has commenced for this phase in collaboration with M. Lindroos, Tempere University, Finland. As many comparative metal on metal systems are based on either a c(2×2) surface alloy or overlayer structure for 0.5ML coverage, this phase was considered the most appropriate starting structure with which to begin full I-V calculations.

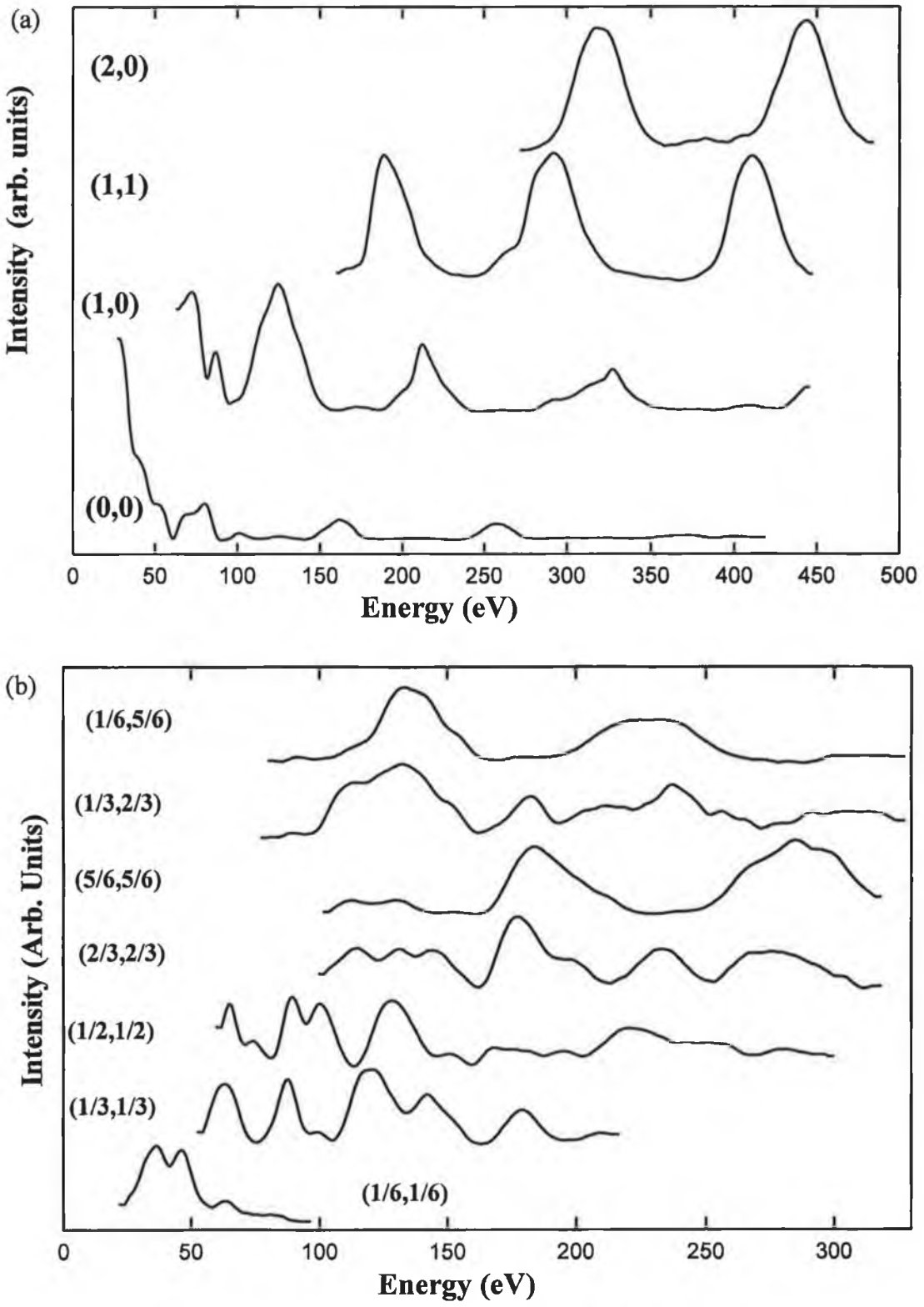

Figure 4.31 *Normalised I-V spectra for Phase III, 0.5ML Sn/Cu{100}; (a) specular and integral beams and (b) fractional order beams. Energies are uncorrected for the Inner potential.*

4.5.4 Phase IV

The monolayer structure proposed by Argile and Rhead for a coverage of 0.625ML is based on a square overlayer of tin with atomic diameters 3.22Å, slightly compressed from the 12–fold metallic diameter of 3.246Å as shown in Figure 4.32 (a). The Sn atoms form closely packed chains rotated by 16° with respect to the [011] direction as shown in Figure 4.33 (a). The four tin atoms occupying the vertices of the unit cell are in four fold hollow positions, but the other four atoms in the unit cell do not occupy high coordinate sites. This arrangement leads to a c(4×4) or p(2√2×2√2)R45° structure with (½, ½) beams not as dominant as in phase II and III. The LEED pattern for phase IV is shown in Figure 4.12. The model of Argile and Rhead and the simulated LEED pattern for this phase are in good agreement with experimental observations as shown in Figure 4.33 (a).

Alternative surface alloy and overlayer models for phase IV with 0.625ML coverage are shown in Figure 4.32 (b) and (c) where the tin atoms are positioned in high-coordination lattice sites. The simulated LEED patterns for these models are shown in Figure 4.33 (b) and (c), with dominant (½, ½) beams, in disagreement with the observed LEED pattern. The double scattering simulation is inadequate to prove that the model proposed by Argile and Rhead is the only correct model. A comparison of the results from these three models shows that some lateral movement of the tin atoms away from lattice sites occurs. In order for uniform density of the tin atoms on the copper surface, all the tin atoms cannot occupy lattice sites. It is this non-symmetric positioning of the Sn atoms in a c(4×4) unit cell that leads to the experimentally observed LEED pattern with no significantly dominant fractional order beams. Similar LEED patterns are generated for overlayer and surface alloy models and therefore require full dynamical LEED I-V to distinguish between them.

The coverage of 0.70ML, based on AS-t plots and line profiles, Figures 4.9/4.14, estimated for maximum perfection of phase IV, is higher than the modelled value of 0.625ML. This discrepancy is due to the accuracy in calculating the position of the break in the AS-t plot accurately for completion of the first monolayer. Also, it can be seen from the line profiles in Figure 4.14 that the spot intensities decrease in intensity for coverages greater than 1ML and in fact show a totally disordered surface for coverages greater than 1ML.

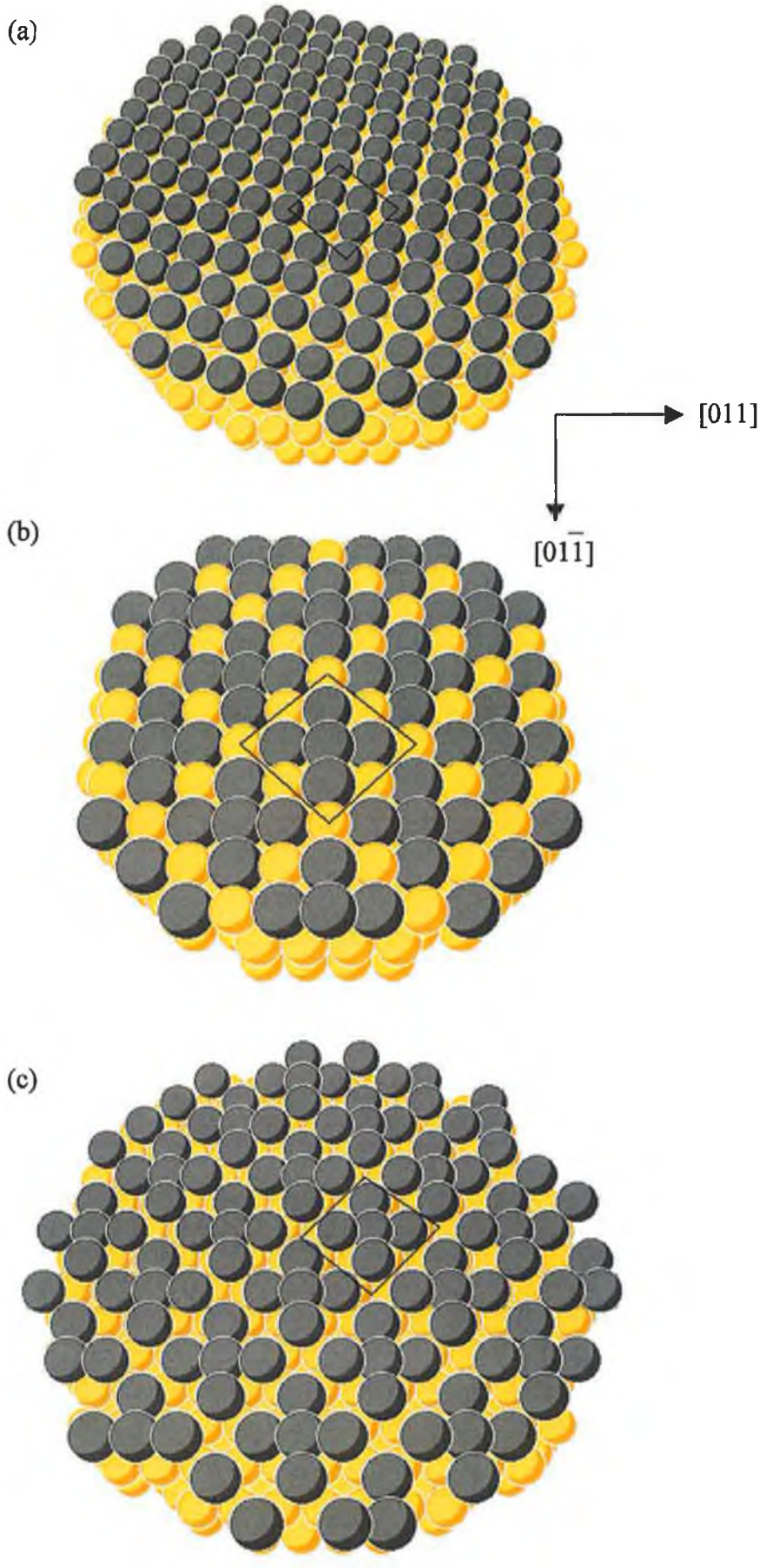

Figure 4.32 *Structural models for Phase IV Sn/Cu{100}; (a) Argile and Rhead, (b) surface alloy model and (c) overlayer model.*

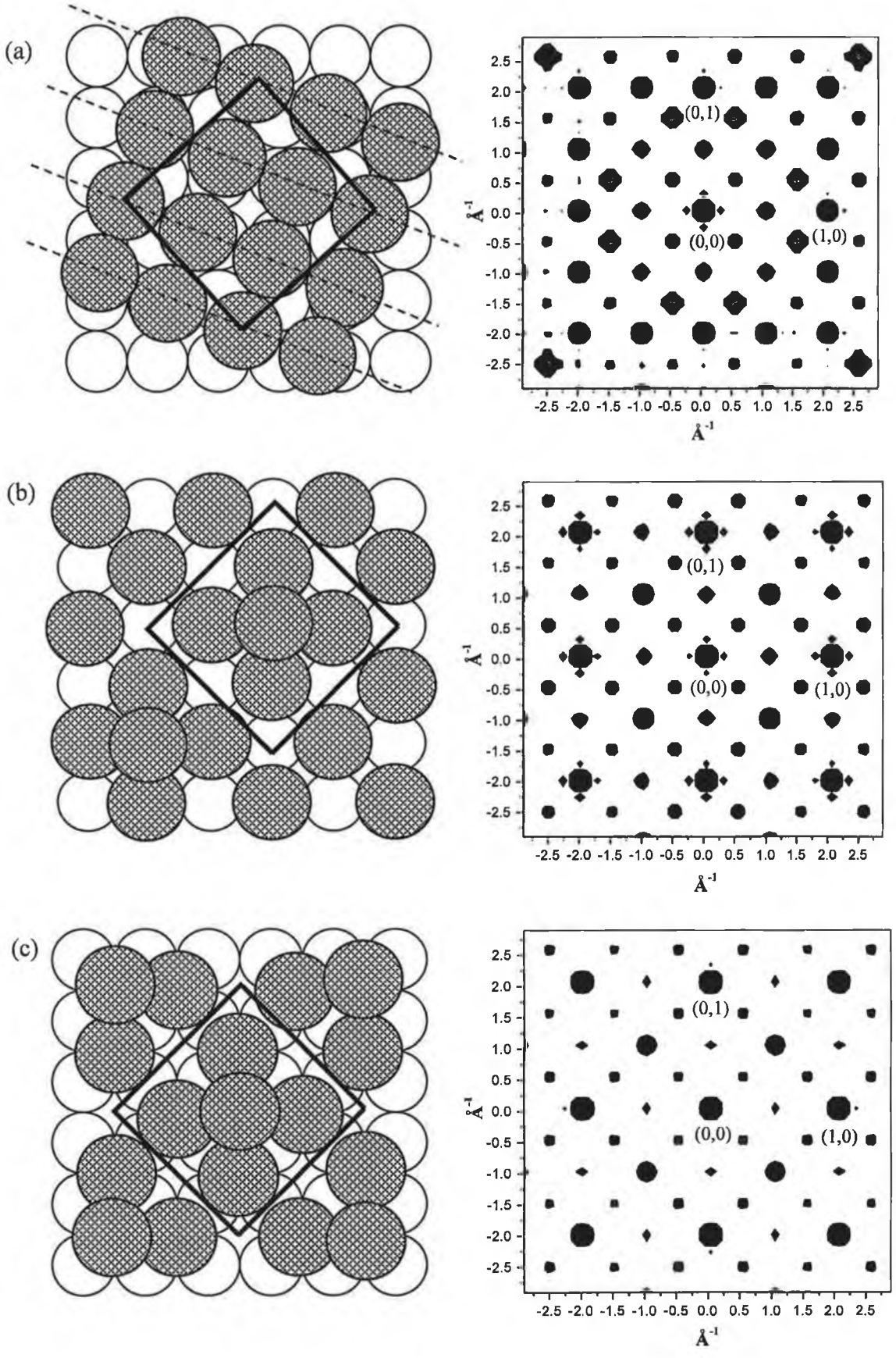

Figure 4.33 *Structural models and simulated LEED for Phase IV Sn/Cu{100}; (a) Argile and Rhead with dashed lines indicating the direction of the Sn rows, (b) surface alloy model and (c) overlayer model.*

The measured I-V spectra for four integral order and seven fractional order beams over a total energy range of 2800eV are shown in Figure 4.34. The intensites of the symmetrically equivalent $(\frac{3}{4},\frac{3}{4})$, $(\frac{1}{2},\frac{1}{2})$ and $(\frac{1}{4},\frac{1}{4})$ beams are calculated over the energy range from 100-200eV and the ratios presented in Table 4.6. The ratios for the simulated LEED patterns are also shown.

	Figure	$R_1 = \frac{I(\frac{3}{4},\frac{3}{4})}{I(\frac{1}{2},\frac{1}{2})}$	$R_2 = \frac{I(\frac{1}{4},\frac{1}{4})}{I(\frac{1}{2},\frac{1}{2})}$	Δ
Experimental	4.34 (b)	0.82	2.27	
Argile and Rhead	4.33 (a)	0.49	0.48	1.82
Overlayer	4.33 (c)	0.128	0.148	2.23
Surface Alloy	4.33 (b)	0.13	0.19	2.19

Table 4.6 *Relative intensity ratios for fractional order beams for phase IV where Δ is a comparative term defined as* $\Delta = \sqrt{(R_1 - R_{1E})^2 + (R_2 - R_{2E})^2}$ *with* R_{1E}*=0.82 and* R_{2E}*=2.27.*

For this complete monolayer phase, it is observed experimentally that the $(\frac{1}{4},\frac{1}{4})$ beam is more intense than the $(\frac{1}{2},\frac{1}{2})$ beam. This is not reflected in the R_2 ratio for any of the three models. The model suggested by Argile and Rhead gives the best agreement with observations, but the Δ value is still high for this model. The large Δ difference between experimental and simulated intensity ratios would indicate that phase IV is not correctly modelled and further strain relief must be considered.

In this case, for phase IV, the overlayer model of Argile & Rhead is shown to be the best initial structure for dynamical LEED analysis.

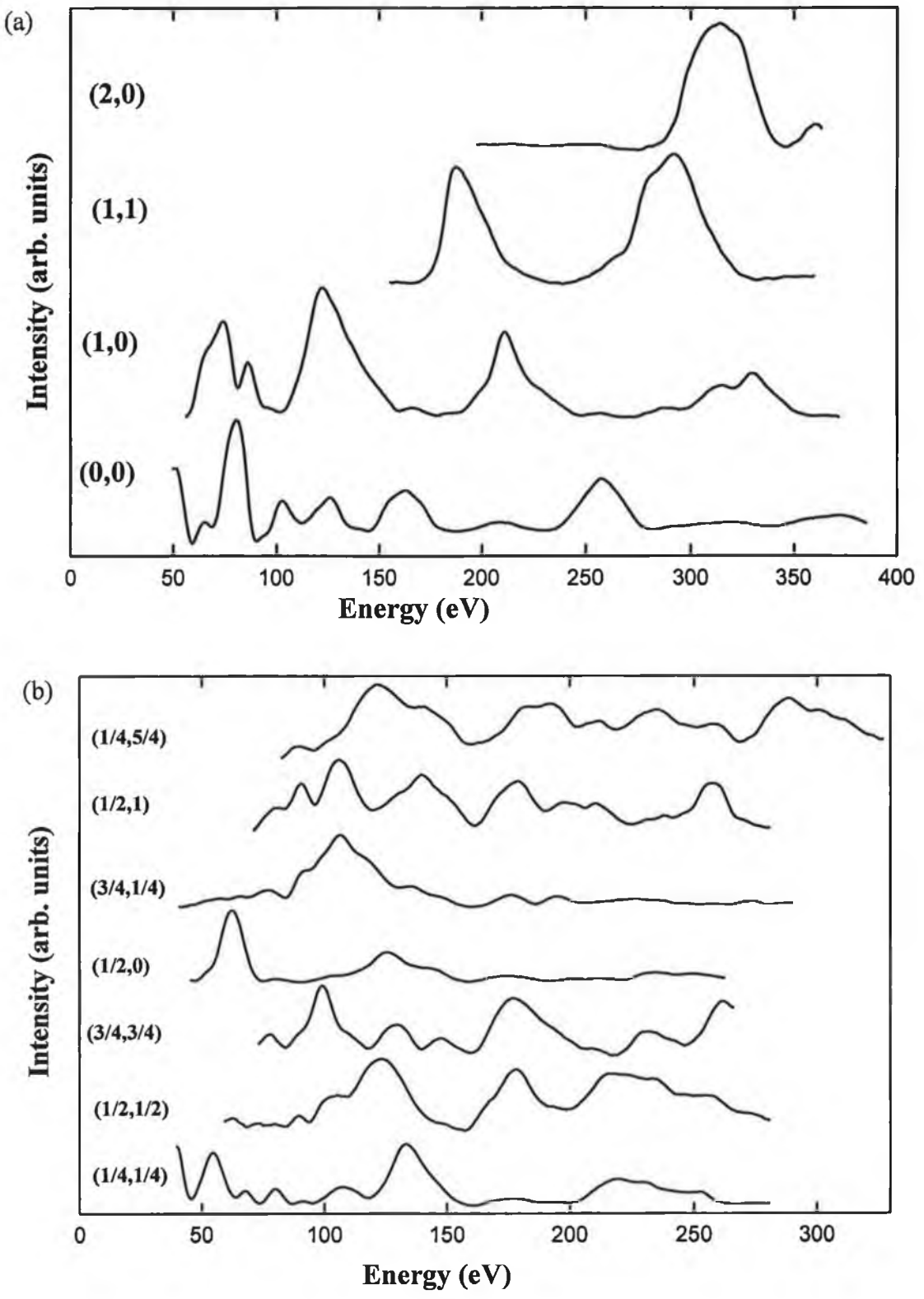

Figure 4.34 *LEED I-V spectra for phase IV of Sn/Cu{100}: (a) specular and integral order beams; and (b) fractional order beams, where the energy is uncorrected for the inner potential.*

4.6 Temperature Programmed Desorption Results

In analysing the Sn/Cu system, there are three different structural models:

(i) Overlayer structure, with the tin located above the first layer of copper.

(ii) Surface alloy structure, where the tin replaces copper in the first layer and the top layer consists of a mixture of tin and copper atoms.

(iii) The tin goes sub-surface, that is, copper diffuses to the top layer and only copper atoms occupy the top layer, with the tin atoms situated in the second layer.

In order to distinguish between these models, TPD studies on the Sn/Cu{100}system were carried out.

Formic acid (HCOOH) and carbon monoxide (CO) are the most common simple gases used to probe surface reactivity. Formic acid is the simplest carboxylic acid forming a strong stable bidentate formate intermediate on copper. Formic acid adsorption on copper is of major chemical interest because the formate intermediate has been shown to be the most stable species involved in the synthesis of methanol. The formate is stable up to about 450K on Cu{100} before it decomposes to yield CO_2 and H_2.

$$HCOOH \rightarrow CO_2 + H_2 \qquad (4.7)$$

Using a method suggested by Redhead [Redhead 1962] this decomposition follows first order kinetics. Estimates for the heat of adsorption for formic acid on copper range from ~12 to 18kcal/mole, depending on coverage [Dubois 1986].

The desorption reaction of formic acid on Cu(110) reveals that the formate appears to orient upright on the surface with the two oxygen atoms bound to equivalent sites [Bowker 1981, 1996]. A structural study of formate on Cu(111) using normal incidence X-ray standing waves (NIXSW) demonstrated that the oxygen atoms of the formate were located in atop sites with the formate bridging two copper atoms [Sotiropoulos 2000]. The site spacing on Cu{100} is 2.55Å and the formate O-O distance is 2.24Å [Sexton 1979]. PhD and SEXAFS studies carried out for formate on Cu{100} show that the oxygen atoms do occupy atop positions with a Cu-O nearest neighbour distance of 1.98±0.04Å as shown if Figure 4.35 [Woodruff 1988]. These results were confirmed by later theoretical studies [Wander 1988] [Mehandru 1989] [Casarin 1994].

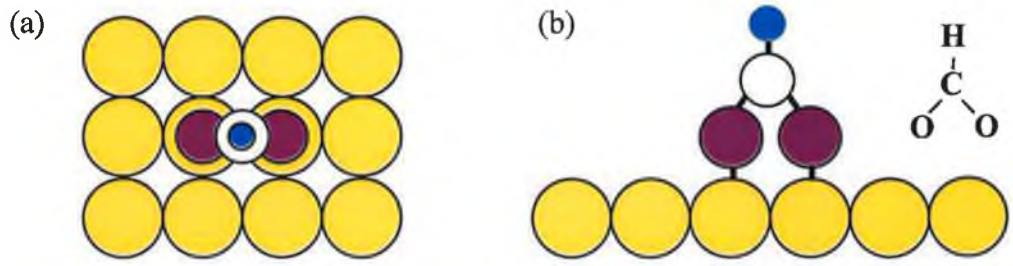

Figure 4.35 *(a) Top view and (b) side view of the geometry of formic acid on copper.*

No evidence for the adsorption of formate on a pure tin substrate or onto a copper-tin alloy structure was found in literature. This indicates that if either behaviour (i) or (ii) occur no formate desorption peak is expected for Sn-Sn sites or Sn-Cu sites in the TPD spectra. However, if the tin goes sub-surface and the copper atoms occupy the top layer, then the formate behaves as on the clean copper crystal and a formate desorption peak is expected around 450K.

Phases I to IV were probed by thermal desorption spectroscopy (TDS) following the decomposition of a formate intermediate to CO_2 and H_2 formed by room temperature dosing of the copper surface with formic acid (HCOOH). Most of the recent structural work is indicative of a geometry in which the two oxygen atoms of the formate bridge two nearest neighbour copper atoms. The formate is stable up to 400K, after which it decomposes with simultaneous evolution of CO_2 and H_2 and some molecular formic acid. Figure 4.36 illustrates the temperature programmed desorption spectra for formate decomposition for saturation formic acid coverage on clean Cu{100} and on phases I-IV. Mass 44 (CO_2), mass 2 (H_2) and mass 46 (HCOOH) desorption spectra are illustrated. The clean Cu{100} surface shows simultaneous desorption of CO_2 and H_2 with a peak temperature of approximately 440K, along with a broad molecular desorption peak. Assuming first order formate decomposition kinetics and a pre-exponential factor of 10^{13} s^{-1} [Redhead 1962], an activation energy of 115kJ mol^{-1} is obtained for formate decomposition on clean Cu{100}.

For phases II-IV, no formate decomposition was detected, suggesting that no areas of free unmodified copper bridge sites were available for adsorption. However, in the case of phase I, a small CO_2 was observed close to the decomposition temperature of the formate intermediate on clean Cu{100}. The result is to be expected for phase I which has areas of unmodified copper sites between the p(2×2) domains. It is evident that

formate does not bond to Sn-Sn bonds or Sn-Cu bonds. The conclusion that may be inferred from these observations is that the tin has not gone sub surface but has formed an overlayer or surface alloy structure.

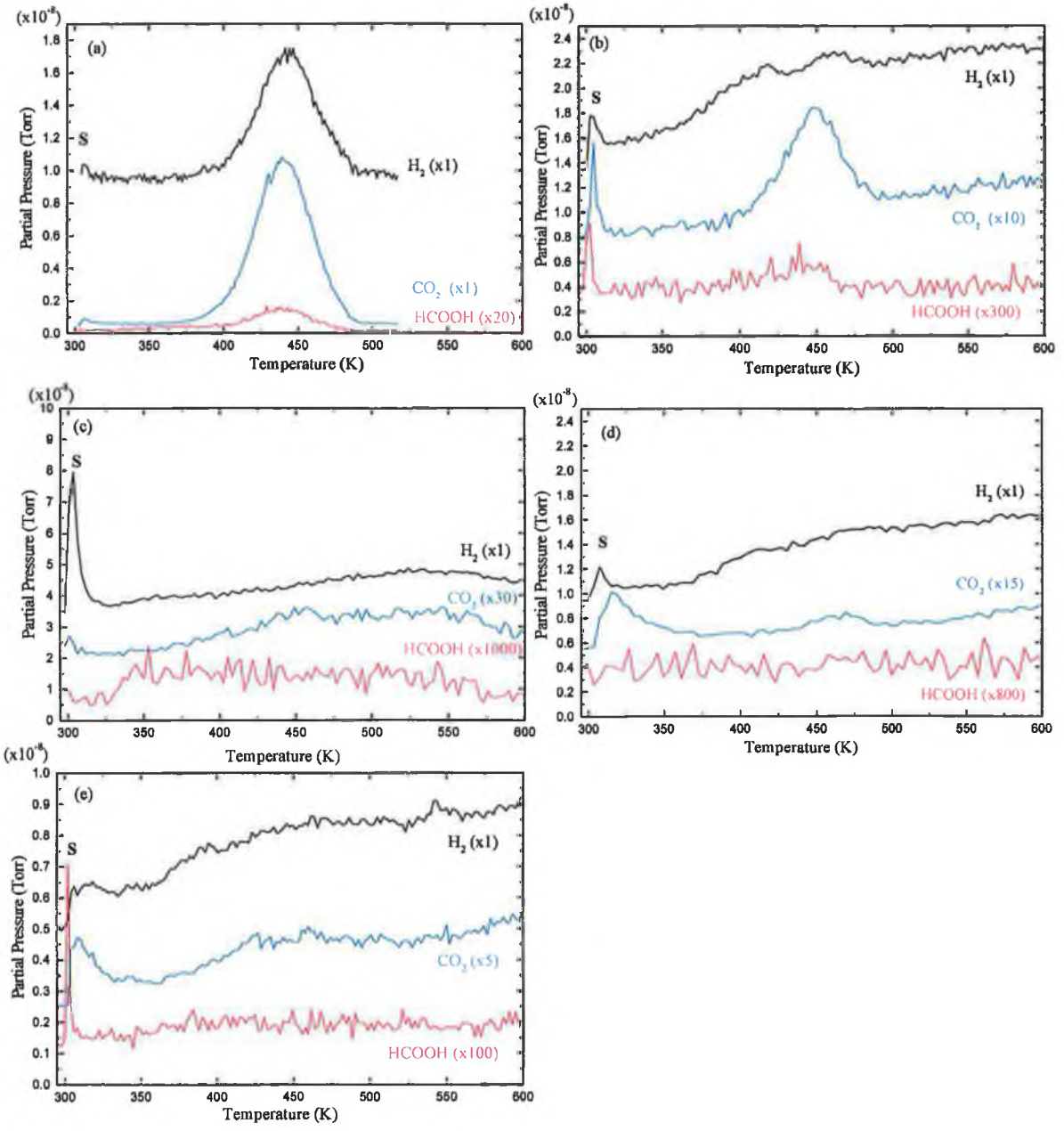

Figure 4.36 *Formic Acid TPD of (a) clean Cu{100} and Sn/Cu{100} submonolayer phases (b) I, (c) II, (d) III and (e) IV.*

4.7 Discussion

The double scattering LEED simulations in Section 4.5 have led to the proposal of several models based on an antiphase domain p(2×2) structure for phase I which are consistent with both the Sn surface coverage and the observed complex split beam LEED pattern. Explanation of phases II and III in terms of c(2×2) structures containing local density modulations (phase II) and substrate reconstruction (phase III) have been demonstrated. The double scattering simulations for these models are in better agreement with the observed LEED patterns than the original structures suggested by Argile and Rhead [Argile 1982]. The overlayer structure reported for Phase IV was accepted as a plausible model for the monolayer coverage based on non-symmetric positioning of Sn atoms in a c(4×4) periodicity.

The double scattering simulations generated similar LEED patterns for models based on the surface alloy and overlayer structures. The ratio of simulated fractional order peak intensities was calculated for each phase. These ratios could be compared to experimental intensity ratios for an energy range from 100-200eV. For phases I and II, the double scattering simulation results could not distinguish between the surface alloy and the overlayer model. The comparison of results for phase III indicated that best agreement with experimental observations were achieved for a surface alloy model. This surface alloy model was simulated with the Sn atoms 10% displaced from the lattice coordinate sites. Argile and Rhead's [Argile 1982] overlayer model gave the best agreement for phase IV. The TPD results in Section 4.6 indicate that the tin does not form a subsurface alloy, but it is unable to differentiate between overlayer and surface alloy models.

LEED I-V spectra were collected for beams common to all phases, including the p(1×1) beams and fractional order beams in c(2×2) positions (other than phase I where these beams are split into quartets centred on the c(2×2) positions). Figure 4.37 (a) illustrates the symmetry averaged (1,0) beam at normal incidence from clean Cu{100} and for phases I to IV. Adsorption of Sn leads to very significant changes in the I-V spectrum of the (1,0) beam for phases II, III and IV. The I-V spectra of the (½,½) beams for phases I to IV illustrated in Figure 4.37 (b) differ strongly, suggesting that the surface geometric structure surrounding Sn adsorbates is significantly different for all four phases.

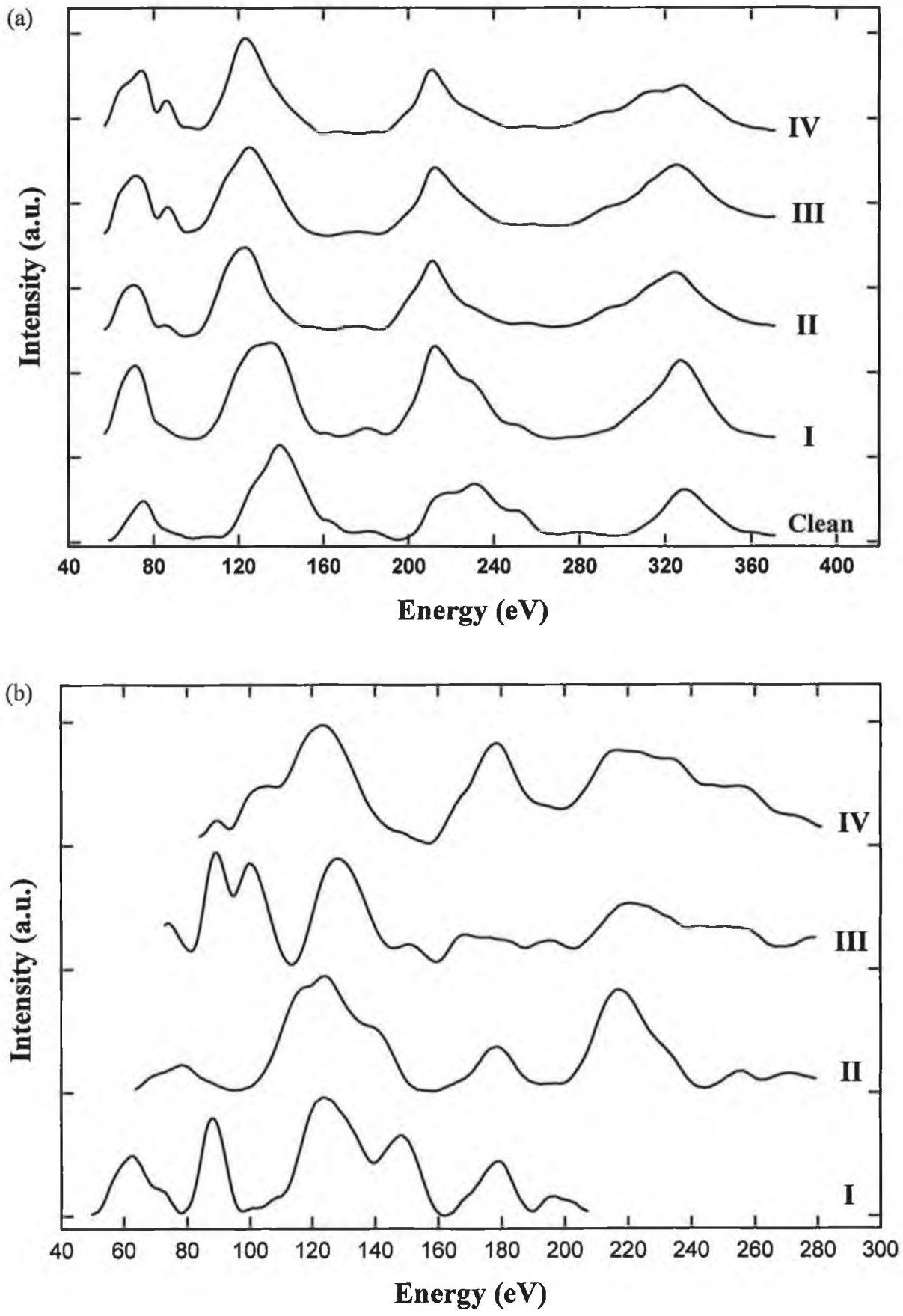

Figure 4.37 *Symmetry averaged normal incidence LEED I-V spectra for clean Cu{100} and Sn phases I to IV: (a) (1,0) beams; (b) (1/2,1/2) beams.*

A number of I-V analyses of simple ordered c(2×2) metallic overlayers on Cu{100} in which the adsorbate leads to a small perturbation of the Cu{100} selvedge structure are available in literature. Perhaps the most relevant is a recent study of the structure of a simple c(2×2)-Na overlayer on Cu{100} in which Na atoms sit in four-fold hollow sites of an essentially structurally unmodified Cu{100} substrate [Mikkelsen 1999]. Sodium has a larger 12-fold coordinate metallic radius than tin (1.91 Å (Na) versus 1.62 Å (Sn)) which both differ substantially from that of copper (1.275 Å). Thus, if both adsorbates adopted a simple overlayer structure without significant modification of the substrate structure, a similar level of modification of the spectral structure of integral order beams may be expected. However, the Sn phases II, III and IV have integral order I-V spectra modified to a greater degree than was the case for Na, including substantial shifts of Bragg peaks. This suggests that adsorption of Sn may lead to a reconstructive modification of the copper surface structure.

This hypothesis is further enhanced by noting that both Argile and Rhead and Abel *et al.* [Abel 1990] observed that Sn adsorption at a substrate temperature below 200K inhibited formation of phases I-IV and instead only a diffuse p(1×1) was observed. The LEED patterns for the ordered phases only became apparent upon warming to between 250 and 350K. Surface diffusion coefficients for metal adatoms on Cu{100} are sufficient even at 200K to allow the formation of an ordered overlayer and to permit local displacive substrate reconstruction. If the Sn/Cu{100} formed overlayer structures at sub-monolayer coverages, then an ordered LEED pattern would be observed, even at 200K. Since no ordered pattern is observed for low temperature growth, Abel *et al.* concluded that the Sn/Cu{100} system forms surface alloy structures.

The results for the Sn/Cu{100} are comparable to a study of Pb/Cu{100} with a c(4×4) surface alloy structure in the medium temperature, low coverage region, which de-alloys to form Pb adsorbed in hollow site c(2×2) domain-wall phases for the low-temperature, high-coverage region. Splitting of the half order spots has been explained by the presence of c(2×2) "heavy" domain boundaries [Bocquet 1998].

For the adsorption of Bi on room temperature Cu{100} a surface alloy forms at 0.35ML which dealloys at coverages between 0.43-0.49 ML to form a c(2×2) four-fold hollow site structure at 0.5ML. At a coverage of 0.6ML Bi/Cu{100}, a p(10×10)

overlayer structure was observed and was interpreted by domain boundaries from a two-dimensional dislocation array meeting in a "pinwheel" arrangement [Meyerheim 1998].

The related Sn/Cu{111} system forms a surface alloy upon deposition of 0.33ML of Sn as demonstrated by alkali ion scattering spectroscopy [Overbury 1992]. The p($\sqrt{3}\times\sqrt{3}$)R30° structure has Sn atoms rippled outwards by approximately 0.4Å with respect to the outermost copper plane. No quantitative information is available to date on changes in the outermost interlayer spacings induced by incorporation of Sn or possible Sn induced buckling in sub-surface layers. The large rippling combined with Sn-induced changes in equilibrium copper positions of substrate atoms in the top two layers would naturally explain the extensive change in integral order LEED spectra including the significant energy shifts of Bragg peaks observed here for the Cu{100}/Sn system. Segregation experiments of Cu{111} doped with 0-0.05% tin found that the maximum surface concentration is 33% and corresponds to a p($\sqrt{3}\times\sqrt{3}$)R30° ordered structure [Erlewein 1977].

Abel *et al.* report a p(1×1) LEED pattern for the adsorption of 0.33ML of Sn on Cu{100} at 170K, while a p(2×2) LEED pattern appears upon warming to 250K [Abel 1990]. The origin of the formation of the split p(2×2) upon deposition at 300K and an unsplit p(2×2) by adsorption at low temperature followed by controlled annealing is unknown at present. In the case of tin deposition of approximately 0.6ML and annealing to around 400K, a p($3\sqrt{2}\times\sqrt{2}$)R45° rotated domain structure (phase III) is observed. Most interestingly, submonolayer Sn deposition was found to lead to an increase in the Cu RBS surface peak. This result would not be expected from simple overlayer growth and the authors suggest that Cu atoms are displaced from their regular lattice sites and that each Sn atom displaces one copper substrate atom. Segregation studies on the Cu{100} doped with 0-0.05% tin found that the maximum surface concentration is 25% and corresponds to a ordered p(2×2) surface alloy structure [Erlewein 1977] [DuPlessis 1996].

These experimental studies show that when thin (<1ML) tin films are evaporated onto copper substrate, followed by annealing, the tin atoms are incorporated into the copper substrate instead of forming an overlayer. This is expected due to the solubility of Sn in Cu.

Recent Modified Embedded Atom Method (MEAM) potential calculations [Aguilar 2000], report that for both Sn/Cu{100} and Sn/Cu{111}, the energetics of the Sn atoms on the surface with Sn atoms incorporated into the surface layer demonstrates that the formation of an ordered surface alloy layer is favoured at submonolayer coverages for both surfaces of copper. The energy difference between placing a single Sn atom on the {100} or {111} surface of Cu or incorporating it into the surface layer substitutionally with a Cu atom, which is the exchanged with the Sn atom and placed on the surface, was evaluated. The MEAM calculations show that the incorporation of Sn into the surface layer is favoured by 0.546eV for the Cu{100} surface and by 0.424eV for the Cu{111} surface. The segregation energies for each system were also calculated indicating that that it is energetically favourable for the tin to segregate from the SnCu bulk crystal to the surface layer for both the {100} and {111} surfaces.

The MEAM calculations [Aguilar 2000] showed that the ordered p(2×2) at 0.25ML for Sn/Cu{100} and the p(3√2×√2)R45° for Sn/Cu{111}are obtained either via deposition of Sn on Cu or by migration of Sn to the surface from a bulk CuSn alloy. These calculations are in agreement with previous evaporation and segregation experiments [Abel 1990] [Overbury 1992] [Erlewein 1977] [DuPlessis 1996].

MEAM calculations, for temperatures from 170K to 600K and deposition of 0.25ML of Sn on Cu{100}, predict the formation of a 2D alloy with a p(2×2) structure. The positions of the Cu atoms within the overlayer are modified from the lattice coordinate sites to accommodate the strain caused by the larger tin atoms. As in the Sn/Cu{111} surface, the Sn atoms are rippled 0.65-0.68Å above the Cu at 100K, with the rippling decreasing as the system is heated from 300-600K. The copper atoms suffer a rearrangement resulting in an octagonal geometry around the Sn atoms.

It is tempting to conclude that Sn/Cu{100} at 0.25 ML monolayers is a surface alloy structure. The I-V spectra of the (½,½) beams for phases I to IV differ strongly, suggesting that the surface geometric structure surrounding Sn adsorbates is significantly different for all four phases. In the case of phase I, the c(2×2) beams shown correspond to the integrated intensity of the four split beams. Phase I is simulated with antiphase domain walls forming as a result of the strain induced at 0.2ML of tin coverage. Phases II and III are proposed as surface alloys based on c(2×2) structures, that have been reported for many bimetallic systems. It should be noted that

the similarity of the (1,0) beam I-V spectra for phase III and IV would not be supportive of a major structural change such as a de-alloying transition to form an overlayer structure for phase IV as per Argile and Rhead. No conclusion is made to when or if dealloying takes place or to what sites the Cu diffuses to after the incorporation of Sn. Clear distinct LEED patterns and TPD studies suggest that pure copper islands form a very small percentage of the surface. In addition, no effect of a large density of step edges to where the Cu migrate to on the surface is observed, in the form of streaks or disorder in the LEED pattern.

Much time has been spent measuring the I-V spectra for the clean Cu and for phases I-IV of the Sn/Cu{100} system as shown in Section 4.5. At least four integral order beams were measured at normal incidence and 10° off normal incidence for each stage. A total of 39 different fractional order beams with a total energy range of about 6000eV were recorded at normal incidence and 10° off normal incidence. This data has been prepared for full dynamical LEED I-V analysis, which has commenced for phase III of the Sn/Cu{100}system, in collaboration with M. Lindroos, Tempere University, Finland.

Further quantitative structural work both by LEED I-V analysis and STM will validate the proposed models and will differentiate between surface alloy and overlayer structures.

Chapter Four References

Abel F., Cohen C., Davies, J.A., Moulin D. and Schmaus D., Appl. Surf. Sci. 44 (1990) 17, Thin film growth of Sn on Cu(100).

Abtew M. and Selvaduray G., Mater. Sci. Eng. 27 (2000) Lead-fee solders in microelectronics.

Aguilar J. F., Ravelo R. and Baskes M.I., Modelling Simul. Mater. Sci. Eng. 8 (2000) 335, Morphology and dynamics of 2D Sn-Cu alloys on (100) and (111) Cu surfaces.

Alcock, N. W., Bonding and structure: structural principles in inorganic and organic chemistry, New York, Ellis Horwood, (1990).

Alkamede P.F.A., Turkenburg W.C. and Van der Weg W.F., Nucl. Instrum. Meth. B 15 (1986) 126, Initial growth of Nickel on Copper (100) studied by Ion-scattering.

Argile C. and Rhead G.E., Surf. Sci. 78 (1978a) 115, Preparation and properties of binary metal monolayers I. Pb and Bi on Cu(100).

Argile C. and Rhead G.E., Surf. Sci. 78 (1978b) 125, Preparation and properties of binary metal monolayers II. Pb and Sn on Al(100).

Argile C. and Rhead G.E., Thin Solid Films 87 (1982) 265, Growth of metal monolayers and ultrathin films on copper: simple and bimetallic layers of lead and tin.

Argile C. and Rhead G.E., Surf. Sci. 135 (1983) 18, Surface alloy formation in ultrathin layers and bimettallic double monolayers: Tin and lead on Cu(100) and Cu(111).

Argile C. and Rhead G.E., Surf. Sci. Rep. 10 (1989) 277, Adsorbed layer and thin film growth modes monitored by Auger electron spectroscopy.

Aruga T., Tochihara H. and Murata Y., Phys. Rev. Lett. 52 (1984) 1794, Rotational Epitaxy of chemisorbed K monolayers on Cu(001).

Bardi U., Rep. Prog. Phys. 57 (1994) 939, The atomic structure of alloy surfaces and surface alloys.

Barnes C.J., Alshamaileh E., Pitkanen T. and Lindroos, Early Stages of surface alloy formation: a diffusion LEED I(V) study *(to be published) (2000).*

Bauer E. and Van der Merwe J.H., Phys. Rev. B 33 (1986) 3658, Structure and growth of crystalline superlattices: From monolayer to superlattice.

Biberian J.P. and Huber M., Surf. Sci. 55 (1976) 259, A model of structures of monolayers adsorbed on (100) faces of metals.

Blum B., Plummer E.W., Davies H.L. and Zehner D.M., J. Vac. Sci. Technol. A9 (1991) 1703, Bismuth induced structures on copper (100).

Bocquet F., Robert S., Gauthier, Duvault J.L. and Klein J., Surf. Sci. 392 (1997) 86, On the low-temperature growth of Pb on Cu(100).

Bocquet F. and Gauthier S., Surf. Sci. 416 (1998) 1, A study of the low temperature submonolayer deposition of Pb on Cu(100).

Bowker M. and Madix R.J., Surf. Sci. 102 (1981) 542, XPS, UPS and thermal desorption studies of the reactions of formaldehyde and formic acid with the Cu(110) surface.

Bowker M., Rowbotham E., Leibsle F.M. and Haq S., Surf. Sci. 349 (1996) 97, The adsorption and decomposition of formic acid on Cu{110}.

Breeman M. and Boerma D.O., Phys. Rev. B 46 (1992) 1703, Sites, mobilities and cluster formation of In atoms on a stepped Cu(100) surface.

Breeman M., Barkema G.T. and Boerma D.O., Phys. Rev. B 49 (1994) 4871, One-dimensional ordering of In atoms in a Cu(100) surface.

Brown D., Noakes T.C.Q., Woodruff D.P., Bailey P. and Le Goaziou Y., J. Phys.: Condens. Matter 11 (1999) 1889, Structure determination of the Cu(100)c(2×2)-Mn and Cu(100)c(2×2)-Au surface alloy phases by medium-energy ion scattering.

Campbell C.T., Annu. Phys. Chem. 41 (1990) 775, Bimetallic surface chemistry.

Casarin M., Granozzi G., Sambi M. and Tondello E., Surf. Sci. 307 (1994) 95, A LCAO-LDF study of formate chemisorption on Cu(100).

Chambliss D.D. and Chiang S., Surf. Sci. Lett. 264 (1992) L187, Surface alloy formation studied by scanning tunneling microscopy: Cu(100) + Au-c(2×2).

Clevenger L.A., Arcot B., Ziegler W., Colgan E.G., Hong Q.Z., d'Heurle F.M., Cabral Jr. C., Gallo T.A. and Harper J.M.E., J. Appl. Phys. 83 (1998) 90, Interdiffusion and phase formation in Cu (Sn) alloy films.

Davis H.L. and Noonan J.R., J. Vac. Sci. Technol. 20 (1982) 842, Cu(100) multilayer relaxation.

Delamare F. and Rhead G.E., Surf. Sci. 35 (1973) 172, First stages of the deposition of bismuth on copper examined by LEED.

DeBeauvais C., Rouxel D., Michailov M. and Mutaftschiev B., Surf. Sci. 324 (1995) 1, Two-dimensional overgrowth in the low submonolayer range: the case of c(2×2)-Pb/Cu(110).

Diehl R.D. and McGrath R., Surf. Sci. Rep. 23 (1996) 43, Structural studies of alkali metal adsorption and coadsorption on metal surfaces.

Diehl R.D. and McGrath R., J. Phys.: Condens. Matter 9 (1997) 951, Current progress in understanding alkali metal adsorption on metal surfaces.

Dubois, L.H., Ellis, T.H. and Kevan S.D., J. Electron Spectrosc. 39 (1986) 27, Direct real-time measurement of adsorption and desorption kinetics on Cu(100).

Du Pleiss J. and Viljoen E.C., Appl. Sur. Sci. 100/101 (1996) 222, Sn segration to low index surfaces of a copper single crystal.

Dyson B.F., Anthony T.R. and Turnbull D., J. Appl. Phys. 38 (1967) 3408, Interstitial Diffusion of copper in Tin.

Erlewein J. and Hofmann S., Surf. Sci. 68 (1977) 71, Segregation of Tin on (111) and (100) surfaces of Copper.

Estrup P.J. and McGrae E.G., Surf. Sci 25 (1971) 1, Surface studies by electron diffraction.

Fowler D.E. and Barth J.V., Phys. Rev. B 52 (1995) 2117, Structure and dynamics of the Cu(001) surface investigated by medium-energy ion scattering.

Fujinaga Y., Surf. Sci. 86 (1979) 581, Surface Structures of Cu-Au and Cu-Pd alloys as observed by LEED.

Gauthier Y., Moritz W. and Hosler W., Surf. Sci. 345 (1996) 53, Surface alloy in the c(4×4) phase of Pb on Cu(100).

Gilarowski G. and Niehus H., Phys. Stat. Sol. (a) 173 (1999) 159, Iridium on Cu(100): Surface Segregation and Alloying.

Graham G.W., Surf. Sci. 184 (1987) 137, An investigation of "Cu(100)-c(2×2)Au": LEED, AES, ISS, ARUPS and XPS results.

Graham G.W., Schmitz P.J. and Thiel P.A., Phys. Rev. B 41 (1990) 3353, Growth of Rh, Pd and Pt films on Cu(100).

Hansen J.C., Benson J.A., Clendening W.D., McEllistrem M.T. and Tobin J.G., Phys. Rev. B 36 (1987) 6186, Temperature-dependent surface morphology of Au/Cu(001).

Hansen M., Constitution of Binary Alloys, McGraw-Hill, New York 1958.

Hayoz J., Naumovic D., Fasel R., Aebi P. and Schlapbach L., Surf. Sci. 373 (1997) 153, Growth of Ag on Cu(001) studied by full-hemispherical X-ray photoelectron diffraction.

Heinz K., Muller S. and Hammer L., J. Phys.:Condens. Matter 11 (1999) 9437. Crystallography of ultrathin iron, cobalt and nickel films grown epitaxially on copper.

Henrion J. and Rhead G.E., Surf. Sci. 29 (1972) 20, LEED Studies of the first stages of deposition and melting lead on low index faces of copper.

Hosler W. and Moritz W., Surf. Sci. 117 (1982) 196, LEED studies of lead on copper (100).

Hosler W., Moritz W., Tamura E. and Feder R., Surf. Sci. 171 (1986) 55, Influence of the scattering potential model on low energy diffraction from Cu(001)-c(2×2)-Pb.

Huang J.S., Zhang J., Cuevas A. and Tu K.N., Mater. Chem. Phys. 49 (1997) 33, Recrystallization and grain growth in bulk Cu and Cu(Sn) alloy.

Jiang Q.T., Fenter P. and Gustafsson T., Phys. Rev. B 44 (1991) 5773, Geometric structure and surface vibrations of Cu(001) determined by medium-energy ion scattering.

Johnson P.D., Woodruff D.P., Farrell H.H., Smith N.V. and Traum M.M., Surf. Sci. 129 (1983) 366, Photoelectron diffraction from Te on Ni(100) and Cu(100).

Jona F., Ref. Prog. Phys. 45 (1982) 527, Low-energy electron diffraction for surface structure analysis.

Jona F., Surf. Sci. 192 (1987a) 398, Results of an international LEED Intensity project I. Reproducibilty of experimental spectra.

Jona F., Jiang P. and Marcus P.M., Surf. Sci. 192 (1987b) 414, Results of an international LEED Intensity project II. Evaluation of structural parameters.

Kim S.H., Lee K.S., Min H.G., Seo J., Hong S.C., Rho T.H. and Kim J.S., Phys. Rev. B 55 (1997) 7904, Subsurface growth of Ni atoms deposited on a Cu(001) surface.

Ku Yi-Sha and Overbury S.H., Surf. Sci. 273 (1992) 341, Surface structure analysis of Sn on Ni(111) by low energy alkali ion scattering .

Lee K.L., Hu C.K. and Tu K.N., J. Appl. Phys. 78 (1995) 4428, In situ scanning electron microscope comparison studies on electromigration of Cu and Cu(Sn) alloys for advanced chip interconnects.

Li W. and Vidali G., Phys. Rev. B 46 (1992) 4356, Corrugation enhancement of Cu(001) induced by low coverage Pb and Bi adsorption.

Li Y.D., Jiang L.Q. and Keol B.E., Phys. Rev. B 49 (1994) 2813, Surface alloy formation and the structure of c(2×2)-Sn/Ni(100) determined by low-energy alkali-ion scattering.

Lind D.M., Dunning F.B., Walters G.K. and Davis H.L., Phys. Rev. B 35 (1987) 9037, Surface-structural analysis by use of spin-polarized low-energy electron diffraction: An investigation of the Cu(100) surface.

Lloyd J.R., J. Phys. D: Appl. Phys. 32 (1999) R109, Electromigration in integration circuit conductors.

Lu S.H., Wang Z.Q., Wu S.C., Lok C.K.C., Quinn J., Li Y.S., Tian D., Jona F. and Marcus P.M., Phys. Rev. B 37 (1988) 4296, Structural and electronic properties of a surface alloy of Pd and Cu on Cu{001}.

Mehandru S.P. and Anderson A.B., Surf.Sci. 219 (1989) 68, Formate adsorption and azimuthal orientation on Cu(100) from molecular orbital theory.

Meyerheim H.L., Zajonz H., Moritz W. and Robinson I.K., Surf. Sci. 381 (1997) L551, Surface alloying and dealloying in Bi/Cu(001) at low coverage.

Meyerheim H.L., De Santis M., Moritz W. and Robinson I.K., Surf. Sci. 418 (1998) 295, Domain-wall interactions in Bi/Cu(001).

Mikkelsen A. and Adams D.L., Phys. Rev. B 60 (1999) 2040, Surface structure of Cu(100)-c(2×2)-Na: A LEED analysis.

Mizuno S., Tochihara H. and Kawamura T., Surf. Sci. 293 (1993) 239, Determination of the c(2×2) structure formed on Cu(001) upon Li adsorption: a low-energy electron diffraction analysis.

Muller S., Kinne A., Kottcke M., Metzler R., Bayer P., Hammer L. and Heinz K., Phys. Rev. Lett. 75 (1995) 2859, In-plane lattice reconstruction of Cu(100).

Murarka S.P. and Hymes S.W., Critical reviews in Solid State and Materials Sciences 20 (1995) 87, Copper metalliztion for ULSI and beyond.

Murray P.W., Stensgaard I., Laegsgaard E. and Besenbacher F., Surf. Sci. 365 (1996) 591, Growth and structure of Pd alloys on Cu (100).

Nagl C., Haller O., Platzgummer E., Schmid M. and Varga P., Surf. Sci. 321 (1994) 237, Submonolayer growth of Pb on Cu(111): surface alloying and de-alloying.

Nagl C., Platzgummer E., Haller O., Schmid M. and Varga P., Surf. Sci. 331-333 (1995) 831, Surface alloying and superstructures of Pb on Cu(100).

Naumovic D., Stuck A., Greber T., Osterwalder J. and Schlapbach L., Surf. Sci. 269/270 (1992) 719, Submonolayer films of Au on Cu(001) studied by photoelectron diffraction.

Noonan J.R. and Davis H.L., J. Vac. Sci. Technol. 17 (1980) 194, 1979 LEED analysis of Cu(100).

Oda O. and Rhead G.E., Surf. Sci. 92 (1980) 467, Adsorption and coadsorption on Ni(100); Quantitative applications of Auger electron spectroscopy to the elements C, P, Pb, Sn.

Overbury S.H. and Ku Y.-S., Phys. Rev. B 46 (1992) 7868, Formation of stable, two-dimensional alloy-surface phases: Sn on Cu(111), Ni(111) and Pt(111).

O'Connor D.J., Yao J. and Shen Y.G., Materials Science Forum 248-249 (1997) 95 Special Surface Structures in Surface Alloy Growth.

Paffett M.T., Logan A.D., Simonson R.J. and Keol B.E., Surf. Sci. 250 (1991) 123, A multitechnique surface science examination of Sn deposition of Pt(100)

Palmberg P.W. and Rhodin T.N., J. Chem. Phys. 49 (1968a) 134, Atomic arrangement of Au(100) and related metal overlayer surface structures. I

Palmberg P.W. and Rhodin T.N., J. Chem. Phys. 49 (1968b) 147, Analysis of Low-Energy Electron-Diffraction patterns from simple overlayer surface structures. II

Panagiotides N., Batchelor D.R. and King D.A., Chem. Phys. Lett. 177 (1991) 419, Simulation of LEED patterns from complex surface structures.

Pendry, J.B., Low Energy Electron Diffraction, Academic Press Inc. (1974).

Pope T.D., Vos M., Tang H.T., Griffiths K., Mitchell I.V., Norton P.R., Liu W., Li Y.S., Mitchell K.A.R., Tian Z.-J. and Black J.E., Surf. Sci. 337 (1995) 79, A structural study of Pd/Cu(100) surface alloys.

Redhead P.A., Vacuum 12 (1962) 203, Thermal desorption of gases.

Reilly J.P., O'Connell D. and Barnes C.J., J. Phys.:Condens. Matter 11 (1999) 8417, Modification of formate stability by alloying: the Cu(100)-c(2×2)-Pt system.

Rhead G.E., Barthes M.-G and Argile C., Thin Solid Films 82 (1981a) 201, Determination of growth modes of ultrathin films from Auger Electron Spectroscopy: An assessment and commentary.

Rhead G.E., Argile C and Barthes M.-G., Surf. Interface Anal. 3 (1981b) 165, Quantitative Auger Electron Spectroscopy of metal monolayers on metals: Evidence for adsorbate/substrate interface effects.

Robert S., Gauthier S., Bocquet F., Duvault J.L. and Klein J., Surf. Sci. 350 (1996) 136, An STM study of the adsorption of Pb on Cu(100): formation of an ordered surface alloy.

Rodriguez J.A., Surf. Sci. Reports 24 (1996) 223, Physical and chemical properties of bimetallic surfaces.

Sasaki T., Tero R., Sueyoshi T. and Iwasawa Y., Surf. Sci. 427-428 (1999) 408, CO-induced destruction of Cu(100)-(2×1)Li studied by HREELS.

Seah M.P. and Dench W.A., Surf. Interface Anal. 1 (1979) 2, Quantative Electron Spectroscopy of surfaces: A standard data base for electron inelastic mean free paths in solids.

Sepulveda A. and Rhead G.E., Surf. Sci. 66 (1977) 436, Auger Electron Spectroscopy of adsorbed metal monolayers: Lead on low-index and stepped copper surfaces.

Sexton B.A., Surf. Sci. 88 (1979) 319, Observation of formate species on a copper (100) surface by high resolution electron energy loss spectroscopy.

Shen Y.G., Yao J., O'Connor D.J., King B.V. and MacDonald R.J., J. Phys.: Condens Matter 8 (1996) 4903, Au-segregated dealloying and Pd-induced clock reconstructing of Cu(001).

Somorjai G.A., Introduction to Surface Chemistry and Catalysis, John Wiley and Sons, Inc., (1994).

Somorjai G.A., Chem. Rev. 96 (1996) 1223, Modern surface science and surface technologies: an introduction.

Sotiropoulus A., Milligan P.K., Cowie B.C.C and Kadodwala M., Surf. Sci. 444 (2000) 52, A structural study of formate on Cu(111).

Tan S., Ghazali A. and Levy J.C.S., Surf. Sci. 392 (1997) 163, Pb/Cu (100) surface superstructures: Monte Carlo and molecular dynamics simulations.

Tersofff J., Phys. Rev. Lett. 74 (1995) 434, Surface-Confined Alloy Formation in Immiscible Systems.

Tobin J.G., Robey S.W. and Shirley D.A., Phys. Rev. B 33 (1986) 2270, Two-dimensional valence-electronic structure of a monolayer of Ag on Cu(001).

Tobin J.G., Hansen J.C. and Wagner M.K., J. Vac. Sci. Technol. A8 (1990) 2494, Probing bimetallic surfaces with photoelectron diffraction: Au/Cu(001) and Fe/Cu(001).

Tu K.N., Materials Chemistry and Physics 46 (1996) 217, Cu/Sn interfacial reactions: thin-film case versus bulk case.

Van Hove, M.A., Weinberg, W.H and Chan, C.-M., Low-Energy Electron Diffraction, Springer Verlag Berlin Heidelberg (1986).

Van Hove M., (1995), Software packages SARCH/LATUSE/PLOT3D Version 4.01, http://electron.lbl.gov/webmain.html.

Venables J.A., Surf. Sci. 299/300 (1994) 798, Atomic processes in crystal growth.

Wander A. and Holland B.W., Surf. Sci. 199 (1988) L403, The structure of formate on Cu(100).

Wang Z.Q., Li Y.S., Lok C.K.C., Quinn J., Jona F. and Marcus P.M., Solid State Comm. 62 (1987) 181, Atomic and electronic structure of a surface alloy – comparison with the bulk alloy.

Wang Z.Q., Lok C.K.C., Quinn J., Li Y.S., and Jona F., J. Phys. C: Solid State Phys 21 (1988) 653, Electronic structure of a surface alloy: Cu{001}c(2×2)-Au.

Woodruff D.P., McConville C.F. and Kilcoyne A.L.D., Surf. Sci. 201 (1988) 228, The structure of the formate species on copper surfaces: new photoelectron diffraction results and SEXAFS data reassessed.

Wuttig M., Knight C.C., Flores T. and Gauthier Y., Surf. Sci. 292 (1993) 89, LEED structure determination of two ordered surface alloys: Cu(100)-c(2×2)Mn and Ni(100)-c(2×2)Mn.

Yao J., Shen Y.G., O'Connor D.J. and King B.V., J. Vac. Sci. Technol. A13 (1995) 1443, Initial growth of ultrathin Pd films on Cu(001).

Chapter Five

Germanium on GaAs(001)

This chapter presents structural information about the initial formation of the Ge/GaAs(001) interface. A review of earlier experimental and theoretical studies of Ge and other adsorbates on GaAs(001) is presented in Section 5.2. In situ sample preparation of the clean (001) surface of GaAs is described in Section 5.3. The evaporation of germanium and the details of the source calibration are discussed in Section 5.4. After a submonolayer deposition of Ge onto the GaAs(001)-(2×4) As-rich surface and annealing to 875K a sharp (1×2) LEED pattern is observed, which is attributed to Ge-Ga dimerization along the [110] direction. After outdiffusion of the first layer arsenic atoms, the germanium dimerizes with the second layer gallium atoms. The location of Ge atoms on the (1×2) reconstructed Ge/GaAs(001) surface has been determined using normal-incidence X-ray standing waves (NIXSW). The $(1\bar{1}1)$, $(11\bar{1})$, $(0\bar{2}2)$ *and* $(0\bar{2}\bar{2})$ *Bragg reflection planes are used for triangulation. These results are discussed in Section 5.5. Core level photoemission results are presented in Section 5.6 for the (1×2) phase at submonolayer coverages of germanium and the (1×2)+(2×1) double domain reconstruction which occurs at a germanium thickness of several monolayers.*

5.1 Introduction

The III-V semiconductors are not typically found in nature, but rather are produced for technological reasons based upon their desirable electronic properties relative to those of the elemental semiconductors, for example silicon. III-V semiconductors have a direct bandgap that is useful for optoelectronic applications such as solid-state lasers and possess enhanced electron transport properties relative to silicon. The surfaces of the compound semiconductors introduce a new degree of freedom that must be considered in the principles of surface reconstructions. A compound semiconductor is formed by two distinct chemical species; a cation (e.g. Ga, In, Zn, Cd) and an anion (e.g. As, Sb, Se, Te) and the possibility of charge transfer between them. In general the dangling-bond orbitals on the cationic species are at a higher energy than the dangling–bonds on the anionic species, so that the charge is transferred from the cation to the anion. In order to obtain a neutral (uncharged) surface, there must be a complete transfer of charge between the cation and anion [Kubby 1996].

Research on gallium arsenide has primarily concentrated on the polar (100) and (111) surfaces and the nonpolar (110) surfaces. In recent years, this work has been extended to studies of higher index planes, in particular the (311) surface [Moriarty 1997]. The GaAs(001) polar surface is the most widely used orientation in the Molecular Beam Epitaxy (MBE) growth of device structures. The structure of the GaAs(001) surface depends on the relative arsenic and gallium concentrations on the surface, as discussed in Section 5.3. Many studies have been completed on the GaAs(110) surface as it corresponds to the cleavage plane of a zincblende crystal. Studies of adsorbates on GaAs range from metals (e.g. Al, In [Spindt 1990]) and semimetals (e.g. Bi, Sb [McGinley 2000]) to semiconductors (e.g. Si [Wassermeier 1995]). The adsorption of adatoms induces the formation of adsorbate-substrate bonds in addition to novel adsorbate-adsorbate structures. The property of the bonding of the adatom on the substrate affects both the structure of the adatoms on the substrate, and the kinetic processes of the overlayer formation [Jing 1994].

Heteroepitaxial films of Ge on GaAs have attracted much attention over the past few years. Germanium is an elemental semiconductor with outstanding physical properties, which give it enormous potential for device applications. Ge has the highest hole mobility-doping product of all the device grade semiconductors. It has a small bandgap of 0.66eV and is nearly lattice matched to GaAs ($\Delta a/a \approx 0.2\%$). Ge has received little attention for integrated circuit applications, despite its superior transport properties to Si, this is primarily due to the lack of a high quality passivating oxide. The advent of MBE and metal organic chemical vapour deposition (MOCVD) crystal growth techniques has led to rapid development of GaAs base technology in recent years. Ge is a material that could significantly improve GaAs based devices [Morkoc 1991]. A Ge based heterojunction bipolar transistor (HBT) is expected to have superior performance compared to AlGaAs-GaAs HBTs. The high hole mobility of Ge offers the possibility of improved p-channel field effect transistors (FETs), while the narrow bandgap of Ge makes it a candidate for GaAs based phototransistors, quantum confinement structures or resonant tunnelling devices with GaAs barriers [Strite 1990a,b]. Ge exhibits strong absorption in the 1.0-1.5 μm wavelength range, which makes it a promising material for the waveguides of electro-optic integrated circuits in GaAs based devices utilising mid-infrared, which includes the important 3-10 μm wavelength region. Pure Ge is transparent at these wavelengths, since it has a relatively large index of refraction, n = 4.0, enabling it to confine light via total internal reflection [Salazar-Hernandez 1999].

The Ge films grown on GaAs substrates may be used as a universal sensitive material for manufacturing various physical sensors. The possibility of manufacturing photodetectors and temperature, strain and Hall sensors has been reported for the Ge/GaAs system [Mitin 1997]. Another application of the Ge/GaAs heterojunction is for use in solar cells [Sieg 1995]. Several materials have been developed for space-based photovoltaic power applications, including Si, GaAs, InP and some thin film polycrystalline cells but no particular material will be suitable for all space applications. GaAs shows many suitable characteristics, it has a radiation hardness that is intermediate between InP and Si and has a 20-25% higher conversion efficiency compared to Si. A major disadvantage of GaAs is its mechanical fragility. This is the motivation for growing GaAs solar cells on more mechanically sturdy Ge substrates. GaAs and Ge have similar thermal expansion coefficients, and theoretically GaAs/Ge forms a near-ideal tandem solar cell [Sieg 1995].

The Ge/GaAs interface is a good candidate for fundamental studies, in that it grows with a predictable structure, exhibits interesting electrical properties and may serve as a good test case for increasingly refined theories of heterostructure interface formation. A review of the research carried out to date, on the Ge/GaAs(001) interface is presented in the following section.

5.2 Review of Semiconductor Systems

In Section 5.2.1 a brief review of structural investigations of comparative adsorbates on GaAs(001) systems is given. These structures have been mostly studied using XSW and STM techniques. An overview of reported studies for Ge/GaAs(001) is presented in Section 5.2.2.

5.2.1 Review of adsorbates on GaAs(001)

The X-ray standing wave technique is capable of locating the position of particular atomic species at a crystal surface. When the structures of adsorbates on III-V compound semiconductor surfaces are analysed by XSW, the group-III atomic site and the group-V atomic site can be distinguished by using noncentrosymmetric {111} reflections. Therefore, two different NIXSW measurements of the (111) and ($1\bar{1}1$)

reflections are proposed by Suigayama *et al.* [Suigayama 1996] to be suitable for the analysis of adsorbates on the GaAs(001) surface. Their investigations of sulphur, antimony and silicon deposition on GaAs(001) are completed by using only two of the {111} reflections [Suigayama 1994, 1995, 1996]. Sulphur is shown to occupy bridge sites on the Ga-terminated GaAs(001) surface, forming bonds with the underlying Ga atoms [Suigayama 1994]. In the case of submonolayers of Si on GaAs(001), NIXSW was used to determine that Si occupies both Ga and As sites in a ratio of 75% and 25%, respectively [Suigayama 1996]. STM studies on this system revealed that the preferential absorption site for Si is the vacant Ga site in the trench between As dimer rows [Wassermeier 1998]. For coverages greater that 0.4ML, Si forms dimer rows on top of the As layer. RHEED patterns for this system, are shown to continuously change with increasing Si coverage from the initial (2×4) to an asymmetric (3×1) pattern [Levermann 1996].

NIXSW results by Suigayama *et al.* [Suigayama 1995] showed the Sb-terminated GaAs(001)-(2×4) surface to be well ordered and consist of symmetric Sb-Sb dimers along the $[1\bar{1}0]$ direction. By monitoring the (111) and $(1\bar{1}1)$ Bragg reflections, they reported a Sb height of 1.81Å and a dimer bond length of 2.95Å. Recent XSW investigations of the Sb/GaAs(001)-(2×4) surface using (004), (022) and (111) Bragg reflections found the Sb-Sb dimer to have a bond length of 2.84Å and a height of 1.72Å above the bulklike (004) Ga atomic plane [Lee 1998]. Lee and Bedzyk [Lee 1998] concluded that using the (022) and (004) reflections at a more conventional Bragg geometry gave a more direct measure of the dimer height and dimer bond length. This was confirmed by the better agreement of their results with other related measurements [Moriarty 1996a] [Whitman 1999] and theoretical calculations [Schmidt 1997] [Srivastava 1997a].

5.2.2 Review of Ge/GaAs(001)

The early stages of the Ge/GaAs(001) interface have been studied by different surface sensitive techniques and theoretical calculations. Some discrepancies have been reported for the temperature dependence on the outdiffusion of As and the formation of an abrupt or mixed interface. In order to address these differences, a short review of some relevant studies is required.

In theoretical studies of Ge-GaAs polar heterojunctions, the electrostatic energy was shown to be an important factor in determining the interfacial atomic configuration [Harrison 1978]. In the case of Ge/GaAs(001), an abrupt junction would have a large interfacial charge accumulation, which would increase the potential energy of the system enormously. A mixed layer of half Ge and half As, or half Ge and half Ga, however, produces an interface that is uncharged with a dipole layer which shifts the bulk potential by a finite amount [Kunc 1981]. Most reported studies have proposed structures based on the formation of such a mixed interface.

Interdiffusion behaviour at the Ge/GaAs(001) interface has been studied by low energy electron-loss spectroscopy (LEELS) and Auger electron spectroscopy (AES) [Tatsuyama 1988]. These results show that no significant interdiffusion between Ge and GaAs occurs for deposition on the sample held at 600K. When the substrate temperature is warmed to 725K the As and Ga atoms diffuse into the outer Ge layer and further annealing at 800K causes the surface electronic structure to become that of GaAs. Similar results were found using low-energy electron microscopy (LEEM) to investigate the temperature dependence on growth modes [Falta 1994]. These studies showed that at 725K Ge growth proceeds in a layer by layer mode, with nucleation of two-dimensional (2D) islands smaller than 150Å across. An increase of growth temperature to 725-750K was shown to enhance surface diffusion.

Mrstik [Mrstik 1983] reported that deposition of submonolayer coverages of Ge on GaAs(100) held at any temperature between 110Kand 525K, produced a poor quality (1×1) LEED pattern, with a large background intensity. Annealing to 675K produced sharp (1×2) LEED spots with very little background intensity. The same high quality LEED pattern was also produced by evaporating directly onto a clean substrate held at a temperature above 675K during deposition. Mrstik [Mrstik 1983] presented LEED and AES studies of Ge overlayers on the (100) surface of GaAs ranging in thickness from 0.1 to about 10 monolayers. He found that Ge coverages of 0.2ML convert the initial clean surface reconstruction into a single domain (1×2) reconstruction attributed to Ge bonding to surface As. This result was consistent with earlier photoemission studies that demonstrated that the Ge adatoms form bonds only to the As atoms until all the surface As is consumed [Bauer 1983]. As the Ge coverage increases beyond 1ML, the Auger measurements indicate that the As diffuses through the Ge overlayer. The single domain

(1×2) reconstruction was maintained up to an overlayer thickness of 4ML, suggesting that the Ge and the outdiffused As overlayer are growing in terms of atomic planes.

After coverages of 4ML, Mrstik [Mrstik 1983] observed that a second (1×2) domain occurs where the double layer mechanism breaks down, and growth proceeds by single atomic planes. This ordered two-domain (1×2)+(2×1) structure is formed at Ge coverages of about 4ML, independent of the initial As concentration in the starting GaAs(100) surface. These results indicate that the interface is not abrupt, but has a mixed Ge-Ga or Ge-As transition layer. In contrast, the higher coverage phase for MBE growth of germanium on GaAs(100) was determined by Neave *et al.* [Neave 1983] to be a c(2×2) abrupt interface by RHEED, ARPES and TEM experiments.

MEIS studies of the MBE growth of 19ML of Ge on the c(2×8)/(2×4) reconstruction of GaAs(100) revealed that this structure formed a sharp (1×2)+(2×1) reconstruction [Falta 1993a]. The surface layer was shown to contain about 0.29ML of Ga and 0.58ML of As on top of the Ge film. Structural and elemental analysis of the clean c(2×8)/(2×4) reconstruction of GaAs(100) showed that the top layer does not only consist of As atoms, but of both 0.25ML of Ga and 0.5ML of As. The surface coverages are close to the amounts of Ga and As segregating on the surface during Ge growth. Therefore, they concluded that the topmost As layer of the GaAs(100)-c(2×8)/(2×4) is removed during Ge deposition, leaving behind a Ga-terminated surface.

The Ge/GaAs(100) interface was investigated by soft X-ray photoemission, LEED and AES, from which the valence-band discontinuity (ΔE_v) was determined to be 0.47±0.05 eV independent of both the initial clean GaAs(100) surface properties and the evolution of the Fermi level [Katnani 1985a]. Ge was grown under As_4 flux coverages from 0.3ML to 5.7ML on the clean GaAs(100) surface held at a temperature of 600K. The 3d core level photoemission spectra were measured for increasing Ge coverages up to a (1×2)+(2×1) structure at 5.7ML, but no fitting routine was applied to deconvolve the lineshapes. For all different surface reconstructions of clean GaAs(100), a monolayer of segregated As was observed at the surface, independent of the Ge adlayer thickness.

Wang *et al.* [Wang 1993, 1994a, 1994b] carried out Scanning Tunnelling Microscopy (STM) and LEED studies of the initial Ge/GaAs(100) interface formation. They found

that the deposition of 0.5ML of Ge onto a clean As-rich GaAs(100)-(2×4) surface followed by annealing to 700K produced a diffuse (2×1) LEED pattern which was attributed to Ge-As dimers along the $[0\bar{1}1]$ direction. However, the STM studies of this surface showed large disordered regions with only local (2×1) as well as some (1×2) ordering. Upon annealing to 875K, a well-ordered (1×2) LEED pattern was obtained and STM images showed large areas of row-like structures, presumably dimer rows. The authors interpreted these results in terms of mixed Ge-Ga dimers orientated along the [011] direction, formed through the desorption of As. The structural models for clean GaAs(100) and the (2×1) Ge-As and (1×2) Ge-Ga terminated surfaces, presented by Wang *et al.* [Wang 1994a, 1994b] are shown in Figure 5.1. The ideal bulk-terminated GaAs semiconductor surface is shown in Figure 5.1 (a). It is well known that these structures are not stable due to the high density of dangling bonds, and that they reconstruct to lower their surface energy. The atom resolved STM images for the observed clean surface of GaAs(100) showed the (2×4) structure produced consisted of two As dimers and two missing dimers in each unit cell. The proposed structural model consistent with the images for GaAs(100)-(2×4) surface is shown in Figure 5.1 (b). A discussion of other proposed structural models for clean GaAs(100) is given in Section 5.3. The proposed structure for the weak (2×1) reconstruction due to Ge-As dimers along the $[0\bar{1}1]$, is shown in Figure 5.1 (c). These rows usually extend less than 100Å, and the spacing between them is normally 8Å. In addition to the (2×1) superstructure, small regions of the original (2×4) structure were reported. Annealing to above 875K produced a sharp (1×2) LEED pattern and STM images revealed dimer rows along the $[0\bar{1}1]$ direction spaced by 8Å along the [011] direction. These dimers were proposed to consist of Ge-Ga dimers along the [011] direction as shown in Figure 5.1 (d).

Recent Reflection Anisotropy Spectroscopy (RAS) studies by Power *et al.* [Power 1998] and Emiliani *et al.* [Emiliani 1999] have reported similar findings. These two independent studies reported that the GaAs(100) (2×4) surface transforms into the well-ordered (1×2) phase passing through a disordered (2×4) phase after annealing above 830 K. They concluded that the formerly proposed (2×1) phase was not observed. The (2×1) LEED pattern observed by Wang *et al.* [Wang 1994a], was explained as a disordered (2×4) phase, in which the Ge atoms randomly substitute one of the As atoms in the surface dimers [Emiliani 1999].

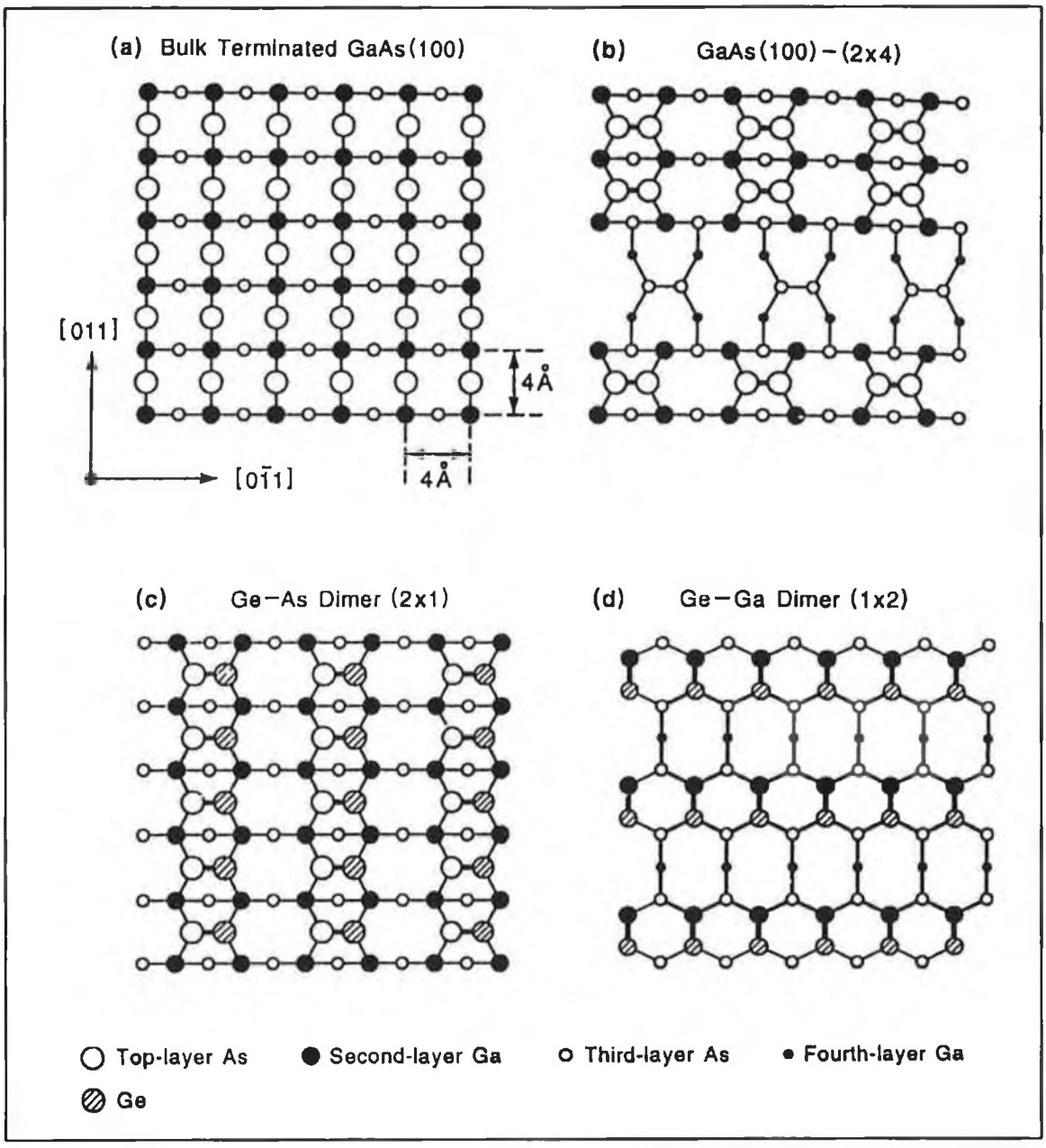

Figure 5.1 *Surface structure models for (a) bulk-truncated GaAs(100) surface with an As-top layer; (b) As-rich (2×4) reconstructed GaAs(100); (c) Ge-As dimerization forming a (2×1) superstructure on GaAs(100); and (d) the (1×2) order formed by Ge-Ga dimerizarion on GaAs(100) [Wang 1994a].*

Theoretical models consistent with Wang *et al. [1993, 1994a, 1994b]* for submonolayer Ge deposition and annealing on GaAs(100) were proposed by Srivastava and Jenkins [Srivastava 1996]. They reported a first principles pseudopotential study of the atomic structure, electronic states and bonding for the GaAs(001)-Ge(2×1) and (1×2) structures. These proposed structural models for the Ge-Ga and Ge-As terminated surfaces are shown in Figure 5.2. For the (2×1) Ge covered structure shown in Figure

5.2 (a), the Ge-As dimer of length 2.35Å was found to be buckled by 0.59Å, with the As atom further above the bulk than the Ge atom. For the (1×2) surface, the Ge-Ga dimer of bond length 2.43 Å is buckled by 0.79Å, with the Ge atoms further above the bulk atoms.

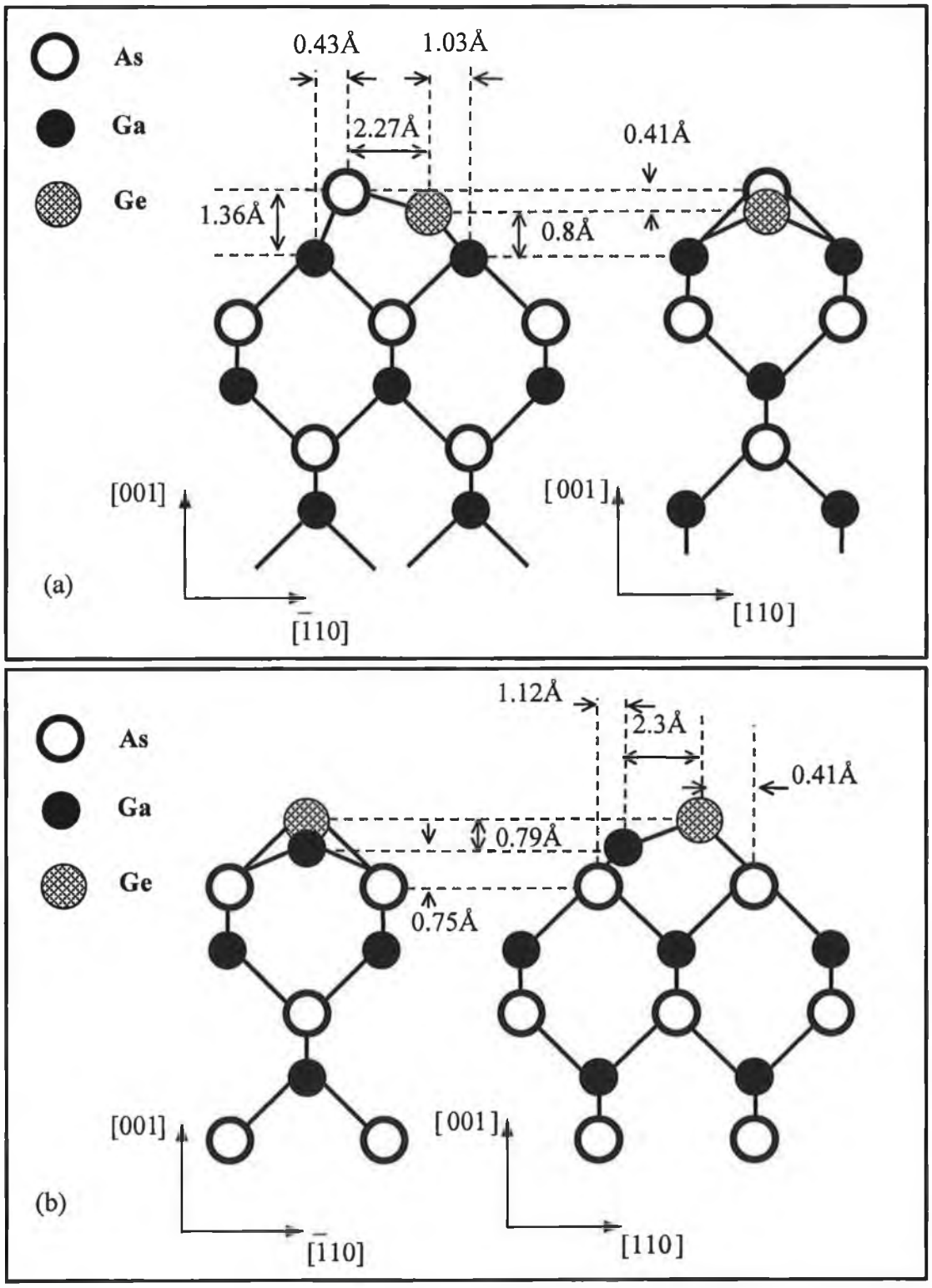

Figure 5.2 *A side view for the atomic geometry for (a) GaAs(100)/Ge(2×1) and (b) GaAs(100)/Ge(1×2) structures [Srivastava 1996].*

Emiliani *et al.* [Emiliani 1999] complemented their RAS investigations with total-energy (TE) minimization using density functional theory within the local-density approximation (DFT-LDA) to determine the surface geometry of the Ge covered GaAs(100) surface. Emiliani *et al.* proposed a Ge-Ga dimer length for the (1×2) phase of 2.48 Å, with the Ge raised up with respect to Ga by 0.76 Å. Dimer buckling is expected due to the chemical non-equivalence of Ge with respect to the more electronegative As and the less electronegative Ga. The calculations of Emiliani [Emiliani 1999] for the Ge-Ga dimer bond length of 2.48 Å show excellent agreement with Srivastava's [Srivastava 1996] determined value of 2.43 Å. Both calculations predict a dimer buckling of ~0.78 ±0.02 Å with Ge atoms further above the bulk atoms. Nevertheless, there is still no experimental evidence for the proposed dimer buckling.

Although this prototypical IV/III-V semiconductor has been investigated by photoemission, STM, MEIS and LEED there is still no consensus regarding the atomic configuration at the interface. The first direct structural investigations of the initial stages of interface formation of Ge/GaAs(100) are reported in Section 5.5.

5.3 Clean GaAs(001) preparation

The following section presents an overview of the stoichiometry of the (2×4)/c(2×8) reconstruction of the GaAs(001) structure, which was used in this work. A discussion of the preparation of a clean GaAs(001) surface and the evaluation of this surface by comparison with published results, is given.

On the MBE grown polar surfaces of zincblende materials, the most studied is the GaAs(001) surface. Because of its zincblende crystal structure, the polar GaAs(001) surface may be terminated by either Ga or As atoms, as shown in Figure 5.3 [Xue 1999]. Experimentally, it is usually terminated with the As layer due to excess use of the group V material in the MBE chamber. However, different Ga and As compositions may be present due to relative fluxes of these species arriving at the surface. At least seven different reconstructions of this surface have been reported depending on experimental growth conditions such as the substrate temperature and the stoichiometry. In order of decreasing As/Ga surface-atom ratio, the most commonly observed reconstructions on GaAs(001) are c(4×4), (2×4)/c(2×8), (1×6), (4×6) and (4×2)/c(8×2).

There has also been poorly ordered (1×3) and (2×6) phases observed. The c(4×4), (2×4) and (4×2) reconstructions are characterised by 2, 1 and 0 outer layers of As, respectively [Srivastava 1997b].

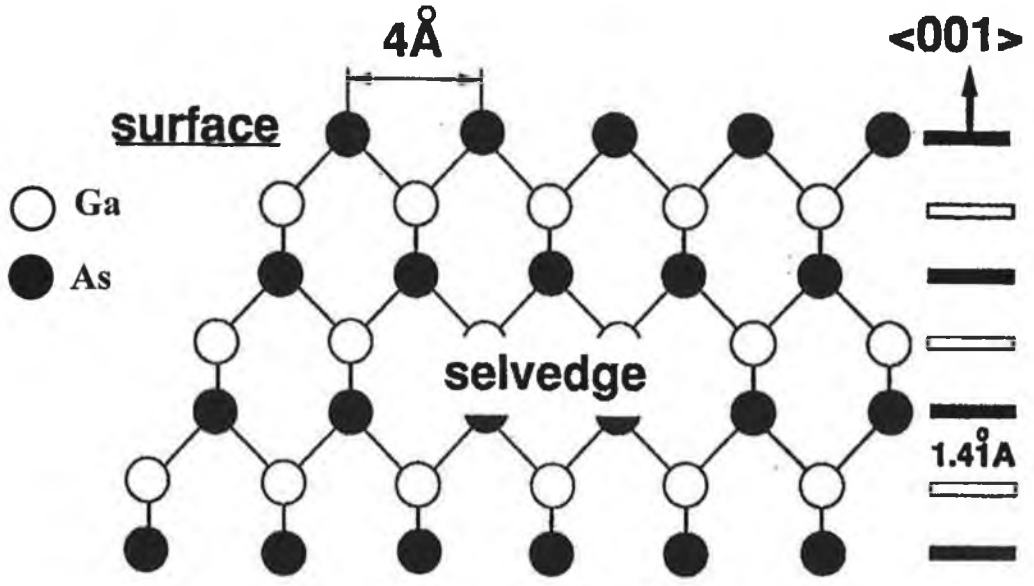

Figure 5.3 *The schematic of a GaAs zincblende structure. At the bulk terminated (1×1) surface each (As) has one unpaired electron with a surface lattice of 4Å. Along the (001) crystal axis alternative As layer and Ga layer occur with an interplanar distance (from As to a neighbouring Ga layer) of 1.41Å [Xue 1999].*

It is well known that MBE growth of GaAs(001) is usually performed under the conditions which lead to an As-terminated (2×4) reconstruction. Since the conditions would essentially result in the best quality for the material grown, the (2×4) reconstruction has been the most extensively studied. Recently reviews of the GaAs(001) surface have been published [Xue 1997] [Kubby 1996] [Srivastava 1997b], with perhaps the most important one being the STM study by Xue *et al.* in 1999 [Xue 1999]. There have been a number of investigations and proposals for the structures of the GaAs(001)-(2×4) reconstruction based upon different numbers of As-As dimers in the topmost layer. Both three-dimer and two-dimer unit cell structures have been observed experimentally by STM [Pashley 1988] [Hashizume 1994,1995] [Broekman 1995] [Moriarty 1996b] [Kubby 1996] [Xue 1997, 1999] and [LaBella 1999], although the resolution of some images suggesting three-dimer structure is not sufficient enough to justify the case.

In a systematic RHEED study Farrell and Palmstrom [Farrell 1990] classified the (2×4) surface into three phases: the α, β and γ phases, as shown in Figure 5.4. Taking kinematic calculations, they concluded that the α phase is made of two As dimers, with second layer Ga dimerization, as shown in Figure 5.4 (c). The unit cell of the β phase is based on three As dimers as illustrated in Figure 5.4 (a) [Chadi 1987]. The γ phase is assigned to the model proposed by Frankel [Frankel 1987]. It has an extra As dimer sitting on the β phase unit, as depicted in Figure 5.4 (d). Based on this scheme, the As coverage is 0.5ML for the α phase, 0.75ML for the β phase and 1.0ML for the γ phase, consistent with that expected from the preparation conditions for each phase. Although, the study of Farrell and Palmstrom [Farrell 1990] is more complicated than previously expected, it for the first time successfully explains the different surface compositions and models reported in the literature.

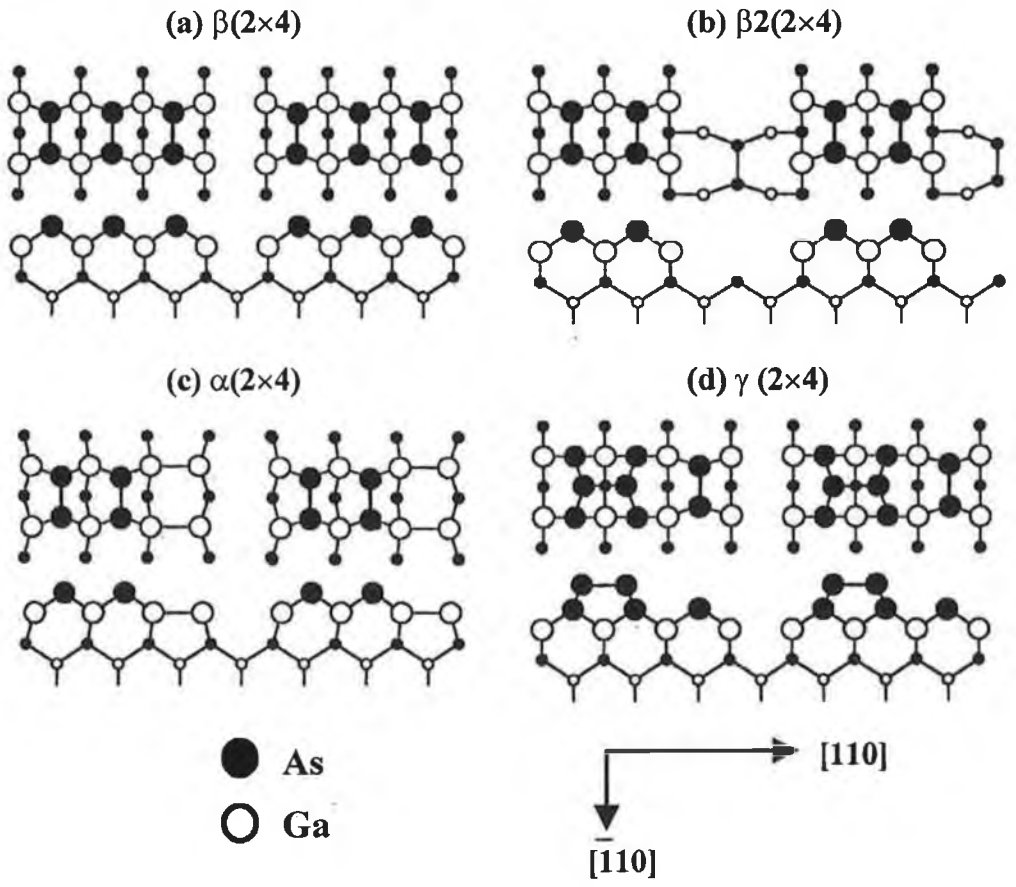

Figure 5.4 *Atomic models (a) three As-dimer model, (b) bilayer two-As-dimer model, (c) two-As-dimer model with second layer Ga dimerized and (d) extra-As dimer model for GaAs(001) [Xue 1999].*

In addition to experimental studies, understanding of the (2×4) surface has been considerably improved by theoretical studies [Drathen 1978] [Northrup 1993, 1994] [Bass 1994] [Schmidt 1996] [Ohno 1996] [Srivastava 1997b]. The most important and common conclusions of these studies are:

(a) the bilayer two As-dimer model 2β(2×4), see Figure 5.4 (b) proposed by Chadi [Chadi 1987] is the most stable structure energetically, and lower in energy by 0.1eV per (1×1) unit than the three As-dimer structure.

(b) The two-As-dimers structure shown in Figure 5.4 (d), proposed by Frankel *et al.* [Frankel 1987] stabilises in limited range of the As chemical potential.

(c) The replacement of the first layer As by additional Ga, as proposed by Falta *et al.* [Falta 1992, 1993b], is unlikely. It changes the stoichiometry and nature of the backbonds between the first and second layers. The resulting energy is much higher than that of the three-As-dimer structure.

The models shown in Figure 5.4 represent the (2×4) As-rich reconstruction of the GaAs(001) surface. The c(2×8) is stoichiometrically equivalent to the c(2×4) As-rich structure. The difference between the (2×4) and the c(2×8) reconstructions arises from the way in which the (2×4) units are arranged relative to one another. Both RHEED and LEED studies show disorder on the surface which may be explained by the presence of both the (2×4) and the c(2×8) domains as shown in Figure 5.5 (b) [Pashley 1988]. In this case, the model for the (2×4) unit is based on a three-As-dimers structure as shown in Figure 5.4 (a). The rows of missing dimers in the unit cell are considered as boundaries between units of three dimers. There are two different types of boundaries on the surface. An in-phase boundary, marked as IP in Figure 5.5 (b) occurs when the units of three dimers line up on either side of the boundary, corresponding to the (2×4) reconstruction. An antiphase boundary (AP), occurs when the centre of the block of three dimers on one side of the boundary lines up with an interface between two dimer units on the other side of the boundary. This leads to a larger unit cell, as shown in Figure 5.5 (b), which is c(2×8). Thus the c(2×8) structure is actually built up from subunits of (2×4) cells. The only difference between these two structures is in the type of boundary formed by the missing-dimer rows. Calculations on the difference in energy between these show it to be only 0.12eV per c(2×8) unit cell, the c(2×8) structure having the lower energy of the two [Chadi 1987]. STM images have confirmed that both types of boundaries are present on the surface, with domains being as small as a few units across [Pashley 1988].

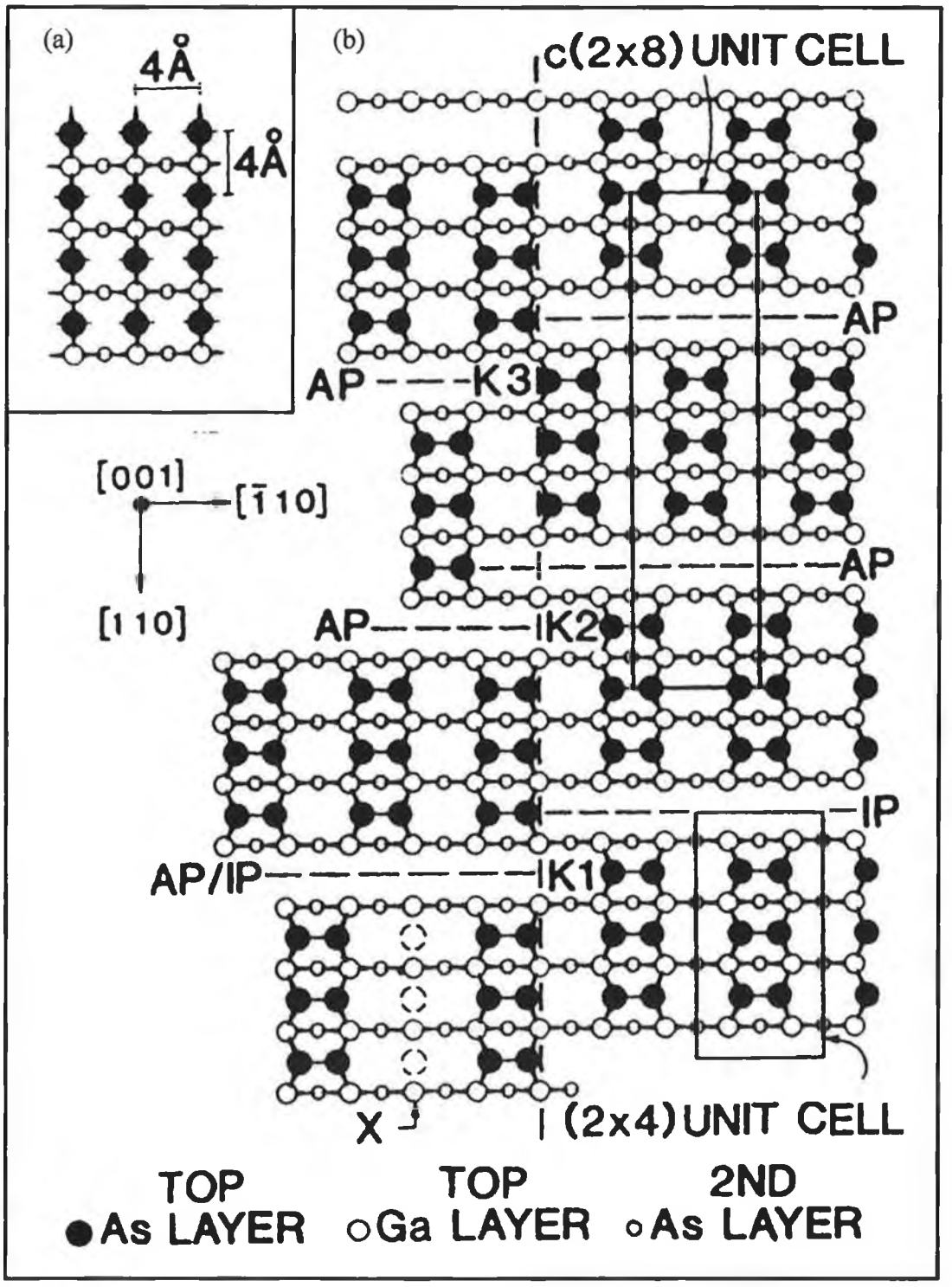

Figure 5.5 *(a) The structure of the unreconstructed GaAs (001) arsenic-rich surface. (b) The missing-dimer model for the GaAs (001) (2×4) surface. The two types of missing-dimer boundary, in-phase (IP) and antiphase (AP), are shown giving rise to (2×4) and c(2×8) structures. The intersection of a domain boundary along the [110] direction with the IP and AP boundaries is shown giving rise to three types of boundary kinks, K1, K2 and K3. Disorder in the arsenic pairing (X) with three missing arsenic atoms (dashed circles) is also illustrated [Pashley 1988].*

The GaAs(001) samples used in this work were grown by Molecular Beam Epitaxy (MBE) by D.I. Westwood, University of Wales, Cardiff. The samples consisted of epitaxial GaAs buffer layers doped n-type with Si at a concentration of 1×10^{18} cm^{-3}. After epilayer growth the samples were covered with a protective layer (several microns thick) of amorphous As. Details of the As capping procedure for GaAs samples are described by Woolf *et al.* [Woolf 1992].

After transfer though air the samples were investigated in an UHV chamber by photoelectron spectroscopy (PES) and Low Energy Electron Diffraction (LEED). The chamber geometry for the Ge/GaAs(001) experiments are described in Sections 3.5 and 3.6. Following degassing overnight at 475K, the As capped sample was annealed in the 575-625K range, to thermally desorb the As cap. The decapping procedure was monitored by the sample temperature, the pressure in the chamber and by a quadrupole mass spectrometer. Successful removal of the As cap was judged by core level photoemission and LEED. After the chamber had returned to its base pressure, the sample was annealed to 725K for about 10 minutes. Sample heating was performed by a hot filament from the backside of the crystal, while the temperature was monitored with a calibrated thermocouple attached to the sample manipulator. A pyrometer was also used to calibrate the temperature and to determine the heating rate. Upon cooling the GaAs(001) surface was shown to exhibit an As-rich (2×4)/c(2×8) reconstruction as shown in Figure 5.6 and 5.7. The clarity of the diffraction pattern photographs is severely affected by the large manipulator head.

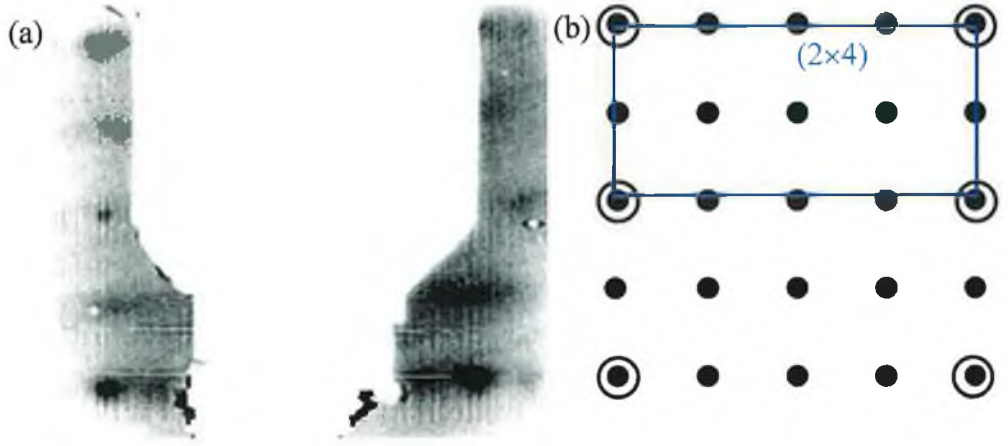

Figure 5.6 (a) *Experimental LEED pattern and (b) representative LEED pattern for the GaAs(001)-(2×4).*

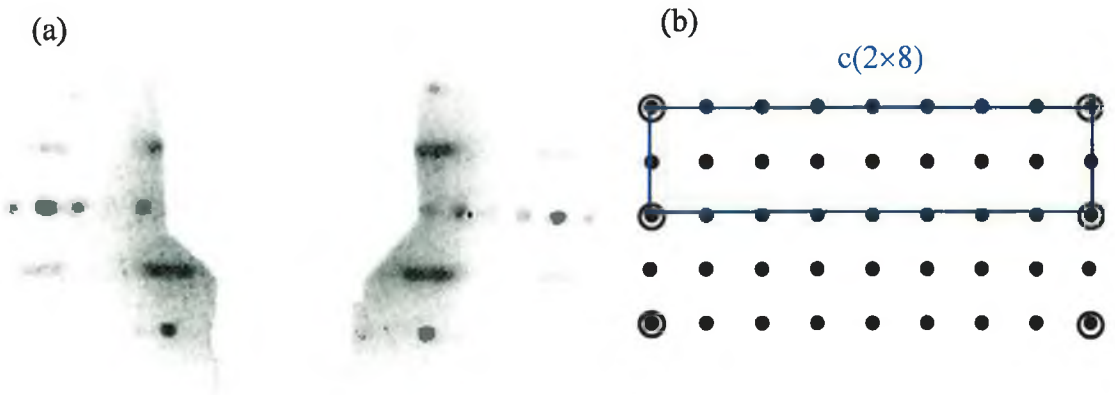

Figure 5.7 *(a) Experimental LEED pattern and (b) representative LEED pattern for the GaAs(001)-c(2×8).*

The core level profiles for the As 3d and Ga 3d core level photoemission spectra of the clean GaAs(001)-(2×4) were compared to previously reported studies of the GaAs(001) surface [Katnani 1985b] [Le Lay 1991] [Spindt 1992]. The parameters used were within the range previously reported values and the results of the curve-fitting procedure for the As 3d and Ga 3d are shown in Figure 5.8.

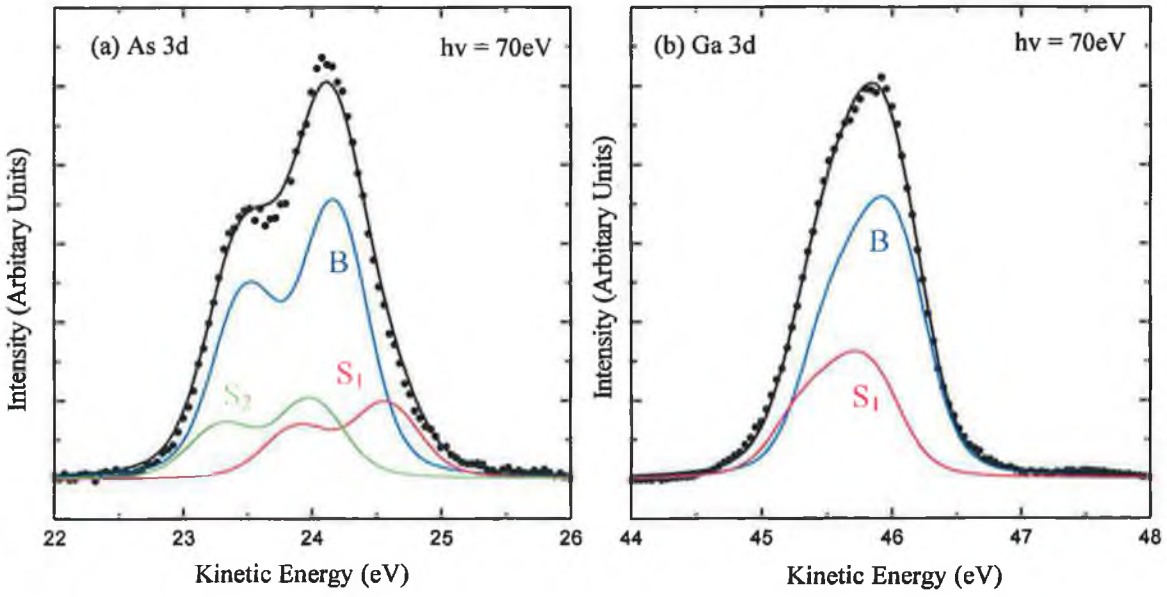

Figure 5.8 *(a) As 3d and (b) Ga 3d line shape for the (2×4)/c(2×8) reconstruction of GaAs(001), taken with 70eV photon energy. The B refers to the bulk component and S_1 and S_2 represent surface components.*

Three components in the As 3d fit were necessary to obtain the minimum χ^2 for the (2×4) surface. The core level-spectrum consists of the bulk As-Ga component (B) and two surface core-level components, S_1 and S_2 as shown in Figure 5.8 (a). A number of previous studies [Katnani 1985b] [Le Lay 1991] [Vitomirov 1992] have identified the higher-BE component as being due to excess As atoms (remaining from the decapping procedure), bonding primarily to other As atoms. Ludeke et al. [Ludeke 1983] identified the low-BE component with the As dimers terminating the (2×4) surface. The Ga 3d core level spectrum in Figure 5.8 (b) requires two components, a bulk Ga-As component (B) and one surface component S_1, due to the reconstructed Ga atoms. The presence of just one core level component is in agreement with the results of Vitmirov et al. [Vitomirov 1992] which shows that the GaAs(001)-(2×4) structure is a three-As dimer unit cell dominant across the surface. If the surface consists of (i) a two dimer-two missing dimer phase, or (ii) a mixture of both phases, the dimerization of underlying Ga as described by Farrell and Palmstrom [Farrell 1990] will give rise to another surface component at lower binding energy. The fitting parameters for the clean GaAs(001)-(2×4) As 3d and Ga 3d core level photoemission spectra is presented together with other photoemission data for germanium on the GaAs(001)-(2×4) surface in Section 5.6.

5.4 Germanium Evaporation Calibration

Germanium was deposited onto the clean GaAs(001)-(2×4) surface from a Knudsen cell operated at 1350K. The rate of germanium evaporation was calibrated by monitoring the intensity profiles for As, Ge and Ga 3d core level photoemission spectra and by LEED. The evolution of the core level photoemission for As 3d, Ge 3d and Ga 3d for increasing coverages of Ge are shown in Figure 5.9. It was found that 0.8ML of germanium evaporated onto the GaAs(001)-(2×4) surface with the sample held at 600K produced a poor quality (1×1) LEED pattern with large background intensity. Annealing the sample to 700K reduces the background intensity and produced weak half-order diffraction beams. Continued annealing of the sample up to 825K results in further sharpening of the diffraction beams, to form a clear (1×2) LEED pattern as shown in Figure 5.10. These observations are in agreement with annealing experiments carried out with STM by Wang *et al.* [Wang 1994a]. As the thickness of the Ge overlayer is increased up to about 4ML, no further change is observed in the LEED pattern.

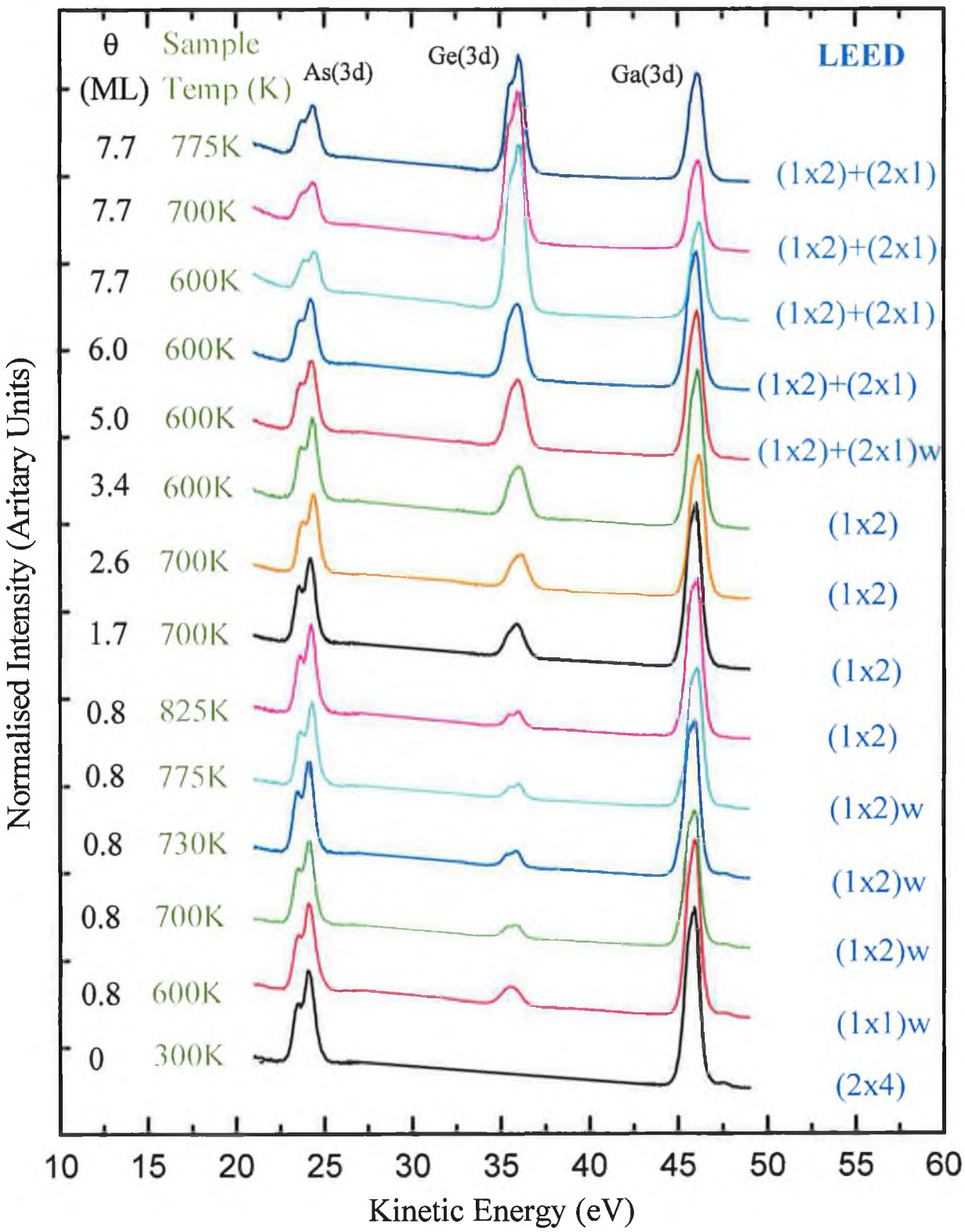

Figure 5.9 *Evolution of the core-level photoemission from As 3d, Ge 3d and Ga 3d at hv=70eV for GaAs(001)-(2×4) and increasing coverage of epitaxial Ge overlayers. Spectra were recorded at room temperature for different Ge coverages and after annealing the substrate to different temperatures. The reconstructions for all stages are shown where* w *represents a weak or diffuse LEED pattern.*

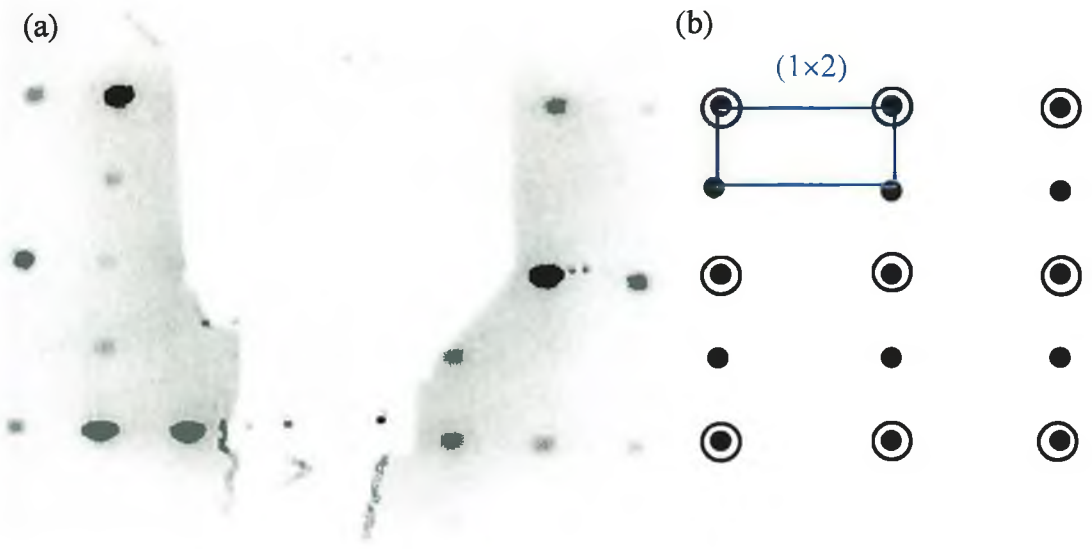

Figure 5.10 *(a) Experimental LEED pattern and (b) representative LEED pattern for the Ge/GaAs(001)-(1×2) reconstruction.*

As the Ge overlayer thickness increases beyond 4ML, weak-fractional order spots from a (2×1) reconstruction appear in addition to those from the original (1×2) reconstruction. These spots get brighter with increasing Ge coverage until, at about 6ML, they are as bright as the fractional-order spots from the (1×2) reconstruction. This is in agreement with earlier results from Bauer *et al.* [Bauer 1982] and Mrstik [Mrstik 1983]. No further change is observed in the LEED pattern after depositing up to an additional 2ML of Ge onto the sample held at 600K. At this stage, further annealing of the sample up to 775K resulted in no changes in the LEED pattern. A photograph of the LEED pattern for the double domain (1×2)+(2×1) reconstruction is shown in Figure 5.11.

Mrstik [Mrstik 1983] observed a single domain (1×2) reconstruction that was maintained up to an overlayer thickness of at least 4ML. He suggested that the Ge and the outdiffused As overlayer were growing in pairs of atomic planes. If the overlayer increased by only a single atomic plane, the new surface atoms would have dangling bonds perpendicular to those of the original starting surface and would form a second domain of (1×2) reconstruction oriented at right angles to the original domain. It is only for Ge coverages greater than 4ML that a second domain begins to form. When the Ge overlayer reaches a thickness of 6ML, the LEED beams from the two domains have equal intensity, indicating that the two domains have an equal area on the surface.

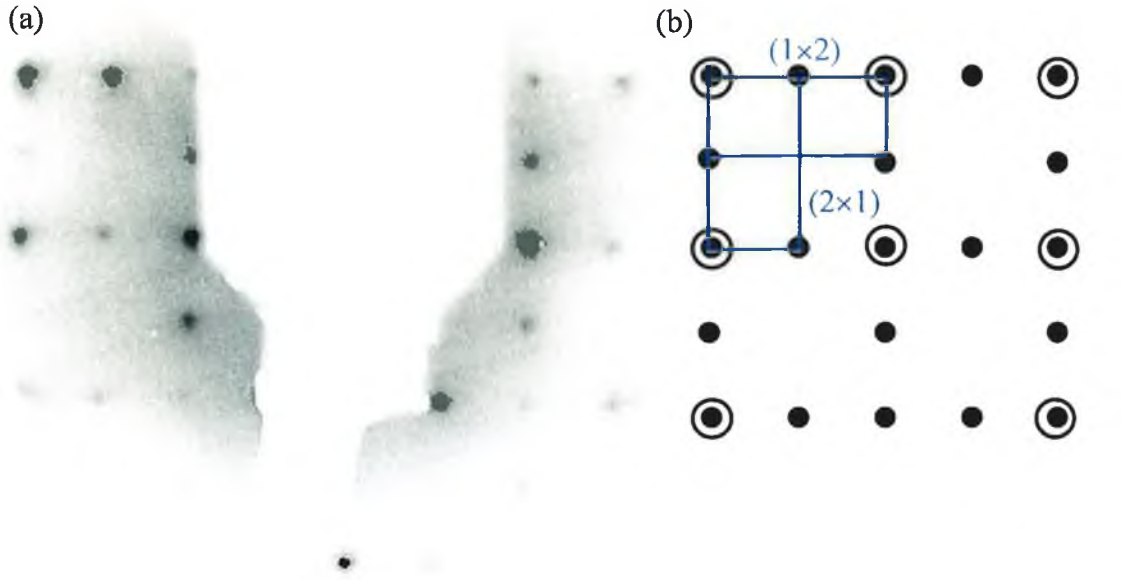

Figure 5.11 *(a) Experimental LEED pattern and (b) representative LEED pattern for the Ge/GaAs(001)-(1×2)+ (2×1) reconstruction.*

In a STM study Wang *et al.* [Wang 1994a] resolved individual (1×2) unit cells of Ge/GaAs(001), in addition to islands with 2.8Å steps height of the same (1×2) reconstruction. They concluded that the Ge grows on the GaAs(001) in a quasi-FM (layer-by-layer) mode due to insufficient surface diffusion at 700K and in the SK (layer-plus-islanding) growth mode at 875K. These results for Ge/GaAs(001)-(1×2) surface cannot be explained in terms of either the structure of the GaAs(001) or the Ge(001) surface. While the 2.8Å GaAs bilayer steps are present on the GaAs(001) surface, the (1×2) and (2×1) structures are not observed. On nominally flat Ge(001) surfaces, approximately equal sized domains of (1×2) and (2×1) order are observed, which are separated by 1.4Å steps. This would indicate that Ge is growing in a bilayer reconstruction.

In this work the integrated intensities of the core level photoemission peaks shown in Figure 5.9, were monitored with increasing Ge coverage. A plot of the As 3d, Ga 3d and Ge 3d intensities as a function of increasing Ge coverage on the GaAs(001)-(2×4) surface is shown in Figure 5.12. The intensities of the spectra are normalised to the clean surface of GaAs which is shown to have a As 3d + Ga 3d intensity of 100%. Initially there are equal amounts of Ga and As atoms in the GaAs(001) bulk structure, ignoring the small percentage of As terminated surface atoms. The growth curve shows that the Ge grows in a double-layer mechanism up to coverages of 6ML, where the slope of both the Ge and combined Ga+As signal changes. This is in agreement with

Mrstik [Mrstik 1983] and Chambers [1988] observations that from 6ML the growth proceeds by single atomic layers.

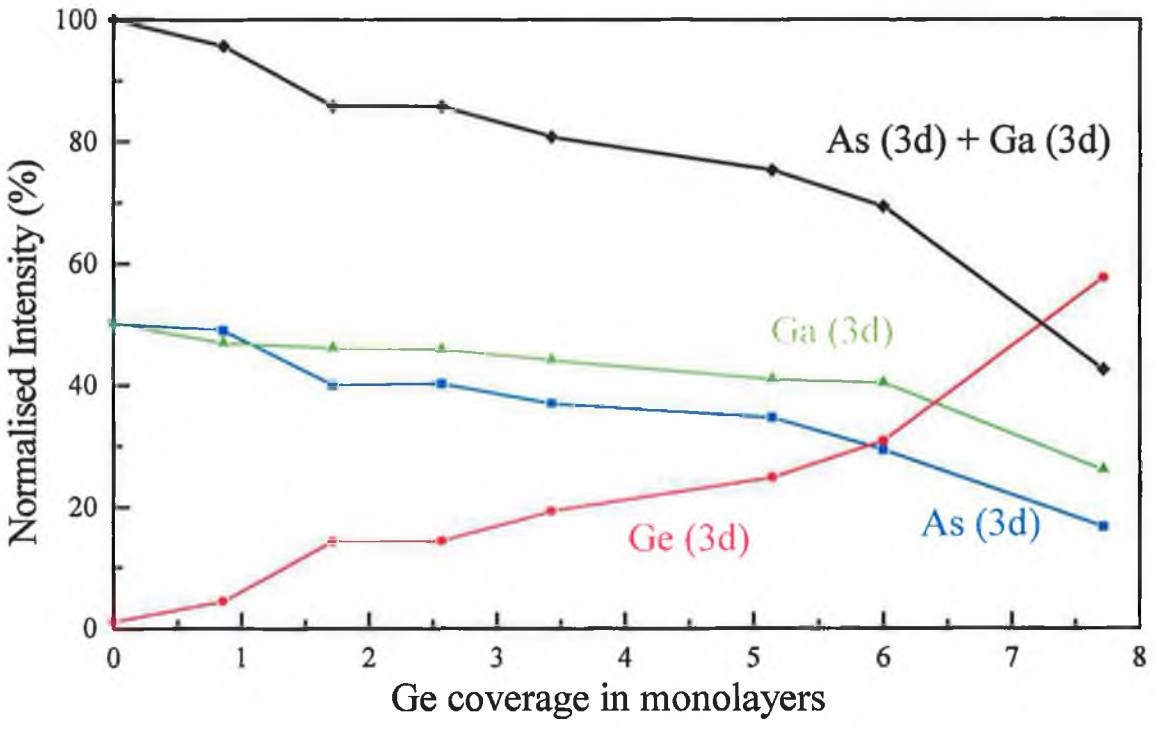

Figure 5.12 *Normalised relative intensities of the As 3d, Ga 3d and Ge 3d core level photoemission peaks as a function of Ge growth on GaAs(001)-(2×4) held at a temperature of 700K. The As 3d + Ga 3d curve represents the combined intensity of Ga and As core 3d levels, which on the clean surface is represented as 100%.*

In this examination of the initial stages of formation of the Ge/GaAs(001) interface, only two different reconstructions, that is the (1×2) and the (1×2)+(2×1), were observed with increasing Ge coverages. The (2×1) reconstruction for low temperature anneals of submonolayer coverages of Ge on GaAs(001) have not been observed. Different studies, as mentioned above, have associated the (1×2) reconstruction with Ge-Ga dimerization along the [110] direction. However, no direct experimental confirmation of the Ge-Ga dimer has been reported. In the following section, X-ray standing wave spectroscopy is used to determine the location of Ge atoms in the (1×2) reconstruction of the Ge/GaAs(001) surface.

5.5 X-ray Standing Wave Spectroscopy Results

The Ge/GaAs(001)-(1×2) X-ray standing wave spectroscopy (XSW) studies were performed at beamline 6.3 of the SRS at Daresbury Laboratory, UK. The experimental set-up for XSW is described in Section 3.5. This beamline has a double crystal monochromator that consists of pairs of single crystals. The InSb(111) crystal pair cover the photon energy range from 1780eV to 5200eV and the Ge(111) crystal pair have a photon energy range from 2010eV to 6000eV. The measured photon flux for these two monochromators are shown in Section 3.5. The X-ray standing wave experiments were carried out with the scattering planes of the sample aligned at normal incidence to the incident beam and scanning through the photon energy about the Bragg peak energy. At normal incidence the Bragg condition becomes:

$$\lambda = 2d_H \tag{5.1}$$

where d_H is the interplanar distance between planes with the Miller indices {hkl}. In a cubic lattice with the lattice constant a, this distance is:

$$d_H = \frac{a}{\sqrt{h^2 + k^2 + l^2}} \tag{5.2}$$

Table 5.1 lists a number of Bragg reflections for GaAs, showing the interplanar distances and the corresponding photon energies

$$E = h\upsilon = hc/\lambda = hc/2d_H \tag{5.3}$$

The polar angle between two planes with indices {hkl} and {h'k'l'} is found by calculating the angle between two vectors normal to those planes.

$$\alpha = \arccos\frac{hh'+kk'+ll'}{\sqrt{h^2 + k^2 + l^2}\sqrt{h'^2+k'^2+l'^2}} \tag{5.4}$$

Bragg Reflection (h,k,l)	Polar angle w.r.t. (001) plane (°)	Interplanar distance (Å) $d_H = \frac{a}{\sqrt{h^2+k^2+l^2}}$	$\frac{\sin\theta}{\lambda} = \frac{1}{2d_H}$	E_{Bragg} (eV) $E = \frac{hc}{2d_H}$
[111]	54.7	3.262	0.1533	1900
[220]	45, 90	1.999	0.2503	3093
[311]	25.2, 72.5	1.704	0.2934	3633
[400]	0	1.413	0.3539	4382

Table 5.1 *Bragg energies and angles relative to the (001) plane for reflection planes in GaAs, with a lattice constant a = 5.65Å.*

When setting the angle for each reflection, the azimuthal angle is first aligned and then the polar angle may be rotated.

The amplitude and phase of a Bragg reflection is given by the structure factor for each crystal plane. The structure factor for a Bragg reflection with n atoms at positions $\mathbf{r_i}$, miller indices h,k,l and a lattice vector **H** is defined as:

$$F_H = \sum_{i=1}^{n} f_i e^{2\pi i \mathbf{H} \mathbf{r}_i} \tag{5.5}$$

In a diamond lattice, the structure factor for a Bragg reflection is zero when even and odd indices h,k,l are mixed or when the sum of h+k+l is an even number but not divisible by four. Hence the [220] [111] [311] and [400] refections shown in Table 5.1, are all permitted in a diamond crystal, whereas the [100] [200] [222] reflections are forbidden. The Bragg reflections observable on Station 6.3 are resticted to lower index reflections, with E_{Bragg}<3700eV. Reflections with Bragg energies higher than 3700eV tend to have regions of reflectivity too narrow for use. Moreover the instrumental broadening of the beamline becomes large at high energies causing broadening and attentuation of the XSW profiles ($\Delta E \sim 1.1$eV at E = 4000eV). The Bragg reflections used in the experiments described here were the lower Bragg energy [220] and [111] reflections.

In a zincblende lattice, which is a diamond lattice where alternate positions are filled with different atoms, these selection rules will only hold true when the two atoms have similar scattering factors f_i. Atomic scattering factors are proportional to the number of electrons of an atom and hence the diamond selection rules can be applied to GaAs (Z_{Ga}=31, Z_{As}=33). The scattering factors for Ga and As about the Bragg energy $\frac{\sin\theta}{\lambda}$ for each reflection, were calculated using tables compiled by Waasmaier [Waasmaier 1995]. Thermal vibrations of atom *i* will reduce the atomic scattering factor f_i by the Debye-Waller factor e^{-M_i}. To account for thermal vibrations in the lattice the Debye-Waller factor D_H, was calculated from

$$D_H = \exp(-B/2d_H^2) \tag{5.6}$$

where B is the thermal parameter at 300K for As and Ga atoms obtained from Reid [Reid 1983]. The struture factors for the different reflection planes were calculated with the program "shadow" on the xserv1 workstation in Daresbury. The required input data for this program are the crystal geometry, the indices of the Bragg reflection planes

(hkl), the atomic scattering factor f_i and the Debye-Waller factor D_H for the different atoms in the crystal. The program calculates the real and imaginary parts of the structure factor F(hkl). For example, the structure factors for the [111] and [220] planes of GaAs are shown in Table 5.2. These structure factor values are used in the fitting calculations of the Bragg reflection for the bulk absorption profiles.

Bragg Reflection (h,k,l)	**E_{Bragg} (eV)** $E = \frac{hc}{2d_H}$	**Debye-Waller D_H**	**Structure Factors**			
			F(0,0,0)		**F(h,k,l)**	
			Re	**Im**	**Re**	**Im**
[111]	1900	0.97	241.1	82.7	144.3	58.5
[220]	3093	0.92	257.1	38.2	191.4	58.5

Table 5.2 *Calculated Debye-Waller factors (D_H) and structure factors for the [111] and [220] Bragg reflection planes of the GaAs crystal with a lattice constant of 5.65Å.*

To determine the position of the adsorbate Ge atom by a triangulation method, its distance to the Bragg scattering plane must be calculated using different sets of planes for triangulation. The Bragg reflections used in these experiments are shown in Table 5.3.

Reflection plane (hkl)	**Polar Angle w.r.t (001) plane**	**Azimuthal Angle w.r.t (001) plane**	**Bragg Energy (eV)**
$(0\bar{2}2)$	315°	315°	3093
$(20\bar{2})$	45°	45°	3093
$(1\bar{1}1)$	307°	0°	1900
$(11\bar{1})$	307°	270°	1900

Table 5.3 *The experimental set-up parameter for the Bragg reflection planes used in the XSW spectroscopy of the Ge/GaAs(001)-(1×2) interface.*

X-ray absorption may be monitored by detection of either the photoemission yield or the intensity of Auger emission. The relative intensities of photoemission and Auger transition peaks for Ge, Ga and As are shown in the survey scan in Figure 5.13.

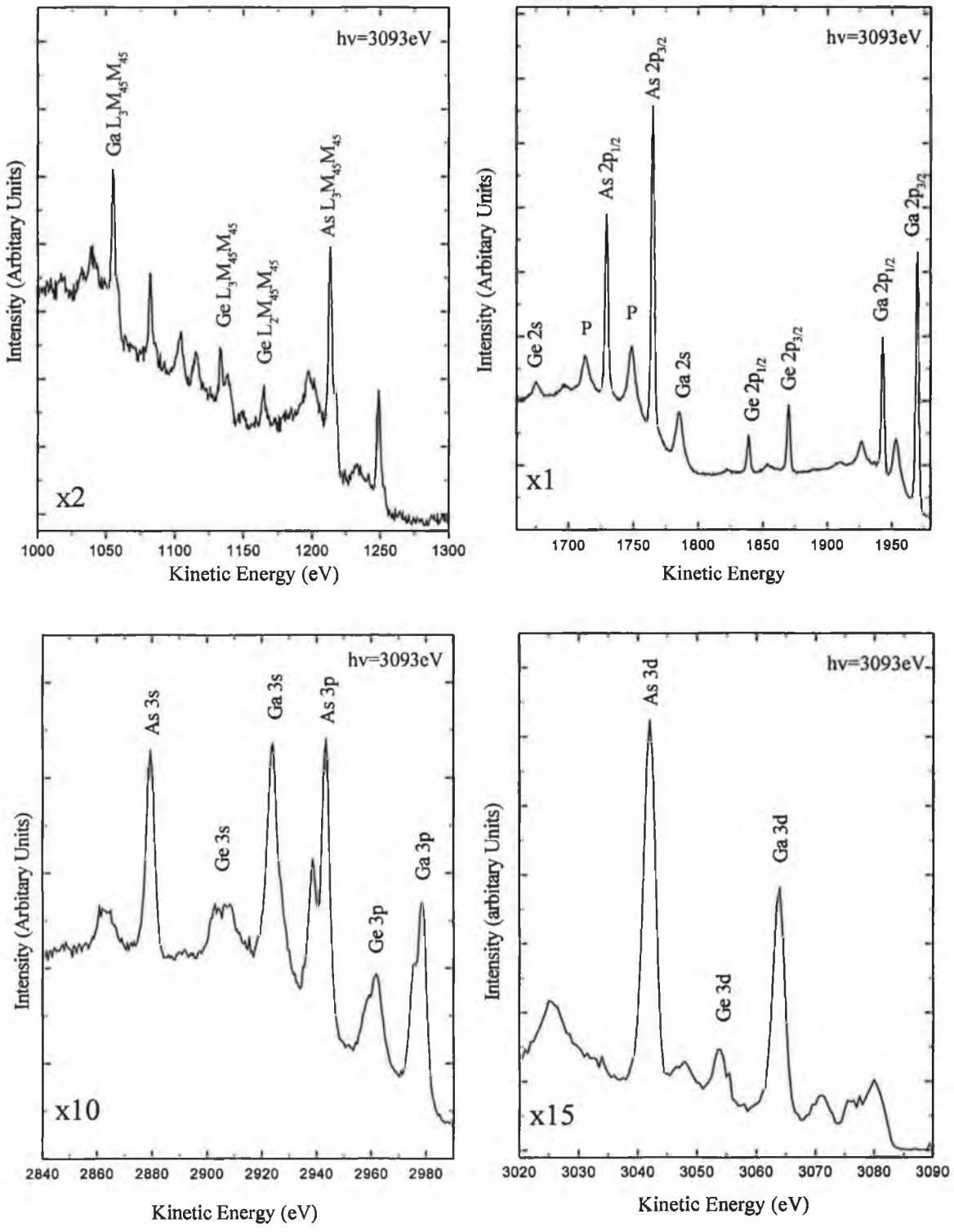

Figure 5.13 *A wide energy range Energy Distribution Curve (EDC) identifying the As, Ge and Ga photoemission and Auger electron peak positions and relative intensities, recorded at a photon energy of 3093eV.*

The NIXSW profiles of the adsorbate and substrate atoms were measured using the photoemission yield from the highest intensity core levels. In this case, the Ge $2p_{3/2}$, As $2p_{3/2}$ and Ga $2p_{3/2}$ core levels at binding energies of 1227eV, 1332eV and 1127eV respectively were used. The $L_3M_{45}M_{45}$ Auger electron emission peaks for Ga and As at kinetic energies of 1055eV and 1213eV and the Ge $L_2M_{45}M_{45}$ peak at 1165eV are also recorded for comparison and as an additional check on the XSW data. The more intense Ge $L_3M_{45}M_{45}$ Auger peak at 1133eV kinetic energy could not be used as it overlaps with an As Auger transition. The photoemission and Auger peaks sit on a background consisting of inelastically scattered secondary electrons. This background was corrected for by subtracting XSW profiles measured at a kinetic energy ~10eV above the peaks as discussed in Section 3.5.2.

The recorded NIXSW profiles for the Ge/GaAs(001)-(1×2) reconstruction are shown in Figures 5.14-5.17. These profiles were analysed using a fortran program called "backfit" written by Prof. Woodruff's group in Warwick University. This program essentially fits a XSW profile to the absorption curve as described in Section 3.5.3. The input parameters supplied to the program are the crystal lattice spacing a, the structure factors F(hkl), the Debye-Waller factors D_H, and the volume of the unit cell V. The program determines the Bragg peak position and the instrumental resolution from the bulk like (off-peak) spectrum. It then fits the coherent distance D and the coherence fraction F_{co} to the normalised profile. An overview of the coherent fractions and coherent positions determined for each detected photoemission and Auger emission species is shown in Table 5.4.

Detected species	$(0\bar{2}2)$ Planes		$(20\bar{2})$ Planes		$(1\bar{1}1)$ Planes		$(11\bar{1})$ Planes	
	D	F_{co}	D	F_{co}	D	F_{co}	D	F_{co}
As 2p	0.00	0.95	0.00	0.95	0.88	0.89	0.11	0.80
Ge 2p	0.00	0.90	0.00	0.95	0.98	0.70	0.02	0.65
Ga 2p	0.00	0.90	0.00	0.95	0.12	0.91	0.85	0.93
As LMM	0.00	0.80	0.00	0.80	0.88	0.96	0.11	0.88
Ge LMM	0.00	0.80	0.00	0.80	0.02	0.68	0.04	0.70
Ga LMM	0.00	0.80	0.00	0.80	0.14	0.92	0.86	0.98

Table 5.4 *NIXSW coherent positions and coherent fractions for the (1×2) Ge/GaAs(001) interface. The coherent positions (D) are given in units of the interlayer spacing.*

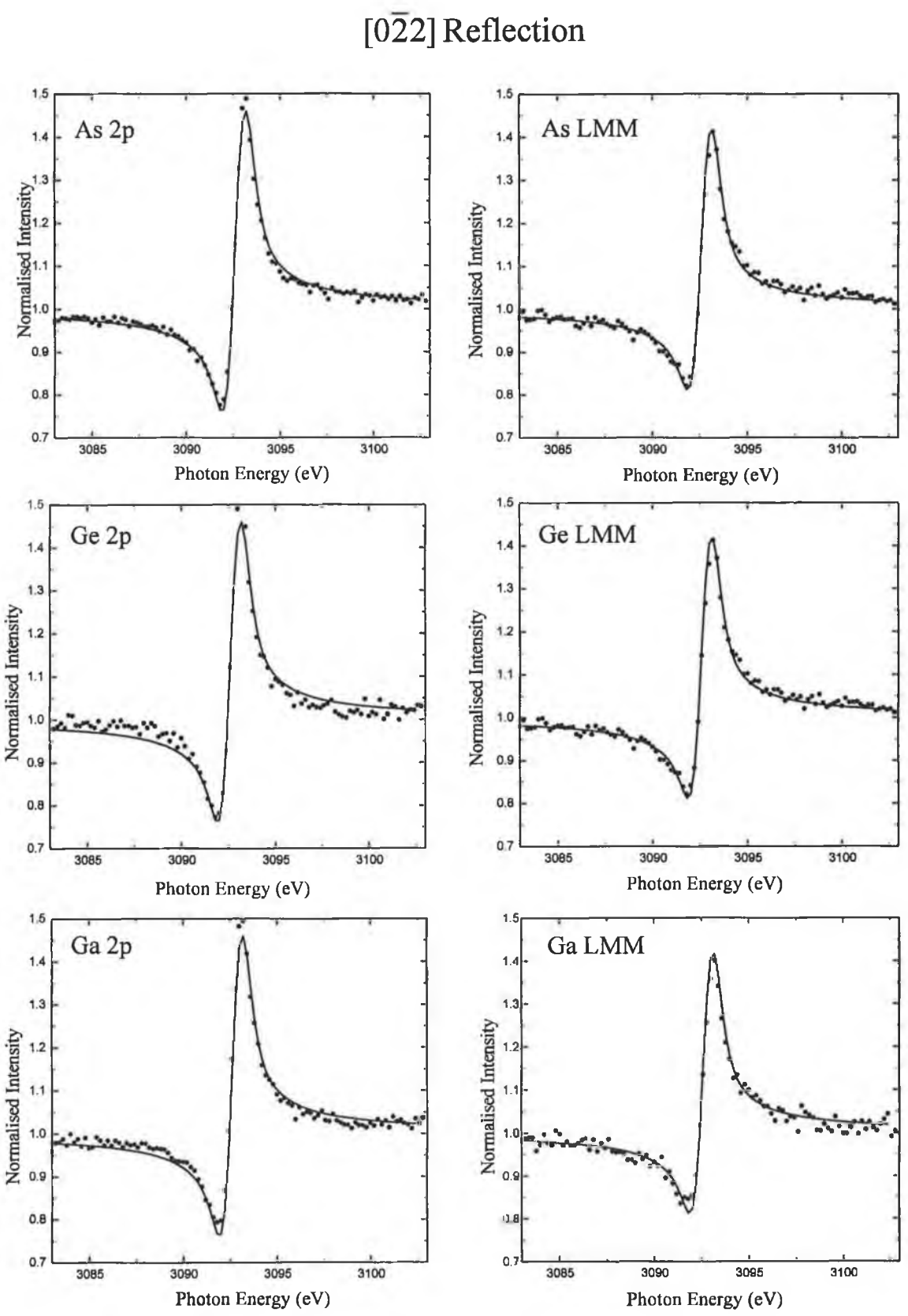

Figure 5.14 *NIXSW profiles from the* $(0\bar{2}2)$ *reflection plane at 3093eV. The 2p photoemission and the LMM Auger emissions are shown for the Ge adsorbate and the As and Ga bulk species.*

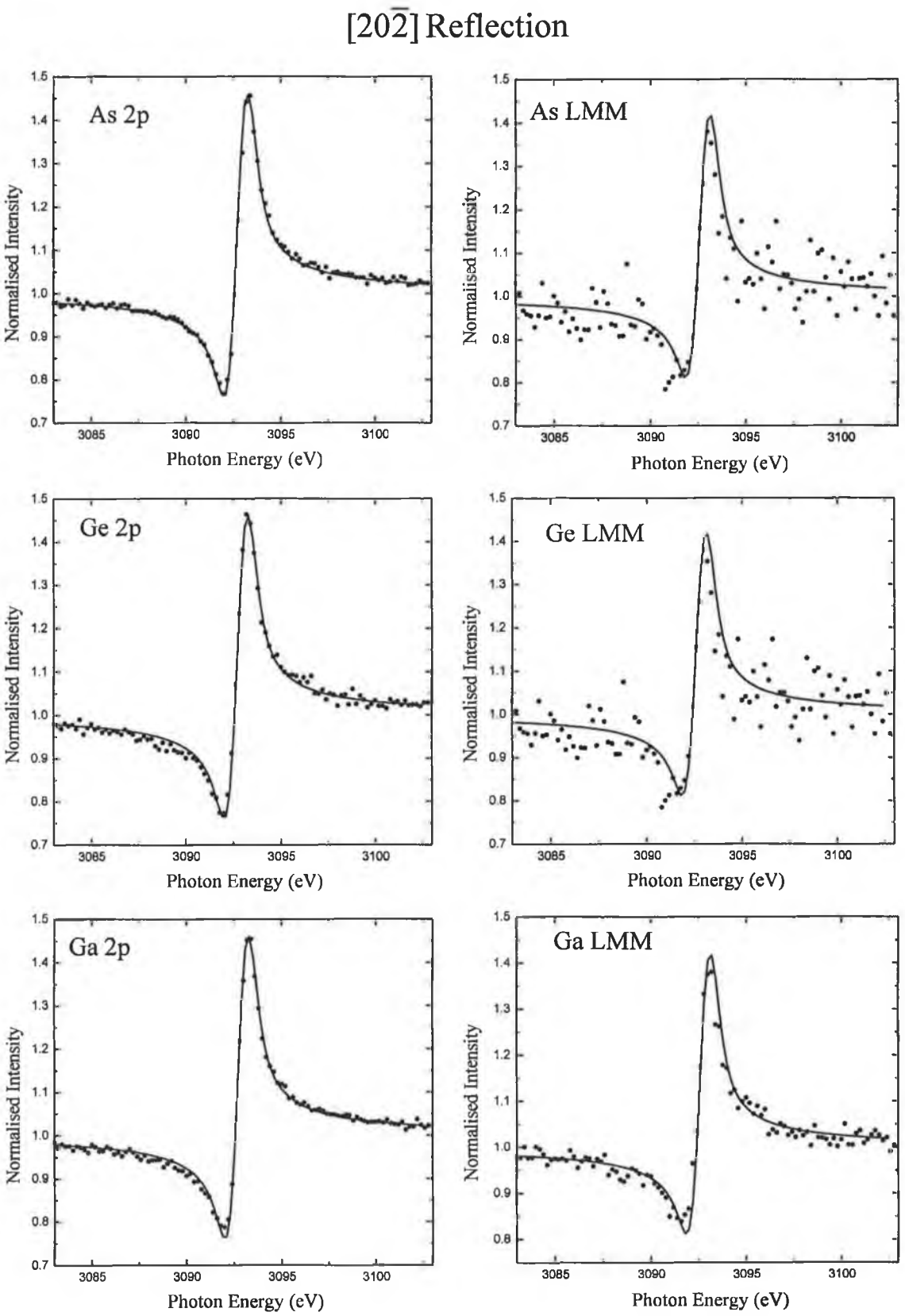

Figure 5.15 *NIXSW profiles from the* (20$\bar{2}$) *reflection plane at 3093eV. The 2p photoemission and the LMM Auger emissions are shown for the Ge adsorbate and the As and Ga bulk species.*

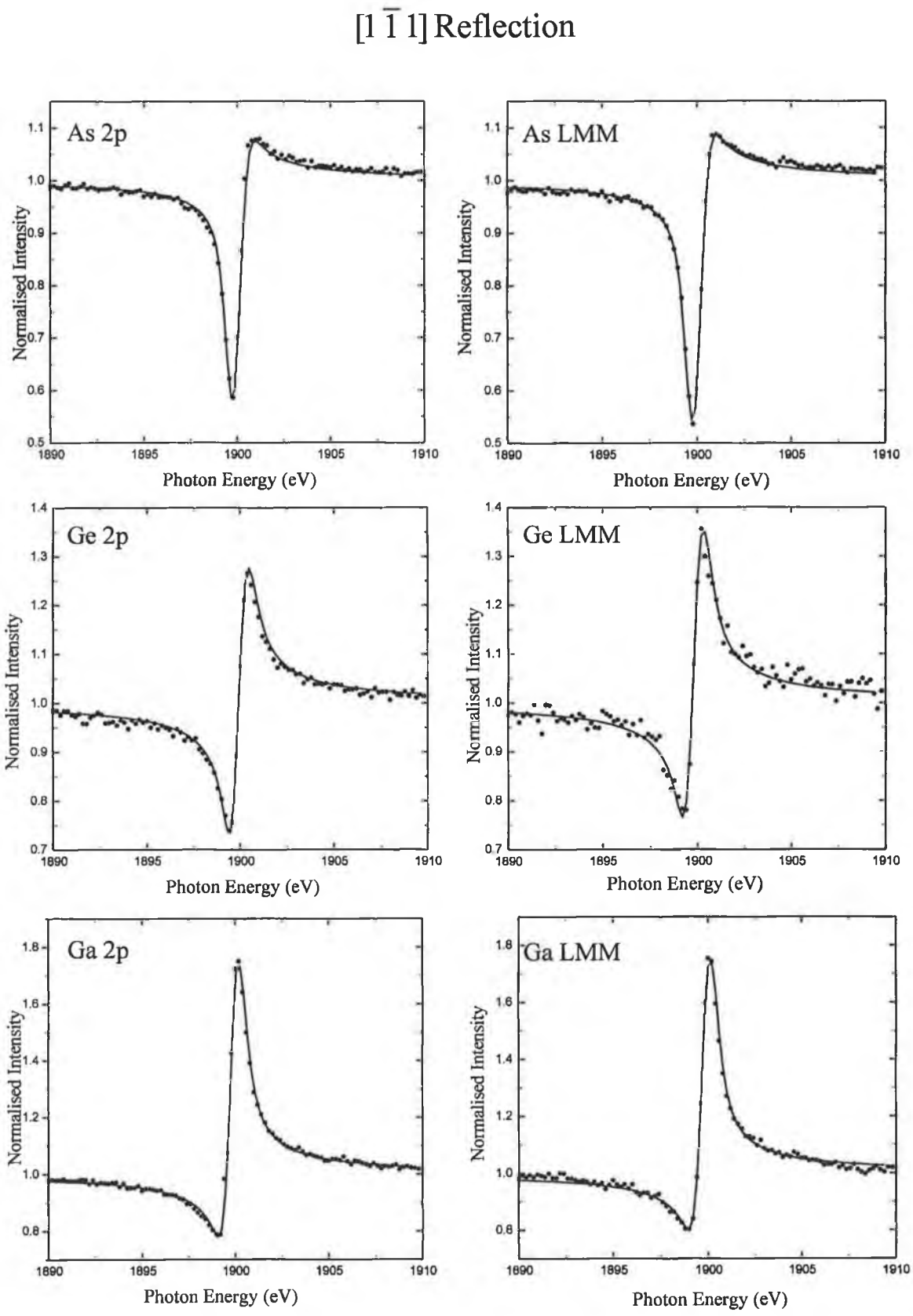

Figure 5.16 *NIXSW profiles from the* (1 $\bar{1}$ 1) *reflection plane at 1900eV. The 2p photoemission and the LMM Auger emissions are shown for the Ge adsorbate and the As and Ga bulk species.*

[1 1 $\bar{1}$] Reflection

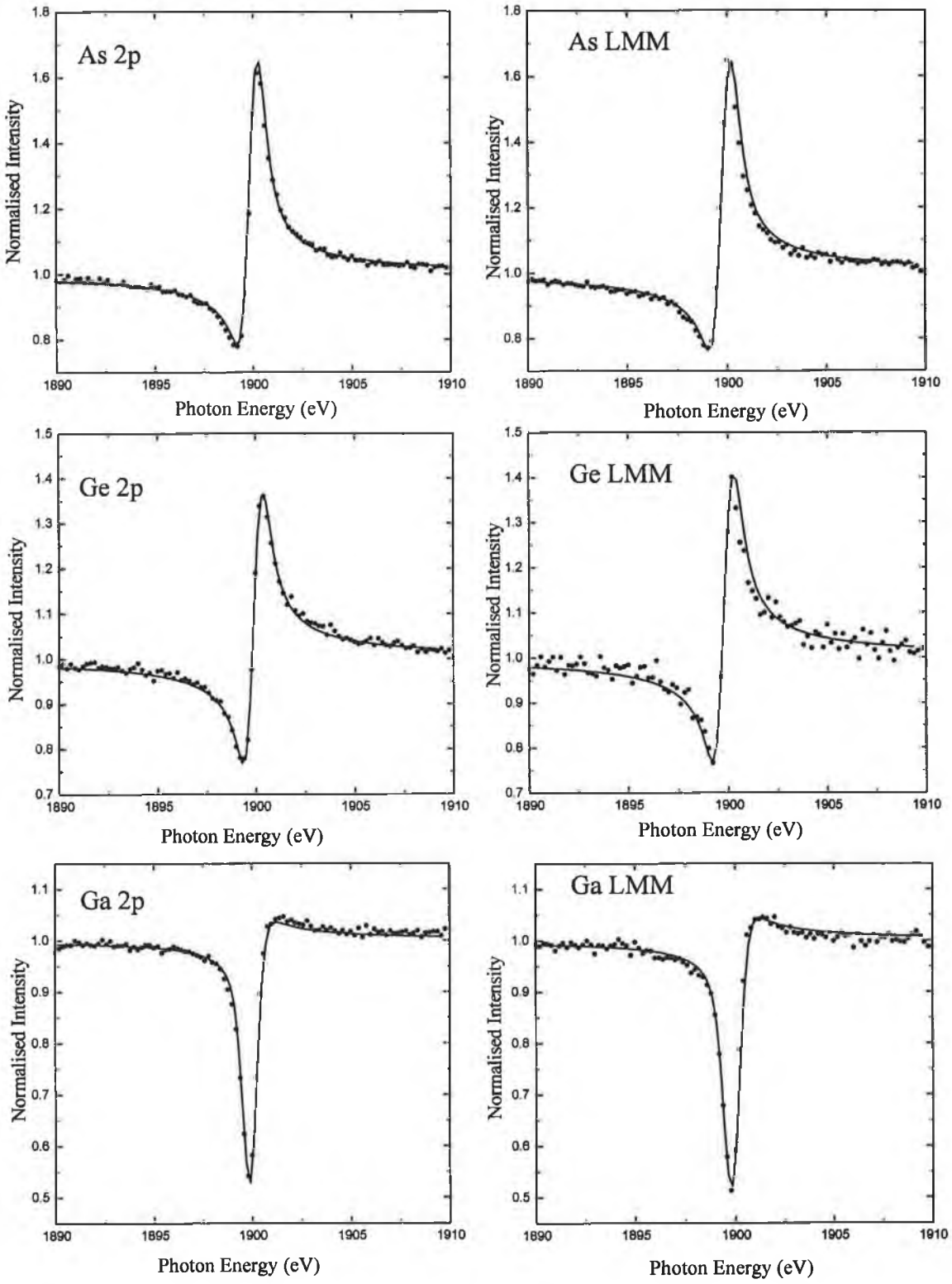

Figure 5.17 *NIXSW profiles from the* (1 1 $\bar{1}$) *reflection plane at 1900eV. The 2p photoemission and the LMM Auger emissions are shown for the Ge adsorbate and the As and Ga bulk species.*

XSW measurements on some of the GaAs planes are complicated by the fact that the arsenic and the gallium atoms in the lattice form two separate layers, for example, in the polar {100} and {111} planes. From geometry, in the $(1\bar{1}1)$ planes the arsenic and gallium atoms are in different layers separated by $\Delta = \frac{1}{4}d_{1\bar{1}1}$. The effective position of the $(1\bar{1}1)$ Bragg scattering plane is somewhere between the Ga-layer and the As-layer. The effective position was taken to be the mean position weighted by the atomic scattering factors of As and Ga, which have values $f_{As} \sim 28.2$ and $f_{Ga} \sim 26.6$ at the Bragg condition, $\frac{\sin\theta}{\lambda} = \frac{1}{2d_H}$. For GaAs the scattering factors of Ga and As are very similar, resulting in an effective scattering plane only marginally closer As-layer, as shown in Figure 5.18 [Bedzyk 1984].

$$d_{Bragg} = \Delta\frac{f_{As}}{f_{As}+f_{Ga}} = 0.51\Delta \qquad (5.7)$$

In other III-V compounds, e.g. InP, the scattering factor for indium is much larger that the scattering factor for phosphorus. This results in the effective $(1\bar{1}1)$ Bragg scattering plane lying much closer to the In-layer than to the P-layer.

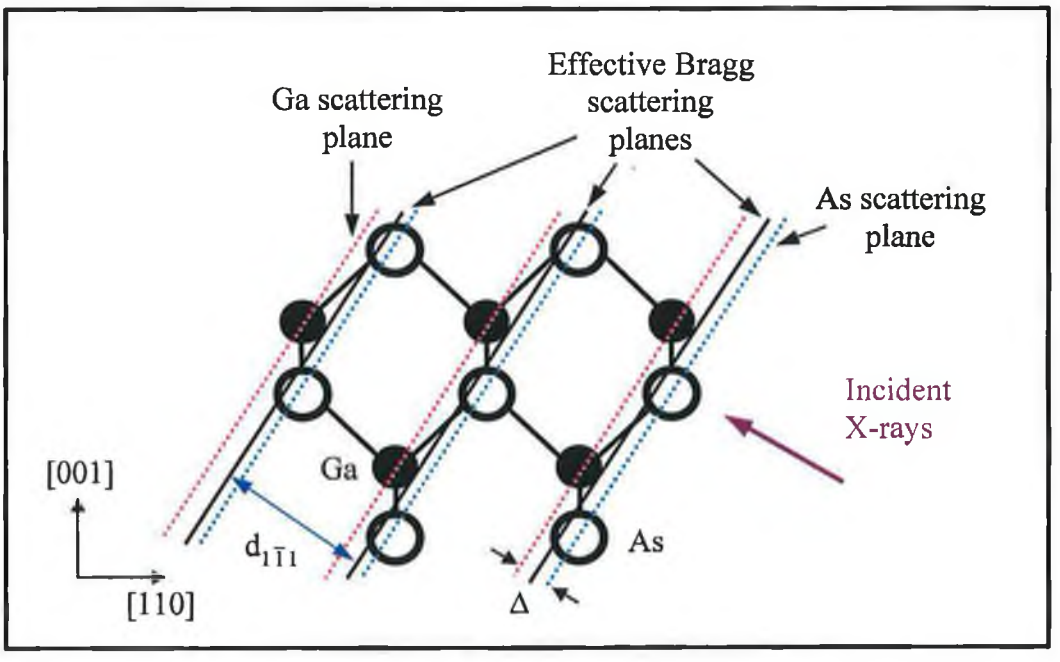

Figure 5.18 *The* $(1\bar{1}1)$ *planes in a zincblende lattice. The gallium and arsenic atoms are in two layers separated by Δ. The actual Bragg scattering plane is between the two layers, marginally closer to the arsenic atoms.*

In the example in Figure 5.18, the As-layer is below and the Ga-layer is above the effective $(1\,\bar{1}\,1)$ Bragg reflection. With an equal weighting for the bulk components the coherent positions for the As and Ga with respect to the $(1\,\bar{1}\,1)$ plane would be 0.875 and 0.125, respectively. Taking the strength of the scattering factors into account the coherent position is calculated to be 0.88 for the As-layer plane and 0.13 for the Ga- with respect to the $(1\,\bar{1}\,1)$ layer. Good agreement with these values can be seen in Table 5.4, which lists the experimental coherent position D and the coherent fraction F_{co} for the $(1\,\bar{1}\,1)$ Bragg reflections. The As 2p spectra has a 0.88±0.01 fractional position and the Ga 2p spectra has a position of 0.12±0.01. The Auger emission spectra for the $(1\,\bar{1}\,1)$ planes yield fractional positions of 0.88±0.01 and 0.14±0.01 for the As LMM and the Ga LMM spectra respectively. The Ge atoms are shown to lie in neither the Ga-layer nor the As-layer with respect to the $(1\,\bar{1}\,1)$ reflection plane. For this Bragg reflection, the Ge 2p spectra have a coherent position of 0.98±0.01 and the Ge LMM spectra have a coherent position of 0.02±0.01. This indicates that the Ge atoms do not just substitute into a Ga or an As site but occupy a position close to the effective $(1\,\bar{1}\,1)$ Bragg scattering plane.

In the case of the $(1\,1\,\bar{1})$ Bragg reflection plane, the As–layer is above and the Ga-layer is below the effective Bragg reflection plane. The results presented in Table 5.4 show a coherent position of 0.11±0.01 for As 2p spectra and 0.85±0.01 for the Ga 2p spectra. Values of 0.11±0.01 and 0.86±0.01 for the As LMM and Ga LMM Auger emission spectra are also obtained for this plane in good agreement with the photoemission XSW data. The Ge atoms are shown to have a coherent position of 0.02±0.01 for the Ge 2p spectra and a coherent position of 0.04±0.01 for the Ge LMM spectra with respect to the $(1\,1\,\bar{1})$ plane. This indicates that the Ge atoms are situated above the effective $(1\,1\,\bar{1})$ Bragg reflection planes and marginally closer to the As-layer.

For the nonpolar $(0\bar{2}2)$ and $(20\bar{2})$ Bragg reflection planes, As and Ga atoms both lie in these planes, in good agreement with the results presented in Table 5.4. The substrate XSW profiles are fitted with coherent positions of 0±0.01 and coherent fractions greater than 0.80±0.04. The Ge atoms are also shown to have a coherent position of 0±0.01 and a coherent fraction greater than 0.8±0.04. The coherent distances of zero for all three atom species, indicates all the As, Ge and Ga atoms lie in the $(0\bar{2}2)$ and $(20\bar{2})$ planes.

The high coherent fractions for the three atom species indicate that the atoms are highly ordered with respect to these reflection planes. The $(0\bar{2}2)$ and $(20\bar{2})$ planes are shown to have consistently higher coherent fractions that the $(1\bar{1}1)$ and $(11\bar{1})$ reflections for the Ge 2p and LMM profiles, as can be seen in Table 5.4. Since the photoemission experiment discussed later in Section 5.6 shows that there is only one germanium site on the surface, a coherent fraction of 1 is expected. However, these reduced values can be attributed to local disorder associated with thermal vibrations, which can reduce the value of the coherent fraction by an appropriate Debye-Waller factor.

From the atomic positions determined using triangulation with the four Bragg reflections, a symmetric Ge-Ga buckled dimer orientated along the [110] direction is proposed. The position of the Ge-Ga dimer with respect to the $(1\bar{1}1)$, $(11\bar{1})$ and the $(20\bar{2})$ Bragg reflection planes are illustrated in Figure 5.19. Ge is found to replace Ga in the continued bulk lattice at a height of 2.06±0.02Å above the top layer As. An interlayer distance of 2.06 Å is slightly larger than the expected 1.99Å separation of the bulk gallium sites predicted in the continued bulk layer. In contrast, Srivastava and Jenkins [Srivastava 1996] proposed a relaxation of the Ge atoms towards the bulk and an interlayer spacing of the 1.54Å, as discussed in Section 5.2.2. A Ge height of 2.06±0.02Å above the top As layer, yields a As-Ge bond length of 3.15 ± 0.02Å. The position of the surface gallium atom in the Ge-Ga dimer has not been determined by NIXSW. However, it is proposed that the Ge-Ga dimer has a bond length of 2.48Å based on a covalent radii of 1.26Å for Ga and 1.22Å for Ge. In addition, the height of the dimerized Ga above the (001) surface is defined by the magnitude of dimer buckling. A Ge-Ga dimer buckling of 0.79Å has been proposed by Srivastava [Srivastava 1996] as shown previously in Figure 5.2. Similar results were reported by Emiliani [Emiliani 1999], with the Ge-Ga dimers determined to have a buckling of 0.76Å on the Ge/GaAs(001)-(1×2). In this work, the surface Ga atoms are positioned in the Ge-Ga dimer using a buckling of 0.79Å, from the results reported by Srivastava [Srivastava 1996]. It has been observed for Ga on the (110) surface of GaAs that the Ga relaxes by moving inwards forming a tilt angle of ~ 30° with respect to the (110) surface. The three dangling bonds of the Ga become nearly planar with a bond angle of 120°. Srivastava [Srivastava 1996] proposed that when the Ge dimerizes with the Ga in the (1×2) reconstruction, the Ge acts somewhat like a group V element, favouring a

pyramidal bonding arrangement after receiving a valence electron from its less electronegative neighbour.

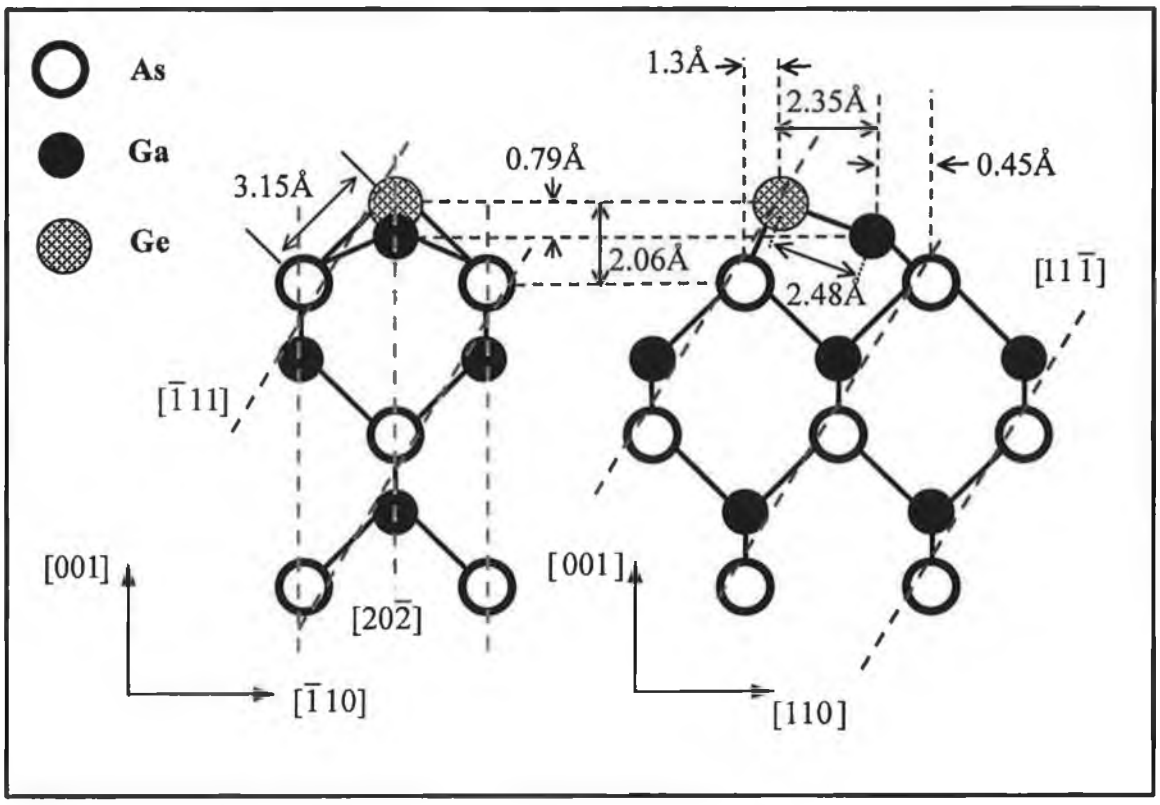

Figure 5.19 *The position of adsorbed germanium on GaAs(001) is shown with respect to the* $(1\bar{1}1)$ *and* $(11\bar{1})$ *planes as determined by NIXSW. The germanium replaces one of the bulk gallium sites in the continued layer and forms a buckled Ge-Ga dimer.*

The model presented in Figure 5.20 for the (1×2) reconstruction of Ge/GaAs(001) has been prepared using SARCH / LATUSE / PLOT3D (Surface ARCHitect/LATticeUSE / PLOT in 3D) Version 4.01. This freeware PC-based software package to create, visualise and analyse surface structures was obtained from Michael Van Hove [Van Hove 1995].

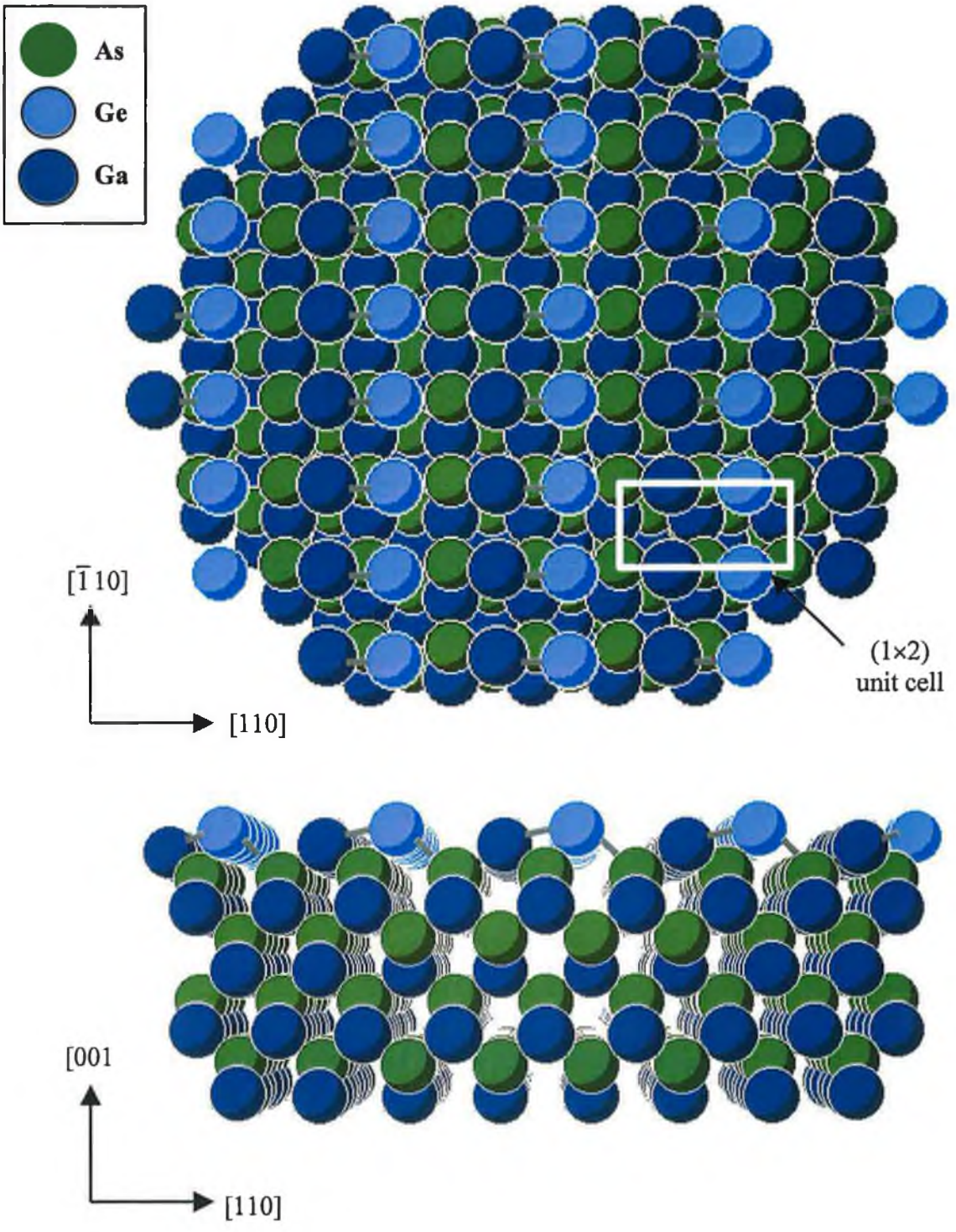

Figure 5.20 *Proposed model for the (1×2) reconstruction of Ge/GaAs(001) depicting the position of the buckled Ge-Ga dimer in the (1×2) unit cell.*

5.6 Core Level Photoelectron Spectroscopy Results

Core level photoemission studies were carried out on the clean GaAs(001)-(2×4) surface and for increasing Ge coverages, up to 7.7ML. The normalised intensity profiles of the As 3d, Ga 3d and Ge 3d core levels are shown in Figure 5.9. The growth curves for Ge/GaAs(001)-(2×4) are presented in Figure 5.12 which shows three distinct coverage phases: (i) 0.8ML coverage of Ge forming a weak (1×2) reconstruction; (ii) 1 - 4 ML coverage of Ge with a sharp (1×2) LEED pattern and (iii) after 6 - 8 ML coverage of Ge a (1×2)+(2×1) double domain structure. The surface core-level shifts (SCLSs) observed in photoemission experiments provide important information concerning the electronic and atomic structure. To understand the type of bonding occurring at each phase for the three different types of atoms, the core level photoemission spectra were resolved into components using a deconvolution program (TCFIT) as described in Section 2.6.2. Although photoemission is not a true structural technique, a correct assignment of the SCLSs of the inequivalent surface atoms can provide useful information about the surface structure. Figures 5.21-5.23 show the As 3d, Ga 3d and Ge 3d normalised core level spectra recorded for the clean surface and after deposition of germanium. For the clean GaAs(001)-(2×4) surface, two surface components (S_1 and S_2) are fitted for the As 3d and one for the Ga 3d spectrum as discussed in Section 5.3.

After the deposition of 0.8ML of germanium, the Ge 3d spectrum in Figure 5.23 (a) is fitted with a single component A, indicating the presence of only one Ge site on the surface. This component A, represents Ge dimerized to Ga in the (1×2) surface unit cell. The As 3d spectra is now resolved with two components, a bulk GaAs component and one SCLS at higher kinetic energy due to the presence of Ge-As bonds. The Ga 3d also has a bulk GaAs component and a surface component from bonding to Ge. This component appears at lower kinetic energy in the Ga spectra as shown in Figure 5.22. This component has a higher binding energy than the bulk Ga, which is indicative of a charge transfer from the Ga to the Ge and so the surface Ge is bonded to the Ga atoms exposed after desorption of the top layer As atoms. Further deposition of Ge up to a 1.7ML coverage, results in Ge bilayer growth with a (1×2) surface termination. A second peak, B, in Figure 5.23 (b), is required in fitting the Ge 3d. This second component is attributed to the formation of Ge-Ge dimers growing on top of the Ge/GaAs(001) interface. No further components are required to fit the Ge 3d core level spectra, for increasing Ge coverage up to 7.7ML.

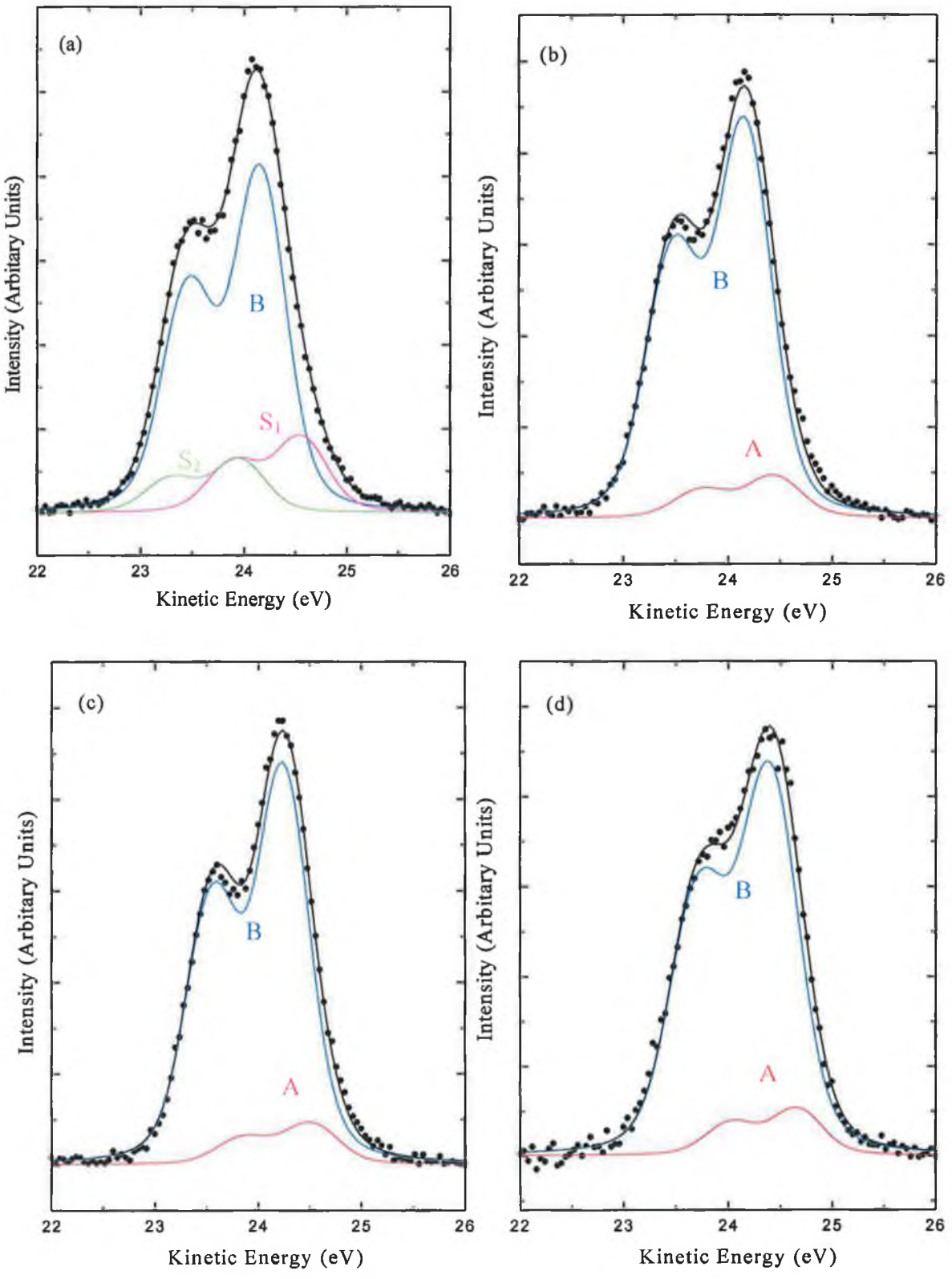

Figure 5.21 *As 3d core level photoemission spectra measured with a photon energy of 70eV for (a) clean GaAs(001)-(2×4), and after deposition of (b) 0.8ML, (c) 1.7ML and (d) 7.7ML of Ge onto the sample held at 700K. B represents the bulk As position and S_1 and S_2 indicate the kinetic energy of surface As components. A represents an As-Ge component.*

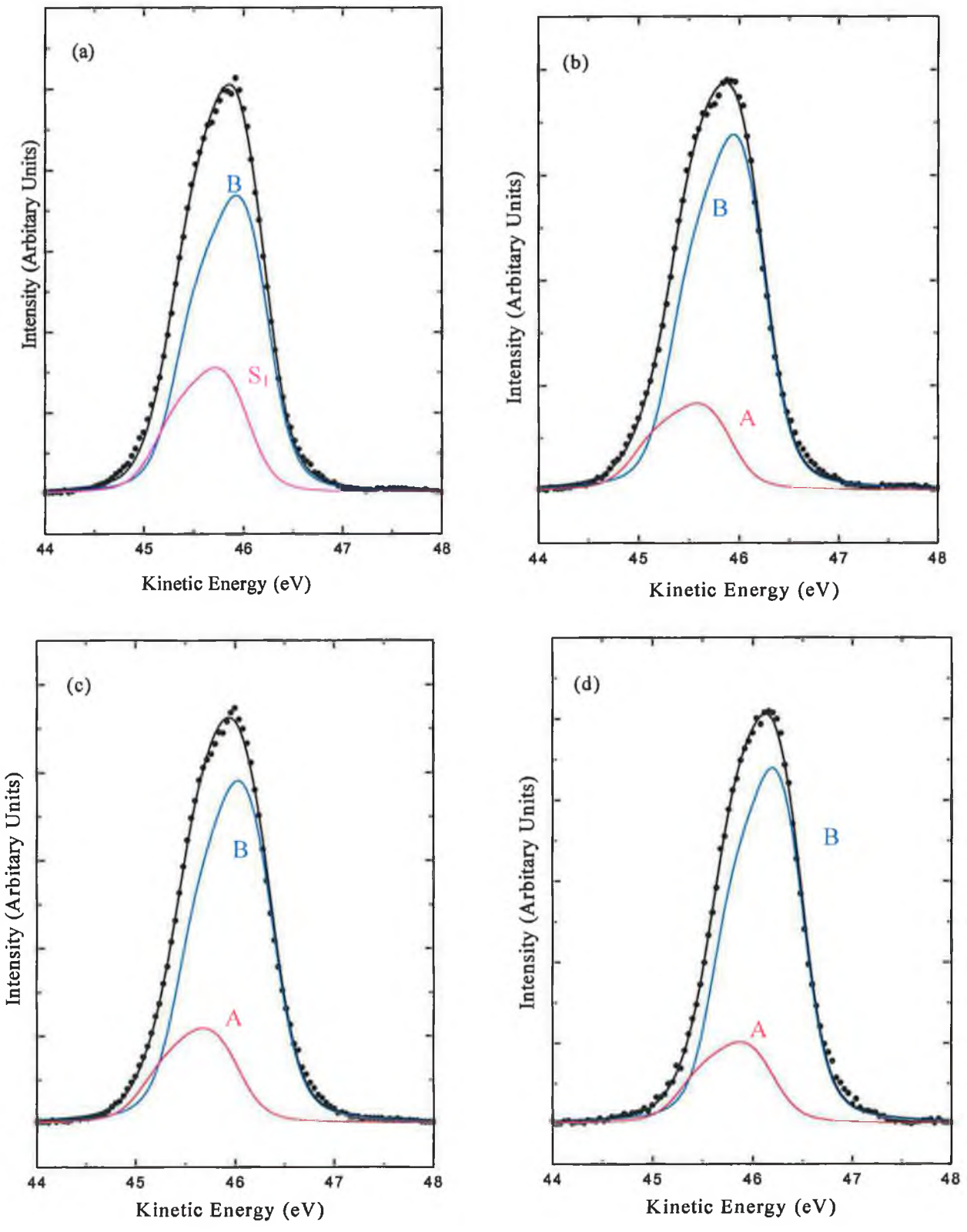

Figure 5.22 *Ga 3d core level photoemission spectra measured with a photon energy of 70eV for (a) clean GaAs(001)-(2×4), and after deposition of (b) 0.8ML, (c) 1.7ML and (d) 7.7ML of Ge onto the sample held at 700K. B represents the bulk Ga position and S_1 indicates the kinetic energy of a surface Ga component. A represents a Ga-Ge component.*

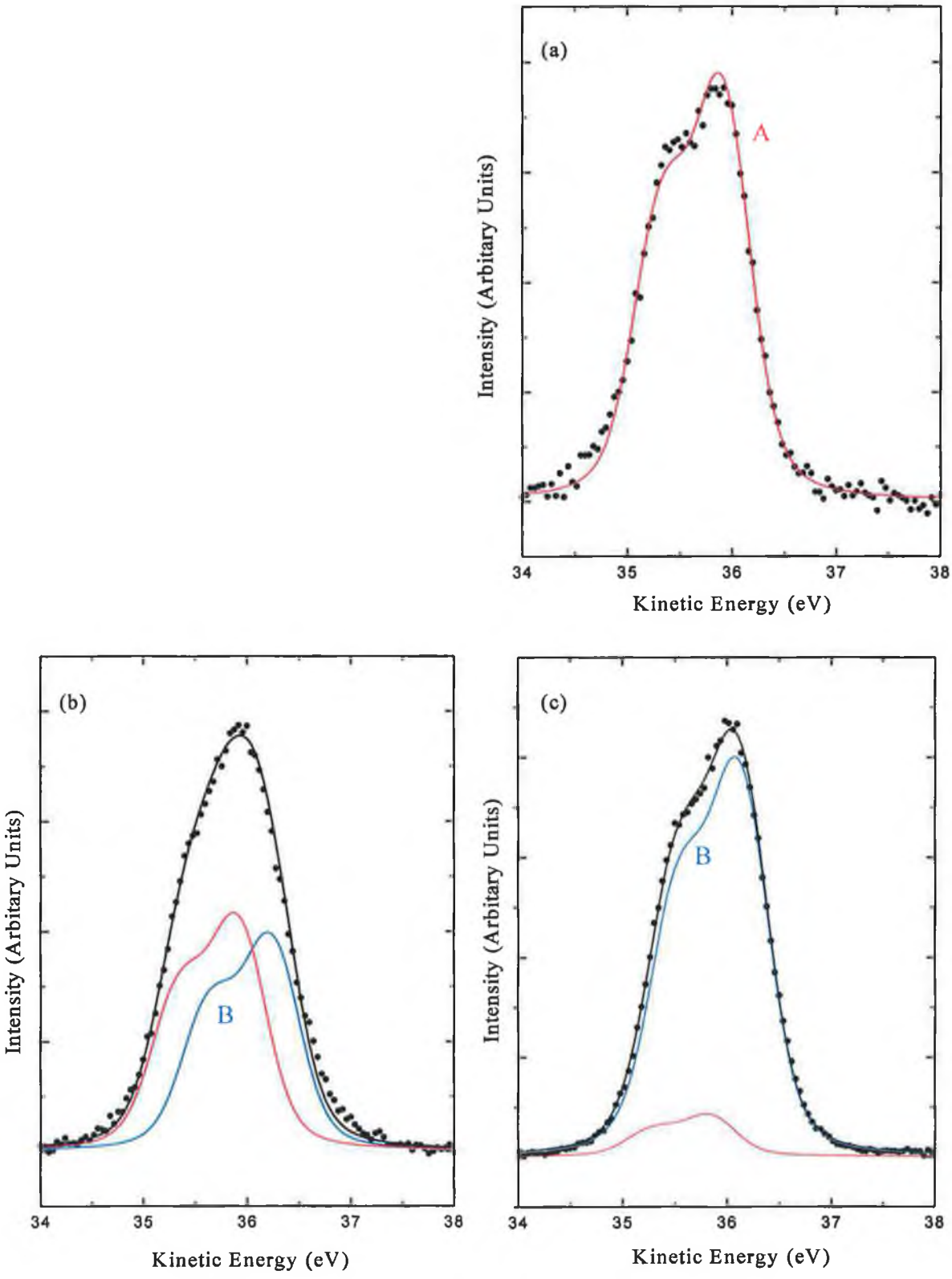

Figure 5.23 *Ge 3d core level photoemission spectra measured with a photon energy of 70eV and after deposition of (a) 0.8ML, (b) 1.7ML and (c) 7.7ML of Ge onto the clean GaAs(001)-(2×4) sample held at 700K. A represents the position of the Ge-Ga dimer and B indicates the kinetic energy of the Ge bonded to Ge on the surface.*

Values of the Gaussian broadening, Lorentzian width, spin-orbit splittings and the branching ratios used to obtain the best fits to the spectra are shown in Table 5.5. Values for the Lorentzian and spin-orbit splitting for As 3d and Ga 3d are consistent with other studies of clean GaAs surfaces [Le Lay 1991] [Moriarty 1994]. The Ge 3d Lorentzian and spin-orbit splitting parameter results are compatible to values obtained for photoemission studies of the clean Ge(100)-(2×1) surface [Goldoni 1996]. The Gaussian broadening is used to represent the instrument response function and the phonon broadening of the core level. The value of 0.48eV used to fit the As 3d and Ga 3d clean surface components is also used to fit the As 3d, Ge 3d and Ga 3d from the Ge/GaAs core level spectra. Branching ratios for the 3d core levels were set equal to the theoretical value of 2/3.

Fitting Parameter	Error	As 3d	Ge 3d	Ga 3d
Gaussian Broadening (eV)	±0.05eV	0.48	0.48	0.48
Lorentzian Broadening (eV)	±0.02eV	0.17	0.19	0.15
Spin-Orbit splitting (eV)	±0.05eV	0.69	0.59	0.46
Branching ratio	±0.05	0.67	0.67	0.67

Table 5.5 *Parameters used to fit the As 3d, Ga 3d and Ge 3d photoemission core levels.*

A comparison of the kinetic energy positions determined in fitting the As 3d, Ga 3d and Ge 3d core level spectra are shown in Table 5.6. The difference in binding energy of the As 3d and Ga 3d core levels for the clean (2×4) surface of GaAs(001) is found to be 21.87±0.04 eV. This energy difference is compatible with results obtained by Le Lay *et al.* [Le Lay 1991] and Waldrop *et al.* [Waldrop 1983] for the clean GaAs surfaces. Upon deposition of Ge, no change occurs in this separation. The As 3d to Ga 3d binding energy difference observed for the Ge/GaAs(001) heterojunction is the same to within experimental error of the bulk GaAs value. In the case of the clean GaAs(001)-(2×4) structure, the SCLS, S_1 of 0.4eV in the As 3d spectra is attributed to an As-dimer terminated surface. Upon adsorption of 0.8ML of Ge on the clean GaAs(001) surface, a new peak A in the As 3d spectra forms at a peak position of +0.28 eV with respect to the bulk As 3d component, as shown in Table 5.6. The A component is due to the surface Ge atoms backbonded to As atoms. The intensity ratio of the bulk As component (B) to the surface As component (A) was determined to be 9.27±0.20, as

shown in Table 5.6. Upon further deposition of Ge up to coverages of 7.7ML, this intensity ratio and the SCLS of the A component remains constant, as shown in Table 5.6. However, the overall intensity of the As 3d spectrum decreases with increasing Ge coverages, as can be observed in Figure 5.9. On the clean GaAs(001) surface, the surface Ga component (S_1) has a SCLS of -0.2eV with respect to the kinetic energy of the bulk gallium component (B). In the Ga 3d spectrum, the SCLS (A in Figure 5.22 (b)) is 0.35eV shifted to lower kinetic energy than the bulk Ga component (B), for a coverage of 0.8ML of Ge/GaAs(001). The intensity ratio of the bulk Ga atoms (B) to the surface Ga atoms (A) is 3.96±0.4. As for the As 3d spectrum, the intensity ratios for the Ga 3d peaks also remains constant with increasing germanium coverages, as can be seen in Table 5.6. The SCLS A also has a constant value of 0.33±0.02eV shifted to lower kinetic energy. These results can be explained by Ge initially bonding to Ga on the surface. For coverages greater than 1ML Ge grows layer-by-layer on top of the Ge-Ga mixed interface. The attenuation of both the As 3d and Ga 3d core levels with fixed intensity ratio (B/A) for increased Ge coverages illustrates that no outdiffusion of either As or Ga atoms occurs. Both signals being equally attenuated by the growing Ge-Ge monolayers.

	Clean	**0.8 ML**	**1.7 ML**	**7.7 ML**
LEED pattern	**(2×4)**	**(1×2)w**	**(1×2)**	**(1×2)+(2×1)**
As 3d Bulk K.E. position (eV)	24.20	24.18	24.26	24.42
K.E. shift of A (eV)	S_1=+0.40	+0.28	+0.27	+0.26
K.E. shift of S_2 (eV)	-0.19			
(Bulk / A) Intensity Ratio		9.47	9.47	8.89
Ge 3d K.E. position of A (eV)		35.93	35.94	35.86
K.E. shift of B (eV)			+0.32	+0.29
(A / B) Intensity Ratio			1.01	0.10
Ga 3d Bulk K.E. position (eV)	46.03	46.04	46.16	46.14
K.E. shift of A (eV)	S_1 =-0.20	-0.35	-0.34	-0.31
(Bulk / A) Intensity Ratio		4.08	3.60	4.21
ΔE (Ga 3d - As 3d)	21.83	21.86	21.90	21.88

Table 5.6 *Comparison of bulk and surface components kinetic energy positions of As 3d, Ga 3d and Ge 3d for clean GaAs(001) and for three phases of Ge growth.*

The Ge 3d core level spectra were resolved into two components, labelled A and B in Figure 5.23. The A component has been attributed to the formation of Ge-Ga dimers on the surface for 0.8ML Ge coverages. The B component is assigned to the formation of Ge-Ge dimers on top of the Ge-Ga dimers. At 1.7ML coverage, the ratio of the Ge-Ga dimer component (A) to the Ge-Ge dimer component (B) are present on the surface in approximately equal quantities, as shown in Table 5.6. The intensity ratio of A/B is 1.01 at this coverage. With increased Ge coverages up to 7.7ML, there is a substantial increase in the intensity of the B component as only a small fraction (~0.10) of the total Ge deposited is bonded to Ga at the interface.

5.7 Discussion

The X-ray standing wave technique is capable of locating the position of particular atomic species adsorbed on a crystal surface. NIXSW is used to differentiate between adsorbate sites on a surface or interface. Previously, NIXSW results for Sb/Ga(001) shows the formation of symmetric Sb-Sb dimers with the Sb atoms occupying equivalent surface sites [Suigayama 1995] [Lee 1998]. For Si/GaAs(001), the Si atoms are reported to have two different sites on the surface occupying both Ga and As sites [Suigayama 1996]. Sulphur is shown to occupy bridge sites on the Ga-terminated GaAs(001) surface, forming bonds with the underlying Ga atoms [Suigayama 1994]. In this work for submonolayer coverages of Ge/GaAs(001), Ge atoms are shown to occupy only one site on the GaAs(001) surface.

NIXSW investigations for the Ge/GaAs(001)-(1×2) surface were carried out using four different planes for triangulation, the noncentrosymmetric $(1\bar{1}1)$ and $(11\bar{1})$ and the $(0\bar{2}2)$ and $(20\bar{2})$ planes at 90° to each other. The high coherent fractions determined for the XSW profiles for these Bragg reflections show the surface to be highly ordered. It is found that the Ge occupies a single site where it dimerizes to the second layer gallium after outdiffusion of the first layer arsenic atoms, forming a (1×2) LEED reconstruction in agreement with proposed models [Wang 1994a] [Srivastava 1996] [Emiliani 1999]. The Ge-Ga dimer of length 2.48Å is found to be positioned at an average height of 1.66Å above the next As layer. The core level photoemission studies presented support the top layer Ge-Ga dimerization at submonolayer coverages. In

contrast, for submonolayer coverages of Ge on the cleaved GaAs(110)-(1×1) surface, Ge forms stable clusters on the surface [Yang 1992a, 1992b]. These clusters are shown by STM to consist of ordered rows along the $[1\bar{1}0]$ direction. The row separation of 5.6Å coincides with the unreconstructed unit cell of Ge.

Core level photoemission studies reveal that for increased coverages of Ge on GaAs(001), Ge continues to grow on the mixed Ge-Ga interface in bilayer steps up to a coverage of 4ML. At 4ML the double layer mechanism breaks down and growth proceeds by single atomic layers with a (1×2)+(2×1) reconstruction. A comparison of LEED I-V profiles for a 9.5ML thickness of Ge on GaAs(001) and for the clean Ge(100) surface were measured by Mrstik [Mrstik 1983]. The surface structure of a thick Ge overlayer should be the same as that of bulk Ge unless interdiffusion effects are significant. These spectra were shown to have good agreement, indicating little or no As interdiffusion occurs [Mrstik 1983].

In conclusion, the initial stages of the Ge/GaAs(001) formation have been investigated combining LEED, XSW and photoemission studies. No (2×1)-Ge phase associated by other authors with a Ge-As dimer terminated phase was observed. A (1×2) reconstruction at submonolayer coverages was shown to be associated with a Ge-Ga terminated surface. For Ge coverages between 1 and 4ML, a (1×2) reconstruction was shown to be Ge terminated with Ge-Ge dimers growing as bilayers. With coverages greater than 6ML, this bilayer growth breaks down and the surface is found to be similar to that of a bulk Ge(001) crystal. Furthermore, no evidence for As or Ga outdiffusion is observed in agreement with previous reports [Mrstik 1983] [Wang 1994a] [Power 1998] [Emiliani 1999].

Chapter Five References

Bass J.M. and Matthai C.C., Phys.Rev. B 50 (1994) 11212, Theoretical simulation of scanning tunnelling microscopy images of the GaAs(001) β(2×4) and β(4×2) surfaces.

Bauer R.S. and Mikkelsen J.C., J. Vac. Sci. Technol. 21 (1982) 491, Surface processes controlling MBE heterojunction formation : GaAs(100)/Ge interfaces.

Bauer R.S. and Sang H.W. Jnr., Surf. Sci. 132 (1983) 479, On the adjustability of the abrupt heterojunction band-gap discontinuity.

Bedyzk M.J., Materlik G. and Kovalchuk M.V., Phys. Rev. B 30 (1984) 2453, X-Ray standing wave – modulated electron emission near absorption edges in centrosymmetric and noncentrosymmetric crystals.

Broekman L., Leckey R., Riley J., Usher B. and Sexton B., Surf. Sci. 331-333 (1995) 1115, Surface atomic structure of the GaAs (001) (2×4) reconstruction.

Chadi D.J., J. Vac. Sci. Technol. A 5 (1987) 834, Atomic structure of GaAs (100)-(2×1) and (2×4) reconstructed surfaces.

Chambers S.A. and T.J. Irwin, Phys. Rev. B 38 (1988) 7484, Epitaxial growth and band bending of n- and p-type Ge on GaAs(001).

Drathen P., Ranke W. and Jacobi K., Surf. Sci. 77 (1978) L162, Composition and structure of differently prepared GaAs(100) surfaces studied by LEED and AES.

Emiliani V., Shkrebtii A.I., Goletti C., Frisch A.M., Fimland B.O., Esser N. and Richter W., Phys. Rev. B 59 (1999) 10657, Ge/GaAs (001) interface formation investigated by reflectance anisotropy spectroscopy.

Falta J., Tromp M., Copel M., Pettit G.D. and Kirchner P.D., Phys. Rev. Lett. 69 (1992) 3068, Structure and composition of GaAs(001) surfaces.

Falta J., Tromp R.M., Copel M., Pettit G .D. and Kirchner P.D., Phys. Rev. B. 48 (1993a) 5282, Ga-As intermixing in a GaAs (001) reconstruction.

Falta J., Tromp M., Copel M., Pettit G.D. and Kirchner P.D., Phys. Rev. Lett. 70 (1993b) 3173, Comment on "structure and composition of the GaAs(001) surfaces".

Falta J., Reuter M.C. and Tromp R.M., Appl. Phys. Lett. 65 (1994) 1680, Growth modes of Ge on GaAs (001).

Farrell H.H. and Palmstrom C.J., J. Vac. Sci. Technol. B 8 (1990) 903, Reflection high-energy electron diffraction characteristic absences in GaAs (100) (2×4)-As: A tool for determining the surface stoichiometry

Frankel, D.J., Yu C., Harbison J.P. and Farrell H.H., J. Vac. Sci. Technol. B 5 (1987) 1113, High-resolution electron-energy-loss spectroscopy studies of GaAs (100) surfaces.

Goldoni A., Modesti S., Dhanak V.R., Sancrotti M. and Santoni A., Phys. Rev. B 54 (1996) 11340, Evidence for three surface components in the 3d core-level photoemission spectra of Ge(100)-(2×1) surface.

Harrison W.A., Kraut E.A., Waldrop J.R. and Grant R.W., Phys. Rev. B 18 (1978) 4402, Polar heterojunction interfaces.

Hashizume T., Xue Q.K., Zhou J., Ichimiya A. and Sakurai T., Phys. Rev. Lett. 73 (1994) 2208, Structures of As-rich GaAs (001)-(2×4) reconstructions.

Hashizume T., Xue Q.K., Zhou J., Ichimiya A. and Sakurai T., Phys. Rev. B 51 (1995) 4200, Determination of the surface structure of the GaAs (001)-(2×4) As-rich phase.

Jing X., Glassford K.M. and Chelikowsky J.R., Surf. Sci. 314 (1994) 289, Ge cluster formation with monolayer and submonolayer coverages on the GaAs(110) surface.

Katnani A.D., Chiaradia P., Sang H.W.Jr., Zurcher P. and Bauer R.S., Phys. Rev. B 31 (1985a) 2146, Microscopic effects at GaAs/Ge(100) molecular-beam-epitaxy interfaces: Synchrotron-radiation photoemission study .

Katnani A.D., Sang H.W.Jr., Chiaradia P. and Bauer R.S., J. Vac. Sci. Technol. B 3 (1985b) 608, Core-level photoemission study of MBE-grown GaAs(111) and (100) surfaces.

Kubby J.A. and Boland J.J., Surf. Sci. Rep. 26 (1996) 61, Scanning tunneling microscopy of semiconductor surfaces.

Kunc K. and Martin R.M., Phys. Rev. B 24 (1981) 3445, Atomic Structure and properties of polar Ge-GaAs (100) interfaces.

LaBella V.P., Yang H., Bullock D.W., Thibado P.M., Kratzer P. and Scheffler M., Phys. Rev. Lett. 83 (1999) 2989, Atomic Structure of the GaAs(001)-(2×4) Surface resolved using Scanning Tunneling Microscopy and First-Principles Theory.

Lee T.-L. and Bedzyk M.J., Phys. Rev. B 57 (1998) R15056, High-resolution structural of the Sb-terminated GaAs(001)-(2×4) surface.

Le Lay G., Mao D., Kahn A., Hwu Y. and Margaritondo G., Phys. Rev. B 43 (1991) 14301, High-resolution synchrotron-radiation core-level spectroscopy of decapped GaAs(100) surfaces.

Levermann A.H., Woolf D.A., Westwood D.I. and Macdonald J.E., Surf. Sci. 352-354 (1996) 812, An investigation by spot profile analysis low energy electron diffraction of Si grown on GaAs (001).

Ludeke R., Chiang, T.C. and Eastman D.E., Physica B+C 117B-118B, (1983) 819, Core-level photoemission studies of MBE-grown semiconductor surfaces.

McGinley C., Cafolla A.A., McLoughlin E., Murphy B., Teehan D., Moriarty P., Woolf D.A., Appl. Surf. Sci. 158 (2000) 292, Core-level photoemission study of Bi-GaAs(111)A interface.

Mitin V.F., Tkhorik Y.A. and Venger E.F., Microelectronics Journal 28 (1997) 617, All-purpose technology of physical sensors on the base of Ge/GaAs heterostructures.

Moriarty P., Murphy B., Roberts L., Cafolla A.A., Hughes G., Koenders L. and Bailey P., Phys. Rev. B 50 (1994) 14237, Photoelectron core-level spectroscopy and scanning tunneling microscopy study of sulphur-treated GaAs(100) surface.

Moriarty P., Beton P.B., Ma Y. -R. Henini M. and Woolf D.A., Phys. Rev. B 53 (1996a) 16148, Adsorbed and substituted Sb dimers on GaAs (001).

Moriarty P., Beton P.H., Ma Y.-R., Dunn A.W., Henini M. and Woolf D.A., J. Vac. Sci. Technol. B 14 (1996b) 943, (2x4)/c(2x8) to (4x2)/c(8x2) transition on GaAs(001) surfaces.

Moriarty P., Ma Y.-R., Dunn A.W., Beton P.H., Henini M., McGinley C., McLoughlin E., Cafolla A.A., Hughes G., Downes S., Teehan D. and Murphy B, Phys. Rev. B 55 (1997) 15397, Absence of long-range ordered reconstruction on the GaAs(311)A.

Morkoc H., Vacuum 42 (1991) 257, New approaches in heteroepitaxy and related devices.

Mrstik B.J., Surf. Sci. 124 (1983) 253, LEED and AES studies of the initial growth of Ge epilayers on GaAs (100).

Neave J.H., Larsen P.K., Joyce B.A., Gowers J. P. and van der Veen J.F., J. Vac. Sci. Technol. B 1 (1983) 668, Some observations on Ge:GaAs(001) and Ge:GaAs(001) interfaces and films.

Northrup J.E. and Froyen S., Phys. Rev. Lett. 71 (1993) 2276, Energetics of GaAs (100)-(2×4) and -(4×2) reconstructions.

Northrup J.E. and Froyen S., Phys. Rev. B 50 (1994) 2015, Structure of GaAs(001) surfaces: The role of electrostatic interactions.

Ohno T, Surf. Sci. 357-358 (1996) 265, First-principles study on the Ga-rich GaAs (001)-(4×2) surface.

Pashley M.D., Haberern K.W. Friday W., Woodall J.M. and Kirchner P.D., Phys. Rev. Lett. 60 (1988) 2176, Structure if GaAs(001) (2×4) -c(2×8) determined by scanning tunneling microscopy.

Power J.R., Weightman P. and Cafolla A.A., Surf. Sci. 402-404 (1998) 566, The initial stages of Ge-GaAs(100) interface formation studied by reflectance anisotropy spectroscopy and low-energy electron diffraction.

Reid J.S., Acta Cryst. A 39 (1983) 1, Debye-Waller factors of zincblende structure materials - A lattice dynamical comparison.

Salazar-Hernandez B., Vidal M.A., Navarro-Contreras, Vazquez-Lopez C., Thin Solid Films 352 (1999) 269, Epitaxial Growth of Strained Ge films on GaAs(001).

Schmidt W.G. and Bechstedt F., Surf. Sci. 360 (1996) L473, Atomic structures of GaAs(100)-(2×4) reconstructions.

Schmidt W.G. and Bechstedt F., Surf. Sci. 377-379 (1997) 11, Comparison of As-rich and Sb-terminated GaAs(100) (2×4) reconstructions.

Sieg R.M., http://eewww.eng.ohio-state.edu/~siegr/ee880r2.htm (1995), GaAs/Ge Solar cells for space power applications.

Spindt C.J., Cao R., Miyano K.E., Lindau I., Spicer W.E. and Pao Y.-C., J. Vac. Sci. Technol. B 8 (1990) 974, Morphological study of Ag, In, Sb and Bi overlayers on GaAs(100).

Spindt C.J., Yamada M., Meissner P.L., Miyano K.E., Kendelwicz T., Herrera-Gomez A., Spicer W.E. and Arko A.J., Phys. Rev. B 45 (1992) 11108, Electronic structure and Schottky-barrier formation on GaAs(100) surfaces prepared by thermal desorption of a protective arsenic coating.

Srivastava G.P. and Jenkins S.J., Surf. Sci. 352-354 (1996) 416, Theoretical studies of GaAs(001)-Ge (2×1) and (1×2) structures.

Srivastava G.P. and Jenkins S.J., Surf. Sci. 377-379 (1997a) 23, Atomic structure and bonding on GaAs(001)/Sb(2×4).

Srivastava G.P., Rep. Prog. Phys. 60 (1997b) 561, Theory of semiconductor surface reconstruction.

Strite S., Biswas D., Kumar N.S. Fradkin M. and Morkoc H., Appl. Phys. Lett. 56 (1990a) 244, Antiphase domain free growth of GaAs on Ge on GaAs/Ge/GaAs heterostructures.

Strite S., Unlu M.S., Adomi K., Gao G.-B., Agarwal A., Rockett A., Morkoc H., Li D., Nakamura Y. and Otsuka N., J. Vac. Sci. Technol. B 8 (1990b) 1131, GaAs/Ge/GaAs heterostructures by molecular beam epitaxy.

Sugiyama M., Maeyama S. and Oshima M., Phys. Rev. B 50 (1994) 4905, Structure of the sulphur-passivated GaAs(001) surface.

Sugiyama M., Maeyama S., Maeda F. and Oshima M., Phys. Rev. B 52 (1995) 2678, X-ray standing-wave study of an Sb-terminated GaAs(001)-(2×4) surface.

Sugiyama M., Maeyama S. and Oshima M., Appl. Phys. Lett. 68 (1996) 3731, X-ray standing wave study of Si-adsorbed GaAs(001) surface.

Tatsuyama C., Ueba H. and Kondo T., Appl. Surf. Sci. 33-34 (1988) 180, Low-Energy-Electron-Loss Spectroscopy of thin Ge layers on a GaAs(100) surface.

Van Hove M., (1995), Software packages SARCH/LATUSE/PLOT3D Version 4.01, http://electron.lbl.gov/webmain.html.

Vitomirov I.M., Raisanen A.D., Finnefrock A.C., Viturro R.E., Brillson L.J., Kirchner P.D., Petit G.D. and Woodall J.M., J. Vac. Sci. Technol. B 10 (1992) 1898, Temperature-dependent chemical and electronic structure of reconstructed GaAs (100) surfaces.

Waasmaier D. and Kirfel A., Acta Cryst. A 51 (1995) 416, New analytical scattering factor functions for free atoms and ions.

Waldrop J.R., Kraut E.A., Kowalczyk S.P. and Grant R.W., Surf. Sci. 132 (1983) 513, Valence-band discontinuities for abrupt (110), (100) and (111) oriented Ge-GaAs heterojunctions.

Wang X. -S., Self K., Loenard D., Bressler-Hill V., Maboudian R., Petroff P.M. and Weinberg W.H., J.Vac.Sci. Technol. B 11 (1993) 1477, Scanning tunneling microscopy studies of Ge/GaAs(100) interface formation.

Wang X. -S., Self K., Bressler-Hill V., Maboudian R. and Weinberg W.H., Phys. Rev. B 49 (1994a) 4775, Initial stages of Ge/GaAs (100) interface formation.

Wang X. -S., Self K. and Weinberg W.H., J. Vac. Sci. Technol. 12 (1994b) 1920, Growth mode of Ge on GaAs (100).

Wassermeier M., Behrend J., Daweritz L. and Ploog K., Phys. Rev. B 52 (1995) R2269, Reconstruction of the GaAs(001) surface induced by submonolayer Si deposition.

Wassermeier M., Kellermann S., Behrend J., Daweritz L. and Ploog K., Surf. Sci. 414 (1998) 298, Submonolayer Si deposition at low temperatures on the GaAs(001)-(2×4) surface studied by scanning tunneling microscopy.

Whitman L.J., Bennett B.R., Kneedler E.M., Jonker B.T. Shanabrook B.V., Surf. Sci. 436 (1999) L707, The structure of Sb-terminated GaAs (001) surfaces.

Woolf D.A., Sobiesierski Z., Westwood D.I. and Williams R.H., J. Appl. Phys. 71 (1992) 4908, The molecular beam epitaxial growth of GaAs/GaAs(111)B: doping and growth temperature studies.

Xue Q.-K., Hashizume T. and Sakurai T, Prog. Surf. Sci. 56 (1997) 1, Scanning tunneling microscopy of III-V compound semiconductor (001) surfaces.

Xue Q.-K., Hashizume T. and Sakurai T, Appl. Surf. Sci. 141 (1999) 244, Scanning tunneling microscopy study of GaAs(001) surfaces.

Yang Y.-N., Luo Y.S. and Weaver J.H., Phys. Rev. B 46 (1992a) 15387, Scanning tunneling microscopy of Ge/GaAs(110). I. Initial nucleation and growth.

Yang Y.-N., Luo Y.S. and Weaver J.H., Phys. Rev. B 46 (1992b) 15395, Scanning tunneling microscopy of Ge/GaAs(110). II. Coalescence and layer-by-layer growth.

Chapter Six

Conclusions and further work

The purpose of this work was to investigate the initial stages of interface formation for the bimetallic Sn/Cu{100} system and the Ge/GaAs(001) semiconductor heterostructure. The two main structural techniques used in this work were low energy electron diffraction (LEED) and X-ray standing wave spectroscopy (XSW).

The fact that XSW provides a quantitative measure of the degree of disorder or multiple site occupation through the coherent fraction makes it almost unique in surface structural methods. By comparison LEED measurements concentrate on the intensity modulations of the diffracted beams and thus selectively provides structural data for those parts of the surface that exhibit good long-range order. In contrast, XSW does not rely on long-range order in the absorber atoms, but sums over these absorbers in all their sites, even if more than one site is occupied. In the simplest case of one site being occupied, the coherent fraction provides a measure of the local disorder, both static and dynamic, for which a Gaussian distribution can be obtained from the attenuation of the coherent fraction by the Debye-Waller factor. However, in the case of multiple sites the coherent fraction is no longer a direct measure of the degree of local order, being dependent on the actual sites and their layer spacings relative to the scattering planes. LEED provides selective information dominated by the long-range ordered component of the surface and largely ignores any disordered components. Of course, if a surface does have mixed sites or a large degree of local disorder, determining the actual spatial distribution giving rise to the measured values of the coherent position and coherent fraction in XSW is difficult, and no solution is unique. Nevertheless, the specific structural models can be tested against these two parameters, so the XSW technique can provide valuable information on complex structures.

In Chapter Four, LEED spectra were recorded for the four submonolayer phases of Sn/Cu{100}. The analysis of the LEED data involved a large computational effort and lots of models were considered and tested. New structural models for the four submonolayer phases are proposed based on a double scattering LEED simulation code. Auger Electron Spectroscopy (AES) was used to determine Sn coverages on the surface. Temperature Programmed Desorption (TPD) was used to eliminate subsurface structures as possible models. Using a combination of these techniques it was not possible to further differentiate between surface alloy and overlayer structures. Clearly, further quantitative structural work both by LEED I-V analysis and STM is required. The LEED data has been prepared for full dynamical LEED I-V analysis, which has

commenced for phase III of the Sn/Cu{100}system, in collaboration with M. Lindroos, Tempere University, Finland. The models presented in this work are being used as the initial starting structures for full dynamical LEED I-V analysis. STM measurements on this system have not been reported to date. An STM experiment of the Sn/Cu{100} system is presently being planned on the newly acquired Omicron UHV STM at Dublin City University. XSW would be a suitable technique for investigation of the Sn/Cu{100) system and would comprehensively show whether the Sn atoms form surface alloy or overlayer structures.

In Chapter Five, NIXSW studies were reported for the investigation of the Ge/GaAs(001)-(1×2) surface. This technique allowed the accurate determination of the position of Ge atoms dimerized to Ga atoms on the GaAs surface. The position of the Ga atoms in the Ge-Ga dimer could not be readily determined. Although photoelectron spectroscopy (PES) is not a true structural technique, a correct assignment of the surface core level shifts of the inequivalent surface atoms can provide useful information about the surface structure. In this study, the combination of XSW and core level PES was used to determine that Ge occupies only one site (Ge-Ga dimer) on the submonolayer Ge/GaAs(001)-(1×2) surface. For increased adsorbate coverages, the Ge-Ga dimer forms a mixed interface on top of which pure Ge layers grow. For thick Ge coverages, ~7.7ML, the surface is seen to resemble that of bulk Ge(001) forming a (1×2)+(2×1) double domain structure. The use of XSW and PES are shown to be good techniques for surface structure determination. The only drawback of these techniques is that synchrotron radiation is required as a suitable radiation source.

LEED I-V measurements are planned on this system using a lanthanum hexaboride filament, which yields higher resolution than the tungsten thoriated filament. Carrying out dynamical LEED I-V calculations, for this highly ordered system, should determine the position of both atoms in the Ge-Ga dimer and the amount of dimer buckling in the (1×2) unit cell. An STM experiment on the Ge/GaAs (1×2) and (1×2)+(2×1) structures is also planned at Dublin City University. High resolution STM might possibly distinguish between a Ge-Ga terminated surface at low coverages and a Ge-Ge terminated surface at high coverages.

List of Publications

Moriarty P., Ma Y. -R., Dunn A.W., Beton P.H., Henini M., McGinley C., McLoughlin E., Cafolla A.A., Hughes G., Downes S., Teehan D. and Murphy B., Phys. Rev. B 55 (1997) 23, Absence of long-range ordered reconstruction on the GaAs (311)A surface.

Cafolla A.A., Mc Ginley C., Mc Loughlin E., Hughes G., Moriarty P., Dunn A.W., Ma Y.-R., Teehan D., Murphy B., Downes S. and Woolf D.A., Surf. Sci. 377-379 (1997) 130, Adsorption of Sb on GaAs (111)B studied by photoemission and low energy electron diffraction.

Mc Ginley C., Cafolla A.A., Mc Loughlin E., Murphy B., Teehan D., Moriarty P. and Woolf D.A., Appl. Surf. Sci. 158 (2000) 292, Core-level photoemission study of the Bi-GaAs (111)A interface.

Mc Loughlin E., Cafolla A.A., AlShamaileh E. and Barnes C.J., *Submitted to Surface Science*, A re-interpretation of the Sn/Cu{100} surface phase diagram.

Mc Loughlin E., Quinn P., Cafolla A.A., Murphy B. and Cowie B., *In preparation*, An X-ray standing wave study of the initial stages of Ge/GaAs(001) interface formation.

Table of Acronyms

ADES	Angle Dispersing Electron Spectrometer
AES	Auger Electron Spectroscopy
ARPES	Angle Resolved Photoelectron Spectroscopy
ARUPS	Angle Resolved Ultraviolet Photoelectron Spectroscopy
CHA	Concentric Hemispherical Analyser
CMA	Cylindrical Mirror Analyser
EELS	Electron Energy Loss Spectroscopy
ESCA	Electron Spectroscopy for Chemical Analysis
EXAFS	Extended X-ray Absorption Fine Structure
HREELS	High Resolution Electron Energy Loss Spectroscopy
LEED	Low Energy Electron Diffraction
LEIS	Low Energy Ion Scattering
MBE	Molecular Beam Epitaxy
MEIS	Medium Energy Ion Scattering
ML	Monolayer
NEXAFS	Near-edge X-ray Absorption Fine Structure
NIXSW	Normal Incidence X-ray Standing Wave
PhD	Photoelectron Diffraction
PES	Photoelectron Spectroscopy
RAS	Reflectance Anisotropy Spectroscopy
RBS	Rutherford Back-Scattering
RHEED	Reflection High Energy Electron Diffraction
SEXAFS	Surface Extended X-ray Absorption Fine Structure
SRS	Synchrotron Radiation Source
STM	Scanning Tunnelling Microscopy
SXPS	Soft X-ray Photoelectron Spectroscopy
TPD	Temperature Programmed Desorption
UHV	Ultra High Vacuum
UPS	Ultraviolet Photoelectron Spectroscopy
XPD	X-ray Photoelectron Diffraction
XPS	X-ray Photoelectron Spectroscopy
XSW	X-ray Standing Wave

List of Figures

Figure 2.17 As 3d core level spectrum fitted with three components showing the surface shifted components.

Figure 3.1 Knudsen cell from W.A. Technology.

Figure 3.2 Graph of vapour pressure (Torr) versus Temperature (K) for tin and germanium.

Figure 3.3 Picture and schematic layout of UHV chamber.

Figure 3.4 Schematic of experimental setup for LEED studies.

Figure 3.5 Energy calibration graph for LEED controller.

Figure 3.6 S-wave phase shifts for copper and tin versus energy.

Figure 3.7 The atom positions for (a) an overlayer and (b) a surface alloy model are shown. The grey circles represent the top layer tin atoms, the orange circles represent the second layer copper atoms and the green circles represent the top layer copper atoms. The substrate unit cell $\begin{pmatrix} A2X & A2Y \\ B2X & B2Y \end{pmatrix}$ is illustrated in black for each model.

Figure 3.8 Schematic of experimental setup for Auger analysis.

Figure 3.9 Illustration of Auger (N(E) peak and differentiated Auger peak (dN(E)/dE).

Figure 3.10 Schematic of experimental setup for temperature programmed desorption studies.

Figure 3.11 Schematic of the experimental UHV chamber for X-ray standing wave studies.

Figure 3.12 (a) InSb(111) and (b) Ge(111) flux output from station 6.3 at Daresbury SRS [McDowell 1986].

Figure 3.13 EDC of the As 2p core level at a photon energy of 3093eV. The kinetic energies of the On peak and Off peak positions used for XSW detection are indicated.

Figure 3.14 NIXSW profile for the $[1\,\bar{1}\,1]$ Bragg reflection in GaAs calculated for coherent distances from 0 to 1. F_{co} is 0.8, E_{Bragg} is 1899.5eV and an instrumental resolution of 0.5eV.

Figure 3.15 NIXSW profiles calculated for a range of coherent fractions, where the E_{Bragg} is 1899.5 eV, D is 1.0 and an instrumental resolution of 0.5eV. A reduction in coherent fraction reduces the height of the XSW profile but does not broaden it.

Figure 3.16 The experimental chamber setup at station 6.2, Daresbury SRS, which used for photoelectron spectroscopy studies.

Figure 3.17 Flux output from (a) the 710 line/mm and (b) the 1800 line/mm gratings, which were used in the toroidal grating monochromator at beamline 6.2 [Turner 1992].

Figure 4.1 Bulk Phase Diagram of Sn-Cu Alloy [Hansen 1958].

Figure 4.2 LEED patterns and models for phases I-IV [Argile 1982]

Figure 4.3 Clean copper bulk crystal structure.

Figure 4.4 Measured specular and integral order beam I-V profiles for clean Cu{100}.

Figure 4.5 Comparison of experimental and calculated best-fit spectra for clean Cu{100} integral beams [Muller 1995].

Figure 4.6 Intensity of the (0,0) beam from Cu{100}, measured as a function of energy, recorded at θ=10° off normal incidence and theoretically generated at normal incidence using double scattering simulations with all copper atoms in ideal lattice sites.

Figure 4.7 The effect on Bragg peak positions by changing the top copper layer position by ±1Å from the bulk lattice spacing of 1.81 Å

Figure 4.8 Growth Sites for adsorbates on Cu{100: (a) surface alloy; (b) four-fold hollow site; (c) bridge site and (d) on-top site, where dz =0Å, 2.27Å, 2.6Å and 2.9Å, respectively, with the copper interplanar spacing $\frac{1}{2}a_0$=1.81Å.

Figure 4.9 Auger Signal (AS) versus coverage in monolayers for tin deposition on Cu{100} at 300K where (a) is taken from Argile 1982 and (b) this experiment. Both sets were measured by monitoring the Cu ($M_{2,3}VV$) auger peak at 63 eV and the Sn ($M_5N_{4,5}N_{4,5}$) auger peak at 430eV. The blue curve in (b) is the theoretical variation obtained by assuming a layer-by-layer growth mode.

Figure 4.10 A negative image of a LEED picture recorded at 120eV by a CCD camera for clean Cu{100} indicating the specular and integral order beams.

Figure 4.11 CCD images of the LEED patterns at 127±2 eV for Phase I, mixed Phase I & Phase II and Phase II, respectively.

Figure 4.12 CCD images of the LEED patterns at 127±2 eV for Phase III, mixed Phase III & Phase IV and Phase IV, respectively.

Figure 4.13 The evolution of LEED line profiles along a line through the (0,1) to (1,0) integral beams taken at 90eV in 1 minute intervals during the evaporation of Sn on Cu{100} at 300K. The spectrum at 0 minutes represents the line profile for clean Cu{100}. After 12 minutes two spots are best resolved from the split quartets of spots centred around the (½,½) position, indicating completion of Phase I. Between 13 to 16 minutes the phases are seen to coexist. Phase II is reaches maximum perfection after 20 minutes deposition.

Figure 4.14 The evolution of LEED spot profiles along the line from the (0,1) to (1,0) integral beams taken at 90eV in 1minute intervals for the evaporation of tin on Cu{100} at 300K. The spectrum at 0 minutes represents the line profile for clean Cu{100}. Phase II and III are shown to coexist up to 26 minutes, with maximum perfection of phase III after 28 minutes. Completion of a full monolayer for phase IV was achieved after 40 minutes. The dotted lines indicate the positions of fractional order spots for phases III and IV.

Figure 4.15 A overview of line profiles for the growth of Sn on Cu{100} is shown with the profiles normalised to the intensity of the (0,1) spot. The (½,½) beam was observed to have maximum intensity in Phase III.

Figure 4.16 Phase I LEED pattern, with labels (a) to (h) indicating the symmetrically equivalent fractional order beams. (a) –(d) represent the (½,½) spot splitting, (e) & (f) represent the (½,0) spot splitting and (g) & (h) represent the (½,1) spot splitting.

Figure 4.17 Domains of a superstructure of nine p(2×2) unit cells separated by antiphase domain walls in a pinwheel arrangement.

Figure 4.18 Surface Alloy and overlayer models and simulated LEED patterns for Phase I based on an antiphase domain wall superstucture of $\begin{bmatrix} 8 & 1 \\ 1 & 8 \end{bmatrix}$. The (½,½) spot splitting of $1/9^{th}$ of the integral order separation, in the simulated LEED pattern is not in agreement with the measured value from experimental LEED pictures of $1/11^{th}$.

Figure 4.19 Proposed surface alloy structure and simulated LEED pattern averaged over the range 100-200eV, for phase I, based on antiphase domain wall superstuctures with n=10.

Figure 4.20 Proposed overlayer structure and simulated LEED pattern averaged over the range 100-200eV, for phase I, based on antiphase domain wall superstuctures with n=10.

Figure 4.21 The specular beam measured at 10° off-normal incidence and the integral order beams measured at normal incidence for phase I, 0.21ML of Sn/Cu{100, uncorrected for Inner Potential.

Figure 4.22 LEED I-V plots for the symmetrically averaged fractional order beams for phase I of Sn/Cu{100}, uncorrected for Inner Potential. (i) The (½,½) beam where (a)-(d) are the four individual quartets and (avg) is the measurement of all four and (ii) (e) & (f) are the (½,0) doublet beams and (g) & (h) are the (½,1) doublet beams.

Figure 4.23 p(2×6) structural models suggested for Phase II; (a) Argile and Rhead overlayer model, (b) the surface alloy model, θ=0.42ML, based on domains of c(2×2) separated by p(2×2) unit cells and (c)) the surface alloy model, θ=0.33ML, based on domains of p(2×2) separated by c(2×2) unit cells.

Figure 4.24 p(2×6) models and generated LEED patterns (100-200eV) for Phase II; (a) Argile and Rhead overlayer model, (b) the surface alloy model, θ=0.42ML, based on domains of c(2×2) separated by p(2×2) unit cells and (c) the surface alloy model, θ=0.33ML, based on domains of p(2×2) separated by c(2×2) unit cells.

Figure 4.25 p(2×6) overlayer models suggested for phase II (a) the overlayer model, θ=0.42ML, based on domains of c(2×2) separated by p(2×2) unit cells and (b) the overlayer model, θ=0.33ML, based on domains of p(2×2) separated by c(2×2) cells.

Figure 4.26 p(2×6) models and simulated LEED patterns (100-200eV) for Phase II; (a), (b) the overlayer model, θ=0.42ML, based on domains of c(2×2) separated by p(2×2) unit cells and (c), (d) the overlayer model, θ=0.33ML, based on domains of p(2×2)

separated by c(2×2) cells. (e) LEED simulation of surface alloy model with θ=0.37ML and (f) LEED simulation of overlayer model with θ=0.37ML

Figure 4.27 I-V spectra for (a) the specular and integral order beams, and (b) fractional beams for Phase II, 0.37ML of Sn/Cu{100}, uncorrected for Inner Potential.

Figure 4.28 Structural models for phase III, 0.5ML Sn/Cu{100}; (a) Argile and Rhead (b) surface alloy model and (c) overlayer model with Sn occupying the ideal four-fold hollow sites.

Figure 4.29 Structural models and simulated LEED patterns for phase III, 0.5ML Sn/Cu{100}; (a) Argile and Rhead (b) surface alloy model and (c) overlayer model with Sn laterally shifted by 0.4Å. In (b) and (c) the red lines indicate the positions of lattice coordinate sites and the arrows indicate the direction of tin atom displacement.

Figure 4.30 Simulated LEED patterns for surface alloy (left) and overlayer (right) structures for Phase III, with increasing lateral movement (a) & (d) 5%, (b) & (e) 10%, (c) & (f) 15%, of Sn atoms along the [010] direction from lattice coordinate sites.

Figure 4.31 Normalised I-V spectra for Phase III, 0.5ML Sn/Cu{100}; (a) specular and integral beams and (b) fractional order beams. Energies are uncorrected for the Inner potential.

Figure 4.32 Structural models for Phase IV Sn/Cu{100}; (a) Argile and Rhead, (b) surface alloy model and (c) overlayer model.

Figure 4.33 Structural models and simulated LEED for Phase IV Sn/Cu{100}; (a) Argile and Rhead with dashed lines indicating the direction of the Sn rows, (b) surface alloy model and (c) overlayer model.

Figure 4.34 LEED I-V spectra for phase IV of Sn/Cu{100}: (a) specular and integral order beams; and (b) fractional order beams, where the energy is uncorrected for the inner potential.

Figure 4.35 (a) Top view and (b) side view of the geometry of formic acid on copper.

Figure 4.36 Formic Acid TPD of (a) clean Cu{100} and Sn/Cu{100} submonolayer phases (b) I, (c) II, (d) III and (e) IV.

Figure 4.37 Symmetry averaged normal incidence LEED I-V spectra for clean Cu{100} and Sn phases I to IV: (a) (1,0) beams; (b) (1/2,1/2) beams.

Figure 5.1 Surface structure models for (a) bulk-truncated GaAs(100) surface with an As-top layer; (b) As-rich (2×4) reconstructed GaAs(100); (c) Ge-As dimerization forming a (2×1) superstructure on GaAs(100); and (d) the (1x2) order formed by Ge-Ga dimerizarion on GaAs(100) [Wang 1994a].

Figure 5.2 A side view for the atomic geometry for (a) GaAs(100)/Ge(2×1) and (b) GaAs(100)/Ge(1×2) structures [Srivastava 1996].

Figure 5.3 The schematic of a GaAs zincblende structure. At the bulk terminated (1×1) surface each (As) has one unpaired electron with a surface lattice of 4Å. Along the

(001) crystal axis alternative As layer and Ga layer occur with an interplanar distance (from As to a neighbouring Ga layer) of 1.41Å [Xue 1999].

Figure 5.4 Atomic models (a) three As-dimer model, (b) bilayer two-As-dimer model, (c) two-As-dimer model with second layer Ga dimerized and (d) extra-As dimer model for GaAs(001) [Xue 1999].

Figure 5.5 (a) The structure of the unreconstructed GaAs (001) arsenic-rich surface. (b) The missing-dimer model for the GaAs (001) (2×4) surface. The two types of missing-dimer boundary, in-phase (IP) and antiphase (AP), are shown giving rise to (2×4) and c(2×8) structures. The intersection of a domain boundary along the [110] direction with the IP and AP boundaries is shown giving rise to three types of boundary kinks, K1, K2 and K3. Disorder in the arsenic pairing (X) with three missing arsenic atoms (dashed circles) is also illustrated [Pashley 1988].

Figure 5.6 (a) Experimental LEED pattern and (b) representative LEED pattern for the GaAs(001)-(2×4).

Figure 5.7 (a) Experimental LEED pattern and (b) representative LEED pattern for the GaAs(001)-c(2×8).

Figure 5.8 (a) As(3d) and (b) Ga(3d) line shape for the (2×4)/c(2×8) reconstruction of GaAs(001), taken with 70eV photon energy. The B refers to the bulk component and S_1 and S_2 represent surface components.

Figure 5.9 Evolution of the core-level photoemission from As 3d, Ge 3d and Ga 3d at hv=70eV for GaAs(001)-(2×4) and increasing coverage of epitaxial Ge overlayers. Spectra were recorded at room temperature for different Ge coverages and after annealing the substrate to different temperatures. The reconstructions for all stages are shown where w represents a weak or diffuse LEED pattern.

Figure 5.10 (a) Experimental LEED pattern and (b) representative LEED pattern for the Ge/GaAs(001)-(1×2) reconstruction.

Figure 5.11 (a) Experimental LEED pattern and (b) representative LEED pattern for the Ge/GaAs(001)-(1×2)+ (2×1) reconstruction.

Figure 5.12 Normalised relative intensities of the As 3d, Ga 3d and Ge 3d core level photoemission peaks as a function of Ge growth on GaAs(001)-(2×4) held at a temperature of 700K. The As 3d + Ga 3d curve represents the combined intensity of Ga and As core 3d levels, which on the clean surface is represented as 100%.

Figure 5.13 A wide energy range Energy Distribution Curve (EDC) identifying the As, Ge and Ga photoemission and Auger electron peak positions and relative intensities, recorded at a photon energy of 3093eV.

Figure 5.14 NIXSW profiles from the reflection plane at 3093eV. The 2p photoemission and the LMM Auger emissions are shown for the Ge adsorbate and the As and Ga bulk species.

Figure 5.15 NIXSW profiles from the $(20\bar{2})$ reflection plane at 3093eV. The 2p photoemission and the LMM Auger emissions are shown for the Ge adsorbate and the As and Ga bulk species.

Figure 5.16 NIXSW profiles from the $(1\,\bar{1}\,1)$ reflection plane at 1900eV. The 2p photoemission and the LMM Auger emissions are shown for the Ge adsorbate and the As and Ga bulk species.

Figure 5.17 NIXSW profiles from the $(11\,\bar{1})$ reflection plane at 1900eV. The 2p photoemission and the LMM Auger emissions are shown for the Ge adsorbate and the As and Ga bulk species.

Figure 5.18 The $(1\,\bar{1}\,1)$ planes in a zincblende lattice. The gallium and arsenic atoms are in two layers separated by Δ. The actual Bragg scattering plane is between the two layers, marginally closer to the arsenic atoms.

Figure 5.19 The position of adsorbed germanium on GaAs(001) is shown with respect to the $(1\,\bar{1}\,1)$ and $(11\,\bar{1})$ planes as determined by NIXSW. The germanium replaces one of the bulk gallium sites in the continued layer and forms a buckled Ge-Ga dimer.

Figure 5.20 Proposed model for the (1×2) reconstruction of Ge/GaAs(001) depicting the position of the buckled Ge-Ga dimer in the (1×2) unit cell.

Figure 5.21 As 3d core level photoemission spectra measured with a photon energy of 70eV for (a) clean GaAs(001)-(2×4), and after deposition of (b) 0.8ML, (c) 1.7ML and (d) 7.7ML of Ge onto the sample held at 700K. B represents the bulk As position and S_1 and S_2 indicate the kinetic energy of surface As components. A represents an As-Ge component.

Figure 5.22 Ga 3d core level photoemission spectra measured with a photon energy of 70eV for (a) clean GaAs(001)-(2×4), and after deposition of (b) 0.8ML, (c) 1.7ML and (d) 7.7ML of Ge onto the sample held at 700K. B represents the bulk Ga position and S_1 indicates the kinetic energy of a surface Ga component. A represents a Ga-Ge component.

Figure 5.23 Ge 3d core level photoemission spectra measured with a photon energy of 70eV and after deposition of (a) 0.8ML, (b) 1.7ML and (c) 7.7ML of Ge onto the clean GaAs(001)-(2×4) sample held at 700K. A represents the position of the Ge-Ga dimer and B indicates the kinetic energy of the Ge bonded to Ge on the surface.

List of Tables

Table 5.4 NIXSW coherent positions and coherent fractions for the (1×2) Ge/GaAs(001) interface. The coherent positions (D) are given in units of the interlayer spacing.

Table 5.5 Parameters used to fit the As 3d, Ga 3d and Ge 3d photoemission core levels.

Table 5.6 Comparison of bulk and surface components kinetic energy positions of As 3d, Ga 3d and Ge 3d for clean GaAs(001) and for three phases of Ge growth.

Appendix A

Modified Double Scattering Simulation Code
from N. Panagiotides, D.R. Batchelor and D.A. King,
Chemical Physics Letters, 171 (1991) 419

```
C    ******* U N I T S : *********
C ENERGY: EV
C LENGTH: ANGSTROM
      PARAMETER (NST=3000,NC=30)
      DIMENSION X1(NST),Y1(NST),Z1(NST),RE1(NST)
      DIMENSION X2(NST),Y2(NST),Z2(NST),RE2(NST)
      DIMENSION U1(NST),V1(NST),W1(NST)
      DIMENSION U2(NST),V2(NST),W2(NST)
      DIMENSION tmpsave(4096),d1(300),d2(300),ene(300)
      COMPLEX SK1(NST),SK2(NST),SM1(NST),SM2(NST)
      DIMENSION FX1(NC),FY1(NC),FZ1(NC),FX2(NC),FY2(NC),FZ2(NC)
      COMPLEX BAS1(NC),BAS2(NC),COM1(NC),COM2(NC),BRA1(NC),BRA2(NC)
      COMPLEX CEL1(NC),CEL2(NC),SN1,SN2,C1,C2,STS,TSS
      COMPLEX SNGL1,SNGL2,TOPSUM,SUBSUM,TSSUM,STSUM,SSYS
      COMPLEX PR1,PR2,BAJ,BAL,CREI,CREK,S1SUM,S2SUM,SSUM
      REAL LAMBDA,KD,KP,KPX,KPY,KPZ,K0,K0Z,K02
      REAL KRAT,MASOV,MASSB,MINAB,WR(8)
      INTEGER COMENS,UNIF1,UNIF2,TEMP
      CHARACTER INDATA1*13, INDATA2*13, OUTDATA*13,indata3*13
C
C READ INPUT AND OUTPUT DATA FILENAMES
C
      WRITE(6,'(A)') ' Enter Energy Parameter FILENAME: '
      READ(6,*) INDATA1
      OPEN(UNIT=5, FILE=INDATA1, STATUS='OLD')
      WRITE(6,'(A)') ' Enter Structure Parameter FILENAME: '
      READ(6,*) INDATA2
      OPEN(UNIT=10, FILE=INDATA2, STATUS='OLD')
      WRITE(6,'(A)') ' Enter LEED Output FILENAME: '
      READ(6,*) OUTDATA
      OPEN(UNIT=11, FILE=OUTDATA, STATUS='unknown')
      WRITE(6,'(A)') ' Enter Phase Parameter FILENAME: '
      READ(6,*) INDATA3

C ** CHANNEL 5 INPUT **
      READ(5,*) E,DAN
C remember the hases are not read in here anymore, see loop 9897 below
      READ(5,*) f1,f2
      READ(5,*) TEMP
      IF (TEMP.EQ.1) THEN
       READ(5,*) MASOV,MASSB
       READ(5,*) TD,T
      END IF
      READ(5,*) AMP,COEF
      READ(5,*) CEN1,WID1
      READ(5,*) CEN2,WID2
C ** CHANNEL 10 INPUT **
      READ(10,*) XSIZE,YSIZE
      READ(10,*) MINAB,DZ
      READ(10,*) COMENS
      IF (COMENS.EQ.1) THEN
       READ(10,*) AX,AY
       READ(10,*) BX,BY
       IF (ABS(AX*BY-AY*BX).LT.1E-4) THEN
        WRITE(6,1000)
        STOP
       END IF
       READ(10,*) NTOP,NSUB
       READ(10,*) (FX1(I),FY1(I),FZ1(I),I=1,NTOP)
       READ(10,*) (FX2(I),FY2(I),FZ2(I),I=1,NSUB)
       CALL SETUP(AX,AY,BX,BY,XSIZE,YSIZE,X1,Y1,IMAX,NST,NC)
C
       KMAX=IMAX
```

```
      DO 7 I=1,IMAX
      X2(I)=X1(I)
      Y2(I)=Y1(I)
7     Z2(I)=Z1(I)-DZ
C
      ELSE
C
      READ(10,*) UNIF1,UNIF2
      IF (UNIF1.EQ.1.AND.UNIF2.EQ.1) THEN
       READ(10,*) A1X,A1Y
       READ(10,*) B1X,B1Y
       IF (ABS(A1X*B1Y-A1Y*B1X).LT.1.E-4) THEN
        WRITE(6,1000)
        STOP
       END IF
       READ(10,*) NTOP
       READ(10,*) (FX1(I),FY1(I),FZ1(I),I=1,NTOP)
       CALL SETUP(A1X,A1Y,B1X,B1Y,XSIZE,YSIZE,X1,Y1,IMAX,NST,NC)
       DO 17 I=1,IMAX
17      Z1(I)=0.
C
       READ(10,*) A2X,A2Y
       READ(10,*) B2X,B2Y
       IF (ABS(A2X*B2Y-A2Y*B2X).LT.1.E-4) THEN
        WRITE(6,1000)
        STOP
       END IF
       READ(10,*) NSUB
       READ(10,*) (FX2(I),FY2(I),FZ2(I),I=1,NSUB)
       CALL SETUP(A2X,A2Y,B2X,B2Y,XSIZE,YSIZE,X2,Y2,KMAX,NST,NC)
       DO 27 K=1,KMAX
27      Z2(K)=-DZ
      END IF
C
      IF (UNIF1.EQ.1.AND.UNIF2.EQ.0) THEN
       READ(10,*) A1X,A1Y
       READ(10,*) B1X,B1Y
       IF (ABS(A1X*B1Y-A1Y*B1X).LT.1.E-4) THEN
        WRITE(6,1000)
        STOP
       END IF
       READ(10,*) NTOP
       READ(10,*) (FX1(I),FY1(I),FZ1(I),I=1,NTOP)
       CALL SETUP(A1X,A1Y,B1X,B1Y,XSIZE,YSIZE,X1,Y1,IMAX,NST,NC)
       DO 37 I=1,IMAX
37      Z1(I)=0.
C
       READ(10,*) KMAX
       READ(10,*) (X2(K),Y2(K),Z2(K),K=1,KMAX)
      END IF
C
      IF (UNIF1.EQ.0.AND.UNIF2.EQ.1) THEN
       READ(10,*) IMAX
       READ(10,*) (X1(I),Y1(I),Z1(I),I=1,IMAX)
C
       READ(10,*) A2X,A2Y
       READ(10,*) B2X,B2Y
       IF (ABS(A2X*B2Y-A2Y*B2X).LT.1.E-4) THEN
        WRITE(6,1000)
        STOP
       END IF
       READ(10,*) NSUB
       READ(10,*) (FX2(K),FY2(K),FZ2(K),K=1,NSUB)
```

```
      CALL SETUP(A2X,A2Y,B2X,B2Y,XSIZE,YSIZE,X2,Y2,KMAX,NST,NC)
      DO 47 K=1,KMAX
47      Z2(K)=-DZ
      END IF
C
      IF (UNIF1.EQ.0.AND.UNIF2.EQ.0) THEN
       READ(10,*) IMAX
       READ(10,*) (X1(I),Y1(I),Z1(I),I=1,IMAX)
C
       READ(10,*) KMAX
       READ(10,*) (X2(K),Y2(K),Z2(K),K=1,KMAX)
      END IF
     END IF
C
1000  FORMAT('****  FUNDAMENTAL LATTICE VECTORS ARE COLINEAR  ****')
c---tms---
c1001  FORMAT(8F9.4)
1001  format(8e10.3)
c---tme---
1002  FORMAT('*****   PRIMARY BEAM ENERGY TOO LOW  *****')
C

C Start of Energy loop here, modification by TAC
C Started 22/5/00

C Set Constants
     PI=3.14159265
     PP=2.*PI
     WID1=64./WID1
     WID2=64./WID2
     COR1X=(CEN1-32./WID1)*PP/MINAB
     COR1Y=(CEN2-32./WID2)*PP/MINAB
     COR2X=(CEN1+31./WID1)*PP/MINAB
     COR2Y=(CEN2-32./WID2)*PP/MINAB
     COR3X=(CEN1-32./WID1)*PP/MINAB
     COR3Y=(CEN2+31./WID2)*PP/MINAB
     COR4X=(CEN1+31./WID1)*PP/MINAB
     COR4Y=(CEN2+31./WID2)*PP/MINAB
     DAN=180./(PI*DAN)
     DAN2=DAN*DAN

C      Set up energy Parameters
     open(unit = 14, file = 'avgfilea.dat',status = 'unknown')
     open(unit = 15, file = 'avgfileb.dat',status = 'unknown')

c     estart = 100
c     eend = 200
c     estep = 3

c       write(*,'(a)') ' Enter Start Energy, eV: '
c       read(*,*) estart
c       write(*,'(a)') ' Enter Stop Energy, eV: '
c       read(*,*) eend
c       write(*,'(a)') ' Enter Energy Step, eV: '
c       read(*,*) estep

c     nen = 1+int(0.5 + (Eend - Estart)/estep)
c       print *, estart,eend,estep,nen
c       pause

C open energy/phase file and read in energies and phases
      open(unit = 9, file = indata3 ,status = 'old')
      do 9897 nn = 1, 300
```

```
      read(9,*,end = 9898) ene(nn),d1(nn),d2(nn)
      print *,nn,ene(nn),d1(nn),d2(nn)
9897  continue
9898  close(9)
      nen = nn-1
      print *,'nen = ',nen
c     pause

      ipix = 32
      jpix = 32
      ibox = 0

C Start Energy Loop here
    do 9876 ie = 1, nen
C Initialise Arrays

    do 9875 kk = 1, nc
     bra1(kk) = (0.0,0.0)
     bra2(kk) = (0.0,0.0)
9875  continue

c     E = Estart + (ie-1)*estep
c     print *,' Energy = ', E
c     PAUSE
    E = ene(ie)
    LAMBDA=SQRT(150.4/E)
    K0=PP/LAMBDA
    K02=K0*K0
    K0Z=-K0
    A1=(EXP(2*(0,1)*D1(ie))-1.)/(2.*(0,1)*K0)
    A2=(EXP(2*(0,1)*D2(ie))-1.)/(2.*(0,1)*K0)
     DO 119 I=1,IMAX
     U1(I)=X1(I)
     V1(I)=Y1(I)
119   W1(I)=Z1(I)
     DO 219 K=1,KMAX
     U2(K)=X2(K)
     V2(K)=Y2(K)
219   W2(K)=Z2(K)
C
    print *,' Energy = ', E
    print *,'A1, A2, D1, D2 = ',a1,a2,d1(ie),d2(ie)
c     PAUSE


    IF (COR1X*COR1X+COR1Y*COR1Y.GE.K0*K0) THEN
     WRITE(6,1002)
     STOP
    END IF
    IF (COR2X*COR2X+COR2Y*COR2Y.GE.K0*K0) THEN
     WRITE(6,1002)
     STOP
    END IF
    IF (COR3X*COR3X+COR3Y*COR3Y.GE.K0*K0) THEN
     WRITE(6,1002)
     STOP
    END IF
    IF (COR4X*COR4X+COR4Y*COR4Y.GE.K0*K0) THEN
     WRITE(6,1002)
     STOP
    END IF
C
C  SIMULATING THERMAL MOTION INDUCED TO THE SCATTERERS DUE TO THE SAMPLE
```

```
C  BEING AT TEMPERATURE ABOVE 0 K
c     IF (TEMP.EQ.1) THEN
c      CALL THERMA(T,TD,PP,MINAB,PI,MASOV,MASSB,X1,Y1,Z1,U1,V1,W1,
c     1 X2,Y2,Z2,U2,V2,W2,IMAX,KMAX,COMENS,NST,NC)
c     END IF
C
C  CALCULATION OF THE EXPONENTIAL FACTORS OF A NORMAL INCIDENCE PRIMARY
C  BEAM
      PR1=1.
      PR2=EXP(-(0,1)*K0Z*DZ)
C


      IF (COMENS.EQ.0) THEN
C  DEALING WITH AN INCOMMENSURATE STRUCTURE
       IF (UNIF1.EQ.0.AND.UNIF2.EQ.0) THEN
       print *,' Calculating IV for (0,0) structure, COMENS=0'
C
C  CALCULATION OF THE MATRIX RE1 (CONNECTED WITH THE ANGULAR SPREAD OF
THE
C  BEAM OF A REAL LEED GUN AND THE TOP LAYER)
       CALL ANGUL1(IMAX,X1,Y1,K02,DAN2,RE1,NST,NC)
C
C  CALCULATION OF THE MATRIX RE2 (CONNECTED WITH THE ANGULAR SPREAD OF
THE
C  BEAM OF A REAL LEED GUN AND THE SECOND LAYER)
       CALL ANGUL1(KMAX,X2,Y2,K02,DAN2,RE2,NST,NC)
C
C  CALCULATION OF THE MATRICES SK1 (ELECTRON SCATTERS FROM THE SECOND
LAYER
C  ATOMS FIRST) AND SK2 (ELECTRON SCATTERS FROM THE TOP LAYER ATOMS FIRST)
       DO 12 I=1,IMAX
       XI=X1(I)
       YI=Y1(I)
       ZI=Z1(I)
       REI=RE1(I)
        DO 13 K=1,KMAX
        DX=XI-X2(K)
        DY=YI-Y2(K)
        DZ=ZI-Z2(K)
        R=SQRT(DX*DX+DY*DY+DZ*DZ)
        SIR=SIN(K0*R)/R
        SK2(K)=SK2(K)+SIR*REI
13       SK1(I)=SK1(I)+SIR*RE2(K)
12       SK1(I)=SK1(I)*PR2
       DO 14 K=1,KMAX
14      SK2(K)=SK2(K)*PR1
C
C  CALCULATION OF THE MATRIX SM1 (ELECTRON SCATTERING BETWEEN TOP LAYER
C  ATOMS FOR STRUCTURES WITH NOT WELL DEFINED PERIODICITY VECTORS)
       CALL INTRA(IMAX,X1,Y1,Z1,SM1,PR1,K0,RE1,NST,NC)
C
C  CALCULATION OF THE MATRIX SM2 (ELECTRON SCATTERING BETWEEN SECOND
LAYER
C  ATOMS  FOR STRUCTURES WITH NOT WELL DEFINED PERIODICITY VECTORS)
       CALL INTRA(KMAX,X2,Y2,Z2,SM2,PR2,K0,RE2,NST,NC)
C
C  CALCULATION OF THE INTENSITIES IN A 64X64 RECIPROCAL SPACE GRID
       JCNT=0
       ssys=0.0
       ain = 0.0
       ic = 1
```

```
      DO 20 KX=0,63
      AKX=(CEN1+(KX-32)/WID1)*PP/MINAB
      DO 20 KY=0,63
      AKY=(CEN2+(KY-32)/WID2)*PP/MINAB
      AKZ=SQRT(K0*K0-AKX*AKX-AKY*AKY)
C
      SNGL1=0.
      TOPSUM=0.
      STSUM=0.
       DO 21 I=1,IMAX
       AKR=AKX*X1(I)+AKY*Y1(I)+AKZ*Z1(I)
       C1=EXP(-(0,1)*AKR)
       SNGL1=SNGL1+C1*RE1(I)
       TOPSUM=TOPSUM+C1*SM1(I)
21      STSUM=STSUM+C1*SK1(I)
C
      SNGL2=0.
      SUBSUM=0.
      TSSUM=0.
       DO 22 K=1,KMAX
       AKR=AKX*X2(K)+AKY*Y2(K)+AKZ*Z2(K)
       C2=EXP(-(0,1)*AKR)
       SNGL2=SNGL2+C2*RE2(K)
       SUBSUM=SUBSUM+C2*SM2(K)
22      TSSUM=TSSUM+C2*SK2(K)
C
      SSYS=A1*(A1*TOPSUM+A2*TSSUM)+A2*(A2*SUBSUM+A1*STSUM)
      SSYS=SSYS*COEF+(PR1*A1*SNGL1+PR2*A2*SNGL2)
      AIN=ABS(SSYS)/(K0*XSIZE*YSIZE)
      AIN=(AMP*AIN)*AIN
c      tmpsave(ic) = AIN
      tmpsave(ic) = tmpsave(ic)+AIN
      ic = ic+1
      JCNT=JCNT+1
      WR(JCNT)=AIN
      IF (JCNT.EQ.8) THEN
       JCNT=0
       WRITE(11,1001) (WR(I),I=1,8)
      END IF
20     CONTINUE
      WRITE(11,1001) (WR(J),J=1,JCNT)
     END IF
C
     IF (UNIF1.EQ.1.AND.UNIF2.EQ.0) THEN
     print *,' Calculating IV for (1,0) structure, COMENS=0'
C
C  CALCULATION OF THE MATRIX RE1 (CONNECTED WITH THE ANGULAR SPREAD OF
THE
C  BEAM OF A REAL LEED GUN AND THE TOP LAYER)
      CALL ANGUL2(IMAX,NTOP,X1,Y1,FX1,FY1,K02,DAN2,RE1,NST,NC)
C
C  CALCULATION OF THE MATRIX RE2 (CONNECTED WITH THE ANGULAR SPREAD OF
THE
C  BEAM OF A REAL LEED GUN AND THE SECOND LAYER)
      CALL ANGUL1(KMAX,X2,Y2,K02,DAN2,RE2,NST,NC)
C
C  CALCULATION OF THE MATRIX BAS1 (THE EXPONENTIALS OF THE ATOMS IN THE
UNIT
C  CELL OF THE TOP LAYER)
      DO 108 I=1,NTOP
108    BAS1(I)=EXP((0,1)*K0Z*FZ1(I))
C  CALCULATION OF THE MATRICES SK1 (ELECTRON SCATTERS FROM THE SECOND
LAYER
```

```
C  ATOMS FIRST) AND SK2 (ELECTRON SCATTERS FROM THE TOP LAYER ATOMS FIRST)
      DO 112 J=1,NTOP
      FXJ=FX1(J)
      FYJ=FY1(J)
      FZJ=FZ1(J)
      BAJ=BAS1(J)
      J1=(J-1)*IMAX
      DO 112 I=1,IMAX
      TXJ=X1(I)+FXJ
      TYJ=Y1(I)+FYJ
      TZJ=Z1(I)+FZJ
      CREI=RE1(I+J1)*BAJ
      IND=I+J1
       DO 113 K=1,KMAX
       DX=TXJ-X2(K)
       DY=TYJ-Y2(K)
       DZ=TZJ-Z2(K)
       R=SQRT(DX*DX+DY*DY+DZ*DZ)
       SIR=SIN(K0*R)/R
       SK2(K)=SK2(K)+SIR*CREI
113      SK1(IND)=SK1(IND)+SIR*RE2(K)
112      SK1(IND)=SK1(IND)*PR2
      DO 114 K=1,KMAX
114    SK2(K)=SK2(K)*PR1
C
C  CALCULATION OF THE MATRIX BRA1 (ELECTRON SCATTERING BETWEEN TOP LAYER
C  ATOMS
      CALL LAYER(X1,Y1,Z1,FX1,FY1,FZ1,BRA1,BAS1,PR1,NTOP,IMAX,K0,
     1  RE1,NST,NC)
C
C  CALCULATION OF THE MATRIX SM2 (ELECTRON SCATTERING BETWEEN SECOND
LAYER
C  ATOMS)
      CALL INTRA(KMAX,X2,Y2,Z2,SM2,PR2,K0,RE2,NST,NC)
C
C  CALCULATION OF THE INTENSITIES IN A 64X64 RECIPROCAL SPACE GRID
      JCNT=0
      ssys=0.0
      ain = 0.0
      ic = 1
      DO 120 KX=0,63
      AKX=(CEN1+(KX-32)/WID1)*PP/MINAB
      DO 120 KY=0,63
      AKY=(CEN2+(KY-32)/WID2)*PP/MINAB
      AKZ=SQRT(K0*K0-AKX*AKX-AKY*AKY)
C
      TOPSUM=0.
       DO 121 J=1,NTOP
       C1=EXP(-(0,1)*(AKX*FX1(J)+AKY*FY1(J)+AKZ*FZ1(J)))
       CEL1(J)=C1
121      TOPSUM=TOPSUM+C1*BRA1(J)
C
      S1SUM=0.
      SNGL1=0.
      STSUM=0.
       DO 122 I=1,IMAX
       AKR=AKX*X1(I)+AKY*Y1(I)+AKZ*Z1(I)
       C1=EXP(-(0,1)*AKR)
       S1SUM=S1SUM+C1
       I1=I-IMAX
       SN1=0.
       STS=0.
       DO 123 J=1,NTOP
```

```
      J1=I1+J*IMAX
      SN1=SN1+CEL1(J)*BAS1(J)*RE1(J1)
123     STS=STS+CEL1(J)*SK1(J1)
      SNGL1=SNGL1+SN1*C1
122     STSUM=STSUM+STS*C1
C
      SNGL2=0.
      SUBSUM=0.
      TSSUM=0.
      DO 124 K=1,KMAX
      AKR=AKX*X2(K)+AKY*Y2(K)+AKZ*Z2(K)
      C2=EXP(-(0,1)*AKR)
      SNGL2=SNGL2+C2*RE2(K)
      SUBSUM=SUBSUM+C2*SM2(K)
124     TSSUM=TSSUM+C2*SK2(K)
C
      TOPSUM=S1SUM*TOPSUM
      SSYS=A1*(A1*TOPSUM+A2*TSSUM)+A2*(A2*SUBSUM+A1*STSUM)
      SSYS=SSYS*COEF+(PR1*A1*SNGL1+PR2*A2*SNGL2)
      AIN=ABS(SSYS)/(K0*XSIZE*YSIZE)
      AIN=(AMP*AIN)*AIN
c       tmpsave(ic) = AIN
      tmpsave(ic) = tmpsave(ic)+AIN
      ic = ic+1
      JCNT=JCNT+1
      WR(JCNT)=AIN
      IF (JCNT.EQ.8) THEN
       JCNT=0
       WRITE(11,1001) (WR(I),I=1,8)
      END IF
120     CONTINUE
      WRITE(11,1001) (WR(J),J=1,JCNT)
     END IF
C
     IF (UNIF1.EQ.0.AND.UNIF2.EQ.1) THEN
     print *,' Calculating IV for (0,1) structure, COMENS=0'
C
C  CALCULATION OF THE MATRIX RE1 (CONNECTED WITH THE ANGULAR SPREAD OF
THE
C  BEAM OF A REAL LEED GUN AND THE TOP LAYER)
      CALL ANGUL1(IMAX,X1,Y1,K02,DAN2,RE1,NST,NC)
C
C  CALCULATION OF THE MATRIX RE2 (CONNECTED WITH THE ANGULAR SPREAD OF
THE
C  BEAM OF A REAL LEED GUN AND THE SECOND LAYER)
      CALL ANGUL2(KMAX,NSUB,X2,Y2,FX2,FY2,K02,DAN2,RE2,NST,NC)
C
C  CALCULATION OF THE MATRIX BAS2 (THE EXPONENTIALS OF THE ATOMS IN THE
UNIT
C  CELL OF THE SECOND LAYER)
    DO 210 I=1,NSUB
210   BAS2(I)=EXP((0,1)*K0Z*FZ2(I))
C
C  CALCULATION OF THE MATRICES SK2 (ELECTRON SCATTERS FROM THE TOP LAYER
C  ATOMS FIRST) AND SK1 (ELECTRON SCATTERS FROM THE SECOND LAYER ATOMS
FIRST)
      DO 212 L=1,NSUB
      FXL=FX2(L)
      FYL=FY2(L)
      FZL=FZ2(L)
      BAL=BAS2(L)
      L1=(L-1)*KMAX
      DO 212 K=1,KMAX
```

```
      TXL=X2(K)+FXL
      TYL=Y2(K)+FYL
      TZL=Z2(K)+FZL
      CREK=RE2(K+L1)*BAL
      IND=K+L1
       DO 213 I=1,IMAX
       DX=X1(I)-TXL
       DY=Y1(I)-TYL
       DZ=Z1(I)-TZL
       R=SQRT(DX*DX+DY*DY+DZ*DZ)
       SIR=SIN(K0*R)/R
       SK1(I)=SK1(I)+SIR*CREK
213      SK2(IND)=SK2(IND)+SIR*RE1(I)
212      SK2(IND)=SK2(IND)*PR1
      DO 214 I=1,IMAX
214    SK1(I)=SK1(I)*PR2
C
C  CALCULATION OF THE MATRIX BRA2 (ELECTRON SCATTERING BETWEEN SECOND
LAYER
C  ATOMS)

      CALL LAYER(X2,Y2,Z2,FX2,FY2,FZ2,BRA2,BAS2,PR2,NSUB,KMAX,K0,
     1  RE2,NST,NC)
C
C  CALCULATION OF THE MATRIX SM1 (ELECTRON SCATTERING BETWEEN TOP LAYER
C  ATOMS OF A STRUCTURE WITH NOT WELL DEFINED PERIODICITY VECTORS)
      CALL INTRA(IMAX,X1,Y1,Z1,SM1,PR1,K0,RE1,NST,NC)
C
C  CALCULATION OF THE INTENSITIES IN A 64X64 RECIPROCAL SPACE GRID
      JCNT=0
      ssys=0.0
      ain = 0.0
      ic = 1
      DO 220 KX=0,63
      AKX=(CEN1+(KX-32)/WID1)*PP/MINAB
      DO 220 KY=0,63
      AKY=(CEN2+(KY-32)/WID2)*PP/MINAB
      AKZ=SQRT(K0*K0-AKX*AKX-AKY*AKY)
C
      SUBSUM=0.
       DO 221 L=1,NSUB
       C2=EXP(-(0,1)*(AKX*FX2(L)+AKY*FY2(L)+AKZ*FZ2(L)))
       CEL2(L)=C2
221      SUBSUM=SUBSUM+C2*BRA2(L)
C
       S2SUM=0.
       SNGL2=0.
       TSSUM=0.
       DO 222 K=1,KMAX
       AKR=AKX*X2(K)+AKY*Y2(K)+AKZ*Z2(K)
       C2=EXP(-(0,1)*AKR)
       S2SUM=S2SUM+C2
       K1=K-KMAX
       SN2=0.
       TSS=0.
       DO 223 L=1,NSUB
       L1=K1+L*KMAX
       SN2=SN2+CEL2(L)*BAS2(L)*RE2(L1)
223      TSS=TSS+CEL2(L)*SK2(L1)
       SNGL2=SNGL2+SN2*C2
222      TSSUM=TSSUM+TSS*C2
C
      SNGL1=0.
```

```
      TOPSUM=0.
      STSUM=0.
       DO 224 I=1,IMAX
       AKR=AKX*X1(I)+AKY*Y1(I)+AKZ*Z1(I)
       C1=EXP(-(0,1)*AKR)
       SNGL1=SNGL1+C1*RE1(I)
       TOPSUM=TOPSUM+C1*SM1(I)
224     STSUM=STSUM+C1*SK1(I)
C
      SUBSUM=S2SUM*SUBSUM
      SSYS=A1*(A1*TOPSUM+A2*TSSUM)+A2*(A2*SUBSUM+A1*STSUM)
      SSYS=SSYS*COEF+(PR1*A1*SNGL1+PR2*A2*SNGL2)
      AIN=ABS(SSYS)/(K0*XSIZE*YSIZE)
      AIN=(AMP*AIN)*AIN
c      tmpsave(ic) = AIN
      tmpsave(ic) = tmpsave(ic)+AIN
      ic = ic+1
      JCNT=JCNT+1
      WR(JCNT)=AIN
      IF (JCNT.EQ.8) THEN
       JCNT=0
       WRITE(11,1001) (WR(I),I=1,8)
      END IF
220    CONTINUE
      WRITE(11,1001) (WR(J),J=1,JCNT)
     END IF
C
     IF (UNIF1.EQ.1.AND.UNIF2.EQ.1) THEN
     print *,' Calculating IV for (1,1) structure, COMENS=0'
C
C  CALCULATION OF THE MATRIX RE1 (CONNECTED WITH THE ANGULAR SPREAD OF
THE
C  BEAM OF A REAL LEED GUN AND THE TOP LAYER)
      CALL ANGUL2(IMAX,NTOP,X1,Y1,FX1,FY1,K02,DAN2,RE1,NST,NC)
C
C  CALCULATION OF THE MATRIX RE2 (CONNECTED WITH THE ANGULAR SPREAD OF
THE
C  BEAM OF A REAL LEED GUN AND THE SECOND LAYER)
      CALL ANGUL2(KMAX,NSUB,X2,Y2,FX2,FY2,K02,DAN2,RE2,NST,NC)
C
C  CALCULATION OF THE MATRIX BAS1 (THE EXPONENTIALS OF THE ATOMS IN THE
UNIT
C  CELL OF THE TOP LAYER)
    DO 308 I=1,NTOP
308   BAS1(I)=EXP((0,1)*K0Z*FZ1(I))
C
C  CALCULATION OF THE MATRIX BAS2 (THE EXPONENTIALS OF THE ATOMS IN THE
UNIT
C  CELL OF THE SECOND LAYER)
    DO 310 I=1,NSUB
310   BAS2(I)=EXP((0,1)*K0Z*FZ2(I))
C
C  CALCULATION OF THE MATRICES SK1 (ELECTRON SCATTERS FROM THE SECOND
LAYER
C  ATOMS FIRST) AND SK2 (ELECTRON SCATTERS FROM THE TOP LAYER ATOMS FIRST)
      DO 312 J=1,NTOP
      FXJ=FX1(J)
      FYJ=FY1(J)
      FZJ=FZ1(J)
      BAJ=BAS1(J)
      J1=(J-1)*IMAX
      DO 312 I=1,IMAX
      TXI=X1(I)+FXJ
```

```
      TYI=Y1(I)+FYJ
      TZI=Z1(I)+FZJ
      IN1=I+J1
      CREI=RE1(IN1)*BAJ
       DO 313 L=1,NSUB
       FXL=TXI-FX2(L)
       FYL=TYI-FY2(L)
       FZL=TZI-FZ2(L)
       BAL=BAS2(L)
       L1=(L-1)*KMAX
       SK=0.
       DO 314 K=1,KMAX
       DX=FXL-X2(K)
       DY=FYL-Y2(K)
       DZ=FZL-Z2(K)
       IN2=K+L1
       R=SQRT(DX*DX+DY*DY+DZ*DZ)
       SIR=SIN(K0*R)/R
       SK2(IN2)=SK2(IN2)+SIR*CREI
314     SK=SK+SIR*RE2(IN2)
313     SK1(IN1)=SK1(IN1)+BAL*SK
312     SK1(IN1)=SK1(IN1)*PR2
      DO 316 L=1,NSUB
      L1=(L-1)*KMAX
      DO 316 K=1,KMAX
      IN2=K+L1
316    SK2(IN2)=SK2(IN2)*PR1
C
C  CALCULATION OF THE MATRIX BRA1 (ELECTRON SCATTERING BETWEEN TOP LAYER
C  ATOMS)

      CALL LAYER(X1,Y1,Z1,FX1,FY1,FZ1,BRA1,BAS1,PR1,NTOP,IMAX,K0,
     1  RE1,NST,NC)
C
C  CALCULATION OF THE MATRIX BRA2 (ELECTRON SCATTERING BETWEEN SECOND
LAYER
C  ATOMS)

      CALL LAYER(X2,Y2,Z2,FX2,FY2,FZ2,BRA2,BAS2,PR2,NSUB,KMAX,K0,
     1  RE2,NST,NC)

C
C CALCULATION OF THE INTENSITIES IN A 64X64 RECIPROCAL SPACE GRID
      JCNT=0
      ssys=0.0
      ain = 0.0
      ic = 1

      DO 320 KX=0,63

      WRITE(6,9753) kx
9753   FORMAT('+',' In KX Loop, KX = ',i6)
      AKX=(CEN1+(KX-32)/WID1)*PP/MINAB

      DO 320 KY=0,63
      WRITE(6,9751) kx,ky
9751   FORMAT('+',' In KY Loop, KX = ',i6,' KY = ',i6)

      AKY=(CEN2+(KY-32)/WID2)*PP/MINAB
      AKZ=SQRT(K0*K0-AKX*AKX-AKY*AKY)
C
      TOPSUM=0.
       DO 321 J=1,NTOP
```

```
      C1=EXP(-(0,1)*(AKX*FX1(J)+AKY*FY1(J)+AKZ*FZ1(J)))
      CEL1(J)=C1
321     TOPSUM=TOPSUM+C1*BRA1(J)
C
      SUBSUM=0.
      DO 322 L=1,NSUB
      C2=EXP(-(0,1)*(AKX*FX2(L)+AKY*FY2(L)+AKZ*FZ2(L)))
      CEL2(L)=C2
322     SUBSUM=SUBSUM+C2*BRA2(L)
C
      S1SUM=0.
      SNGL1=0.
      STSUM=0.
      DO 323 I=1,IMAX
      AKR=AKX*X1(I)+AKY*Y1(I)+AKZ*Z1(I)
      C1=EXP(-(0,1)*AKR)
      S1SUM=S1SUM+C1
      I1=I-IMAX
      SN1=0.
      STS=0.
      DO 324 J=1,NTOP
      J1=I1+J*IMAX
      SN1=SN1+CEL1(J)*BAS1(J)*RE1(J1)
324     STS=STS+CEL1(J)*SK1(J1)
      SNGL1=SNGL1+SN1*C1
323     STSUM=STSUM+STS*C1
C
      S2SUM=0.
      SNGL2=0.
      TSSUM=0.
      DO 325 K=1,KMAX
      AKR=AKX*X2(K)+AKY*Y2(K)+AKZ*Z2(K)
      C2=EXP(-(0,1)*AKR)
      S2SUM=S2SUM+C2
      K1=K-KMAX
      SN2=0.
      TSS=0.
      DO 326 L=1,NSUB
      L1=K1+L*KMAX
      SN2=SN2+CEL2(L)*BAS2(L)*RE2(L1)
326     TSS=TSS+CEL2(L)*SK2(L1)
      SNGL2=SNGL2+SN2*C2
325     TSSUM=TSSUM+TSS*C2
C
      TOPSUM=S1SUM*TOPSUM
      SUBSUM=S2SUM*SUBSUM
      SSYS=A1*(A1*TOPSUM+A2*TSSUM)+A2*(A2*SUBSUM+A1*STSUM)
      SSYS=SSYS*COEF+(PR1*A1*SNGL1+PR2*A2*SNGL2)
      AIN=ABS(SSYS)/(K0*XSIZE*YSIZE)
      AIN=(AMP*AIN)*AIN
c      tmpsave(ic) = AIN
      tmpsave(ic) = tmpsave(ic)+AIN
      ic = ic+1
      JCNT=JCNT+1
      WR(JCNT)=AIN
      IF (JCNT.EQ.8) THEN
       JCNT=0
       WRITE(11,1001) (WR(I),I=1,8)
      END IF
320     CONTINUE
      WRITE(11,1001) (WR(I),I=1,JCNT)
     END IF
C
```

```
      ELSE


C Comens = 1 so....
C  DEALING WITH A COMMENSURATE STRUCTURE

       print *,' Calculating IV for Commensurate structure, COMENS=1'
C
C  CALCULATION OF THE MATRIX RE1 (CONNECTED WITH THE ANGULAR SPREAD OF
THE
C  BEAM OF A REAL LEED GUN AND THE TOP LAYER)


c       print *,' Ntop = ',ntop,' imax = ',imax
c       pause
       CALL ANGUL2(IMAX,NTOP,X1,Y1,FX1,FY1,K02,DAN2,RE1,NST,NC)
C
C  CALCULATION OF THE MATRIX RE2 (CONNECTED WITH THE ANGULAR SPREAD OF
THE
C  BEAM OF A REAL LEED GUN AND THE SECOND LAYER)

c       print *,' Nsub = ',nsub,' KMAX = ',kmax
c       pause
       CALL ANGUL2(KMAX,NSUB,X2,Y2,FX2,FY2,K02,DAN2,RE2,NST,NC)
C
C  CALCULATION OF THE MATRIX BAS1 (THE EXPONENTIALS OF THE ATOMS IN THE
UNIT
C  CELL OF THE TOP LAYER)
      DO 408 I=1,NTOP
408   BAS1(I)=EXP((0,1)*K0Z*FZ1(I))
C
C  CALCULATION OF THE MATRIX BAS2 (THE EXPONENTIALS OF THE ATOMS IN THE
UNIT
C  CELL OF THE SECOND LAYER)
      DO 410 I=1,NSUB
410   BAS2(I)=EXP((0,1)*K0Z*FZ2(I))
C
C  CALCULATION OF THE MATRIX BRA1 USED FOR THE CALCULATION OF MULTIPLE
C  SCATTERING WITHIN THE TOP LAYER WHEN THIS LAYER FORMS A BRAVAIS NET
       CALL LAYER(X1,Y1,Z1,FX1,FY1,FZ1,BRA1,BAS1,PR1,NTOP,IMAX,K0,
     1 RE1,NST,NC)
C
C  CALCULATION OF THE MATRIX BRA2 USED FOR THE CALCULATION OF MULTIPLE
C  SCATTERING WITHIN THE SECOND LAYER WHEN THIS LAYER FORMS A BRAVAIS NET
       CALL LAYER(X2,Y2,Z2,FX2,FY2,FZ2,BRA2,BAS2,PR2,NSUB,KMAX,K0,
     1 RE2,NST,NC)
C
C  CALCULATION OF THE MATRIX COM1 USED FOR THE CALCULATION OF MULTIPLE
C  SCATTERING BETWEEN THE ATOMS OF THE UNIT CELL OF A COMMENSURATE
STRUCTURE
C  WHEN THE INCOMING ELECTRON SCATTERS FROM THE SECOND LAYER FIRST
       CALL INTER(X2,Y2,Z2,FX1,FY1,FZ1,FX2,FY2,FZ2,DZ,0,COM1,BAS2,
     1 PR2,NTOP,NSUB,KMAX,K0,RE2,NST,NC)
C
C  CALCULATION OF THE MATRIX COM2 USED FOR THE CALCULATION OF MULTIPLE
C  SCATTERING BETWEEN THE ATOMS OF THE UNIT CELL OF A COMMENSURATE
STRUCTURE
C  WHEN THE INCOMING ELECTRON SCATTERS FROM THE TOP LAYER FIRST
       CALL INTER(X1,Y1,Z1,FX2,FY2,FZ2,FX1,FY1,FZ1,DZ,1,COM2,BAS1,
     1 PR1,NSUB,NTOP,IMAX,K0,RE1,NST,NC)
C
C CALCULATION OF THE INTENSITIES IN A 64X64 RECIPROCAL SPACE GRID
       JCNT=0
```

```
      ssys=0.0
      ain = 0.0
      ic = 1

      DO 420 KX=0,63
      AKX=(CEN1+(KX-32)/WID1)*PP/MINAB
      DO 420 KY=0,63
      AKY=(CEN2+(KY-32)/WID2)*PP/MINAB
      AKZ=SQRT(K0*K0-AKX*AKX-AKY*AKY)
C
      STSUM=0.
      TOPSUM=0.
       DO 421 J=1,NTOP
       C1=EXP(-(0,1)*(AKX*FX1(J)+AKY*FY1(J)+AKZ*FZ1(J)))
       CEL1(J)=C1
       STSUM=STSUM+COM1(J)*C1
421     TOPSUM=TOPSUM+BRA1(J)*C1
C
      TSSUM=0.
      SUBSUM=0.
       DO 422 L=1,NSUB
       C2=EXP(-(0,1)*(AKX*FX2(L)+AKY*FY2(L)+AKZ*FZ2(L)))
       CEL2(L)=C2
       TSSUM=TSSUM+COM2(L)*C2
422     SUBSUM=SUBSUM+BRA2(L)*C2

      SNGL1=0.
      SNGL2=0.
      S1SUM=0.
      S2SUM=0.
      CC=EXP((0,1)*AKZ*DZ)
       DO 426 I=1,IMAX
       AKR=AKX*X1(I)+AKY*Y1(I)+AKZ*Z1(I)
       C1=EXP(-(0,1)*AKR)
       C2=C1*CC
       S1SUM=S1SUM+C1
       S2SUM=S2SUM+C2
       I1=I-IMAX
       SN1=0.
        DO 427 J=1,NTOP
        J1=I1+J*IMAX
427      SN1=SN1+CEL1(J)*BAS1(J)*RE1(J1)
       SNGL1=SNGL1+C1*SN1
       SN2=0.
        DO 428 L=1,NSUB
        L1=I1+L*IMAX
428      SN2=SN2+CEL2(L)*BAS2(L)*RE2(L1)
426     SNGL2=SNGL2+C2*SN2
C
      TSSUM=S2SUM*TSSUM
      TOPSUM=S1SUM*TOPSUM
      STSUM=S1SUM*STSUM
      SUBSUM=S2SUM*SUBSUM
      SSYS=A1*(A1*TOPSUM+A2*TSSUM)+A2*(A2*SUBSUM+A1*STSUM)
      SSYS=SSYS*COEF+(PR1*A1*SNGL1+PR2*A2*SNGL2)
      AIN=ABS(SSYS)/(K0*XSIZE*YSIZE)
      AIN=(AMP*AIN)*AIN
      JCNT=JCNT+1
      WR(JCNT)=AIN
      IF (JCNT.EQ.8) THEN
       JCNT=0
       WRITE(11,1001) (WR(I),I=1,8)
      END IF
```

```
      tmpsave(ic) = tmpsave(ic)+AIN
      ic = ic+1
420   CONTINUE
      WRITE(11,1001) (WR(I),I=1,JCNT)
     END IF

C      End of Energy LOOP
      print *,' Finished loop ',ie,' energy = ',E
      print *
9876  continue

C Find min and max of file and average data
      tmin = tmpsave(1)
      tmax = tmpsave(1)
      do 2018 k = 1,4096
        tmpsave(k) = tmpsave(k)/float(nen)
        if(tmpsave(k) .lt. tmin) tmin = tmpsave(k)
        if(tmpsave(k) .gt. tmax) tmax = tmpsave(k)
2018    continue
      print *,' Min, Max = ',tmin,tmax
c       pause

C Scale data
      do 2019 k = 1, 4096
       tmpsave(k) = 255.0*((tmpsave(k)-tmin)/(tmax-tmin))
2019    continue

C Write averaged pixels into IV file
      do 2020 ii = 1,64
        do 2010 jj = 1,64
          k = (ii-1)*64+jj
          write(14,*) ii,jj,tmpsave(k)
2010      continue
2020    continue
      close(14)

C Write averaged pixels into IV file rotated by 90 degrees
      do 2040 ii = 1,64
        do 2030 jj = 1,64
          k = (jj-1)*64+ii
          write(15,*) ii,jj,tmpsave(k)
2030      continue
2040    continue
      close(15)

     STOP
     END
C
C
C ********************** SUBROUTINE AREA ************************
C
C
C  THE NEXT TWO SUBROUTINES CALCULATE THE MATRICES RE1 AND RE2, WHICH ARE
C  CONNECTED WITH THE ANGULAR SPREAD OF THE BEAM OF A REAL LEED GUN
     SUBROUTINE ANGUL1(MAX,X,Y,K02,DAN2,RE,NST,NC)
     DIMENSION X(NST),Y(NST),RE(NST)
     REAL K02
c----tms----
     write(6,*) 'sub ANGUL1'
c----tme----
     DO 106 K=1,MAX
     RX=X(K)
```

```
      RY=Y(K)
106   RE(K)=EXP(-(RX*RX+RY*RY)*K02/(4.*DAN2))
      RETURN
      END
C
C
      SUBROUTINE ANGUL2(MAX,N12,X,Y,FX,FY,K02,DAN2,RE,NST,NC)
      DIMENSION X(NST),Y(NST),RE(NST)
      DIMENSION FX(NC),FY(NC)
      REAL K02

c----tms----
      write(6,*) 'sub ANGUL2'
c----tme----
      DO 104 I=1,MAX
      DO 104 J=1,N12
      I1=I+(J-1)*MAX
      RX=X(I)+FX(J)
      RY=Y(I)+FY(J)
104   RE(I1)=EXP(-(RX*RX+RY*RY)*K02/(4.*DAN2))
      RETURN
      END
C
C
      SUBROUTINE LAYER(X,Y,Z,FX,FY,FZ,BRA,BAS,PR,N12,MAX,K0,RE,NST,NC)
C  CALCULATES MATRICES BRA1, BRA2 USED FOR THE CALCULATION OF THE
CONTRIBUTION
C  TO DOUBLE SCATTERING OF THE TOP LAYER IF IT HAS A BRAVAIS LATTICE
      DIMENSION X(NST),Y(NST),Z(NST),RE(NST)
      DIMENSION FX(NC),FY(NC),FZ(NC)
      COMPLEX BRA(NC),BAS(NC),PR
      REAL K0,DZ1
c       print *,' Layer 1: ',bra(1)
c----tms----
      write(6,*) 'sub LAYER'
c----tme----
      DO 422 J=1,N12
      TX=FX(J)
      TY=FY(J)
      TZ=FZ(J)
       DO 423 I=1,MAX
       XI=X(I)-TX
       YI=Y(I)-TY
       ZI=Z(I)-TZ
       DO 423 L=1,N12

       DX=XI+FX(L)
       DY=YI+FY(L)
       DZ1=ZI+FZ(L)
       R=SQRT(DX*DX+DY*DY+DZ1*DZ1)
       IF (R-1.E-4) 423,423,424
424    BRA(J)=BRA(J)+BAS(L)*SIN(K0*R)/R*RE(I+(L-1)*MAX)
423    CONTINUE

       BRA(J)=BRA(J)*PR
422    continue
c       print *,' Layer 2: ',bra(1)
c       pause
      RETURN
      END
C
C
      SUBROUTINE INTER(X,Y,Z,GX1,GY1,GZ1,GX2,GY2,GZ2,DZ,ICV,COM,BAS,PR,
```

```
     1N1,N2,MAX,K0,RE,NST,NC)
C  CALCULATES MATRICES COM1, COM2 USED FOR THE CALCULATION OF THE
CONTRIBUTION
C  TO DOUBLE SCATTERING OF A COMMENSURATE SYSTEM, WHEN THE ELECTRON
SCATTERS
C  FROM THE THE SECOND LAYER (COM1) OR THE TOP LAYER (COM2) FIRST
      DIMENSION X(NST),Y(NST),Z(NST),RE(NST)
      DIMENSION GX1(NC),GY1(NC),GZ1(NC)
      DIMENSION GX2(NC),GY2(NC),GZ2(NC)
      COMPLEX BAS(NC),COM(NC),PR
      REAL K0
c----tms----
      write(6,*) 'sub INTER'
c----tme----
      DO 622 J=1,N1
      TX=GX1(J)
      TY=GY1(J)
      TZ=GZ1(J)-ICV*DZ
       DO 623 K=1,MAX
       XK=TX-X(K)
       YK=TY-Y(K)
       ZK=TZ-Z(K)
       DO 623 L=1,N2
       DX=XK-GX2(L)
       DY=YK-GY2(L)
       DZ=ZK-GZ2(L)
       R=SQRT(DX*DX+DY*DY+DZ*DZ)
623    COM(J)=COM(J)+BAS(L)*SIN(K0*R)/R*RE(K+(L-1)*MAX)
622   COM(J)=COM(J)*PR
      RETURN
      END
C
C
      SUBROUTINE INTRA(MAX,X,Y,Z,SM,PR,K0,RE,NST,NC)
C  CALCULATES THE MATRIX SM1 (INTRALAYER SCATTERING OF THE FIRST LAYER) FOR
C  A SYSTEM WITH NOT WELL DEFINED FUNDAMENTAL PERIODICITY VECTORS
      DIMENSION X(NST),Y(NST),Z(NST),RE(NST)
      COMPLEX SM(NST),PR
      REAL K0
c----tms----
      write(6,*) 'sub INTRA'
c----tme----
      DO 122 I=1,MAX
      XI=X(I)
      YI=Y(I)
      ZI=Z(I)
      REI=RE(I)
       DO 122 K=1,I-1
       DX=X(K)-XI
       DY=Y(K)-YI
       DZ=Z(K)-ZI
       R=SQRT(DX*DX+DY*DY+DZ*DZ)
       SIR=SIN(K0*R)/R
       SM(K)=SM(K)+SIR*REI
122    SM(I)=SM(I)+SIR*RE(K)
      DO 123 I=1,MAX
123   SM(I)=SM(I)*PR
      RETURN
      END
C
C
      SUBROUTINE SETUP(AX,AY,BX,BY,XSIZE,YSIZE,X,Y,IMAX,NST,NC)
C  USING THE FUNDAMENTAL PERIODICITY VECTORS OF THE TOP LAYER & SUBSTRATE
```

```
C  CALCULATES THE COORDINATES OF THE UNIT CELLS OF THESE TWO LAYERS
C  WITHIN A RECTANGULAR AREA OF SIZES XSIZE, YSIZE
      DIMENSION X(NST),Y(NST)
c----tms----
      write(6,*) 'sub SETUP'
c----tms----
      DET=AX*BY-AY*BX
      I=0
      A0=0.4
      N1MAX=INT(XSIZE/A0)
      N2MAX=INT(YSIZE/A0)
      DO 92 N1=1,N1MAX
      XX=N1*A0-A0/2.
      DO 92 N2=1,N2MAX
      YY=N2*A0-A0/2.
      AM1=(XX*BY-YY*BX)/DET
      AM2=(YY*AX-XX*AY)/DET
      F1=AM1+0.5
      F2=AM2+0.5
      IF (F1.LT.0.) F1=F1-1.
      IF (F2.LT.0.) F2=F2-1.
      M1=INT(F1)
      M2=INT(F2)
      X0=M1*AX+M2*BX
      Y0=M1*AY+M2*BY
      IF ((N1-1)*A0.LE.X0.AND.N1*A0.GT.X0) THEN
       IF ((N2-1)*A0.LE.Y0.AND.N2*A0.GT.Y0) THEN
        I=I+1
        X(I)=X0-XSIZE/2.
        Y(I)=Y0-YSIZE/2.
       END IF
      END IF
92    CONTINUE
      IMAX=I
      RETURN
      END
C
C
```

Appendix B

S-wave Phase Shifts for tin and copper
calculated using
the Barbieri/Van Hove Phase Shift package from
Barbieri, A. and Van Hove, M.A., (1995)
private communication
(http://electron.lbl.gov/leedpack/)

Energy (eV)	S-wave Phase Shift (rad) Sn	Cu
1	3.90665	3.3282
2	3.86201	3.29387
3	3.81807	3.26008
4	3.77483	3.22682
5	3.73228	3.19409
6	3.69041	3.16187
7	3.64920	3.13017
8	3.60865	3.09896
9	3.56875	3.06825
10	3.52948	3.03803
11	3.49085	3.00828
12	3.45282	2.97901
13	3.41541	2.9502
14	3.37859	2.92184
15	3.34236	2.89394
16	3.30671	2.86647
17	3.27162	2.83944
18	3.23710	2.81284
19	3.20313	2.78665
20	3.16970	2.76088
21	3.13680	2.73552
22	3.10443	2.71056
23	3.07257	2.68599
24	3.04122	2.66181
25	3.01037	2.63801
26	2.98000	2.61458
27	2.95012	2.59152
28	2.92071	2.56882
29	2.89177	2.54647
30	2.86329	2.52448
31	2.83525	2.50282
32	2.80766	2.48151
33	2.78050	2.46052
34	2.75377	2.43986
35	2.72745	2.41952
36	2.70155	2.3995
37	2.67605	2.37978
38	2.65095	2.36036
39	2.62624	2.34125
40	2.60191	2.32242
41	2.57796	2.30388
42	2.55438	2.28562
43	2.53115	2.26764
44	2.50829	2.24993
45	2.48577	2.23248
46	2.46360	2.2153
47	2.44176	2.19837
48	2.42025	2.1817
49	2.39906	2.16527
50	2.37819	2.14908
51	2.35764	2.13313
52	2.33739	2.11741
53	2.31743	2.10192
54	2.29777	2.08665
55	2.27840	2.07161
56	2.25931	2.05678
57	2.24050	2.04215
58	2.22196	2.02774
59	2.20368	2.01353

60	2.18567	1.99951
61	2.16791	1.98569
62	2.15039	1.97207
63	2.13313	1.95862
64	2.11610	1.94536
65	2.09931	1.93228
66	2.08275	1.91938
67	2.06641	1.90665
68	2.05030	1.89408
69	2.03440	1.88168
70	2.01871	1.86944
71	2.00323	1.85736
72	1.98795	1.84543
73	1.97287	1.83365
74	1.95798	1.82202
75	1.94328	1.81054
76	1.92877	1.79919
77	1.91444	1.78799
78	1.90028	1.77692
79	1.88630	1.76598
80	1.87249	1.75517
81	1.85885	1.74449
82	1.84537	1.73393
83	1.83204	1.7235
84	1.81887	1.71318
85	1.80586	1.70298
86	1.79299	1.69289
87	1.78026	1.68291
88	1.76768	1.67303
89	1.75524	1.66327
90	1.74293	1.6536
91	1.73075	1.64404
92	1.71870	1.63457
93	1.70677	1.62521
94	1.69497	1.61593
95	1.68329	1.60675
96	1.67173	1.59765
97	1.66028	1.58864
98	1.64894	1.57972
99	1.63771	1.57088
100	1.62658	1.56213
101	1.61556	1.55345
102	1.60464	1.54485
103	1.59383	1.53632
104	1.58310	1.52787
105	1.57247	1.51949
106	1.56194	1.51118
107	1.55149	1.50294
108	1.54113	1.49477
109	1.53085	1.48666
110	1.52066	1.47862
111	1.51055	1.47063
112	1.50052	1.46271
113	1.49057	1.45485
114	1.48069	1.44705
115	1.47088	1.4393
116	1.46115	1.43161
117	1.45149	1.42397
118	1.44190	1.41639
119	1.43237	1.40885
120	1.42291	1.40137
121	1.41351	1.39393
122	1.40417	1.38655

123	1.39490	1.37921
124	1.38569	1.37192
125	1.37653	1.36467
126	1.36743	1.35746
127	1.35838	1.3503
128	1.34939	1.34318
129	1.34046	1.3361
130	1.33157	1.32907
131	1.32274	1.32207
132	1.31395	1.31511
133	1.30521	1.30818
134	1.29653	1.3013
135	1.28788	1.29445
136	1.27929	1.28763
137	1.27074	1.28085
138	1.26223	1.27411
139	1.25376	1.2674
140	1.24534	1.26072
141	1.23696	1.25407
142	1.22862	1.24746
143	1.22032	1.24088
144	1.21206	1.23432
145	1.20383	1.2278
146	1.19565	1.22131
147	1.18750	1.21485
148	1.17939	1.20841
149	1.17132	1.20201
150	1.16328	1.19563
151	1.15528	1.18928
152	1.14731	1.18296
153	1.13937	1.17667
154	1.13148	1.1704
155	1.12361	1.16416
156	1.11578	1.15795
157	1.10798	1.15176
158	1.10021	1.1456
159	1.09248	1.13947
160	1.08478	1.13336
161	1.07711	1.12727
162	1.06947	1.12122
163	1.06187	1.11518
164	1.05429	1.10917
165	1.04675	1.10319
166	1.03923	1.09723
167	1.03175	1.0913
168	1.02430	1.08539
169	1.01688	1.0795
170	1.00949	1.07364
171	1.00213	1.06781
172	0.99480	1.062
173	0.98751	1.05621
174	0.98024	1.05045
175	0.97300	1.04471
176	0.96580	1.039
177	0.95862	1.03331
178	0.95147	1.02764
179	0.94436	1.022
180	0.93728	1.01639
181	0.93022	1.0108
182	0.92320	1.00523
183	0.91621	0.99969
184	0.90925	0.99418
185	0.90232	0.98868

186	0.89542	0.98322
187	0.88855	0.97778
188	0.88171	0.97236
189	0.87491	0.96697
190	0.86813	0.96161
191	0.86139	0.95627
192	0.85468	0.95095
193	0.84800	0.94566
194	0.84135	0.9404
195	0.83474	0.93516
196	0.82816	0.92995
197	0.82161	0.92477
198	0.81509	0.91961
199	0.80860	0.91448
200	0.80215	0.90937
201	0.79573	0.90429
202	0.78935	0.89924
203	0.78299	0.89421
204	0.77667	0.88921
205	0.77039	0.88424
206	0.76413	0.87929
207	0.75791	0.87437
208	0.75173	0.86948
209	0.74557	0.86461
210	0.73946	0.85977
211	0.73337	0.85496
212	0.72732	0.85018
213	0.72130	0.84542
214	0.71532	0.84069
215	0.70937	0.83599
216	0.70345	0.83131
217	0.69757	0.82666
218	0.69172	0.82204
219	0.68591	0.81745
220	0.68013	0.81288
221	0.67438	0.80834
222	0.66867	0.80382
223	0.66299	0.79934
224	0.65735	0.79488
225	0.65174	0.79045
226	0.64616	0.78604
227	0.64061	0.78166
228	0.63510	0.77731
229	0.62962	0.77298
230	0.62418	0.76868
231	0.61876	0.7644
232	0.61338	0.76015
233	0.60803	0.75593
234	0.60271	0.75173
235	0.59742	0.74756
236	0.59217	0.74341
237	0.58694	0.73928
238	0.58175	0.73518
239	0.57658	0.7311
240	0.57145	0.72705
241	0.56634	0.72302
242	0.56126	0.71901
243	0.55621	0.71502
244	0.55119	0.71106
245	0.54619	0.70711
246	0.54122	0.70319
247	0.53627	0.69929
248	0.53135	0.6954

249	0.52646	0.69154
250	0.52159	0.6877
251	0.51674	0.68387
252	0.51191	0.68006
253	0.50710	0.67627
254	0.50232	0.67249
255	0.49755	0.66873
256	0.49281	0.66498
257	0.48808	0.66125
258	0.48336	0.65753
259	0.47866	0.65382
260	0.47398	0.65012
261	0.46931	0.64644
262	0.46465	0.64276
263	0.46001	0.63909
264	0.45537	0.63543
265	0.45074	0.63178
266	0.44612	0.62813
267	0.44151	0.62449
268	0.43690	0.62085
269	0.43229	0.61721
270	0.42769	0.61357
271	0.42308	0.60994
272	0.41848	0.6063
273	0.41387	0.60266
274	0.40926	0.59902
275	0.40464	0.59537
276	0.40001	0.59171
277	0.39537	0.58805
278	0.39072	0.58438
279	0.38606	0.5807
280	0.38138	0.577
281	0.37669	0.57329
282	0.37198	0.56957
283	0.36724	0.56582
284	0.36248	0.56206
285	0.35770	0.55828
286	0.35288	0.55448
287	0.34804	0.55065
288	0.34317	0.54679
289	0.33826	0.54291
290	0.33331	0.539
291	0.32832	0.53506
292	0.32329	0.53108
293	0.31821	0.52707
294	0.31309	0.52301
295	0.30792	0.51892
296	0.30269	0.51479
297	0.29741	0.51061
298	0.29207	0.50639
299	0.28666	0.50211
300	0.28119	0.49779

Appendix C

Structural Parameter Files for Sn/Cu{100}

1. Phase I Overlayer model
2. Phase I Surface Alloy model
3. Phase II Argile and Rhead Model
4. Phase II Overlayer Model
5. Phase II Surface Alloy Model
6. Phase III Argile and Rhead Model
7. Phase III Overlayer Model
8. Phase III Surface Alloy Model
9. Phase IV Argile and Rhead Model
10. Phase IV Overlayer Model
11. Phase IV Surface Alloy Model

Format of Structural Parameter Files

When the structural parameter file is called, the program reads in the values for

XSIZE, YSIZE
MINAB, DZ
COMENS

Then there are five different formats for structural parameter files that depend on the choices made. The program reads in the atoms positions in the following order for:

(a) *A commensurate structure*

A2X, A2Y
B2X, B2Y
NTOP, NSUB
FX1, FY1, FZ1
FX2, FY2, FZ2

(b) An incommensurate structure; Uniform Overlayer, Uniform Substrate (1,1)

A1X, A1Y
B1X, B1Y
NTOP
FX1, FY1, FZ1
A2X, A2Y
B2X, B2Y
NSUB
FX2, FY2, FZ2

(c) An incommensurate structure; Uniform Overlayer, Non-uniform Substrate (1,0)

A1X, A1Y
B1X, B1Y
NTOP
FX1, FY1, FZ1
KMAX
X2, Y2, Z2

(d) *An incommensurate structure; Non-uniform Overlayer, Uniform Substrate (0,1)*

IMAX
X1, Y1, Z1
A2X, A2Y
B2X, B2Y
NSUB
FX2, FY2, FZ2

(e) *An incommensurate structure; Non-uniform Overlayer, Non-uniform Substrate (0,0)*

IMAX
X1, Y1, Z1
KMAX
X2, Y2, Z2

1. Phase I Overlayer model

71.4,71.4 XSIZE,YSIZE
2.55,2.27 MINAB,DZ
0 COMENS
0,1 UNIF1,UNIF2
140 NUMBER OF TIN ATOMS

-30.6000	-35.7000	0.000000
-25.5000	-35.7000	0.000000
-20.4000	-35.7000	0.000000
-30.6000	-30.6000	0.000000
-25.5000	-30.6000	0.000000
-20.4000	-30.6000	0.000000
-30.6000	-25.5000	0.000000
-25.5000	-25.5000	0.000000
-20.4000	-25.5000	0.000000
-30.6000	-20.4000	0.000000
-25.5000	-20.4000	0.000000
-20.4000	-20.4000	0.000000
-33.1500	-10.2000	0.000000
-28.0500	-10.2000	0.000000
-22.9500	-10.2000	0.000000
-33.1500	-5.10000	0.000000
-28.0500	-5.10000	0.000000
-22.9500	-5.10000	0.000000
-33.1500	0.000000	0.000000
-28.0500	0.000000	0.000000
-22.9500	0.000000	0.000000
-33.1500	5.10000	0.000000
-28.0500	5.10000	0.000000
-22.9500	5.10000	0.000000
-35.7000	15.3000	0.000000
-30.6000	15.3000	0.000000
-25.5000	15.3000	0.000000
-20.4000	15.3000	0.000000
-35.7000	20.4000	0.000000
-30.6000	20.4000	0.000000
-25.5000	20.4000	0.000000
-20.4000	20.4000	0.000000
-35.7000	25.5000	0.000000
-30.6000	25.5000	0.000000
-25.5000	25.5000	0.000000
-20.4000	25.5000	0.000000
-35.7000	30.6000	0.000000
-30.6000	30.6000	0.000000
-25.5000	30.6000	0.000000
-20.4000	30.6000	0.000000
-10.2000	-33.1500	0.000000
-5.10000	-33.1500	0.000000
0.000000	-33.1500	0.000000
5.10000	-33.1500	0.000000
-10.2000	-28.0500	0.000000
-5.10000	-28.0500	0.000000
0.000000	-28.0500	0.000000
5.10000	-28.0500	0.000000
-10.2000	-22.9500	0.000000
-5.10000	-22.9500	0.000000
0.000000	-22.9500	0.000000
5.10000	-22.9500	0.000000
-10.2000	-17.8500	0.000000
-5.10000	-17.8500	0.000000
0.000000	-17.8500	0.000000
5.10000	-17.8500	0.000000
-12.7500	-7.65000	0.000000
-7.65000	-7.65000	0.000000
-2.55000	-7.65000	0.000000
2.55000	-7.65000	0.000000
-12.7500	-2.55000	0.000000
-7.65000	-2.55000	0.000000
-2.55000	-2.55000	0.000000
2.55000	-2.55000	0.000000
-12.7500	2.55000	0.000000
-7.65000	2.55000	0.000000
-2.55000	2.55000	0.000000
2.55000	2.55000	0.000000

2.55	0
0	2.55

AX AY
BX BY
1 NSUB
-1.275 -1.275 0.0 COPPER POSITIONS IN SUBSTRATE LATTICE

-12.7500	7.65000	0.000000
-7.65000	7.65000	0.000000
-2.55000	7.65000	0.000000
2.55000	7.65000	0.000000
-10.2000	17.8500	0.000000
-5.10000	17.8500	0.000000
0.000000	17.8500	0.000000
5.10000	17.8500	0.000000
-10.2000	22.9500	0.000000
-5.10000	22.9500	0.000000
0.000000	22.9500	0.000000
5.10000	22.9500	0.000000
-10.2000	28.0500	0.000000
-5.10000	28.0500	0.000000
0.000000	28.0500	0.000000
5.10000	28.0500	0.000000
-10.2000	33.1500	0.000000
-5.10000	33.1500	0.000000
0.000000	33.1500	0.000000
5.10000	33.1500	0.000000
15.3000	-35.7000	0.000000
20.4000	-35.7000	0.000000
25.5000	-35.7000	0.000000
30.6000	-35.7000	0.000000
15.3000	-30.6000	0.000000
20.4000	-30.6000	0.000000
25.5000	-30.6000	0.000000
30.6000	-30.6000	0.000000
15.3000	-25.5000	0.000000
20.4000	-25.5000	0.000000
25.5000	-25.5000	0.000000
30.6000	-25.5000	0.000000
15.3000	-20.4000	0.000000
20.4000	-20.4000	0.000000
25.5000	-20.4000	0.000000
30.6000	-20.4000	0.000000
12.7500	-10.2000	0.000000
17.8500	-10.2000	0.000000
22.9500	-10.2000	0.000000
28.0500	-10.2000	0.000000
12.7500	-5.10000	0.000000
17.8500	-5.10000	0.000000
22.9500	-5.10000	0.000000
28.0500	-5.10000	0.000000
12.7500	0.000000	0.000000
17.8500	0.000000	0.000000
22.9500	0.000000	0.000000
28.0500	0.000000	0.000000
12.7500	5.10000	0.000000
17.8500	5.10000	0.000000
22.9500	5.10000	0.000000
28.0500	5.10000	0.000000
15.3000	15.3000	0.000000
20.4000	15.3000	0.000000
25.5000	15.3000	0.000000
30.6000	15.3000	0.000000
15.3000	20.4000	0.000000
20.4000	20.4000	0.000000
25.5000	20.4000	0.000000
30.6000	20.4000	0.000000
15.3000	25.5000	0.000000
20.4000	25.5000	0.000000
25.5000	25.5000	0.000000
30.6000	25.5000	0.000000
15.3000	30.6000	0.000000
20.4000	30.6000	0.000000
25.5000	30.6000	0.000000
30.6000	30.6000	0.000000

2. Phase I Surface Alloy model

71.4,71.4 XSIZE,YSIZE
2.55,2.27 MINAB,DZ
0 COMENS
0,0 UNIF1,UNIF2
140 **IMAX (NUMBER OF TIN ATOMS)**

-35.7000	-35.7000	0.000000
-30.6000	-35.7000	0.000000
-25.5000	-35.7000	0.000000
-20.4000	-35.7000	0.000000
-35.7000	-30.6000	0.000000
-30.6000	-30.6000	0.000000
-25.5000	-30.6000	0.000000
-20.4000	-30.6000	0.000000
-35.7000	-25.5000	0.000000
-30.6000	-25.5000	0.000000
-25.5000	-25.5000	0.000000
-20.4000	-25.5000	0.000000
-35.7000	-20.4000	0.000000
-30.6000	-20.4000	0.000000
-25.5000	-20.4000	0.000000
-20.4000	-20.4000	0.000000
-33.1500	-10.2000	0.000000
-28.0500	-10.2000	0.000000
-22.9500	-10.2000	0.000000
-33.1500	-5.10000	0.000000
-28.0500	-5.10000	0.000000
-22.9500	-5.10000	0.000000
-33.1500	0.000000	0.000000
-28.0500	0.000000	0.000000
-22.9500	0.000000	0.000000
-33.1500	5.10000	0.000000
-28.0500	5.10000	0.000000
-22.9500	5.10000	0.000000
-35.7000	15.3000	0.000000
-30.6000	15.3000	0.000000
-25.5000	15.3000	0.000000
-20.4000	15.3000	0.000000
-35.7000	20.4000	0.000000
-30.6000	20.4000	0.000000
-25.5000	20.4000	0.000000
-20.4000	20.4000	0.000000
-35.7000	25.5000	0.000000
-30.6000	25.5000	0.000000
-25.5000	25.5000	0.000000
-20.4000	25.5000	0.000000
-35.7000	30.6000	0.000000
-30.6000	30.6000	0.000000
-25.5000	30.6000	0.000000
-20.4000	30.6000	0.000000
-10.2000	-33.1500	0.000000
-5.10000	-33.1500	0.000000
0.000000	-33.1500	0.000000
5.10000	-33.1500	0.000000
-10.2000	-28.0500	0.000000
-5.10000	-28.0500	0.000000
0.000000	-28.0500	0.000000
5.10000	-28.0500	0.000000
-10.2000	-22.9500	0.000000
-5.10000	-22.9500	0.000000
0.000000	-22.9500	0.000000
5.10000	-22.9500	0.000000
-10.2000	-17.8500	0.000000
-5.10000	-17.8500	0.000000
0.000000	-17.8500	0.000000
5.10000	-17.8500	0.000000
-12.7500	-7.65000	0.000000
-7.65000	-7.65000	0.000000
-2.55000	-7.65000	0.000000
2.55000	-7.65000	0.000000
-12.7500	-2.55000	0.000000
-7.65000	-2.55000	0.000000
-2.55000	-2.55000	0.000000
2.55000	-2.55000	0.000000
-12.7500	2.55000	0.000000
-7.65000	2.55000	0.000000
-2.55000	2.55000	0.000000
2.55000	2.55000	0.000000
-12.7500	7.65000	0.000000
-7.65000	7.65000	0.000000
-2.55000	7.65000	0.000000
2.55000	7.65000	0.000000
-10.2000	17.8500	0.000000
-5.10000	17.8500	0.000000
0.000000	17.8500	0.000000
5.10000	17.8500	0.000000
-10.2000	22.9500	0.000000
-5.10000	22.9500	0.000000
0.000000	22.9500	0.000000
5.10000	22.9500	0.000000
-10.2000	28.0500	0.000000
-5.10000	28.0500	0.000000
0.000000	28.0500	0.000000
5.10000	28.0500	0.000000
-10.2000	33.1500	0.000000
-5.10000	33.1500	0.000000
0.000000	33.1500	0.000000
5.10000	33.1500	0.000000
15.3000	-35.7000	0.000000
20.4000	-35.7000	0.000000
25.5000	-35.7000	0.000000
30.6000	-35.7000	0.000000
15.3000	-30.6000	0.000000
20.4000	-30.6000	0.000000
25.5000	-30.6000	0.000000
30.6000	-30.6000	0.000000
15.3000	-25.5000	0.000000
20.4000	-25.5000	0.000000
25.5000	-25.5000	0.000000
30.6000	-25.5000	0.000000
15.3000	-20.4000	0.000000
20.4000	-20.4000	0.000000
25.5000	-20.4000	0.000000
30.6000	-20.4000	0.000000
12.7500	-10.2000	0.000000
17.8500	-10.2000	0.000000
22.9500	-10.2000	0.000000
28.0500	-10.2000	0.000000
12.7500	-5.10000	0.000000
17.8500	-5.10000	0.000000
22.9500	-5.10000	0.000000
28.0500	-5.10000	0.000000
12.7500	0.000000	0.000000
17.8500	0.000000	0.000000
22.9500	0.000000	0.000000
28.0500	0.000000	0.000000
12.7500	5.10000	0.000000
17.8500	5.10000	0.000000
22.9500	5.10000	0.000000
28.0500	5.10000	0.000000
15.3000	15.3000	0.000000
20.4000	15.3000	0.000000
25.5000	15.3000	0.000000
30.6000	15.3000	0.000000
15.3000	20.4000	0.000000
20.4000	20.4000	0.000000
25.5000	20.4000	0.000000
30.6000	20.4000	0.000000
15.3000	25.5000	0.000000
20.4000	25.5000	0.000000
25.5000	25.5000	0.000000
30.6000	25.5000	0.000000
15.3000	30.6000	0.000000
20.4000	30.6000	0.000000
30.6000	30.6000	0.000000
25.5000	30.6000	0.000000

1428 **KMAX (NUMMER OF COPPER ATOMS)**

-35.7	-33.15	-0.47	-35.7	-28.05	-0.47	-35.7	-22.95	-0.47

-35.7	-17.85	-0.47
-35.7	-15.3	-0.47
-35.7	-12.75	-0.47
-35.7	-10.2	-0.47
-35.7	-7.65	-0.47
-35.7	-5.1	-0.47
-35.7	-2.55	-0.47
-35.7	0	-0.47
-35.7	2.55	-0.47
-35.7	5.1	-0.47
-35.7	7.65	-0.47
-35.7	10.2	-0.47
-35.7	12.75	-0.47
-35.7	17.85	-0.47
-35.7	22.95	-0.47
-35.7	28.05	-0.47
-35.7	33.15	-0.47
-33.15	-35.7	-0.47
-33.15	-33.15	-0.47
-33.15	-30.6	-0.47
-33.15	-28.05	-0.47
-33.15	-25.5	-0.47
-33.15	-22.95	-0.47
-33.15	-20.4	-0.47
-33.15	-17.85	-0.47
-33.15	-15.3	-0.47
-33.15	-12.75	-0.47
-33.15	-7.65	-0.47
-33.15	-2.55	-0.47
-33.15	2.55	-0.47
-33.15	7.65	-0.47
-33.15	10.2	-0.47
-33.15	12.75	-0.47
-33.15	15.3	-0.47
-33.15	17.85	-0.47
-33.15	20.4	-0.47
-33.15	22.95	-0.47
-33.15	25.5	-0.47
-33.15	28.05	-0.47
-33.15	30.6	-0.47
-33.15	33.15	-0.47
-30.6	-33.15	-0.47
-30.6	-28.05	-0.47
-30.6	-22.95	-0.47
-30.6	-17.85	-0.47
-30.6	-15.3	-0.47
-30.6	-12.75	-0.47
-30.6	-10.2	-0.47
-30.6	-7.65	-0.47
-30.6	-5.1	-0.47
-30.6	-2.55	-0.47
-30.6	0	-0.47
-30.6	2.55	-0.47
-30.6	5.1	-0.47
-30.6	7.65	-0.47
-30.6	10.2	-0.47
-30.6	12.75	-0.47
-30.6	17.85	-0.47
-30.6	22.95	-0.47
-30.6	28.05	-0.47
-30.6	33.15	-0.47
-28.05	-35.7	-0.47
-28.05	-33.15	-0.47
-28.05	-30.6	-0.47
-28.05	-28.05	-0.47
-28.05	-25.5	-0.47
-28.05	-22.95	-0.47
-28.05	-20.4	-0.47
-28.05	-17.85	-0.47
-28.05	-15.3	-0.47
-28.05	-12.75	-0.47
-28.05	-7.65	-0.47
-28.05	-2.55	-0.47
-28.05	2.55	-0.47
-28.05	7.65	-0.47
-28.05	10.2	-0.47
-28.05	12.75	-0.47
-28.05	15.3	-0.47
-28.05	17.85	-0.47
-28.05	20.4	-0.47
-28.05	22.95	-0.47
-28.05	25.5	-0.47
-28.05	28.05	-0.47
-28.05	30.6	-0.47
-28.05	33.15	-0.47
-25.5	-33.15	-0.47
-25.5	-28.05	-0.47
-25.5	-22.95	-0.47
-25.5	-17.85	-0.47
-25.5	-15.3	-0.47
-25.5	-12.75	-0.47
-25.5	-10.2	-0.47
-25.5	-7.65	-0.47
-25.5	-5.1	-0.47
-25.5	-2.55	-0.47
-25.5	0	-0.47
-25.5	2.55	-0.47
-25.5	5.1	-0.47
-25.5	7.65	-0.47
-25.5	10.2	-0.47
-25.5	12.75	-0.47
-25.5	17.85	-0.47
-25.5	22.95	-0.47
-25.5	28.05	-0.47
-25.5	33.15	-0.47
-22.95	-35.7	-0.47
-22.95	-33.15	-0.47
-22.95	-30.6	-0.47
-22.95	-28.05	-0.47
-22.95	-25.5	-0.47
-22.95	-22.95	-0.47
-22.95	-20.4	-0.47
-22.95	-17.85	-0.47
-22.95	-15.3	-0.47
-22.95	-12.75	-0.47
-22.95	-7.65	-0.47
-22.95	-2.55	-0.47
-22.95	2.55	-0.47
-22.95	7.65	-0.47
-22.95	10.2	-0.47
-22.95	12.75	-0.47
-22.95	15.3	-0.47
-22.95	17.85	-0.47
-22.95	20.4	-0.47
-22.95	22.95	-0.47
-22.95	25.5	-0.47
-22.95	28.05	-0.47
-22.95	30.6	-0.47
-22.95	33.15	-0.47
-20.4	-33.15	-0.47
-20.4	-28.05	-0.47
-20.4	-22.95	-0.47
-20.4	-17.85	-0.47
-20.4	-15.3	-0.47
-20.4	-12.75	-0.47
-20.4	-10.2	-0.47
-20.4	-7.65	-0.47
-20.4	-5.1	-0.47
-20.4	-2.55	-0.47
-20.4	0	-0.47
-20.4	2.55	-0.47
-20.4	5.1	-0.47
-20.4	7.65	-0.47
-20.4	10.2	-0.47
-20.4	12.75	-0.47
-20.4	17.85	-0.47
-20.4	22.95	-0.47
-20.4	28.05	-0.47
-20.4	33.15	-0.47
-17.85	-35.7	-0.47
-17.85	-33.15	-0.47
-17.85	-30.6	-0.47
-17.85	-28.05	-0.47
-17.85	-25.5	-0.47
-17.85	-22.95	-0.47
-17.85	-20.4	-0.47
-17.85	-17.85	-0.47
-17.85	-15.3	-0.47
-17.85	-12.75	-0.47
-17.85	-10.2	-0.47
-17.85	-7.65	-0.47
-17.85	-5.1	-0.47
-17.85	-2.55	-0.47
-17.85	0	-0.47
-17.85	2.55	-0.47
-17.85	5.1	-0.47
-17.85	7.65	-0.47
-17.85	10.2	-0.47
-17.85	12.75	-0.47
-17.85	15.3	-0.47
-17.85	17.85	-0.47
-17.85	20.4	-0.47
-17.85	22.95	-0.47
-17.85	25.5	-0.47
-17.85	28.05	-0.47
-17.85	30.6	-0.47
-17.85	33.15	-0.47
-15.3	-35.7	-0.47
-15.3	-33.15	-0.47
-15.3	-30.6	-0.47
-15.3	-28.05	-0.47
-15.3	-25.5	-0.47
-15.3	-22.95	-0.47
-15.3	-20.4	-0.47
-15.3	-17.85	-0.47
-15.3	-15.3	-0.47
-15.3	-12.75	-0.47
-15.3	-10.2	-0.47
-15.3	-7.65	-0.47
-15.3	-5.1	-0.47
-15.3	-2.55	-0.47
-15.3	0	-0.47
-15.3	2.55	-0.47
-15.3	5.1	-0.47
-15.3	7.65	-0.47
-15.3	10.2	-0.47
-15.3	12.75	-0.47
-15.3	15.3	-0.47
-15.3	17.85	-0.47
-15.3	20.4	-0.47
-15.3	22.95	-0.47
-15.3	25.5	-0.47
-15.3	28.05	-0.47
-15.3	30.6	-0.47
-15.3	33.15	-0.47
-12.75	-35.7	-0.47
-12.75	-33.15	-0.47
-12.75	-30.6	-0.47
-12.75	-28.05	-0.47
-12.75	-25.5	-0.47
-12.75	-22.95	-0.47
-12.75	-20.4	-0.47
-12.75	-17.85	-0.47
-12.75	-15.3	-0.47
-12.75	-12.75	-0.47
-12.75	-10.2	-0.47
-12.75	-5.1	-0.47
-12.75	0	-0.47
-12.75	5.1	-0.47
-12.75	10.2	-0.47
-12.75	12.75	-0.47
-12.75	15.3	-0.47
-12.75	17.85	-0.47
-12.75	20.4	-0.47
-12.75	22.95	-0.47
-12.75	25.5	-0.47
-12.75	28.05	-0.47
-12.75	30.6	-0.47
-12.75	33.15	-0.47
-10.2	-35.7	-0.47
-10.2	-30.6	-0.47
-10.2	-25.5	-0.47
-10.2	-20.4	-0.47
-10.2	-15.3	-0.47
-10.2	-12.75	-0.47
-10.2	-10.2	-0.47
-10.2	-7.65	-0.47

-10.2	-5.1	-0.47
-10.2	-2.55	-0.47
-10.2	0	-0.47
-10.2	2.55	-0.47
-10.2	5.1	-0.47
-10.2	7.65	-0.47
-10.2	10.2	-0.47
-10.2	12.75	-0.47
-10.2	15.3	-0.47
-10.2	20.4	-0.47
-10.2	25.5	-0.47
-10.2	30.6	-0.47
-7.65	-35.7	-0.47
-7.65	-33.15	-0.47
-7.65	-30.6	-0.47
-7.65	-28.05	-0.47
-7.65	-25.5	-0.47
-7.65	-22.95	-0.47
-7.65	-20.4	-0.47
-7.65	-17.85	-0.47
-7.65	-15.3	-0.47
-7.65	-12.75	-0.47
-7.65	-10.2	-0.47
-7.65	-5.1	-0.47
-7.65	0	-0.47
-7.65	5.1	-0.47
-7.65	10.2	-0.47
-7.65	12.75	-0.47
-7.65	15.3	-0.47
-7.65	17.85	-0.47
-7.65	20.4	-0.47
-7.65	22.95	-0.47
-7.65	25.5	-0.47
-7.65	28.05	-0.47
-7.65	30.6	-0.47
-7.65	33.15	-0.47
-5.1	-35.7	-0.47
-5.1	-30.6	-0.47
-5.1	-25.5	-0.47
-5.1	-20.4	-0.47
-5.1	-15.3	-0.47
-5.1	-12.75	-0.47
-5.1	-10.2	-0.47
-5.1	-7.65	-0.47
-5.1	-5.1	-0.47
-5.1	-2.55	-0.47
-5.1	0	-0.47
-5.1	2.55	-0.47
-5.1	5.1	-0.47
-5.1	7.65	-0.47
-5.1	10.2	-0.47
-5.1	12.75	-0.47
-5.1	15.3	-0.47
-5.1	20.4	-0.47
-5.1	25.5	-0.47
-5.1	30.6	-0.47
-2.55	-35.7	-0.47
-2.55	-33.15	-0.47
-2.55	-30.6	-0.47
-2.55	-28.05	-0.47
-2.55	-25.5	-0.47
-2.55	-22.95	-0.47
-2.55	-20.4	-0.47
-2.55	-17.85	-0.47
-2.55	-15.3	-0.47
-2.55	-12.75	-0.47
-2.55	-10.2	-0.47
-2.55	-5.1	-0.47
-2.55	0	-0.47
-2.55	5.1	-0.47
-2.55	10.2	-0.47
-2.55	12.75	-0.47
-2.55	15.3	-0.47
-2.55	17.85	-0.47
-2.55	20.4	-0.47
-2.55	22.95	-0.47
-2.55	25.5	-0.47
-2.55	28.05	-0.47
-2.55	30.6	-0.47
-2.55	33.15	-0.47
0	-35.7	-0.47
0	-30.6	-0.47
0	-25.5	-0.47
0	-20.4	-0.47
0	-15.3	-0.47
0	-12.75	-0.47
0	-10.2	-0.47
0	-7.65	-0.47
0	-5.1	-0.47
0	-2.55	-0.47
0	0	-0.47
0	2.55	-0.47
0	5.1	-0.47
0	7.65	-0.47
0	10.2	-0.47
0	12.75	-0.47
0	15.3	-0.47
0	20.4	-0.47
0	25.5	-0.47
0	30.6	-0.47
2.55	-35.7	-0.47
2.55	-33.15	-0.47
2.55	-30.6	-0.47
2.55	-28.05	-0.47
2.55	-25.5	-0.47
2.55	-22.95	-0.47
2.55	-20.4	-0.47
2.55	-17.85	-0.47
2.55	-15.3	-0.47
2.55	-12.75	-0.47
2.55	-10.2	-0.47
2.55	-5.1	-0.47
2.55	0	-0.47
2.55	5.1	-0.47
2.55	10.2	-0.47
2.55	12.75	-0.47
2.55	15.3	-0.47
2.55	17.85	-0.47
2.55	20.4	-0.47
2.55	22.95	-0.47
2.55	25.5	-0.47
2.55	28.05	-0.47
2.55	30.6	-0.47
2.55	33.15	-0.47
5.1	-35.7	-0.47
5.1	-30.6	-0.47
5.1	-25.5	-0.47
5.1	-20.4	-0.47
5.1	-15.3	-0.47
5.1	-12.75	-0.47
5.1	-10.2	-0.47
5.1	-7.65	-0.47
5.1	-5.1	-0.47
5.1	-2.55	-0.47
5.1	0	-0.47
5.1	2.55	-0.47
5.1	5.1	-0.47
5.1	7.65	-0.47
5.1	10.2	-0.47
5.1	12.75	-0.47
5.1	15.3	-0.47
5.1	20.4	-0.47
5.1	25.5	-0.47
5.1	30.6	-0.47
7.65	-35.7	-0.47
7.65	-33.15	-0.47
7.65	-30.6	-0.47
7.65	-28.05	-0.47
7.65	-25.5	-0.47
7.65	-22.95	-0.47
7.65	-20.4	-0.47
7.65	-17.85	-0.47
7.65	-15.3	-0.47
7.65	-12.75	-0.47
7.65	-10.2	-0.47
7.65	-7.65	-0.47
7.65	-5.1	-0.47
7.65	-2.55	-0.47
7.65	0	-0.47
7.65	2.55	-0.47
7.65	5.1	-0.47
7.65	7.65	-0.47
7.65	10.2	-0.47
7.65	12.75	-0.47
7.65	15.3	-0.47
7.65	17.85	-0.47
7.65	20.4	-0.47
7.65	22.95	-0.47
7.65	25.5	-0.47
7.65	28.05	-0.47
7.65	30.6	-0.47
7.65	33.15	-0.47
10.2	-35.7	-0.47
10.2	-33.15	-0.47
10.2	-30.6	-0.47
10.2	-28.05	-0.47
10.2	-25.5	-0.47
10.2	-22.95	-0.47
10.2	-20.4	-0.47
10.2	-17.85	-0.47
10.2	-15.3	-0.47
10.2	-12.75	-0.47
10.2	-10.2	-0.47
10.2	-7.65	-0.47
10.2	-5.1	-0.47
10.2	-2.55	-0.47
10.2	0	-0.47
10.2	2.55	-0.47
10.2	5.1	-0.47
10.2	7.65	-0.47
10.2	10.2	-0.47
10.2	12.75	-0.47
10.2	15.3	-0.47
10.2	17.85	-0.47
10.2	20.4	-0.47
10.2	22.95	-0.47
10.2	25.5	-0.47
10.2	28.05	-0.47
10.2	30.6	-0.47
10.2	33.15	-0.47
12.75	-35.7	-0.47
12.75	-33.15	-0.47
12.75	-30.6	-0.47
12.75	-28.05	-0.47
12.75	-25.5	-0.47
12.75	-22.95	-0.47
12.75	-20.4	-0.47
12.75	-17.85	-0.47
12.75	-15.3	-0.47
12.75	-12.75	-0.47
12.75	-7.65	-0.47
12.75	-2.55	-0.47
12.75	2.55	-0.47
12.75	7.65	-0.47
12.75	10.2	-0.47
12.75	12.75	-0.47
12.75	15.3	-0.47
12.75	17.85	-0.47
12.75	20.4	-0.47
12.75	22.95	-0.47
12.75	25.5	-0.47
12.75	28.05	-0.47
12.75	30.6	-0.47
12.75	33.15	-0.47
15.3	-33.15	-0.47
15.3	-28.05	-0.47
15.3	-22.95	-0.47
15.3	-17.85	-0.47
15.3	-15.3	-0.47
15.3	-12.75	-0.47
15.3	-10.2	-0.47
15.3	-7.65	-0.47
15.3	-5.1	-0.47
15.3	-2.55	-0.47
15.3	0	-0.47
15.3	2.55	-0.47
15.3	5.1	-0.47

15.3	7.65	-0.47
15.3	10.2	-0.47
15.3	12.75	-0.47
15.3	17.85	-0.47
15.3	22.95	-0.47
15.3	28.05	-0.47
15.3	33.15	-0.47
17.85	-35.7	-0.47
17.85	-33.15	-0.47
17.85	-30.6	-0.47
17.85	-28.05	-0.47
17.85	-25.5	-0.47
17.85	-22.95	-0.47
17.85	-20.4	-0.47
17.85	-17.85	-0.47
17.85	-15.3	-0.47
17.85	-12.75	-0.47
17.85	-7.65	-0.47
17.85	-2.55	-0.47
17.85	2.55	-0.47
17.85	7.65	-0.47
17.85	10.2	-0.47
17.85	12.75	-0.47
17.85	15.3	-0.47
17.85	17.85	-0.47
17.85	20.4	-0.47
17.85	22.95	-0.47
17.85	25.5	-0.47
17.85	28.05	-0.47
17.85	30.6	-0.47
17.85	33.15	-0.47
20.4	-33.15	-0.47
20.4	-28.05	-0.47
20.4	-22.95	-0.47
20.4	-17.85	-0.47
20.4	-15.3	-0.47
20.4	-12.75	-0.47
20.4	-10.2	-0.47
20.4	-7.65	-0.47
20.4	-5.1	-0.47
20.4	-2.55	-0.47
20.4	0	-0.47
20.4	2.55	-0.47
20.4	5.1	-0.47
20.4	7.65	-0.47
20.4	10.2	-0.47
20.4	12.75	-0.47
20.4	17.85	-0.47
20.4	22.95	-0.47
20.4	28.05	-0.47
20.4	33.15	-0.47
22.95	-35.7	-0.47
22.95	-33.15	-0.47
22.95	-30.6	-0.47
22.95	-28.05	-0.47
22.95	-25.5	-0.47
22.95	-22.95	-0.47
22.95	-20.4	-0.47
22.95	-17.85	-0.47
22.95	-15.3	-0.47
22.95	-12.75	-0.47
22.95	-7.65	-0.47
22.95	-2.55	-0.47
22.95	2.55	-0.47
22.95	7.65	-0.47
22.95	10.2	-0.47
22.95	12.75	-0.47
22.95	15.3	-0.47
22.95	17.85	-0.47
22.95	20.4	-0.47
22.95	22.95	-0.47
22.95	25.5	-0.47
22.95	28.05	-0.47
22.95	30.6	-0.47
22.95	33.15	-0.47
25.5	-33.15	-0.47
25.5	-28.05	-0.47
25.5	-22.95	-0.47
25.5	-17.85	-0.47
25.5	-15.3	-0.47
25.5	-12.75	-0.47
25.5	-10.2	-0.47
25.5	-7.65	-0.47
25.5	-5.1	-0.47
25.5	-2.55	-0.47
25.5	0	-0.47
25.5	2.55	-0.47
25.5	5.1	-0.47
25.5	7.65	-0.47
25.5	10.2	-0.47
25.5	12.75	-0.47
25.5	17.85	-0.47
25.5	22.95	-0.47
25.5	28.05	-0.47
25.5	33.15	-0.47
28.05	-35.7	-0.47
28.05	-33.15	-0.47
28.05	-30.6	-0.47
28.05	-28.05	-0.47
28.05	-25.5	-0.47
28.05	-22.95	-0.47
28.05	-20.4	-0.47
28.05	-17.85	-0.47
28.05	-15.3	-0.47
28.05	-12.75	-0.47
28.05	-7.65	-0.47
28.05	-2.55	-0.47
28.05	2.55	-0.47
28.05	7.65	-0.47
28.05	10.2	-0.47
28.05	12.75	-0.47
28.05	15.3	-0.47
28.05	17.85	-0.47
28.05	20.4	-0.47
28.05	22.95	-0.47
28.05	25.5	-0.47
28.05	28.05	-0.47
28.05	30.6	-0.47
28.05	33.15	-0.47
30.6	-33.15	-0.47
30.6	-28.05	-0.47
30.6	-22.95	-0.47
30.6	-17.85	-0.47
30.6	-15.3	-0.47
30.6	-12.75	-0.47
30.6	-10.2	-0.47
30.6	-7.65	-0.47
30.6	-5.1	-0.47
30.6	-2.55	-0.47
30.6	0	-0.47
30.6	2.55	-0.47
30.6	5.1	-0.47
30.6	7.65	-0.47
30.6	10.2	-0.47
30.6	12.75	-0.47
30.6	17.85	-0.47
30.6	22.95	-0.47
30.6	28.05	-0.47
30.6	33.15	-0.47
33.15	-35.7	-0.47
33.15	-33.15	-0.47
33.15	-30.6	-0.47
33.15	-28.05	-0.47
33.15	-25.5	-0.47
33.15	-22.95	-0.47
33.15	-20.4	-0.47
33.15	-17.85	-0.47
33.15	-15.3	-0.47
33.15	-12.75	-0.47
33.15	-10.2	-0.47
33.15	-7.65	-0.47
33.15	-5.1	-0.47
33.15	-2.55	-0.47
33.15	0	-0.47
33.15	2.55	-0.47
33.15	5.1	-0.47
33.15	7.65	-0.47
33.15	10.2	-0.47
33.15	12.75	-0.47
33.15	15.3	-0.47
33.15	17.85	-0.47
33.15	20.4	-0.47
33.15	22.95	-0.47
33.15	25.5	-0.47
33.15	28.05	-0.47
33.15	30.6	-0.47
33.15	33.15	-0.47
-36.975	-36.975	-2.27
-36.975	-34.425	-2.27
-36.975	-31.875	-2.27
-36.975	-29.325	-2.27
-36.975	-26.775	-2.27
-36.975	-24.225	-2.27
-36.975	-21.675	-2.27
-36.975	-19.125	-2.27
-36.975	-16.575	-2.27
-36.975	-14.025	-2.27
-36.975	-11.475	-2.27
-36.975	-8.925	-2.27
-36.975	-6.375	-2.27
-36.975	-3.825	-2.27
-36.975	-1.275	-2.27
-36.975	1.275	-2.27
-36.975	3.825	-2.27
-36.975	6.375	-2.27
-36.975	8.925	-2.27
-36.975	11.475	-2.27
-36.975	14.025	-2.27
-36.975	16.575	-2.27
-36.975	19.125	-2.27
-36.975	21.675	-2.27
-36.975	24.225	-2.27
-36.975	26.775	-2.27
-36.975	29.325	-2.27
-36.975	31.875	-2.27
-34.425	-36.975	-2.27
-34.425	-34.425	-2.27
-34.425	-31.875	-2.27
-34.425	-29.325	-2.27
-34.425	-26.775	-2.27
-34.425	-24.225	-2.27
-34.425	-21.675	-2.27
-34.425	-19.125	-2.27
-34.425	-16.575	-2.27
-34.425	-14.025	-2.27
-34.425	-11.475	-2.27
-34.425	-8.925	-2.27
-34.425	-6.375	-2.27
-34.425	-3.825	-2.27
-34.425	-1.275	-2.27
-34.425	1.275	-2.27
-34.425	3.825	-2.27
-34.425	6.375	-2.27
-34.425	8.925	-2.27
-34.425	11.475	-2.27
-34.425	14.025	-2.27
-34.425	16.575	-2.27
-34.425	19.125	-2.27
-34.425	21.675	-2.27
-34.425	24.225	-2.27
-34.425	26.775	-2.27
-34.425	29.325	-2.27
-34.425	31.875	-2.27
-31.875	-36.975	-2.27
-31.875	-34.425	-2.27
-31.875	-31.875	-2.27
-31.875	-29.325	-2.27
-31.875	-26.775	-2.27
-31.875	-24.225	-2.27
-31.875	-21.675	-2.27
-31.875	-19.125	-2.27
-31.875	-16.575	-2.27
-31.875	-14.025	-2.27
-31.875	-11.475	-2.27
-31.875	-8.925	-2.27
-31.875	-6.375	-2.27
-31.875	-3.825	-2.27

-31.875	-1.275	-2.27
-31.875	1.275	-2.27
-31.875	3.825	-2.27
-31.875	6.375	-2.27
-31.875	8.925	-2.27
-31.875	11.475	-2.27
-31.875	14.025	-2.27
-31.875	16.575	-2.27
-31.875	19.125	-2.27
-31.875	21.675	-2.27
-31.875	24.225	-2.27
-31.875	26.775	-2.27
-31.875	29.325	-2.27
-31.875	31.875	-2.27
-29.325	-36.975	-2.27
-29.325	-34.425	-2.27
-29.325	-31.875	-2.27
-29.325	-29.325	-2.27
-29.325	-26.775	-2.27
-29.325	-24.225	-2.27
-29.325	-21.675	-2.27
-29.325	-19.125	-2.27
-29.325	-16.575	-2.27
-29.325	-14.025	-2.27
-29.325	-11.475	-2.27
-29.325	-8.925	-2.27
-29.325	-6.375	-2.27
-29.325	-3.825	-2.27
-29.325	-1.275	-2.27
-29.325	1.275	-2.27
-29.325	3.825	-2.27
-29.325	6.375	-2.27
-29.325	8.925	-2.27
-29.325	11.475	-2.27
-29.325	14.025	-2.27
-29.325	16.575	-2.27
-29.325	19.125	-2.27
-29.325	21.675	-2.27
-29.325	24.225	-2.27
-29.325	26.775	-2.27
-29.325	29.325	-2.27
-29.325	31.875	-2.27
-26.775	-36.975	-2.27
-26.775	-34.425	-2.27
-26.775	-31.875	-2.27
-26.775	-29.325	-2.27
-26.775	-26.775	-2.27
-26.775	-24.225	-2.27
-26.775	-21.675	-2.27
-26.775	-19.125	-2.27
-26.775	-16.575	-2.27
-26.775	-14.025	-2.27
-26.775	-11.475	-2.27
-26.775	-8.925	-2.27
-26.775	-6.375	-2.27
-26.775	-3.825	-2.27
-26.775	-1.275	-2.27
-26.775	1.275	-2.27
-26.775	3.825	-2.27
-26.775	6.375	-2.27
-26.775	8.925	-2.27
-26.775	11.475	-2.27
-26.775	14.025	-2.27
-26.775	16.575	-2.27
-26.775	19.125	-2.27
-26.775	21.675	-2.27
-26.775	24.225	-2.27
-26.775	26.775	-2.27
-26.775	29.325	-2.27
-26.775	31.875	-2.27
-24.225	-36.975	-2.27
-24.225	-34.425	-2.27
-24.225	-31.875	-2.27
-24.225	-29.325	-2.27
-24.225	-26.775	-2.27
-24.225	-24.225	-2.27
-24.225	-21.675	-2.27
-24.225	-19.125	-2.27
-24.225	-16.575	-2.27
-24.225	-14.025	-2.27
-24.225	-11.475	-2.27
-24.225	-8.925	-2.27
-24.225	-6.375	-2.27
-24.225	-3.825	-2.27
-24.225	-1.275	-2.27
-24.225	1.275	-2.27
-24.225	3.825	-2.27
-24.225	6.375	-2.27
-24.225	8.925	-2.27
-24.225	11.475	-2.27
-24.225	14.025	-2.27
-24.225	16.575	-2.27
-24.225	19.125	-2.27
-24.225	21.675	-2.27
-24.225	24.225	-2.27
-24.225	26.775	-2.27
-24.225	29.325	-2.27
-24.225	31.875	-2.27
-21.675	-36.975	-2.27
-21.675	-34.425	-2.27
-21.675	-31.875	-2.27
-21.675	-29.325	-2.27
-21.675	-26.775	-2.27
-21.675	-24.225	-2.27
-21.675	-21.675	-2.27
-21.675	-19.125	-2.27
-21.675	-16.575	-2.27
-21.675	-14.025	-2.27
-21.675	-11.475	-2.27
-21.675	-8.925	-2.27
-21.675	-6.375	-2.27
-21.675	-3.825	-2.27
-21.675	-1.275	-2.27
-21.675	1.275	-2.27
-21.675	3.825	-2.27
-21.675	6.375	-2.27
-21.675	8.925	-2.27
-21.675	11.475	-2.27
-21.675	14.025	-2.27
-21.675	16.575	-2.27
-21.675	19.125	-2.27
-21.675	21.675	-2.27
-21.675	24.225	-2.27
-21.675	26.775	-2.27
-21.675	29.325	-2.27
-21.675	31.875	-2.27
-19.125	-36.975	-2.27
-19.125	-34.425	-2.27
-19.125	-31.875	-2.27
-19.125	-29.325	-2.27
-19.125	-26.775	-2.27
-19.125	-24.225	-2.27
-19.125	-21.675	-2.27
-19.125	-19.125	-2.27
-19.125	-16.575	-2.27
-19.125	-14.025	-2.27
-19.125	-11.475	-2.27
-19.125	-8.925	-2.27
-19.125	-6.375	-2.27
-19.125	-3.825	-2.27
-19.125	-1.275	-2.27
-19.125	1.275	-2.27
-19.125	3.825	-2.27
-19.125	6.375	-2.27
-19.125	8.925	-2.27
-19.125	11.475	-2.27
-19.125	14.025	-2.27
-19.125	16.575	-2.27
-19.125	19.125	-2.27
-19.125	21.675	-2.27
-19.125	24.225	-2.27
-19.125	26.775	-2.27
-19.125	29.325	-2.27
-19.125	31.875	-2.27
-16.575	-36.975	-2.27
-16.575	-34.425	-2.27
-16.575	-31.875	-2.27
-16.575	-29.325	-2.27
-16.575	-26.775	-2.27
-16.575	-24.225	-2.27
-16.575	-21.675	-2.27
-16.575	-19.125	-2.27
-16.575	-16.575	-2.27
-16.575	-14.025	-2.27
-16.575	-11.475	-2.27
-16.575	-8.925	-2.27
-16.575	-6.375	-2.27
-16.575	-3.825	-2.27
-16.575	-1.275	-2.27
-16.575	1.275	-2.27
-16.575	3.825	-2.27
-16.575	6.375	-2.27
-16.575	8.925	-2.27
-16.575	11.475	-2.27
-16.575	14.025	-2.27
-16.575	16.575	-2.27
-16.575	19.125	-2.27
-16.575	21.675	-2.27
-16.575	24.225	-2.27
-16.575	26.775	-2.27
-16.575	29.325	-2.27
-16.575	31.875	-2.27
-14.025	-36.975	-2.27
-14.025	-34.425	-2.27
-14.025	-31.875	-2.27
-14.025	-29.325	-2.27
-14.025	-26.775	-2.27
-14.025	-24.225	-2.27
-14.025	-21.675	-2.27
-14.025	-19.125	-2.27
-14.025	-16.575	-2.27
-14.025	-14.025	-2.27
-14.025	-11.475	-2.27
-14.025	-8.925	-2.27
-14.025	-6.375	-2.27
-14.025	-3.825	-2.27
-14.025	-1.275	-2.27
-14.025	1.275	-2.27
-14.025	3.825	-2.27
-14.025	6.375	-2.27
-14.025	8.925	-2.27
-14.025	11.475	-2.27
-14.025	14.025	-2.27
-14.025	16.575	-2.27
-14.025	19.125	-2.27
-14.025	21.675	-2.27
-14.025	24.225	-2.27
-14.025	26.775	-2.27
-14.025	29.325	-2.27
-14.025	31.875	-2.27
-11.475	-36.975	-2.27
-11.475	-34.425	-2.27
-11.475	-31.875	-2.27
-11.475	-29.325	-2.27
-11.475	-26.775	-2.27
-11.475	-24.225	-2.27
-11.475	-21.675	-2.27
-11.475	-19.125	-2.27
-11.475	-16.575	-2.27
-11.475	-14.025	-2.27
-11.475	-11.475	-2.27
-11.475	-8.925	-2.27
-11.475	-6.375	-2.27
-11.475	-3.825	-2.27
-11.475	-1.275	-2.27
-11.475	1.275	-2.27
-11.475	3.825	-2.27
-11.475	6.375	-2.27
-11.475	8.925	-2.27
-11.475	11.475	-2.27
-11.475	14.025	-2.27
-11.475	16.575	-2.27
-11.475	19.125	-2.27
-11.475	21.675	-2.27
-11.475	24.225	-2.27
-11.475	26.775	-2.27
-11.475	29.325	-2.27

-11.475	31.875	-2.27
-8.925	-36.975	-2.27
-8.925	-34.425	-2.27
-8.925	-31.875	-2.27
-8.925	-29.325	-2.27
-8.925	-26.775	-2.27
-8.925	-24.225	-2.27
-8.925	-21.675	-2.27
-8.925	-19.125	-2.27
-8.925	-16.575	-2.27
-8.925	-14.025	-2.27
-8.925	-11.475	-2.27
-8.925	-8.925	-2.27
-8.925	-6.375	-2.27
-8.925	-3.825	-2.27
-8.925	-1.275	-2.27
-8.925	1.275	-2.27
-8.925	3.825	-2.27
-8.925	6.375	-2.27
-8.925	8.925	-2.27
-8.925	11.475	-2.27
-8.925	14.025	-2.27
-8.925	16.575	-2.27
-8.925	19.125	-2.27
-8.925	21.675	-2.27
-8.925	24.225	-2.27
-8.925	26.775	-2.27
-8.925	29.325	-2.27
-8.925	31.875	-2.27
-6.375	-36.975	-2.27
-6.375	-34.425	-2.27
-6.375	-31.875	-2.27
-6.375	-29.325	-2.27
-6.375	-26.775	-2.27
-6.375	-24.225	-2.27
-6.375	-21.675	-2.27
-6.375	-19.125	-2.27
-6.375	-16.575	-2.27
-6.375	-14.025	-2.27
-6.375	-11.475	-2.27
-6.375	-8.925	-2.27
-6.375	-6.375	-2.27
-6.375	-3.825	-2.27
-6.375	-1.275	-2.27
-6.375	1.275	-2.27
-6.375	3.825	-2.27
-6.375	6.375	-2.27
-6.375	8.925	-2.27
-6.375	11.475	-2.27
-6.375	14.025	-2.27
-6.375	16.575	-2.27
-6.375	19.125	-2.27
-6.375	21.675	-2.27
-6.375	24.225	-2.27
-6.375	26.775	-2.27
-6.375	29.325	-2.27
-6.375	31.875	-2.27
-3.825	-36.975	-2.27
-3.825	-34.425	-2.27
-3.825	-31.875	-2.27
-3.825	-29.325	-2.27
-3.825	-26.775	-2.27
-3.825	-24.225	-2.27
-3.825	-21.675	-2.27
-3.825	-19.125	-2.27
-3.825	-16.575	-2.27
-3.825	-14.025	-2.27
-3.825	-11.475	-2.27
-3.825	-8.925	-2.27
-3.825	-6.375	-2.27
-3.825	-3.825	-2.27
-3.825	-1.275	-2.27
-3.825	1.275	-2.27
-3.825	3.825	-2.27
-3.825	6.375	-2.27
-3.825	8.925	-2.27
-3.825	11.475	-2.27
-3.825	14.025	-2.27
-3.825	16.575	-2.27
-3.825	19.125	-2.27
-3.825	21.675	-2.27
-3.825	24.225	-2.27
-3.825	26.775	-2.27
-3.825	29.325	-2.27
-3.825	31.875	-2.27
-1.275	-36.975	-2.27
-1.275	-34.425	-2.27
-1.275	-31.875	-2.27
-1.275	-29.325	-2.27
-1.275	-26.775	-2.27
-1.275	-24.225	-2.27
-1.275	-21.675	-2.27
-1.275	-19.125	-2.27
-1.275	-16.575	-2.27
-1.275	-14.025	-2.27
-1.275	-11.475	-2.27
-1.275	-8.925	-2.27
-1.275	-6.375	-2.27
-1.275	-3.825	-2.27
-1.275	-1.275	-2.27
-1.275	1.275	-2.27
-1.275	3.825	-2.27
-1.275	6.375	-2.27
-1.275	8.925	-2.27
-1.275	11.475	-2.27
-1.275	14.025	-2.27
-1.275	16.575	-2.27
-1.275	19.125	-2.27
-1.275	21.675	-2.27
-1.275	24.225	-2.27
-1.275	26.775	-2.27
-1.275	29.325	-2.27
-1.275	31.875	-2.27
1.275	-36.975	-2.27
1.275	-34.425	-2.27
1.275	-31.875	-2.27
1.275	-29.325	-2.27
1.275	-26.775	-2.27
1.275	-24.225	-2.27
1.275	-21.675	-2.27
1.275	-19.125	-2.27
1.275	-16.575	-2.27
1.275	-14.025	-2.27
1.275	-11.475	-2.27
1.275	-8.925	-2.27
1.275	-6.375	-2.27
1.275	-3.825	-2.27
1.275	-1.275	-2.27
1.275	1.275	-2.27
1.275	3.825	-2.27
1.275	6.375	-2.27
1.275	8.925	-2.27
1.275	11.475	-2.27
1.275	14.025	-2.27
1.275	16.575	-2.27
1.275	19.125	-2.27
1.275	21.675	-2.27
1.275	24.225	-2.27
1.275	26.775	-2.27
1.275	29.325	-2.27
1.275	31.875	-2.27
3.825	-36.975	-2.27
3.825	-34.425	-2.27
3.825	-31.875	-2.27
3.825	-29.325	-2.27
3.825	-26.775	-2.27
3.825	-24.225	-2.27
3.825	-21.675	-2.27
3.825	-19.125	-2.27
3.825	-16.575	-2.27
3.825	-14.025	-2.27
3.825	-11.475	-2.27
3.825	-8.925	-2.27
3.825	-6.375	-2.27
3.825	-3.825	-2.27
3.825	-1.275	-2.27
3.825	1.275	-2.27
3.825	3.825	-2.27
3.825	6.375	-2.27
3.825	8.925	-2.27
3.825	11.475	-2.27
3.825	14.025	-2.27
3.825	16.575	-2.27
3.825	19.125	-2.27
3.825	21.675	-2.27
3.825	24.225	-2.27
3.825	26.775	-2.27
3.825	29.325	-2.27
3.825	31.875	-2.27
6.375	-36.975	-2.27
6.375	-34.425	-2.27
6.375	-31.875	-2.27
6.375	-29.325	-2.27
6.375	-26.775	-2.27
6.375	-24.225	-2.27
6.375	-21.675	-2.27
6.375	-19.125	-2.27
6.375	-16.575	-2.27
6.375	-14.025	-2.27
6.375	-11.475	-2.27
6.375	-8.925	-2.27
6.375	-6.375	-2.27
6.375	-3.825	-2.27
6.375	-1.275	-2.27
6.375	1.275	-2.27
6.375	3.825	-2.27
6.375	6.375	-2.27
6.375	8.925	-2.27
6.375	11.475	-2.27
6.375	14.025	-2.27
6.375	16.575	-2.27
6.375	19.125	-2.27
6.375	21.675	-2.27
6.375	24.225	-2.27
6.375	26.775	-2.27
6.375	29.325	-2.27
6.375	31.875	-2.27
8.925	-36.975	-2.27
8.925	-34.425	-2.27
8.925	-31.875	-2.27
8.925	-29.325	-2.27
8.925	-26.775	-2.27
8.925	-24.225	-2.27
8.925	-21.675	-2.27
8.925	-19.125	-2.27
8.925	-16.575	-2.27
8.925	-14.025	-2.27
8.925	-11.475	-2.27
8.925	-8.925	-2.27
8.925	-6.375	-2.27
8.925	-3.825	-2.27
8.925	-1.275	-2.27
8.925	1.275	-2.27
8.925	3.825	-2.27
8.925	6.375	-2.27
8.925	8.925	-2.27
8.925	11.475	-2.27
8.925	14.025	-2.27
8.925	16.575	-2.27
8.925	19.125	-2.27
8.925	21.675	-2.27
8.925	24.225	-2.27
8.925	26.775	-2.27
8.925	29.325	-2.27
8.925	31.875	-2.27
11.475	-36.975	-2.27
11.475	-34.425	-2.27
11.475	-31.875	-2.27
11.475	-29.325	-2.27
11.475	-26.775	-2.27
11.475	-24.225	-2.27
11.475	-21.675	-2.27
11.475	-19.125	-2.27
11.475	-16.575	-2.27
11.475	-14.025	-2.27
11.475	-11.475	-2.27
11.475	-8.925	-2.27

11.475	-6.375	-2.27
11.475	-3.825	-2.27
11.475	-1.275	-2.27
11.475	1.275	-2.27
11.475	3.825	-2.27
11.475	6.375	-2.27
11.475	8.925	-2.27
11.475	11.475	-2.27
11.475	14.025	-2.27
11.475	16.575	-2.27
11.475	19.125	-2.27
11.475	21.675	-2.27
11.475	24.225	-2.27
11.475	26.775	-2.27
11.475	29.325	-2.27
11.475	31.875	-2.27
14.025	-36.975	-2.27
14.025	-34.425	-2.27
14.025	-31.875	-2.27
14.025	-29.325	-2.27
14.025	-26.775	-2.27
14.025	-24.225	-2.27
14.025	-21.675	-2.27
14.025	-19.125	-2.27
14.025	-16.575	-2.27
14.025	-14.025	-2.27
14.025	-11.475	-2.27
14.025	-8.925	-2.27
14.025	-6.375	-2.27
14.025	-3.825	-2.27
14.025	-1.275	-2.27
14.025	1.275	-2.27
14.025	3.825	-2.27
14.025	6.375	-2.27
14.025	8.925	-2.27
14.025	11.475	-2.27
14.025	14.025	-2.27
14.025	16.575	-2.27
14.025	19.125	-2.27
14.025	21.675	-2.27
14.025	24.225	-2.27
14.025	26.775	-2.27
14.025	29.325	-2.27
14.025	31.875	-2.27
16.575	-36.975	-2.27
16.575	-34.425	-2.27
16.575	-31.875	-2.27
16.575	-29.325	-2.27
16.575	-26.775	-2.27
16.575	-24.225	-2.27
16.575	-21.675	-2.27
16.575	-19.125	-2.27
16.575	-16.575	-2.27
16.575	-14.025	-2.27
16.575	-11.475	-2.27
16.575	-8.925	-2.27
16.575	-6.375	-2.27
16.575	-3.825	-2.27
16.575	-1.275	-2.27
16.575	1.275	-2.27
16.575	3.825	-2.27
16.575	6.375	-2.27
16.575	8.925	-2.27
16.575	11.475	-2.27
16.575	14.025	-2.27
16.575	16.575	-2.27
16.575	19.125	-2.27
16.575	21.675	-2.27
16.575	24.225	-2.27
16.575	26.775	-2.27
16.575	29.325	-2.27
16.575	31.875	-2.27
19.125	-36.975	-2.27
19.125	-34.425	-2.27
19.125	-31.875	-2.27
19.125	-29.325	-2.27
19.125	-26.775	-2.27
19.125	-24.225	-2.27
19.125	-21.675	-2.27
19.125	-19.125	-2.27
19.125	-16.575	-2.27
19.125	-14.025	-2.27
19.125	-11.475	-2.27
19.125	-8.925	-2.27
19.125	-6.375	-2.27
19.125	-3.825	-2.27
19.125	-1.275	-2.27
19.125	1.275	-2.27
19.125	3.825	-2.27
19.125	6.375	-2.27
19.125	8.925	-2.27
19.125	11.475	-2.27
19.125	14.025	-2.27
19.125	16.575	-2.27
19.125	19.125	-2.27
19.125	21.675	-2.27
19.125	24.225	-2.27
19.125	26.775	-2.27
19.125	29.325	-2.27
19.125	31.875	-2.27
21.675	-36.975	-2.27
21.675	-34.425	-2.27
21.675	-31.875	-2.27
21.675	-29.325	-2.27
21.675	-26.775	-2.27
21.675	-24.225	-2.27
21.675	-21.675	-2.27
21.675	-19.125	-2.27
21.675	-16.575	-2.27
21.675	-14.025	-2.27
21.675	-11.475	-2.27
21.675	-8.925	-2.27
21.675	-6.375	-2.27
21.675	-3.825	-2.27
21.675	-1.275	-2.27
21.675	1.275	-2.27
21.675	3.825	-2.27
21.675	6.375	-2.27
21.675	8.925	-2.27
21.675	11.475	-2.27
21.675	14.025	-2.27
21.675	16.575	-2.27
21.675	19.125	-2.27
21.675	21.675	-2.27
21.675	24.225	-2.27
21.675	26.775	-2.27
21.675	29.325	-2.27
21.675	31.875	-2.27
24.225	-36.975	-2.27
24.225	-34.425	-2.27
24.225	-31.875	-2.27
24.225	-29.325	-2.27
24.225	-26.775	-2.27
24.225	-24.225	-2.27
24.225	-21.675	-2.27
24.225	-19.125	-2.27
24.225	-16.575	-2.27
24.225	-14.025	-2.27
24.225	-11.475	-2.27
24.225	-8.925	-2.27
24.225	-6.375	-2.27
24.225	-3.825	-2.27
24.225	-1.275	-2.27
24.225	1.275	-2.27
24.225	3.825	-2.27
24.225	6.375	-2.27
24.225	8.925	-2.27
24.225	11.475	-2.27
24.225	14.025	-2.27
24.225	16.575	-2.27
24.225	19.125	-2.27
24.225	21.675	-2.27
24.225	24.225	-2.27
24.225	26.775	-2.27
24.225	29.325	-2.27
24.225	31.875	-2.27
26.775	-36.975	-2.27
26.775	-34.425	-2.27
26.775	-31.875	-2.27
26.775	-29.325	-2.27
26.775	-26.775	-2.27
26.775	-24.225	-2.27
26.775	-21.675	-2.27
26.775	-19.125	-2.27
26.775	-16.575	-2.27
26.775	-14.025	-2.27
26.775	-11.475	-2.27
26.775	-8.925	-2.27
26.775	-6.375	-2.27
26.775	-3.825	-2.27
26.775	-1.275	-2.27
26.775	1.275	-2.27
26.775	3.825	-2.27
26.775	6.375	-2.27
26.775	8.925	-2.27
26.775	11.475	-2.27
26.775	14.025	-2.27
26.775	16.575	-2.27
26.775	19.125	-2.27
26.775	21.675	-2.27
26.775	24.225	-2.27
26.775	26.775	-2.27
26.775	29.325	-2.27
26.775	31.875	-2.27
29.325	-36.975	-2.27
29.325	-34.425	-2.27
29.325	-31.875	-2.27
29.325	-29.325	-2.27
29.325	-26.775	-2.27
29.325	-24.225	-2.27
29.325	-21.675	-2.27
29.325	-19.125	-2.27
29.325	-16.575	-2.27
29.325	-14.025	-2.27
29.325	-11.475	-2.27
29.325	-8.925	-2.27
29.325	-6.375	-2.27
29.325	-3.825	-2.27
29.325	-1.275	-2.27
29.325	1.275	-2.27
29.325	3.825	-2.27
29.325	6.375	-2.27
29.325	8.925	-2.27
29.325	11.475	-2.27
29.325	14.025	-2.27
29.325	16.575	-2.27
29.325	19.125	-2.27
29.325	21.675	-2.27
29.325	24.225	-2.27
29.325	26.775	-2.27
29.325	29.325	-2.27
29.325	31.875	-2.27
31.875	-36.975	-2.27
31.875	-34.425	-2.27
31.875	-31.875	-2.27
31.875	-29.325	-2.27
31.875	-26.775	-2.27
31.875	-24.225	-2.27
31.875	-21.675	-2.27
31.875	-19.125	-2.27
31.875	-16.575	-2.27
31.875	-14.025	-2.27
31.875	-11.475	-2.27
31.875	-8.925	-2.27
31.875	-6.375	-2.27
31.875	-3.825	-2.27
31.875	-1.275	-2.27
31.875	1.275	-2.27
31.875	3.825	-2.27
31.875	6.375	-2.27
31.875	8.925	-2.27
31.875	11.475	-2.27
31.875	14.025	-2.27
31.875	16.575	-2.27
31.875	19.125	-2.27
31.875	21.675	-2.27
31.875	24.225	-2.27

3. Phase II Argile and Rhead Model

40.8,40.8
2.55,2.27
0
0,1
112
X,Y,Z CO-ORDINATES OF TIN ATOMS

-20.4000	-20.4000	0.000000
-20.4000	-17.3400	0.130000
-20.4000	-14.2800	0.330000
-20.4000	-11.2200	0.330000
-20.4000	-8.16000	0.130000
-15.3000	-20.4000	0.000000
-15.3000	-17.3400	0.130000
-15.3000	-14.2800	0.330000
-15.3000	-11.2200	0.330000
-15.3000	-8.16000	0.130000
-10.2000	-20.4000	0.000000
-10.2000	-17.3400	0.130000
-10.2000	-14.2800	0.330000
-10.2000	-11.2200	0.330000
-10.2000	-8.16000	0.130000
-5.10000	-20.4000	0.000000
-5.10000	-17.3400	0.130000
-5.10000	-14.2800	0.330000
-5.10000	-11.2200	0.330000
-5.10000	-8.16000	0.130000
0.000000	-20.4000	0.000000
0.000000	-17.3400	0.130000
0.000000	-14.2800	0.330000
0.000000	-11.2200	0.330000
0.000000	-8.16000	0.130000
5.10000	-20.4000	0.000000
5.10000	-17.3400	0.130000
5.10000	-14.2800	0.330000
5.10000	-11.2200	0.330000
5.10000	-8.16000	0.130000
10.2000	-20.4000	0.000000
10.2000	-17.3400	0.130000
10.2000	-14.2800	0.330000
10.2000	-11.2200	0.330000
10.2000	-8.16000	0.130000
15.3000	-20.4000	0.000000
15.3000	-17.3400	0.130000
15.3000	-14.2800	0.330000
15.3000	-11.2200	0.330000
15.3000	-8.16000	0.130000
-20.4000	-5.10000	0.000000
-20.4000	-2.04000	0.130000
-20.4000	1.02000	0.330000
-20.4000	4.08000	0.330000
-20.4000	7.14000	0.130000
-15.3000	-5.10000	0.000000
-15.3000	-2.04000	0.130000
-15.3000	1.02000	0.330000
-15.3000	4.08000	0.330000
-15.3000	7.14000	0.130000
-10.2000	-5.10000	0.000000
-10.2000	-2.04000	0.130000
-10.2000	1.02000	0.330000
-10.2000	4.08000	0.330000
-10.2000	7.14000	0.130000
-5.10000	-5.10000	0.000000

2.55 0
0 2.55
1
-1.275 1.275 0.0

XSIZE,YSIZE
MINAB,DZ
COMENS
UNIF1,UNIF2
NUMBER OF TIN ATOMS
X,Y,Z CO-ORDINATES OF TIN ATOMS

-5.10000	-2.04000	0.130000
-5.10000	1.02000	0.330000
-5.10000	4.08000	0.330000
-5.10000	7.14000	0.130000
0.000000	-5.10000	0.000000
0.000000	-2.04000	0.130000
0.000000	1.02000	0.330000
0.000000	4.08000	0.330000
0.000000	7.14000	0.130000
5.10000	-5.10000	0.000000
5.10000	-2.04000	0.130000
5.10000	1.02000	0.330000
5.10000	4.08000	0.330000
5.10000	7.14000	0.130000
10.2000	-5.10000	0.000000
10.2000	-2.04000	0.130000
10.2000	1.02000	0.330000
10.2000	4.08000	0.330000
10.2000	7.14000	0.130000
15.3000	-5.10000	0.000000
15.3000	-2.04000	0.130000
15.3000	1.02000	0.330000
15.3000	4.08000	0.330000
15.3000	7.14000	0.130000
-20.4000	10.2000	0.000000
-20.4000	13.2600	0.130000
-20.4000	16.3200	0.330000
-20.4000	19.3800	0.330000
-15.3000	10.2000	0.000000
-15.3000	13.2600	0.130000
-15.3000	16.3200	0.330000
-15.3000	19.3800	0.330000
-10.2000	10.2000	0.000000
-10.2000	13.2600	0.130000
-10.2000	16.3200	0.330000
-10.2000	19.3800	0.330000
-5.10000	10.2000	0.000000
-5.10000	13.2600	0.130000
-5.10000	16.3200	0.330000
-5.10000	19.3800	0.330000
0.000000	10.2000	0.000000
0.000000	13.2600	0.130000
0.000000	16.3200	0.330000
0.000000	19.3800	0.330000
5.10000	10.2000	0.000000
5.10000	13.2600	0.130000
5.10000	16.3200	0.330000
5.10000	19.3800	0.330000
10.2000	10.2000	0.000000
10.2000	13.2600	0.130000
10.2000	16.3200	0.330000
10.2000	19.3800	0.330000
15.3000	10.2000	0.000000
15.3000	13.2600	0.130000
15.3000	16.3200	0.330000
15.3000	19.3800	0.330000

AX AY
BX BY
NSUB
COPPER POSITIONS IN SUBSTRATE LATTICE

4. Phase II Overlayer Model

40.8,40.8 XSIZE,YSIZE
2.55,2.27 MINAB,DZ
0 COMENS
0,1 UNIF1,UNIF2
104

-20.4000	-20.4000	0.000000	-10.2000	0.000000	0.000000
-17.8500	-17.8500	0.000000	-10.2000	5.10000	0.000000
-20.4000	-15.3000	0.000000	-7.65000	7.65000	0.000000
-20.4000	-10.2000	0.000000	-5.10000	-5.10000	0.000000
-17.8500	-7.65000	0.000000	-2.55000	-2.55000	0.000000
-15.3000	-20.4000	0.000000	-5.10000	0.000000	0.000000
-12.7500	-17.8500	0.000000	-5.10000	5.10000	0.000000
-15.3000	-15.3000	0.000000	-2.55000	7.65000	0.000000
-15.3000	-10.2000	0.000000	0.000000	-5.10000	0.000000
-12.7500	-7.65000	0.000000	2.55000	-2.55000	0.000000
-10.2000	-20.4000	0.000000	0.000000	0.000000	0.000000
-7.65000	-17.8500	0.000000	0.000000	5.10000	0.000000
-10.2000	-15.3000	0.000000	2.55000	7.65000	0.000000
-10.2000	-10.2000	0.000000	5.10000	-5.10000	0.000000
-7.65000	-7.65000	0.000000	7.65000	-2.55000	0.000000
-5.10000	-20.4000	0.000000	5.10000	0.000000	0.000000
-2.55000	-17.8500	0.000000	5.10000	5.10000	0.000000
-5.10000	-15.3000	0.000000	7.65000	7.65000	0.000000
-5.10000	-10.2000	0.000000	10.2000	-5.10000	0.000000
-2.55000	-7.65000	0.000000	12.7500	-2.55000	0.000000
0.000000	-20.4000	0.000000	10.2000	0.000000	0.000000
2.55000	-17.8500	0.000000	10.2000	5.10000	0.000000
0.000000	-15.3000	0.000000	12.7500	7.65000	0.000000
0.000000	-10.2000	0.000000	15.3000	-5.10000	0.000000
2.55000	-7.65000	0.000000	17.8500	-2.55000	0.000000
5.10000	-20.4000	0.000000	15.3000	0.000000	0.000000
7.65000	-17.8500	0.000000	15.3000	5.10000	0.000000
5.10000	-15.3000	0.000000	17.8500	7.65000	0.000000
5.10000	-10.2000	0.000000	-20.4000	10.2000	0.000000
7.65000	-7.65000	0.000000	-17.8500	12.7500	0.000000
10.2000	-20.4000	0.000000	-20.4000	15.3000	0.000000
12.7500	-17.8500	0.000000	-15.3000	10.2000	0.000000
10.2000	-15.3000	0.000000	-12.7500	12.7500	0.000000
10.2000	-10.2000	0.000000	-15.3000	15.3000	0.000000
12.7500	-7.65000	0.000000	-10.2000	10.2000	0.000000
15.3000	-20.4000	0.000000	-7.65000	12.7500	0.000000
17.8500	-17.8500	0.000000	-10.2000	15.3000	0.000000
15.3000	-15.3000	0.000000	-5.10000	10.2000	0.000000
15.3000	-10.2000	0.000000	-2.55000	12.7500	0.000000
17.8500	-7.65000	0.000000	-5.10000	15.3000	0.000000
-20.4000	-5.10000	0.000000	0.000000	10.2000	0.000000
-17.8500	-2.55000	0.000000	2.55000	12.7500	0.000000
-20.4000	0.000000	0.000000	0.000000	15.3000	0.000000
-20.4000	5.10000	0.000000	5.10000	10.2000	0.000000
-17.8500	7.65000	0.000000	7.65000	12.7500	0.000000
-15.3000	-5.10000	0.000000	5.10000	15.3000	0.000000
-12.7500	-2.55000	0.000000	10.2000	10.2000	0.000000
-15.3000	0.000000	0.000000	12.7500	12.7500	0.000000
-15.3000	5.10000	0.000000	10.2000	15.3000	0.000000
-12.7500	7.65000	0.000000	15.3000	10.2000	0.000000
-10.2000	-5.10000	0.000000	17.8500	12.7500	0.000000
-7.65000	-2.55000	0.000000	15.3000	15.3000	0.000000

2.55	0	AX AY
0	2.55	BX BY
1		NSUB
-1.275	-1.275 0.0	COPPER POSITIONS IN SUBSTRATE LATTICE

5. Phase II Surface Alloy Model

```
40.8,40.8                                   XSIZE,YSIZE
2.55,2.27                                   MINAB,DZ
0                                           COMENS
0,1                                         UNIF1.UNIF2
104
  -20.4000    -20.4000     0.000000          -10.2000     0.000000     0.000000
  -17.8500    -17.8500     0.000000          -10.2000     5.10000      0.000000
  -20.4000    -15.3000     0.000000          -7.65000     7.65000      0.000000
  -20.4000    -10.2000     0.000000          -5.10000    -5.10000      0.000000
  -17.8500    -7.65000     0.000000          -2.55000    -2.55000      0.000000
  -15.3000    -20.4000     0.000000          -5.10000     0.000000     0.000000
  -12.7500    -17.8500     0.000000          -5.10000     5.10000      0.000000
  -15.3000    -15.3000     0.000000          -2.55000     7.65000      0.000000
  -15.3000    -10.2000     0.000000           0.000000   -5.10000      0.000000
  -12.7500    -7.65000     0.000000           2.55000    -2.55000      0.000000
  -10.2000    -20.4000     0.000000           0.000000    0.000000     0.000000
  -7.65000    -17.8500     0.000000           0.000000    5.10000      0.000000
  -10.2000    -15.3000     0.000000           2.55000     7.65000      0.000000
  -10.2000    -10.2000     0.000000           5.10000    -5.10000      0.000000
  -7.65000    -7.65000     0.000000           7.65000    -2.55000      0.000000
  -5.10000    -20.4000     0.000000           5.10000     0.000000     0.000000
  -2.55000    -17.8500     0.000000           5.10000     5.10000      0.000000
  -5.10000    -15.3000     0.000000           7.65000     7.65000      0.000000
  -5.10000    -10.2000     0.000000           10.2000    -5.10000      0.000000
  -2.55000    -7.65000     0.000000           12.7500    -2.55000      0.000000
   0.000000   -20.4000     0.000000           10.2000     0.000000     0.000000
   2.55000    -17.8500     0.000000           10.2000     5.10000      0.000000
   0.000000   -15.3000     0.000000           12.7500     7.65000      0.000000
   0.000000   -10.2000     0.000000           15.3000    -5.10000      0.000000
   2.55000    -7.65000     0.000000           17.8500    -2.55000      0.000000
   5.10000    -20.4000     0.000000           15.3000     0.000000     0.000000
   7.65000    -17.8500     0.000000           15.3000     5.10000      0.000000
   5.10000    -15.3000     0.000000           17.8500     7.65000      0.000000
   5.10000    -10.2000     0.000000          -20.4000     10.2000      0.000000
   7.65000    -7.65000     0.000000          -17.8500     12.7500      0.000000
   10.2000    -20.4000     0.000000          -20.4000     15.3000      0.000000
   12.7500    -17.8500     0.000000          -15.3000     10.2000      0.000000
   10.2000    -15.3000     0.000000          -12.7500     12.7500      0.000000
   10.2000    -10.2000     0.000000          -15.3000     15.3000      0.000000
   12.7500    -7.65000     0.000000          -10.2000     10.2000      0.000000
   15.3000    -20.4000     0.000000          -7.65000     12.7500      0.000000
   17.8500    -17.8500     0.000000          -10.2000     15.3000      0.000000
   15.3000    -15.3000     0.000000          -5.10000     10.2000      0.000000
   15.3000    -10.2000     0.000000          -2.55000     12.7500      0.000000
   17.8500    -7.65000     0.000000          -5.10000     15.3000      0.000000
  -20.4000    -5.10000     0.000000           0.000000    10.2000      0.000000
  -17.8500    -2.55000     0.000000           2.55000     12.7500      0.000000
  -20.4000     0.000000    0.000000           0.000000    15.3000      0.000000
  -20.4000     5.10000     0.000000           5.10000     10.2000      0.000000
  -17.8500     7.65000     0.000000           7.65000     12.7500      0.000000
  -15.3000    -5.10000     0.000000           5.10000     15.3000      0.000000
  -12.7500    -2.55000     0.000000           10.2000     10.2000      0.000000
  -15.3000     0.000000    0.000000           12.7500     12.7500      0.000000
  -15.3000     5.10000     0.000000           10.2000     15.3000      0.000000
  -12.7500     7.65000     0.000000           15.3000     10.2000      0.000000
  -10.2000    -5.10000     0.000000           17.8500     12.7500      0.000000
  -7.65000    -2.55000     0.000000           15.3000     15.3000      0.000000
    5.1   0                                   AX    AY
    0    15.3                                 BX    BY
    19                                        NSUB
-1.275          -1.275          0.0           -1.275          11.475          0.0
 1.275          -1.275          0.0            1.275          11.475          0.0
-1.275           1.275          0.0            2.55            0.0            1.8
 1.275           1.275          0.0            0.0             2.55           1.8
-1.275           3.825          0.0            2.55            5.1            1.8
 1.275           3.825          0.0            0.0             7.65           1.8
-1.275           6.375          0.0            2.55            7.65           1.8
 1.275           6.375          0.0            2.55            10.2           1.8
-1.275           8.925          0.0            0.0             12.75          1.8
 1.275           8.925          0.0
```

6. Phase III Argile and Rhead Model

30.6,30.6 XSIZE,YSIZE
2.55,2.27 MINAB,DZ
0 COMENS
0,1 UNIF1,UNIF2
76

-15.3000	-15.3000	0.000000	0.612000	-12.1380	0.130000
-12.1380	-14.6880	0.130000	4.48800	-8.26200	0.130000
-8.26200	-10.8120	0.130000	-2.55000	2.55000	0.000000
-15.3000	0.00000	0.000000	0.612000	3.16200	0.130000
-12.1380	0.611999	0.130000	4.48800	7.03800	0.130000
-8.26200	4.48800	0.130000	0.00000	-15.3000	0.000000
-15.3000	15.3000	0.000000	3.16200	-14.6880	0.130000
-14.6880	-12.1380	0.130000	7.03800	-10.8120	0.130000
-10.8120	-8.26200	0.130000	0.000000	0.000000	0.000000
-14.6880	3.16200	0.130000	3.16200	0.611999	0.130000
-10.8120	7.03800	0.130000	7.03800	4.48800	0.130000
-13.3620	-5.71200	0.130000	0.000000	15.3000	0.000000
-13.3620	9.58800	0.130000	9.58800	-13.3620	0.130000
-5.71200	-13.3620	0.130000	2.55000	-2.55000	0.000000
-12.7500	-2.55000	0.000000	5.71200	-1.93800	0.130000
-9.58800	-1.93800	0.130000	9.58800	1.93800	0.130000
-5.71200	1.93800	0.130000	2.55000	12.7500	0.000000
-12.7500	12.7500	0.000000	5.71200	13.3620	0.130000
-9.58800	13.3620	0.130000	5.10000	-5.10000	0.000000
-10.2000	-5.10000	0.000000	8.26200	-4.48800	0.130000
-7.03800	-4.48800	0.130000	12.1380	-0.612000	0.130000
-3.16200	-0.612000	0.130000	5.10000	10.2000	0.000000
-10.2000	10.2000	0.000000	8.26200	10.8120	0.130000
-7.03800	10.8120	0.130000	12.1380	14.6880	0.130000
-3.16200	14.6880	0.130000	7.65000	-7.65000	0.000000
-7.65000	-7.65000	0.000000	10.8120	-7.03800	0.130000
-4.48800	-7.03800	0.130000	14.6880	-3.16200	0.130000
-0.612000	-3.16200	0.130000	7.65000	7.65000	0.000000
-7.65000	7.65000	0.000000	10.8120	8.26200	0.130000
-4.48800	8.26200	0.130000	14.6880	12.1380	0.130000
-0.612000	12.1380	0.130000	10.2000	-10.2000	0.000000
-5.10000	-10.2000	0.000000	13.3620	-9.58800	0.130000
-1.93800	-9.58800	0.130000	10.2000	5.10000	0.000000
1.93800	-5.71200	0.130000	13.3620	5.71200	0.130000
-5.10000	5.10000	0.000000	12.7500	-12.7500	0.000000
-1.93800	5.71200	0.130000	12.7500	2.55000	0.000000
1.93800	9.58800	0.130000	15.3000	-15.3000	0.000000
-2.55000	-12.7500	0.000000	15.3000	0.000000	0.000000

2.55	0	AX	AY
0	2.55	BX	BY
1		NSUB	
1.275	1.275 0.0	COPPER POSITIONS IN SUBSTRATE LATTICE	

7. Phase III Overlayer Model

33.15,33.15 XSIZE,YSIZE
2.55,2.27 MINAB,DZ
0 COMENS
0,1 UNIF1,UNIF2
76

-15.3000	-15.3000	0.000000
-12.4950	-12.4950	0.000000
-10.4550	-10.4550	0.000000
-15.3000	0.000000	0.000000
-12.4950	2.80500	0.000000
-10.4550	4.84500	0.000000
-15.3000	15.3000	0.000000
-15.0450	-9.94500	0.000000
-13.0050	-7.90500	0.000000
-15.0450	5.35500	0.000000
-13.0050	7.39500	0.000000
-9.94500	-15.0450	0.000000
-7.90500	-13.0050	0.000000
-12.7500	-2.55000	0.000000
-9.94500	0.255000	0.000000
-7.90500	2.29500	0.000000
-12.7500	12.7500	0.000000
-10.2000	-5.10000	0.000000
-7.39500	-2.29500	0.000000
-5.35500	-0.255000	0.000000
-10.2000	10.2000	0.000000
-7.39500	13.0050	0.000000
-5.35500	15.0450	0.000000
-7.65000	-7.65000	0.000000
-4.84500	-4.84500	0.000000
-2.80500	-2.80500	0.000000
-7.65000	7.65000	0.000000
-4.84500	10.4550	0.000000
-2.80500	12.4950	0.000000
-5.10000	-10.2000	0.000000
-2.29500	-7.39500	0.000000
-0.255000	-5.35500	0.000000
-5.10000	5.10000	0.000000
-2.29500	7.90500	0.000000
-0.255000	9.94500	0.000000
-2.55000	-12.7500	0.000000
0.255000	-9.94500	0.000000
2.29500	-7.90500	0.000000
-2.55000	2.55000	0.000000

0.255000	5.35500	0.000000
2.29500	7.39500	0.000000
0.000000	-15.3000	0.000000
2.80500	-12.4950	0.000000
4.84500	-10.4550	0.000000
0.000000	0.000000	0.000000
2.80500	2.80500	0.000000
4.84500	4.84500	0.000000
0.000000	15.3000	0.000000
5.35500	-15.0450	0.000000
7.39500	-13.0050	0.000000
2.55000	-2.55000	0.000000
5.35500	0.255000	0.000000
7.39500	2.29500	0.000000
2.55000	12.7500	0.000000
5.10000	-5.10000	0.000000
7.90500	-2.29500	0.000000
9.94500	-0.255000	0.000000
5.10000	10.2000	0.000000
7.90500	13.0050	0.000000
9.94500	15.0450	0.000000
7.65000	-7.65000	0.000000
10.4550	-4.84500	0.000000
12.4950	-2.80500	0.000000
7.65000	7.65000	0.000000
10.4550	10.4550	0.000000
12.4950	12.4950	0.000000
10.2000	-10.2000	0.000000
13.0050	-7.39500	0.000000
15.0450	-5.35500	0.000000
10.2000	5.10000	0.000000
13.0050	7.90500	0.000000
15.0450	9.94500	0.000000
12.7500	-12.7500	0.000000
12.7500	2.55000	0.000000
15.3000	-15.3000	0.000000
15.3000	0.000000	0.000000

2.55	0	AX AY
0	2.55	BX BY
1		NSUB
0.0	0.0 0.0	COPPER POSITIONS IN SUBSTRATE LATTICE

8. Phase III Surface Alloy Model

```
30.6,30.6                                   XSIZE,YSIZE
2.55,2.27                                   MINAB,DZ
0                                           COMENS
0,1                                         UNIF1,UNIF2
76
  -15.3000    -15.3000    0.000000      -2.55000    2.55000    0.000000
  -12.4950    -12.4950    0.000000       0.255000   5.35500    0.000000
  -10.4550    -10.4550    0.000000       2.29500    7.39500    0.000000
  -15.3000     0.000000   0.000000       0.000000  -15.3000    0.000000
  -12.4950     2.80500    0.000000       2.80500   -12.4950    0.000000
  -10.4550     4.84500    0.000000       4.84500   -10.4550    0.000000
  -15.3000     15.3000    0.000000       0.000000   0.000000   0.000000
  -15.0450    -9.94500    0.000000       2.80500    2.80500    0.000000
  -13.0050    -7.90500    0.000000       4.84500    4.84500    0.000000
  -15.0450     5.35500    0.000000       0.000000   15.3000    0.000000
  -13.0050     7.39500    0.000000       5.35500   -15.0450    0.000000
  -9.94500    -15.0450    0.000000       7.39500   -13.0050    0.000000
  -7.90500    -13.0050    0.000000       2.55000   -2.55000    0.000000
  -12.7500    -2.55000    0.000000       5.35500    0.255000   0.000000
  -9.94500     0.255000   0.000000       7.39500    2.29500    0.000000
  -7.90500     2.29500    0.000000       2.55000    12.7500    0.000000
  -12.7500     12.7500    0.000000       5.10000   -5.10000    0.000000
  -10.2000    -5.10000    0.000000       7.90500   -2.29500    0.000000
  -7.39500    -2.29500    0.000000       9.94500   -0.255000   0.000000
  -5.35500    -0.255000   0.000000       5.10000    10.2000    0.000000
  -10.2000     10.2000    0.000000       7.90500    13.0050    0.000000
  -7.39500     13.0050    0.000000       9.94500    15.0450    0.000000
  -5.35500     15.0450    0.000000       7.65000   -7.65000    0.000000
  -7.65000    -7.65000    0.000000       10.4550   -4.84500    0.000000
  -4.84500    -4.84500    0.000000       12.4950   -2.80500    0.000000
  -2.80500    -2.80500    0.000000       7.65000    7.65000    0.000000
  -7.65000     7.65000    0.000000       10.4550    10.4550    0.000000
  -4.84500     10.4550    0.000000       12.4950    12.4950    0.000000
  -2.80500     12.4950    0.000000       10.2000   -10.2000    0.000000
  -5.10000    -10.2000    0.000000       13.0050   -7.39500    0.000000
  -2.29500    -7.39500    0.000000       15.0450   -5.35500    0.000000
 -0.255000    -5.35500    0.000000       10.2000    5.10000    0.000000
  -5.10000     5.10000    0.000000       13.0050    7.90500    0.000000
  -2.29500     7.90500    0.000000       15.0450    9.94500    0.000000
 -0.255000     9.94500    0.000000       12.7500   -12.7500    0.000000
  -2.55000    -12.7500    0.000000       12.7500    2.55000    0.000000
  0.255000    -9.94500    0.000000       15.3000   -15.3000    0.000000
   2.29500    -7.90500    0.000000       15.3000    0.000000   0.000000

2.55      -2.55                         AX    AY
2.55       2.55                         BX    BY
4                                       NSUB
1.275      1.275      0.0               COPPER POSITIONS IN SUBSTRATE LATTICE
1.275     -1.275      0.0
```

9. Phase IV Argile and Rhead Model

33.15,33.15 XSIZE,YSIZE
2.55,2.27 MINAB,DZ
0 COMENS
0,1 UNIF1,UNIF2
97

-15.3000	-15.3000	0.000000
-14.2290	-12.2655	0.300000
-11.2710	-13.3620	0.300000
-8.13450	-14.2290	0.300000
-13.3365	-9.23100	0.300000
-10.3020	-10.3020	0.000000
-7.03800	-11.1690	0.300000
-12.1380	-6.06900	0.300000
-9.23100	-7.03800	0.300000
-5.96700	-8.13450	0.300000
-5.10000	-15.3000	0.000000
-4.02900	-12.2655	0.300000
-1.07100	-13.3620	0.300000
2.06550	-14.2290	0.300000
-3.13650	-9.23100	0.300000
-0.102000	-10.3020	0.000000
3.16200	-11.1690	0.300000
-1.93800	-6.06900	0.300000
0.968999	-7.03800	0.300000
4.23300	-8.13450	0.300000
5.10000	-15.3000	0.000000
6.17100	-12.2655	0.300000
9.12900	-13.3620	0.300000
12.2655	-14.2290	0.300000
7.06350	-9.23100	0.300000
10.0980	-10.3020	0.000000
13.3620	-11.1690	0.300000
8.26200	-6.06900	0.300000
11.1690	-7.03800	0.300000
14.4330	-8.13450	0.300000
15.3000	-15.3000	0.000000
-15.3000	-5.10000	0.000000
-14.2290	-2.06550	0.300000
-11.2710	-3.16200	0.300000
-8.13450	-4.02900	0.300000
-13.3365	0.968999	0.300000
-10.3020	-0.102000	0.000000
-7.03800	-0.969001	0.300000
-12.1380	4.13100	0.300000
-9.23100	3.16200	0.300000
-5.96700	2.06550	0.300000
-5.10000	-5.10000	0.000000
-4.02900	-2.06550	0.300000
-1.07100	-3.16200	0.300000
2.06550	-4.02900	0.300000
-3.13650	0.968999	0.300000
-0.102000	-0.102000	0.000000
3.16200	-0.969001	0.300000
-1.93800	4.13100	0.300000
0.968999	3.16200	0.300000
4.23300	2.06550	0.300000
5.10000	-5.10000	0.000000
6.17100	-2.06550	0.300000
9.12900	-3.16200	0.300000
12.2655	-4.02900	0.300000
7.06350	0.968999	0.300000
10.0980	-0.102000	0.000000
13.3620	-0.969001	0.300000
8.26200	4.13100	0.300000
11.1690	3.16200	0.300000
14.4330	2.06550	0.300000
15.3000	-5.10000	0.000000
-15.3000	5.10000	0.000000
-14.2290	8.13450	0.300000
-11.2710	7.03800	0.300000
-8.13450	6.17100	0.300000
-13.3365	11.1690	0.300000
-10.3020	10.0980	0.000000
-7.03800	9.23100	0.300000
-12.1380	14.3310	0.300000
-9.23100	13.3620	0.300000
-5.96700	12.2655	0.300000
-5.10000	5.10000	0.000000
-4.02900	8.13450	0.300000
-1.07100	7.03800	0.300000
2.06550	6.17100	0.300000
-3.13650	11.1690	0.300000
-0.102000	10.0980	0.000000
3.16200	9.23100	0.300000
-1.93800	14.3310	0.300000
0.968999	13.3620	0.300000
4.23300	12.2655	0.300000
5.10000	5.10000	0.000000
6.17100	8.13450	0.300000
9.12900	7.03800	0.300000
12.2655	6.17100	0.300000
7.06350	11.1690	0.300000
10.0980	10.0980	0.000000
13.3620	9.23100	0.300000
8.26200	14.3310	0.300000
11.1690	13.3620	0.300000
14.4330	12.2655	0.300000
15.3000	5.10000	0.000000
-15.3000	15.3000	0.000000
-5.10000	15.3000	0.000000
5.10000	15.3000	0.000000
15.3000	15.3000	0.000000

2.55 0 AX AY
0 2.55 BX BY
1 NSUB
1.275 1.275 0.0 COPPER POSITIONS IN SUBSTRATE LATTICE

10. Phase IV Overlayer Model

35.7,35.7 XSIZE,YSIZE
2.55,2.27 MINAB,DZ
0 COMENS
0,1 UNIF1,UNIF2
109

-15.3000	-15.3000	0.000000
-12.7500	-15.3000	0.000000
-7.65000	-15.3000	0.000000
-15.3000	-12.7500	0.000000
-10.2000	-12.7500	0.000000
-10.2000	-10.2000	0.000000
-12.7500	-10.2000	0.000000
-7.65000	-10.2000	0.000000
-15.3000	-7.65000	0.000000
-10.2000	-7.65000	0.000000
-5.10000	-15.3000	0.000000
-2.55000	-15.3000	0.000000
2.55000	-15.3000	0.000000
-5.10000	-12.7500	0.000000
0.000000	-12.7500	0.000000
0.000000	-10.2000	0.000000
-2.55000	-10.2000	0.000000
2.55000	-10.2000	0.000000
-5.10000	-7.65000	0.000000
0.000000	-7.65000	0.000000
5.10000	-15.3000	0.000000
7.65000	-15.3000	0.000000
12.7500	-15.3000	0.000000
5.10000	-12.7500	0.000000
10.2000	-12.7500	0.000000
10.2000	-10.2000	0.000000
7.65000	-10.2000	0.000000
12.7500	-10.2000	0.000000
5.10000	-7.65000	0.000000
10.2000	-7.65000	0.000000
15.3000	-15.3000	0.000000
15.3000	-12.7500	0.000000
15.3000	-7.65000	0.000000
-15.3000	-5.10000	0.000000
-12.7500	-5.10000	0.000000
-7.65000	-5.10000	0.000000
-15.3000	-2.55000	0.000000
-10.2000	-2.55000	0.000000
-10.2000	0.000000	0.000000
-12.7500	0.000000	0.000000
-7.65000	0.000000	0.000000
-15.3000	2.55000	0.000000
-10.2000	2.55000	0.000000
-5.10000	-5.10000	0.000000
-2.55000	-5.10000	0.000000
2.55000	-5.10000	0.000000
-5.10000	-2.55000	0.000000
0.000000	-2.55000	0.000000
0.000000	0.000000	0.000000
-2.55000	0.000000	0.000000
2.55000	0.000000	0.000000
-5.10000	2.55000	0.000000
0.000000	2.55000	0.000000
5.10000	-5.10000	0.000000
7.65000	-5.10000	0.000000
12.7500	-5.10000	0.000000
5.10000	-2.55000	0.000000
10.2000	-2.55000	0.000000
10.2000	0.000000	0.000000
7.65000	0.000000	0.000000
12.7500	0.000000	0.000000
5.10000	2.55000	0.000000
10.2000	2.55000	0.000000
15.3000	-5.10000	0.000000
15.3000	-2.55000	0.000000
15.3000	2.55000	0.000000
-15.3000	5.10000	0.000000
-12.7500	5.10000	0.000000
-7.65000	5.10000	0.000000
-15.3000	7.65000	0.000000
-10.2000	7.65000	0.000000
-10.2000	10.2000	0.000000
-12.7500	10.2000	0.000000
-7.65000	10.2000	0.000000
-15.3000	12.7500	0.000000
-10.2000	12.7500	0.000000
-5.10000	5.10000	0.000000
-2.55000	5.10000	0.000000
2.55000	5.10000	0.000000
-5.10000	7.65000	0.000000
0.000000	7.65000	0.000000
0.000000	10.2000	0.000000
-2.55000	10.2000	0.000000
2.55000	10.2000	0.000000
-5.10000	12.7500	0.000000
0.000000	12.7500	0.000000
5.10000	5.10000	0.000000
7.65000	5.10000	0.000000
12.7500	5.10000	0.000000
5.10000	7.65000	0.000000
10.2000	7.65000	0.000000
10.2000	10.2000	0.000000
7.65000	10.2000	0.000000
12.7500	10.2000	0.000000
5.10000	12.7500	0.000000
10.2000	12.7500	0.000000
15.3000	5.10000	0.000000
15.3000	7.65000	0.000000
15.3000	12.7500	0.000000
-15.3000	15.3000	0.000000
-12.7500	15.3000	0.000000
-7.65000	15.3000	0.000000
-5.10000	15.3000	0.000000
-2.55000	15.3000	0.000000
2.55000	15.3000	0.000000
5.10000	15.3000	0.000000
7.65000	15.3000	0.000000
12.7500	15.3000	0.000000
15.3000	15.3000	0.000000

2.55	0	AX AY
0	2.55	BX BY
1		NSUB
1.275	1.275	0.0 COPPER POSITIONS IN SUBSTRATE LATTICE

11. Phase IV Surface Alloy Model

30.6,30.6 XSIZE,YSIZE
2.55,2.27 MINAB,DZ
0 COMENS
0,1 UNIF1,UNIF2
109

-15.3000	-15.3000	0.000000
-12.7500	-15.3000	0.000000
-7.65000	-15.3000	0.000000
-15.3000	-12.7500	0.000000
-10.2000	-12.7500	0.000000
-10.2000	-10.2000	0.000000
-12.7500	-10.2000	0.000000
-7.65000	-10.2000	0.000000
-15.3000	-7.65000	0.000000
-10.2000	-7.65000	0.000000
-5.10000	-15.3000	0.000000
-2.55000	-15.3000	0.000000
2.55000	-15.3000	0.000000
-5.10000	-12.7500	0.000000
0.000000	-12.7500	0.000000
0.000000	-10.2000	0.000000
-2.55000	-10.2000	0.000000
2.55000	-10.2000	0.000000
-5.10000	-7.65000	0.000000
0.000000	-7.65000	0.000000
5.10000	-15.3000	0.000000
7.65000	-15.3000	0.000000
12.7500	-15.3000	0.000000
5.10000	-12.7500	0.000000
10.2000	-12.7500	0.000000
10.2000	-10.2000	0.000000
7.65000	-10.2000	0.000000
12.7500	-10.2000	0.000000
5.10000	-7.65000	0.000000
10.2000	-7.65000	0.000000
15.3000	-15.3000	0.000000
15.3000	-12.7500	0.000000
15.3000	-7.65000	0.000000
-15.3000	-5.10000	0.000000
-12.7500	-5.10000	0.000000
-7.65000	-5.10000	0.000000
-15.3000	-2.55000	0.000000
-10.2000	-2.55000	0.000000
-10.2000	0.000000	0.000000
-12.7500	0.000000	0.000000
-7.65000	0.000000	0.000000
-15.3000	2.55000	0.000000
-10.2000	2.55000	0.000000
-5.10000	-5.10000	0.000000
-2.55000	-5.10000	0.000000
2.55000	-5.10000	0.000000
-5.10000	-2.55000	0.000000
0.000000	-2.55000	0.000000
0.000000	0.000000	0.000000
-2.55000	0.000000	0.000000
2.55000	0.000000	0.000000
-5.10000	2.55000	0.000000
0.000000	2.55000	0.000000
5.10000	-5.10000	0.000000
7.65000	-5.10000	0.000000
12.7500	-5.10000	0.000000
5.10000	-2.55000	0.000000
10.2000	-2.55000	0.000000
10.2000	0.000000	0.000000
7.65000	0.000000	0.000000
12.7500	0.000000	0.000000
5.10000	2.55000	0.000000
10.2000	2.55000	0.000000
15.3000	-5.10000	0.000000
15.3000	-2.55000	0.000000
15.3000	2.55000	0.000000
-15.3000	5.10000	0.000000
-12.7500	5.10000	0.000000
-7.65000	5.10000	0.000000
-15.3000	7.65000	0.000000
-10.2000	7.65000	0.000000
-10.2000	10.2000	0.000000
-12.7500	10.2000	0.000000
-7.65000	10.2000	0.000000
-15.3000	12.7500	0.000000
-10.2000	12.7500	0.000000
-5.10000	5.10000	0.000000
-2.55000	5.10000	0.000000
2.55000	5.10000	0.000000
-5.10000	7.65000	0.000000
0.000000	7.65000	0.000000
0.000000	10.2000	0.000000
-2.55000	10.2000	0.000000
2.55000	10.2000	0.000000
-5.10000	12.7500	0.000000
0.000000	12.7500	0.000000
5.10000	5.10000	0.000000
7.65000	5.10000	0.000000
12.7500	5.10000	0.000000
5.10000	7.65000	0.000000
10.2000	7.65000	0.000000
10.2000	10.2000	0.000000
7.65000	10.2000	0.000000
12.7500	10.2000	0.000000
5.10000	12.7500	0.000000
10.2000	12.7500	0.000000
15.3000	5.10000	0.000000
15.3000	7.65000	0.000000
15.3000	12.7500	0.000000
-15.3000	15.3000	0.000000
-12.7500	15.3000	0.000000
-7.65000	15.3000	0.000000
-5.10000	15.3000	0.000000
-2.55000	15.3000	0.000000
2.55000	15.3000	0.000000
5.10000	15.3000	0.000000
7.65000	15.3000	0.000000
12.7500	15.3000	0.000000
15.3000	15.3000	0.000000

10.2 0 AX AY
0 10.2 BX BY
22 NSUB

1.275	1.275	0.0
1.275	3.825	0.0
1.275	6.375	0.0
1.275	8.925	0.0
3.825	1.275	0.0
3.825	3.825	0.0
3.825	6.375	0.0
3.825	8.925	0.0
6.375	1.275	0.0
6.375	3.825	0.0
6.375	6.375	0.0
6.375	8.925	0.0
8.925	1.275	0.0
8.925	3.825	0.0
8.925	6.375	0.0
8.925	8.925	0.0
5.1	0.0	1.8
2.55	2.55	1.8
0.0	5.1	1.8
7.65	2.55	1.8
2.55	7.65	1.8
7.65	7.65	1.8